Laser Doppler Vibrometry for Cardiovascular Monitoring and Photoacoustic Imaging

Doctoral Thesis

to be awarded the degree of

Doctor in Mechanical Engineering (Dr.-Ing.)

submitted by

Laura Mignanelli, M.Sc.

from Loreto, Italy

approved by the Faculty of
Mathematics/Computer Science and Mechanical Engineering,
Clausthal University of Technology

Date of oral examination
02.02.2021

Dean:	Prof. Dr.-Ing. Volker Wesling
Chairperson of the Board of Examiners:	Prof. Dr.-Ing Christian Bohn
Supervising Tutor:	Prof. Dr.-Ing. Christian Rembe
Reviewer:	Prof. Dr. Regina Semmler-Ludwig
Reviewer:	Prof. Lorenzo Scalise, PhD

To my family

Foreword

This dissertation is based on my work as research assistant at the Institute for Electrical Information Technology at the Clausthal University of Technology.
First and foremost, I would like to thank Prof.Dr.-Ing.Christian Rembe for the opportunity he gave me to do my PhD under his valuable guidance and mentorship and for contributing to my personal and professional development.
I thank Prof. Dr. Regina Semmler-Ludwig and Prof. Lorenzo Scalise, PhD for reviewing my doctoral thesis.

During my time at the institute, I had the opportunity to meet very nice colleagues and I am very grateful for it. As is common in an academic environment, colleagues come and go, but some of them will always remain in my heart, such as my most-of-the-time-office-mate Thorben Ziemer whom I thank for everything he did for me as colleague and as a friend.
A special thanks goes to Dr.-Ing. Robert Kowarsch, Dr.-Ing. Georg Bauer and Xiaodong Cao, for all the valuable talks (scientific and unscientific), and advice throughout my time at the institute.
Several thanks go to Marvin Schewe for letting me use the device he developed, for the photos he took for my thesis and for his valuable support when I needed it.
Thanks to all of my other colleagues in the metrology and control system group for all their useful discussions.
A great thank goes to the technicians of the electric and mechanic workshops Tobias Jäger, Kerstin Hecht, Max Bendix, Volker Lührig and Christian Schubert for the construction of the electrical and mechanical components I needed for my research.
Thanks to our institute secretary Marion Bollmann for always being there for me and for making all of the bureaucratic tasks a lot easier.
Many thanks go to Fabian Uhrner of the Institute of Organic Chemistry for helping me by building gelatin-based phantoms.
A huge thank goes to Prof. Paolo Castellini, PhD and Prof. Milena Martarelli, PhD for borrowing me their pulsed laser for the very firsts measurements.
A special thank goes to the researchers of the Institute of Non-Metallic Materials Raschid Al-Mukadam, Dr.-Ing. Hansjörg Bornhöft and Dr.-Ing. Gundula Helsch for letting me use their testing instrumentation.
Thanks to Rogin Gilbert for the valuable discussion about parameter identification and for being such a good friend.
Thanks to all the students I supervised for contributing to my research, and to all

the students and friends and relatives of mine who took part in my measurements as subjects.

When I first came to Clausthal, I meet a very special family which treated me as a daughter; I thank Bernhard and Barbara Kraft from the bottom of my heart. Clausthal gave me the occasion to meet very true friends Francesca El-Louzi, Franziska Kowarsch, Maria Angeles Martinez Page, and Jessica Pfau who I would like to thank for making my stay in Clausthal a wonderful time. The biggest thank goes to Lucia Cortina Eduarte for being always there for me and for literally everything she did for me starting from backing cakes to taking care of me the whole time as my family would do.

Many thanks go to Gabi Riemann for her moral support and advises.

I would like to thank my life-long-friends Carolina Volpini and Marea Graciotti for being always there for me.

I am particularly thankful to Nicoletta Paolini for helping me understand that no matter how distant you are, if you really want to, you can always find a way to be close to each other, even closer than ever.

Let me express my sincere appreciation to my parents, my sister Chiara and my grandparents' siblings for all the love they provided me during this time and for conferring me the strength I needed. My heartfelt gratitude goes to my boyfriend Julian Riemann for teaching me to never give up, for believing in me, and for his unwavering support and patience during these years.

Clausthal-Zellerfeld, Feruary 2021 *Laura Mignanelli*

Abstract

Nowadays, techniques for health monitoring mainly require physical contact with patients, which is not always ideal. Non-contact health monitoring has become an important research topic in the last decades.
The non-contact detection of a patient's health condition represents a beneficial tool in different biomedical fields. Examples can be found in intensive care, home health care, the nursing of the elderly, the monitoring of physical efforts, and in human-machine interactions.

Cardiovascular diseases (CV) are one of the most spread causes of death in developed countries. Their monitoring techniques involve physical contact with patients. A non-contact technique for cardiovascular monitoring could overcome problems related to the contact with the patient such as skin lesions. It could also expand the availability of monitoring to those cases where contact is not possible or should be avoided to reduce the exposure of medical personnel to biochemical hazard conditions.

Several research groups have investigated different techniques for non-contact monitoring of health; among them, the laser Doppler Vibrometry (LDVy) has one of the highest accuracies and signal to noise ratios for cardiorespiratory signals detection. Moreover, the simplicity of data processing, the long-distance measurement range, and the high bandwidth make the laser Doppler vibrometer (LDV) suitable for daily measurements.

LDVy is an interferometric technique employed for the measurements of displacement or velocity signals in various fields. In particular, it is deployed in the biomedical field for the extraction of several cardiovascular parameters, such as the PR-time. Generally, the extraction of these parameters requires ideal measuring conditions (measuring spot and laser direction), which are not realistic for daily monitoring in non-laboratory conditions, and especially in tracking applications.

The first scientific hypothesis of this work is that the PR-time detected with LDV has an acceptable uncertainty for a realistic variety of measurement spot positions and angles of the incident laser beam. Therefore, I investigated the uncertainty contribution to the detection of the PR-time from LDV signals resulting from the laser beam direction and from the measurement point position; these investigations were carried out with a multipoint laser Doppler vibrometer.
The uncertainties were evaluated according to the Guide to the Expression of Uncertainty in Measurement. Successively, the ranges of PR-time values where it is possible to state with 95% certainty that a diagnosis is correct are identified.

Normal values of PR-time are included in the range 120 ms − 200 ms. For single value measurements with precise alignment the reliable range for the detection of the healthy condition is 146.4 ms − 173.6 ms. The detection of CV diseases is reliable for measured values lower than 93.6 ms and greater than 226.4 ms.
For mean value measurements with precise alignment the reliable range for the detection of the healthy condition is 126.6 ms − 193.4 ms. The detection of CV diseases is reliable for measured values lower than 113.4 ms and greater than 206.6 ms. Therefore, for measured values included in the mentioned ranges, the detection of the PR-time and relative diagnosis with the LDVy in non-laboratory conditions is reliable.
The method for the estimation of the uncertainty contribution proposed in this work can be applied to other cardiovascular parameters extracted with the LDVy.

Recently, the LDVy was employed for the detection of tumors in tissue-mimic phantoms as a non-contact alternative to the ultrasound sensors employed in photoacoustic imaging (PAI). A non-contact method has considerable advantages for photoacustic imaging, too. Several works present the possibility to perform PAI measurements with LDVy. However, a successful detection of the signals generated by a tumor depends on the metrological characteristics of the LDV, on the properties of the tumor and of the tissue. The conditions under which a tumor is detectable with the laser Doppler vibrometer has not been investigated yet.

The second scientific hypothesis of this work is that, under certain conditions, photoacoustic imaging measurements with LDVy are feasible. Therefore, I identified those conditions to determine the detection limits of LDVy for PAI measurements. These limits were deduced by considering the metrological characteristics of a commercial LDV, the dimensions and the position of the tumor in the tissue. I derived a model for the generation and propagation of PA signals and its detection with an LDV. The model was validated by performing experiments on silicone tissue-micking phantoms. The validated model with breast-tissue parameters reveals the limits of tumor detection with LDVy-based PAI.
The results show that commercial LDVs can detect tumors with a minimal radius of ≈ 350 µm reliably if they are located at a maximal depth in tissue of ≈ 2 cm. Depending on the position of the detection point, the maximal depth can diminish and depending on the absorption characteristics of the tumor, the detection range increases.

Contents

Nomenclature

ACRONYMS, ABBREVIATIONS AND DEFINITIONS

1D	One-dimensional/One Dimension
3D	Three-dimensional/Three Dimensions
3D-LDV	Three-dimensional-LDV
A/D	Analog/Digital
ANS	Autonomic Nervous System
AV	Atrioventricular
AV-Block	Atrioventricular Block
BC	Bragg Cell
BMI	Body Mass Index
BP	Blood Pressure
BS	Beam Splitter
C	First prominent peak at the end of the typical VCG signal of a heartbeat acquired on the thorax
CD-wave	Third wave of the typical VCG signal of a heartbeat acquired on the thorax
CV	Cardiovascular
D	Second prominent peak at the end of the typical VCG signal of a heartbeat acquired on the thorax
D/A	Digital/Analog
DC	Direct Current
DFG	Deutsche Forschungsgemeinschaft
DLDV	Self-made Differential Laser Doppler Vibrometer
DSC	Differential Scanning Calorimetry
ECG	Electrocardiogram

GUM	Guide to the Expression of Uncertainties in Measurements
HR	Heart Rate
HRV	Heart Rate Variability
IR	Infrared
LaVIR	Self-made Laser Doppler Vibrometer IR
LDV	Laser Doppler Vibrometer
LDVy	Laser Doppler Vibrometry
LUS	Laser Ultrasound
LVET	Left Ventricular Ejection Time
MEMS	Micro-Electro-Mechanical Systems
MPE	Maximal Permissible Exposure
MPV	Multipoint Vibrometer
NICU	Neontal Intensive Care Unit
P-wave	First characteristic wave of the ECG
PA	Photoacoustic
PAI	Photoacoustic Imaging
PBS	Polarized Beam Splitter
PD	Photodiode
PET	Polyethylene terephthalate
PPG	Photopletismography
PPT	Pulse Transit Time
P_{V}	Maximum of P_{V}-wave
P_{V}-wave	First wave of the typical VCG signal of a heartbeat acquired on the thorax
PWV	Pulse Wave Velocity
PZT	Lead zirconate titanate
QRS-complex	Second characteristic wave of the ECG
R-peak	Peak of the QRS-complex
RMS	Root Mean Square

RP	Respiration Period
R_V	Negative peak of the R_V-wave
R_V-wave	Second wave of the typical VCG signal of a heartbeat acquired on the thorax
SCG	Seismocardiography
SLDV	Scanning Laser Doppler Vibrometer
T-wave	Third wave wave of the ECG
TIA	Transimpedance Amplifier
US	Ultrasound
VCG	Optical Vibrocardiography

CONSTANTS

π	Mathematical constant ..... $\pi = 3.14159...$
c	Speed of light ..... $c = 299792458$ m/s
h	Plank constant ..... $h = 6.62607015 \cdot 10^{-34}$ Js

COMMON SYMBOLS

B	Bandwidth ..... Hz
f	Frequency ..... Hz
HR	Heart Rate ..... bpm
i	Summation index, running index ..... −
J	Maximum value for the summation index j ..... −
j	Summation index, running index ..... −
N	Maximum value for the summation index i ..... −
PR	Time interval between the start of the P-wave and the start of the QRS-complex (Also referred to as PR-interval, PR-time PQ-interval or PQ-time) ..... s
s	Displacement ..... m
SNR	Signal to Noise Ratio ..... dB
$s'_{\mathrm{RL},\mathbb{I}}$	Displacement resolution limit for the case $\mathbb{I}$ ..... $\mathrm{m}/\sqrt{\mathrm{Hz}}$
$s_{\mathrm{RL},\mathbb{I}}(B)$	Displacement resolution limit for the bandwidth B for the case $\mathbb{I}$ m

t	Time	s
U	Voltage	V
v	Velocity	m/s
γ	Angle between the vibration vector and the direction of the laser beam of the LDV	°
λ	Wavelength	m

CHAPTER 3: LIST OF SYMBOLS

f_{BC}	Frequency shift operated by the Bragg cell	Hz
f_{D}	Doppler frequency shift	Hz
k	Wavenumber	m^{-1}
K_{PD}	Sensitivity of the photodiode	A/W
M	Modulation index	−
n	Refraction index	−
OPL	Optical Path Length	m
R_{TIA}	Transimpedance	Ω
s_0	Displacement vibration amplitude	m
U_{sn}	Root mean square shot noise	V
U_{TIA}	Output voltage of the amplifier	V
$U_{\mathrm{TIA,RMS}}$	Root mean square of the output signal of the amplifier	V
W_{m}	Optical power of the measurement laser beam	W
W_{r}	Optical power of the reference laser beam	W
ϵ	Heterodyne efficiency	−
Ω	Modulation frequency	Hz
ω	Angular frequency	rad/s
ϕ	Doppler phase shift	rad
ϕ_0	Initial phase	°
Ψ	Reflective index	−

CHAPTER 4: LIST OF SYMBOLS

$A_{\Delta,\mathbb{I}}$	Measurement deviation of type-A resulting from $\mathbb{I}$ ..... s
b	Span of the type-B uncertainty ..... s
$B_{\Delta,\mathbb{I}}$	Measurement deviation of type-B resulting from $\mathbb{I}$ ..... s
$c_{\mathrm{p},\varphi,\vartheta}$	Maximum value of the normalized cross-correlation ..... –
$\boldsymbol{e}_{\mathbb{I}}$	Unit vector for the configuration defined by $\mathbb{I}$ ..... –
$\boldsymbol{E}_{\mathbb{I}}$	Matrix for the change of coordinates for the condition defined by the subscrit $\mathbb{I}$ ..... –
g	Generic function ..... –
K	Coverage factor ..... –
$LDV_{\mathbb{I}}$	LDV in the configuration $\mathbb{I}$ ..... –
m	Generic measurement ..... –
$P_{\mathrm{V}}R_{\mathrm{V},\mathbb{I}}$	Time interval between the P_{V} and R_{V} points (Also referred to as $P_{\mathrm{V}}R_{\mathrm{V}}$-time) for the case $\mathbb{I}$ ..... s
RR	Interval between two consecutive R-peaks in the ECG (Also referred to as RR-interval) ..... s
$sd_{\mathbb{I}}$	Empirical standard deviation for the case $\mathbb{I}$ ..... s
$t_{(68\%)}(N)$	Student-t factor for a confidence interval of 68.27% for N measurements ..... –
$t_{P_{\mathrm{V}}}$	Time instant of the P_{V}-point in the VCG signal ..... s
$t_{R_{\mathrm{V}}}$	Time instant of the R_{V}-point in the VCG signal ..... s
u	Uncertainty ..... s
$u_{\mathrm{A},\mathbb{I}}$	Type-A uncertainty resulting from the contribution of $\mathbb{I}$ ..... s
U_{belt}	Signal obtained from the respiratory belt V
$u_{\mathrm{B},\mathbb{I}}$	Type-B uncertainty resulting from the contribution of $\mathbb{I}$ ..... s
u_{c}	Combined uncertainty ..... s
u_{e}	Expanded uncertainty ..... s
U_{ECG}	Voltage signal delivered by the II-lead of the ECG V
$\boldsymbol{v}_{\mathbb{I}}$	3D-velocity vector for the case $\mathbb{I}$ ..... m/s

$v_{\mathbb{I}}$	Velocity signals acquired with the laser beam oriented in the direction defined by the unit vector $\boldsymbol{e}_{\mathbb{I}}$ ..... m/s
w_j	Generic quantity with $j = 1, .., J$ ..... –
x	Cartesian coordinate x ..... m
y	Cartesian coordinate y ..... m
z	Cartesian coordinate z ..... m
α	Significance level ..... –
$\Delta_{\mathrm{ECG,VCG},\mathbb{I}}$	Calibration factor between the ECG and VCG for the condition deined by the subscript $\mathbb{I}$ ..... s
$\Delta P_{\mathrm{V}} R_{\mathrm{V}\mathbb{I}}$	Difference between the $P_{\mathrm{V}} R_{\mathrm{V}}$ in the reference condition and $P_{\mathrm{V}} R_{\mathrm{V}\mathbb{I}}$ s
μ	Expected value ..... ms
σ	Standard deviation ..... ms
φ	Angle in the xy-plane that identifies the direction of the laser beam of a LDV (or of a measuring head of the MPV) ..... °
$\varphi_{\mathbb{I}}$	Angle φ for the configuration described by the subscript $\mathbb{I}$ ..... °
ϑ	Angle between the direction of the laser beam of a LDV (or of a measuring head of the MPV) and the xy-plane ..... °
$\vartheta_{\mathbb{I}}$	Angle ϑ for the configuration described by the subscript $\mathbb{I}$ ..... °

CHAPTER 5: LIST OF SYMBOLS

A_{e}	Specific optical energy deposition ..... $\mathrm{J/m^3}$
B_{rel}	Relative bandwidth ..... –
C_{P}	Heat capacity at constant pressure ..... J/(kg K)
C_{V}	Heat capacity at constant volume ..... J/(kg K)
d	Width of the tissue mimicking phantom ..... m
d_i	Width of the phantoms used for the computation of the acoustic attenuation with $i = 1, 2$ ..... m
d_{height}	Height of the tissue mimicking phantom ..... m
E_0	Energy at the surface of the phantom ..... J

$E_{\mathbb{I}}$	Energy	J
$f_{\mathbb{I}}$	Frequency described by $\mathbb{I}$	Hz
F_0	Fluence at the surface of the phantom	$\mathrm{J/m^2}$
$F_{\mathbb{I}}$	Fluence	$\mathrm{J/m^2}$
G	Constant	$\mathrm{m^2/s}$
g	Function	$\mathrm{m^2/s^2}$
$\boldsymbol{H}$	Hessian Matrix	–
$H(\cdot)$	Heaviside function	–
L	Loss term	–
l_i	Final length of the specimen i with $i = 1, ..., 10$	m
$l_{0,i}$	Initial length of the specimen i with $i = 1, ..., 10$	m
NEP	Noise equivalent pressure	$\mathrm{Pa}/\sqrt{\mathrm{Hz}}$
p	Pressure rise due to thermoelastic expansion	Pa
p_0	Initial pressure rise due to thermoelastic expansion	Pa
p_{in}	Pressure wave traveling inward	Pa
p_{inr}	Pressure wave traveling inward and reflected on the origin	Pa
p_{M}	Maximum of the pressure signal accounting for the acoustic attenuation	Pa
$p_{\hat{\mathrm{M}}}$	Maximum of the pressure signal	Pa
p_{out}	Pressure wave traveling outward	Pa
$p_{\mathrm{RMS},\mathbb{I}}$	Root mean square pressure resolution for the case $\mathbb{I}$	Pa
q	Positive constant that depends on the tissue water content, for soft tissue q is almost 1	–
r	Distance from the center of the sphere	m
$\boldsymbol{r}$	Position vector in spherical coordinates	m
R^2	Coefficient of determination	–
r_{D_i}	Distance between the detection point and the center of the absorbing sphere S_i	m
r_{PL}	Radius of the laser beam at the surface of the phantom	m

R_S	Radius of the sphere	m
$R_\mathrm{S,min}$	Radius of the minimal detectable spherical object	m
S_i	Sphere with $i = 1, 2, 3$	–
S_s	Power spectral density of the displacement signal	m^2/Hz
S_v	Power spectral density of the velocity signal	$\mathrm{m}^2/(\mathrm{s}^2\mathrm{Hz})$
$s_\hat{\mathrm{M}}$	Maximum of the displacement signal	m
s_M	Maximum of the displacement signal accounting for the acoustic attenuation	m
T	Temperature rise due to PA effect	Pa
t_delay	Delay between arrival time of the PA wave	s
V	Volume	m^3
v'_RL	Velocity resolution limit	$\mathrm{m}^2/(\mathrm{s}^2\sqrt{\mathrm{Hz}})$
$v_\mathrm{RL}(B)$	Velocity resolution limit for a given bandwidth B	m/s
$v_{\mathrm{s},\mathbb{I}}$	Sound velocity in soft or breast tissue or in $\mathbb{I}$	m/s
$v_\hat{\mathrm{M}}$	Maximum of the velocity signal	m/s
v_M	Maximum of the velocity signal accounting for the acoustic attenuation	m/s
$\boldsymbol{v}_{\mathrm{M},\mathbb{I}}$	Vector of the data v_M for the case $\mathbb{I}$	m/s
$v_{\mathrm{M},\mathbb{I}}$	Data of v_M for the case $\mathbb{I}$	m/s
Z	Acoustic impedance	Rayl
z_{S_i}	Depth of the sphere S_i	m
α_0	Acoustic attenuation coefficient	dB/(MHz cm)
α_{T°	Coefficient of linear thermal expansion	K^{-1}
β	Coefficient of volumetric thermal expansion	K^{-1}
Δp_M	Maximal deviation between $\lvert\Delta p_\mathrm{M,H}\rvert$ and $\lvert\Delta p_\mathrm{M,L}\rvert$	%
$\Delta p_{\mathrm{M},\mathbb{I}}$	Percental pressure deviation with respect to the frequency $f_\mathbb{I}$	%
Γ	Grüneisen Parameter	–
κ	Isothermal compressibility	Pa^{-1}

μ_{a}	Optical absorption coefficient ..... m^{-1}
$\mu_{\mathrm{a,sil}}$	Optical absorption coefficient of the silicone rubber spheres ... m^{-1}
μ_{att}	Acoustic attenuation ..... dB/cm or Np/cm
$\overline{\mu}_{\mathrm{att}}$	Mean acoustic attenuation between the $f_{\mathrm{L},-3\mathrm{dB}}$ and $f_{\mathrm{H},-3\mathrm{dB}}$ dB/cm or Np/cm
μ_{eff}	Effective optical attenuation in tissue ..... m^{-1}
$\mu_{\mathrm{tot,sil}}$	Total optical attenuation coefficient of the silicone rubber .... m^{-1}
$\Psi_{\mathrm{air/sil}}$	Reflective factor at the surface skin/air ..... –
ρ	Density ..... $\mathrm{kg/m}^3$
τ	Duration of the bipolar signal ..... s
ξ	Angle of the polarizer ..... °

Subscripts $\mathbb{I}$

	No subscript
$_{-3\mathrm{dB}}$	Half-power bandwidth
$_{90°}$	Configuration with the laser beam oriented with $\vartheta = 90°$
$_{\mathrm{F}_i}$	Filtered with the technique F_i $(i = 1, 2, 3)$
$_{\mathrm{art}}$	Artificial VCG signal
$_{\mathrm{breath}}$	Breathing component of the VCG signal on the thorax
$_{\mathrm{c}}$	Central
$_{\mathrm{comp}}$	Compensation between ECG and VCG
$_{\mathrm{DLDV}}$	Infrared Self-made differential LDV
$_{\mathrm{end}}$	First zero-point of the spectrum
$_{\mathrm{H}}$	Higher/Upper limit of the Bandwidth
$_{i}$	Configuration/Sample $i = 1, ..., N$
$_{\mathrm{IR}}$	Infrared LDV
$_{\mathrm{US}}$	Ultrasound sensor
$_{\mathrm{L}}$	Lower limit of the Bandwidth
$_{\hat{\mathrm{M}}}$	Maximum
$_{\mathrm{mean}}$	Mean value

meas	Experiments
noise	Noise component of the VCG signal on the thorax
p	Measurement point
ref	Reference/ideal VCG signal on the thorax without disturbances
sil	Silicone rubber
skin	Skin
S	Sphere
sim	Simulation
x	x-direction of the Cartesian coordinate system
y	y-direction of the Cartesian coordinate system
z	z-direction of the Cartesian coordinate system
φ,ϑ	Arbitrary direction defined by the angles φ and ϑ
ϑ	Configuration the laser beam oriented with $\vartheta = 40°, 60°120°, 140°$

OPERATORS

$*$	Convolution
$\cdot$	Scalar product
$\det \boldsymbol{A}$	Determinant of $\boldsymbol{A}$
$\max(i, j)$	Maximum value between i and j
$\overline{a}$	Mean value of a
$\parallel \boldsymbol{a} \parallel$	Norm of the vector $\boldsymbol{a}$
$\mid \cdot \mid$	Absolute value

1. Introduction

Non-contact health monitoring has become an important research topic in the last decades. The non-contact detection of the health condition of patients represents a beneficial tool in different biomedical fields [1–5].
Examples can be found in intensive care, home health care, the nursing of the elderly, monitoring of physical efforts, rehabilitation, and human-machine interactions such as measuring the stress of drivers.

Applications like home health care, rehabilitation, or the nursing of the elderly would be improved by measuring the health condition of the patient with an instrument fixed on the ceiling. With digital imaging processing and a tracking system, it could be possible to recognize the patient and to perform a measurement of their vital signs every time they are needed.
A non-contact method would be very helpful to avoid lesions and infections to premature babies in neonatal intensive care units (NICUs). In fact, these babies are usually monitored with several contact instruments which load their tiny bodies when attached to their sensitive skin [1, 2, 6, 7].

Traditional monitoring methods require cables or sensors attached to the body, which restrict movements. A non-contact technique opens the possibility to monitor the vital functions of athletes during rehabilitation [8] and during competition, allowing medical staff to determine if the athletes are in the proper condition for high physical loads.
An additional field of application for non-contact health monitoring techniques is offered by the increasing networking and digitization of the industrial society. The new concept of industry known as the industrial internet of things [9, 10], contemplates more interaction between human and machine. Human and machine have to work in close coordination. In critical work steps, the willingness or the ability of the human to assume or maintain control should be reliably assessed before the transfer of the control from a human to a machine, or conversely. For this task, in non-laboratory conditions, it is first necessary to detect relevant medical parameters non-invasively. The detected parameters give information about the level of attention of the person. In this way, the willingness and the capability of the human to take over control can be identified [11–19].

Nowadays, techniques for health monitoring mainly require contact with patients. In some occasions, a contact-technique is inconvenient or difficult to apply on peculiar groups of patients, such as a baby in a NICU, or patients with burned skin [1–3].

Cardiovascular (CV) diseases are one of the most spread causes of death in developed countries, and the main instrumentation for cardiovascular monitoring and diagnosis requires contact with the patient. An example is the electrocardiogram (ECG).

The ECG delivers information such as the heart rate (HR) and heart rate variability (HRV). The HR and HRV are among the primary vital signs used to detect arrhythmia, heart block or other heart diseases. ECG measures the electrical signal that triggers the contraction of the heart muscles by placing electrodes in standard positions. Trained personnel are required because misplacing the electrodes may lead to erroneous measurements.
Electrodes are single-use and uncomfortable for both long-term and daily measurements, especially if the subject has extremely sensitive or burned skin. The patient mobility and comfort can be limited by the several cables [1]. Moreover, the cables may represent a potential risk of strangulation for infants.

Photopletismography (PPG) is a non-invasive alternative to ECG for the analysis of the HR and the HRV. PPG is an optical measuring technique where a small sensor placed on the ear lobe or on the fingertip measures the peripheral pulse.
The measuring principle is based on the change of light absorption during a cardiac cycle. The light absorption changes depending on the concentration of the oxyhemoglobin, which is related to the change of blood volume due to the pressure pulse. The skin is illuminated with a red or infrared light source and the reflected or transmitted light is measured [20]. PPG gives a quick indication of the cardiac rhythm [2]. For this reason, PPG has been extensively used in wearable sensors to monitor the cardiac activity during the day and during physical activity. However, the PPG proved to be less accurate, more vulnerable to motion artifacts and less reliable for long term recording in respect to the ECG [2, 3].

A non-contact technique for the detection of the electrical signal of the heart would allow overcoming the limitations of ECG mentioned above. Moreover, it would reduce the risk of exposure of medical personnel to toxic material and biochemical hazard conditions. In addition, ECG has limitations in combination with magnetic resonance imaging. A non-contact technique could overcome this problem, too [21, 22].

The blood pressure (BP) is another vital parameter that can be monitored at home. Blood pressure provides information regarding the functionality of the cardiovascular system. The measurement of the continuous pressure waveform in real time is possible with an invasive technique, such as intra-arterial pressure catheters. This technique is not suitable for daily practice [23].

Tonometry is a non-invasive alternative to monitor the pressure wave. This technology is a contact method and suffers drawbacks like the compression of the artery against the bone; the artery is flattened because of the presence of the sensor and measurement of the undisturbed pulse is not possible. Difficulties performing

measurements are found in obese patients and usually specialized personnel is required [23].

The arterial stiffness is also an important parameter related to CV risk. Arterial stiffness is estimated by knowing the pulse wave velocity (PWV). The PWV is measured with applanation tonometry. This method consists of placing two contact sensors on the carotid artery and on the groin. Applanation tonometry calculates the time delay of the pulse wave between the two sensors. Since the distance between the two measurement locations is known, the PWV can be calculated.
The drawbacks of this technique are the same mentioned for the case of the tonometry for the measurement of the pressure wave.
Moreover, the position of the sensor is individuated by palpation and this can be uncomfortable for the patient who has to be undressed.
A non-contact monitoring technique could be quite helpful also for the monitoring of peculiar respiratory events in infants to prevent sudden infant death.

The spirometer is the standard device to measure breathing parameters; it is invasive and it requires a cooperation of the patient. Therefore, its application on infants is difficult to achieve [24, 25].

A non-contact technique would be convenient and recommended in the above-mentioned cases and in many others, too. In the last decades, several research groups have investigated different techniques for non-contact monitoring of health. The non-contact methods are based on different working principles as reported in Scalise [1], Kranjec, Beguš, et al. [2] and Al-Naji, Gibson, et al. [3].
The main categories are:

1. radar-based monitoring system [26–33],
2. laser-based monitoring system [21, 22, 34–45] ,
3. image-based monitoring system [20, 46–52],
4. other methods [53–57].

The radar-based method includes continuous wave, frequency modulated or ultra-wide band pulsed radar. These methods exploit different principles such as time of flight, phase-shift and Doppler effect. An antenna is used to transmit electromagnetic radiations. The radiation reaches the target and the antenna detects the reflected signal. For radar-based methods which rely on the Doppler effect, the phase difference between the sending and receiving signal is proportional to the movement of the target according to the Doppler effect.
In this case, the target is the human body which vibrates because of vital signs like respiration, blood flow, muscle contraction, and other vibration sources. Laser-based methods also rely on the Doppler effect.
The principle of functioning of laser-based monitoring systems is the same as that of

the electromagnetic one but it uses laser light instead of a radar, and the measuring spot is very small.
The laser Doppler technique has been introduced in Yeh and Cummins [58]. A common laser-based system which has been used to extract several medical parameters is the laser Doppler vibrometer (LDV) [59]. The extraction of CV parameters from vibration signals acquired with an LDV is called optical Vibrocardiography (VCG) [21].

Laser-based techniques can extract cardiorespiratory signals at long-operative distances, while the radar techniques has limitations.
In particular, at distances greater than one meter the signals obtained with radar techniques are affected by noise caused by the increased free space loss. Therefore, to achieve high resolution and sensitivity at greater distances, radar sensors with both high-frequency and high output power are required. This is a drawback because possible biological effects on the human body are generated [2, 3]. Moreover, it is quite difficult to focalize the electromagnetic waves generated by the radar on one single point, while this is natural with a laser beam.

The image-based monitoring methods use a camera for the acquisition and can be classified depending of the physical quantity measured. There are thermal, color and motion imaging methods.
Thermal imaging systems capture the heat variations caused by the pulsatile blood flow or by the respiration at a certain location of the human body.
The color-based imaging system employs the principle of PPG. The skin is illuminated with a designated light source - red and/or infrared - or ambient light [20]. Depending on the blood volume variation, the optical properties of the skin change and, consequently, the reflected light detected with a camera changes. Physiological information is extracted through signal processing.
The measuring principle of motion-based systems is the recording of the movement of the skin. The video is processed and the cardiorespiratory activity is recognized.
In addition to the electromagnetic-, laser- and image-based methods, other solutions are presented in literature.
Mesleh, Skopin, et al. [53] demonstrate that it is possible to detect the activities of the heart from human speech. Alternative applications propose magnetic induction, capacitive coupling, and ultrasonic sensing methods for the detection of vital signs [1, 54–57].

References [1–4] report a detailed descriptions of the above mentioned techniques. In references [2, 3], the authors performed a comparison of the advantages and disadvantages in terms of costs, measurement duration, reliability, data processing complexity, detection range, and other parameters of these techniques.

Relevant for this thesis is laser Doppler vibrometry (LDVy). LDVy has the highest accuracy and signal to noise ratio among the above-described methods for the detection of cardiorespiratory signals [2]. Other advantages of using LDVy as a non-contact method for medical applications are the immunity to radio-frequency

noise, the simplicity of data processing, the long-distance measurement range, and the high bandwidth. Disadvantages are the high costs, the complex optical interface, and the possibility to measure only one subject at time. However, current research is focused on overcoming these limitations [60–65].

Vibrations originated by the human body itself are in the velocity range of mm/s and displacement range of mm. The resolution of LDV allows for the detection of velocity and displacement smaller of a factor 10^3 and 10^5 than the ones originated by the human body.

In Tabatabai, Oliver, et al. [66], the authors review the applications of LDV in biomedical field. They can be summarized in:

- hearing [67–71],
- dentistry [72, 73],
- biometrics [42, 74–76],
- monitoring of cardiovascular and respiratory activity [6, 7, 21–25, 43–45, 60, 77–87],
- monitoring of muscular activity [88, 89],
- detection of aortic aneurysm [35–37],
- integration of implants non invasively [38],
- heart valve testing [39, 40, 90].

The monitoring of cardiovascular parameters is of particular interest for this work. Pinotti, Paone, et al. [43] presented one of the first studies utilizing the LDV for the detection of vibration on human body. The authors performed preliminary tests for the registration of the pressure pulse on the carotid artery. Several studies to assess the possibility to detect CV parameters followed [6, 7, 21–25, 44, 45, 60, 77–87]. These studies are based on the fact that vascular movements propagate through tissues and generate skin motion. These movements can be detected with LDV (for details and references, see Chapter 2).

All of these works demonstrate that LDV is capable of detecting several parameters. However, there are still open questions about what the limits of LDV for the estimation of CV parameters and what the uncertainties of the parameters extracted from the vibrations are.

The detection of cardiovascular parameters from the vibration signals is affected by interfering factors like undesired disturbances (noise, breathing and involuntary movements), setup features (metrological properties of the measuring instrument, measurement point and so forth) and uncertainties resulting from the post processing (filtering, algorithms).

Usually, during the post-processing of these signals, the measuring conditions are considered to be ideal and only the uncertainties related to the algorithms used are calculated [23].
However, variations from the ideal situation are always present in practice. These variations lead to a deformation of the velocity and displacement signals and, therefore, the derived cardiovascular parameters are affected by uncertainties.
In particular, Luik, Mignanelli, et al. [91] demonstrated the feasibility of LDV for heart rhythm detection and for the PR-time detection[a].
Measurements were obtained under optimized conditions such as the position of the measured point.
A detailed uncertainty analysis for the variation of the realistic variety of parameters is still missing in the state of the art. Statements about the reliability of the measurements are missing, too.

The **first scientific hypothesis** of this work is that the PR-time detected with LDV has an acceptable uncertainty for a realistic variety of measurement spot positions and angles of the incident laser beam that allow a reliable statement of the healthy condition of the patient.

In this work, I investigate the uncertainty contribution resulting from the laser beam direction and from the measurement point position on the typical pattern of the vibration signals with a multipoint LDV. The uncertainty analysis is performed with a different approach with respect to Luik, Mignanelli, et al. [91].
The aim is to quantify the uncertainties resulting from the above mentioned interferences and evaluate their effects on the detection of the PR-time and, consequentely, on the reliability of the diagnosis. In this way, it is possible to understand the limits and the suitability of the application of LDV for health monitoring, especially for daily clinical routine and generally for tracking applications.
The method for the estimation of the uncertainty contribution proposed in this work can be applied to other cardiovascular parameters extracted with LDV.

It is not only possible to obtain medical information from the vibrations generated by the human body itself. It is also possible to generate vibrations in the human body to obtain information about it. This is the case of classical ultrasound (US) [92], and photoacoustic imaging (PAI) or photoacoustic tomography [93–96].

Classical medical ultrasounds or ultrasonography is an imaging technique for internal body structures such as blood vessels, joints, tendons, muscles, and internal organs. Ultrasound probes are used to send ultrasound pulses into the body part of interest and to receive it back after being reflected from the internal structures. The boundary between structures with different acoustic properties reflects the ultrasonic wave. The received signal is recorded and converted in an image called sonogram [92].

[a] The PR-time is an important CV parameter; see Paragraph 4.1.2.3

The main applications of PAI are the imaging of molecules, microvasculature, tumors, brain, and small animals [93–96]. PAI is an imaging technique based on the photoacoustic effect. It requires the use of a short-pulse light source for the irradiation of the tissue, which leads to the generation of a broadband photoacoustic (PA) wave. PA waves propagate through the tissue. They are normally detected with ultrasound transducers and an image is computed.

In addition to the applications mentioned in Tabatabai, Oliver, et al. [66], in the last years, LDV has been tested for contactless ultrasound imaging with a laser ultrasonics approach in the human body [97] and for contactless photoacoustic imaging (PAI) [98–101].

The drawbacks of the classical ultrasound technology mainly stem from the contact nature of the technique such as the need of a coupling medium and the sensitivity to tissue compression. The pressure applied on the probe by the operator performing the measurement has an influence on the image-quality.

These disadvantages can be improved with full non-contact laser ultrasound (LUS) imaging [97]. LUS uses the same principle as medical ultrasounds but it uses laser light instead of ultrasound sensors for both the generation and the detection of the ultrasonic waves. The excitation is performed with a pulse laser (eye- and skin-safe). The optical energy is converted into acoustic energy on the surface of the target and an interferometer detects the generated wave on the surface.

In Zhang, Fincke, et al. [97], the authors demonstrate the feasibility of a full non-contact ultrasound system for measurements in tissue-mimicking phantoms, in animal tissue, and in humans in-vivo.

Photoacoustic imaging can benefit from non-contact methods. As for the case of LUS, non-contact PAI overcomes the limitations of ultrasound contact sensors commonly used for it.

In addition, non-contact PAI would expand the application field of PAI to in-vivo measurements where contact with the sensor is infeasible.

Similarly, as for LUS, a pulse laser is used for the generation of acoustic waves. The laser source in LUS minimizes the penetration of the light into the tissue to generate a wave on the surface.

Conversely, PAI laser sources maximize the optical penetration depth by using wavelengths where the optical absorption is low to visualize optical absorbers at the given wavelength as, for example, in hemoglobin. LUS is more advantageous with respect to PAI for the imaging of deep anatomical structure since the optical attenuation is greater than acoustic attenuation.

However, PAI presents advantages with respect to LUS if the investigated biological structures do not have a great acoustic contrast but relevant differences in optical properties as for the case of early stage tumors. Therefore, for the detection of early-stage tumors PAI is more promising than LUS.

In this work, the LDVy as a non-contact alternative to US-sensor technique for PAI is investigated. The detection of PAI signals occurs with ultrasounds

transducers, generally piezoelectric transducers. A non-contact detection of the photoacoustic signals, even if it is not necessary, is desirable in peculiar applications like image guided surgery, wound assessment and ophthalmology [98].
As reported in Tian, Feng, et al. [98], the US transducers used for PAI present a high sensitivity but are limited due to their finite aperture size, the contact nature of the devices, and the need of a coupling medium. The narrow frequency bandwidth of these sensors also represents a limitation. The low and high frequency components of the signals are not detected, leading to a limited imaging spatial resolution.
Therefore, the optical detection of ultrasound represents a valid alternative to the contact US-technologies.

Several research groups investigated different optical techniques for PA applications. As reported in Tian, Feng, et al. [98], there are optical non-contact sensors and optical contact sensors. The latter needs a coupling medium between the sample and the sensors for the detection of the signals.
Optical contact sensors are, for example, Fabry-Perot polymer film sensors, micro-ring sensors and fiber-Bragg grating sensors [102–108]. For this work, the non-contact optical sensors are relevant.
Non-contact optical sensors are mostly based on interferometric techniques and camera detection [109–117]. LDV measures broadband signals and its sensitivity is good enough to detect photoacoustic waves at the surface - in terms of displacement or velocity - generated from a laser pulse with a fluence allowed for application on human tissue.

In the literature, several works present applications of LDV for PAI (see Chapter 2) and show the possibility to perform PAI measurements with LDV. An example is the work of Tian, Feng, et al. [98]. The authors presented a study of an all-optical non-contact PAI by using a commercial laser Doppler vibrometer and performed successfully experiments on a pig brain with an artificial tumor as an absorbing object.

It should be noted that, the amplitude and the time duration of the PA signals are related to the geometry and the optical characteristics of the investigated object.
The laser excitation originates greater or smaller signal amplitudes depending on

1. the position of the absorbing object,
2. the dimensions of the absorbing object,
3. the optical, thermal, and mechanical characteristics of the absorbing object and
4. the optical, thermal, and mechanical characteristics of the surrounding material.

A successful detection of the generated signals depends also on the metrological characteristics of the detector.

The **second scientific hypothesis** of this work is that, under certain conditions, PAI measurements with LDV are feasible. These conditions are related to the four points mentioned above and to the metrological characteristics of the LDV.

In addition to verifying the first scientific hypothesis, the second task of this work is to determine the conditions under which PAI measurements with LDV are feasible, i.e. to the determine the limits of LDVy for PAI.
These limits can be deduced by considering the metrological characteristics of LDV and the geometry of the investigated object and by relating the minimal detectable displacement or velocity of LDV to the smaller detectable object. This aspect has not yet been investigated. In this thesis, a model for the generation and propagation of PA signals and its detection with a LDV is proposed and validated with experiments on silicone rubber tissue-micking phantoms. The validated model with breast-tissue parameters reveals the limits of tumor detection with LDVy-based PAI.
The capability of LDV for PAI measurements is compared to the one of US sensors employed for PAI.

To summarize, the main objectives of this thesis are:

1. to quantify the uncertainties for the detection of the PR-time with LDV, identify the ranges where the measurement is reliable and offer a method to calculate the uncertainty contribution to other CV parameters,

2. to investigate the feasibility of LDV for the detection of photoacoustic signals, theoretically and experimentally.

After preliminary chapters about the state of the art (Chapter 2) and the LDV technology (Chapter 3), Chapter 4 presents the analysis of the first topic. The second topic is addressed in Chapter 5. Chapter 6 presents the conclusions and outlook of this work.

2. State of the Art

In this work, LDVy is employed to measure the physiological vibrations on the human body. Physiological vibrations are, for example, the pulsating motion of blood in vessels or the contraction of the heart.
These vibrations usually have frequency components within 0-100 Hz [118, 119]. The LDV signals acquired on the skin are strictly related to the motion of the underlying vessel or of other anatomical structures.
Since the measuring points are mostly chosen where the vessel is adjacent to the skin, the amplitude of the vibrations can be estimated with a physical model of fluid flow in elastic vessels [74] and stress-strain relationship.

Properties like radius, wall thickness and incremental elastic modulus vary from blood vessel to blood vessel and thus, the generated vibrations during the blood flow present different amplitudes depending on the measuring location and on the anatomic and physiologic characteristics of the subject. Experimental studies show that changes in the diameter dimension during a heartbeat can vary from values around 0.24 mm for the brachial artery and values around 2.8 mm for the ascending aorta [120]. The carotid artery presents a diameter variation of about 0.4 mm.

The expected displacement amplitude of a vibration measurement is included in the range of $10^{-4} - 10^{-3}$ m. Common ultrasound systems such as the one used in reference [121] measure pressure and present a resolution of $1.3 \cdot 10^{-5}$ m for the detection of changes of the diameter of the vessel.
Commercial LDVs present a typical displacement resolution of about 30 fm/$\sqrt{\text{Hz}}$ in optimal conditions [59]. Usually, they have a 2 MHz bandwidth. With these resolution and bandwidth characteristics, the minimal detectable displacement is estimated to be about 42 pm, which is almost factor $10^7 - 10^8$ smaller than the vibration amplitude of the vessel. Infrared (IR) LDV technology at 1550 nm wavelength can measure even smaller amplitudes.

As mentioned in the introduction (Chapter 1), photopletismography (PPG) is a less-invasive alternative to ECG and it has been extensively used in wearable sensors to monitor the cardiac activity during the day and during physical activity. Jeyhani, Mahdiani, et al. [122] presented a comparison between PPG signals and ECG signals for the detection of the heart rate variability (HRV). The authors extracted the typical indicators of the HRV with two different algorithms. The algorithm that provides the best results delivers a mean relative error for HRV parameters obtained from PPG greater than the mean relative error for the same HRV parameters obtained from optical Vibrocardiography (VCG) signals at the

carotid and at the thorax by Morbiducci, Scalise, et al. [21] and Scalise and Morbiducci [22].
In particular, the mean relative errors for the HRV indicators SDNN and RMSSD[a] obtained with the PPG are respectively 2.47% and 5.55% [122]. For the VCG at the carotid the mean errors of the same indicators are 1.12% and 2.94%, respectively; for the VCG at the heart, they are 0.38% and 1.05% for male subjects and 1.25% and 2.80% for female subjects [21, 22].
Thus, LDV is more suitable and reliable for the detection of cardiovascular parameters in comparison to photopletismography.

Generally, LDV presents several advantages compared with other alternative techniques for monitoring the CV activity [2, 3].
The bandwidth of LDV is sufficient to detect all the relevant components of the vibrations in human body for the extraction of CV parameters.
LDV presents high accuracy and signal to noise ratio and the data processing for the extraction of CV parameter is relatively simple.
Concerning the set-up properties, LDV allows long distance measurements, while, for example, the image-based methods mentioned in the introduction (Chapter 1) are limited to short distances.

According to [2, 3], the main disadvantages of LDV are related to the motion artifacts, the high costs, the complex optical interface and the possibility to measure only one subject at a time. However, the high costs and the possibility to measure one subject at a time can be overcome. In fact, scientists are aimed to realize a miniaturized and low cost silicon photonics integrated LDV [123, 124].
The possibility to measure more subjects at time can be obtained with a multipoint laser doppler vibrometer (MPV)[61–65] (see Section 3.3).
Recently, the multipoint vibrometer MPV-800 from the company Polytec GmbH was released on the market. The MPV-800 allows for the simultaneous measurement of forty-eight sites with a working-distance up to 5 m [61]. Moreover, with the MPV-800 both simultaneous vibrations at different points and simultaneous 3D-vibrations can be measured (see Section 3.3).

Since the LDV has been shown to be successful for measuring the vibrations on human body, the interest to expand its applications in other biomedical fields has grown. The detection of the vibration induced to the body like in photoacoustic imaging is an example.

In this chapter, the state of the art of the LDV-applications relevant for this thesis is introduced. Section 2.1 summarizes the previous works about detection of cardiovascular parameters with LDV. Section 2.2 describes previous studies about using LDVy and other interferometric techniques for photoacoustic imaging.

[a]SDNN and RMSSD are explained in Section 4.1. SDNN is the standard deviation of the time interval between heartbeats (NN). RMSSD is the square root of the mean squared differences of successive time interval between heartbeats.

2.1. Monitoring of Cardiovascular and Respiration Activity

Seismocardiography (SGC) is the measurement of the mechanical vibrations generated by the heart to detect cardiovascular parameters.
In recent studies different technologies have been employed. Examples are uniaxial and triaxial piezoelectric accelerometers and uniaxial and triaxial micro-electro-mechanical systems (MEMS) accelerometers, gyroscopes, LDV, etc [125–127]. Reference [128] presents a review of these methods.

This section presents the current research status of the applications of LDV for the detection of cardiovascular (CV) activity, i.e. of optical vibrocardiography (VCG). In Pinotti, Paone, et al. [43] the authors carried out preliminary tests on the carotid artery for the registration of the pressure pulse. Reference [44] presents the approach of measuring the vibration on human body with LDV. The assumption is that vascular movements propagate through the tissue generating skin motion; the amplitude of the skin motion is detectable with LDV. The studies that followed were aimed to assess the possibility to detect different CV parameters. Researchers focused on the detection of the heart rate (HR) and heart rate variability (HRV) by measuring the vibrations mostly on the thorax and on the carotid artery. These studies matched the parameter extracted from the VCG and from a simultaneous recording using a standard technique such as the ECG. The results show that the monitor of the cardiac rate with the LDV is comparable to the reference method [21, 22].

Different research groups evaluated the arterial stiffness by measuring the pulse transit time (PTT) and pulse wave velocity (PWV) with LDV. The changes of the characteristics of the pulse waveform during the propagation relate to obstructions or arterial conditions.
Information about the propagation of the pulse waveform was obtained by simultaneously recording the vibrations generated by arteries at different locations. De Melis, Morbiducci, et al. [83] show that the PTT in young healthy volunteers measured with LDV and arterial applanation tonometry (proved technique for the determination of PTT) are equivalent.
Campo, Segers, et al. [85] reported similar results. Moreover, the same authors measured phantom arteries mimicking real life conditions with a multichannel LDV [45, 84].
The PWV values measured from LDV signals in elastic vessels agree with the theoretically expected values. Other experiments were carried out with a dual-beam LDV in tissue mimicking phantoms and healthy volunteers [123]. The PWV values estimated in these works are reliable.

The blood pressure waveform is detectable with LDV according to the assumption that the displacement on the skin is related to the change of diameter of the

vessel due to the pulse wave. The displacement signal is obtainable by integrating the LDV-velocity signal acquired on the tissue overlying arteries. The recorded waveforms with LDV cannot be directly related to pressure values. A calibration is needed to convert the LDV signal to the pressure signal [79]. In Casacanditella, Cosoli, et al. [82], the authors calibrated the VCG signals on the carotid by means of brachial diastolic and mean blood pressure values measured via the oscillometric method using an exponential model.
The authors observed that the LDV technology allows for the detection of mechanical events of the carotid artery related to hemodynamics with a very high sensitivity. The calibration of the LDV signals can be carried out also with a tonometer measuring on the radial artery as in [23]. The systolic blood pressure measured with LDV has a mean deviation of 8% with respect to the tonometric data, as reported in [23].
The authors also identified the uncertainty due to the integration process, which results in 15%. This uncertainty is not negligible, but it is comparable to the ones of the standard blood pressure measuring devices.
Casacanditella, Cosoli, et al. [81] also presented the LDV-technique as an indirect method for the non-contact measurement of carotid blood pressure. Here, the authors analyzed the LDV traces in comparison to the photoplethysmogram (PPG) to determine the left ventricular ejection time (LVET) at carotid level. The results show a deviation lower than 10% between the two techniques.

The respiration activity can also be monitored with LDV [6, 7, 25].
In particular, measurements on the thorax or abdomen were carried out to determine the respiration rate (RP) of adults and of infants in neonatal intensive care unit (NICU). Usually, a reference measurement with a spirometer is performed. The two techniques show a strong agreement.
The LDV measurements on infants in NICU allow also for the precise identification of irregular inspiration/expiration acts, hiccups and apnea [6, 7, 25]. The change of cardiovascular activity over a respiration cycle is also an important topic for psycho-physiologists. Sirevaag, Casaccia, et al. [80] show that LDV-signals can deliver information of cardiorespiratory interactions.

Cardiac mechanics events generate vibrations which are also detectable with LDVy. In De Melis, Morbiducci, et al. [78], VCG traces allowed for the recognition of heart sounds relative to the closure of the mitral valve, and the closure of the aortic and pulmonary valve. The filling time, which is a critical parameter for the cardiac functionality, could also be measured. The authors performed a comparison between VCG signals acquired on the thorax and digital phonocardiography signals to identify cardiac events. LDV was compared also to other auscultation devices, such as the stethoscope. Certain morphological features are identified as unique to specific heart murmurs [129, 130].

In VCG signals acquired on the thorax, it is possible to distinguish between the vibration pattern generated by the contraction of the atria and the vibration

pattern generated by the contraction of the ventricles; this allows for the detection of the interval between the two contractions. The time interval between these two contractions is called PR-time and it is a very important parameter for a cardiologist [91, 131] (See Section 4.1). In Luik, Mignanelli, et al. [91], measurements on the thorax of healthy subjects present a different pattern with respect to the one of subjects affected by CV diseases. Therefore, atrio-ventricular (AV) blocks are identifiable [91]. In Luik and Kroschel [86], a method to detect atrial fibrillation is presented. Its reliability has not been proven yet.

An important aspect of VCG measurements is the position of the measurement spot. Several studies were carried out to investigate the reliability of the acquisition point by means of scanning and multipoint vibrometers [77, 87, 91, 132].
In Casaccia, Sirevaag, et al. [77] scanning measurements on the carotid were performed to find evidence for local generation of the carotid artery and the importance of precise targeting is highlighted. The spatial distribution of the signal strength can be used as a targeting criterion itself.
In [87], the authors presented a criterion for checking suitable measurement points on the carotid. Multichannel measurements on the thorax performed on one subject revealed a large area where the typical pattern can be detected [91]. Algorithms and filtering techniques to extrapolate the desired parameters from VCG signals efficiently can also be found in literature [86, 133].
To summarize, the detection of cardiovascular parameters from vibration signals is very promising. However, VCG measurements are affected by interfering effects. These effects need to be identified and analyzed. In this way, reliable measurements of cardiovascular parameters can be performed also for daily use at home and in clinical practice. For the daily use at home or in clinic, a miniaturized and cost accessible compact LDV would be required.

The scope of this work is to clarify the limits of LDV for the estimation of the CV parameters. In particular, this work aims to identify and analyze the uncertainty of VCG measurements for the detection of the PR-time and its reliability to make statements about the health condition of the patient.
Uncertainties can be generated by interfering effects such as undesired disturbances, setup features and post processing.

Usually, the measuring conditions are considered to be ideal and only the uncertainty of algorithms and post-processing are estimated [23].
Variations from the ideal situation lead to an uncertainty of the measured velocity and displacement signals and, therefore, of the derived cardiovascular parameter. The uncertainties resulting from setup features are determined in this work.
Moreover, the method proposed for the estimation of the different uncertainty contributions may be extended to other CV parameters. Some typical parameters used to estimate uncertainties are the root mean square error, the mean absolute error and the correlation coefficient. However, in this work, the uncertainty estimation is performed according to the *Guide to the Expression of Uncertainty*

in Measurements [134]. Moreover, the statistical significance of the results is discussed.

2.2. Non-contact Photoacoustic Imaging with Laser Doppler Vibrometry

In this section, previous studies on optical detection of ultrasound for photoacoustic imaging (PAI) are presented.
Particular attention is given to the applications exploiting LDV.

Optical detection of ultrasound can be performed with optical contact sensors like Fabry-Perot polymer film sensors [102–105], micro-ring sensors [106, 107], fiber-Bragg grating sensors [108], and optical non-contact sensors [109–117]. The optical contact sensors need a coupling medium between the sample and the sensors for the detection of the signal. The optical non-contact sensors can overcome some limitations of the contact sensors and they could expand the detection of US to applications where contact is impractical. As already mentioned in the introduction (Chapter 1), the ultrasound transducers used for PAI are generally piezoelectric transducers which present a high sensitivity ($10^{-3} - 10^{-6}$ Pa/$\sqrt{\text{Hz}}$ [135]). However, beside the need of a coupling medium, their finite aperture size is disadvantageous for the quality of the reconstructed image [98]. The narrow frequency bandwidth of these sensors represents also a limitation. In fact, a bad imaging spatial resolution is obtained if the low and high frequency components of the signals are not detected [98]; this presents an additional limitation for the detection of objects with different sizes.

Monchalin [136] presented a review about various optical methods to detect ultrasounds. The author distinguishes between non interferometric and interferometric techniques.
Some years later, Dewhurst and Shan [137] also presented a review of the interferometer systems used for ultrasound detection and Dong, Sun, et al. [138] performed a review of ultrasound detection technology for photoacoustic imaging. Laser Doppler Vibrometry (LDVy) belongs to the free-space-optics category [138].

Free-space-optics have been widely investigated. Examples are presented in the references [109–113]. In [112, 113, 139, 140], the authors used a pulse laser and a confocal Fabry-Perot interferometer in differential configuration for the detection of endogenous and exogenous inclusions in ex-vivo chicken breast and calf brain specimens. They demonstrated that inclusions down to 0.3 mm in size can be detected at depths approaching 1 cm.
Payne, Venugopalan, et al. [141] presented a time-resolved, high-resolution interferometer with up to Å-displacement resolution to detect subsurface blood vessels in tissue phantoms and a human forearm in-vivo.

In [142], the authors modified a Mach-Zehnder interferometer to measure surface displacements generated with the photoacoustic effect with an axial resolution of 0.1 nm with a bandwidth of 80 MHz. The authors provide an algorithm to extract the optical attenuation depth.
Carp, Guerra, et al. [143], with the setup of Payne, Venugopalan, et al. [142] show the possibility to detect the two walls of a tube with a 200 µm diameter at a depth of about 1 cm. Some years later, Carp and Venugopalan [109] provided with the same method, better than 200 µm lateral and 30 µm axial resolution at about 1 cm depth in highly scattering in-vitro and in-vivo model systems.

Speirs and Bishop [144] presented a non-contact pressure sensor for use in photoacoustic tomography based on a Michelson interferometer. The authors obtained tomographic images of blood vessel phantoms with sub-millimeter resolution at depths of several millimeters.

Eom, Park, et al. [145] proposed a method based on a fiber-optic heterodyne interferometer to detect photoacoustic signals in a phantom that contains PET fibers. Successively, Eom, Park, et al. [146] measured the displacement of the blood vasculature of a chicken chorioallantoic membrane with the fiber-optic heterodyne interferometer of reference [145]. The authors analyzed the capability of in vivo 3D-bioimaging and showed that blood vessel structures placed as deep as 3.5 mm are recognizable.

Hochreiner, Bauer-Marschallinger, et al. [110] reported measurements on chicken skin and on tissue mimicking phantom with a non-contact two and three dimensional photoacoustic imaging methods based on a optical fiber-based Mach-Zender interferometer. The authors obtained a minimal detectable displacement corresponding to a minimal detectable pressure for the center frequency of the bandwidth of 380 Pa with a bandwidth of 20 MHz (See Subsection 5.5.3). The values reduces to 50 Pa with a bandwidth of 5 MHz.

The LDV is composed by a laser and a heterodyne interformeter. Since LDV measures broadband signals, it is suitable for photoacoustic detection. Researches that exploited LDV for PAI showed that the sensitivity of LDV is sufficient to detect photoacoustic waves generated from a laser pulse with a fluence allowed for application on human tissue.
Haupt and Wynn [101] presented a LDV-based system for the generation of ultrasound images of a subject with a photoacoustic excitation and without physically contact with the subject.
Olsson, Gren, et al. [100] measured photoacoustic signals in silicone phantoms along a line with a scanning laser vibrometer. The authors used a holographic algorithm to reconstruct the acoustic waves. In this way, the authors could detect absorbing objects at a depth of 16.5 mm.

Xu, Wang, et al. [99] investigated the feasibility of non-contact measurements of photacoustic signals with a commercial laser Doppler vibrometer (RSV-150 Polytec GmbH) . The vibrometer used has a $0 - 2$ MHz measurement bandwidth

and it was integrated to a rotational photoacoustic data acquisition system. This system resolves spherical inclusions with dimension of 500 µm and multi-layered structure with optical contrast in strongly scattering medium. The same LDV was implemented in the set up of Tian, Feng, et al. [98]. In [98], the authors showed the possibility to delineate the boundaries of an artificial tumor in a pig brain. The authors also measured the noise equivalent detection limits of their system and it results in 810 Pa over 1.2 MHz bandwidth.

The reported studies show that PAI with LDV is possible. However, it is necessary to specify that the amplitude of the PA signals is related to the geometry and the optical characteristics of the absorbing object. A smaller object or an object with low absorption coefficient delivers lower amplitude of the signals. The dimension of the smallest detectable object is related to the minimal detectable displacement of the LDV.

In this work, the limits of detection for LDV depending on the metrological characteristics of the device and on the geometry of the investigated object are analyzed.

In Chapter 5, I introduced at first the typical signals generated from a spherical absorbing object and I examined the suitability of the LDV for PAI also in comparison with ultrasonic transducers. In this way, it is possible to state which are the limits of LDV for PAI and when measurements with LDV are feasible or an ultrasonic transducer is needed.
Examples of measurements performed in a tissue mimicking-phantom with a self-made differential vibrometer are also shown and the reliability of the measurement is analyzed.

3. Laser Doppler Vibrometry

In this chapter, the basics of laser Doppler Vibrometry (LDVy) are explained (Section 3.1). An extensive description of the measuring principle is reported in Rembe, Siegmund, et al. [59] and Chiariotti, Rembe, et al. [147].
Here, I limited the explanation of LDVy to the relevant aspects for the understanding of this thesis. Hence, particular importance is given to the resolution (Section 3.2).

In the last years, I supervised the building process of a self-made LDV (Laser Vibrometer InfraRed: LaVIR) with a 1550 nm wavelength [148, 149].
The description of LaVIR can be found in the theses of Fröhner [148] and Reinert [149], which I supervised. A first version of LaVIR is presented in Figure 3.1.

However, the current version of LaVIR has been enhanced by a colleague of mine, Marvin Schewe, working for a Deutsche Forschungsgemeinschaft (DFG) Project[a].
The current version of the self-made vibrometer is presented in Figure 3.2 and has a differential configuration with an external reference beam [150].
In this work, the abbreviation DLDV refers to the self-made differential IR-LDV.
Finally, the full-field vibrometry is briefly presented (Section 3.3).

3.1. Theory of Laser Doppler Vibrometry

Laser Doppler vibrometry (LDVy) is an interferometric technique which is widely used in various engineering applications. LDVy allows for the measurement of displacement or velocity vibrations without contact.
The displacement resolution, s'_{RL} is about 30 fm/$\sqrt{\mathrm{Hz}}$ in optimal conditions, while the velocity resolution v'_{RL} rises from $\approx$ 0.5 nm/s$\sqrt{\mathrm{Hz}}$ to $\approx$ 0.6 µm/s$\sqrt{\mathrm{Hz}}$ in the frequency range from 0 to 2 MHz [59].

Besides the several applications for non-destructive testing, system identification and damage detection in automotive, aerospace industrial and civil field, the laser Doppler vibrometer (LDV) has been shown to be suitable also for biomedical applications thanks to its non-invasiveness and its metrological properties.

Most of commercially available LDV systems use a Helium-Neon laser source (633 nm). In the last decades, the progress in telecommunication, security and military applications has led to the development of LDVs with infrared (IR)

[a]DFG-Project grant 404875250.

technology. In particular, the light at 1550 nm proves to be suitable since it does not penetrate the eye, and it is a class I laser even with 10 mW power.
For a comparison, Helium-Neon lasers are class II with 1 mW laser power. This implicates that the IR-technology has numerous advantages in terms of signal quality.
Moreover, at 1550 nm the skin penetration depth of the light is small [66]. Therefore, more light is scattered back to the device; this leads to an enhancement of the signal for application on the skin.

A LDV is composed by a laser and an interferometer. The laser, as already stated, usually has a wavelength of $\lambda = 633$ nm or $\lambda = 1550$ nm and the most common interferometer configuration used is the Mach-Zender one [59].

Figure 3.1 shows the setup of a single point LDV. The first beam splitter (PBS1) splits the laser beam in two beams: the reference (in green) and the measurement beam (in red). The measurement beam is shifted in frequency by an acoustoptic modulator, Bragg cell (BC). The reference beam remains inside the measurement head while the measurement beam is sent through the objective and impinges on the target.
The objective is composed by focusing optics and a quarter-wave plate. If the target is moving, the light scattered back from the target (in yellow) has a shift in frequency due to the Doppler effect. Usually, the vibrometer has a back-scattered configuration, i.e. the source and the observation point are in the same location.
The Doppler shift f_{D} can be expressed as

$$f_{\mathrm{D}} = \frac{2v}{\lambda} \cos\gamma, \tag{3.1}$$

where v is the velocity of the target, λ is the laser wavelength and γ is the angle between the directions of the velocity and of the laser beam.
If the refraction index n of the propagating medium does not change in space and time [59], the Doppler shift can be expressed in terms of phase $\phi(t)$ or displacement $s(t)$ over time t as follows

$$f_{\mathrm{D}} = \frac{1}{2\pi}\frac{d\phi(t)}{dt} = \frac{k}{2\pi}\frac{d\mathrm{OPL}(t)}{dt} = \frac{2kn}{2\pi}\frac{ds(t)}{dt} = \frac{2nv(t)}{\lambda}, \tag{3.2}$$

where OPL is the optical path length, $s(t)$ is the displacement of the target, $v(t)$ is the instantaneous velocity of the object in the direction of the laser beam and $k = 2\pi/\lambda$ is the wavenumber of coherent light in vacuum.
The back-scattered light is collected by the measuring head and then combined with the reference beam in the beam splitter (BS). The combined laser beams are detected by the photodiodes PD1 and PD2 as shown in Figure 3.1.
The signals detected at the photodiodes PD1 and PD2 are π radians out of phase and they are sent as input to a differential amplifier with the transimpeadance R_{TIA} (balanced detector).

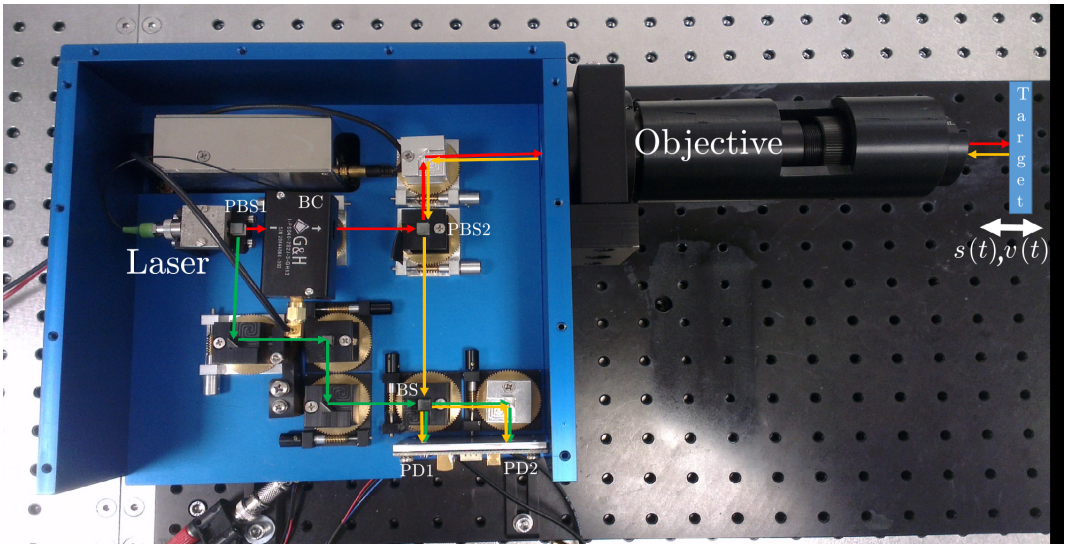

Figure 3.1.: Schema of the self-made infrared single-point LDV.

The use of a differential amplifier is advantageous because it improves the signal to noise ratio (SNR). Moreover, the DC components of the signals, if equal, are canceled.
The output signal of the amplifier is the voltage signal U_{TIA}

$$U_{\mathrm{TIA}} = 2 \cdot R_{\mathrm{TIA}} \cdot K_{\mathrm{PD}} \cdot \epsilon \cdot \sqrt{\Psi}\sqrt{W_{\mathrm{r}} W_{\mathrm{m}}} \cos(2\pi f_{\mathrm{BC}} t - \phi(t) + \phi_0), \tag{3.3}$$

where ϵ is the heterodyne efficiency ($0 < \epsilon < 1$), K_{PD} is the sensitivity of the photodiodes, Ψ is the reflectivity of the object, W_{r} and W_{m} are the optical power of the reference and measurement beam respectively, f_{BC} is the frequency shift operated by the Bragg cell, $\phi(t)$ is the Doppler phase shift, and ϕ_0 is initial phase of the interference signal. The negative sign of the Doppler phase shift $\phi(t)$ defines the direction of the vibration. If the target moves toward the LDV, the vibration has a positive sign, if the target moves away from the LDV, the vibration has a negative sign.

If the measured object is moving with a sinusoidal vibration, it generates a modulation of the measurement light and $\phi(t)$ can be expressed as

$$\phi(t) = M \cdot \sin(\Omega t), \tag{3.4}$$

where Ω is the modulation frequency and M the modulation index. The signal is demodulated and the velocity or the displacement of the target is inferred. The demodulation of the signal can be performed with analog or digital techniques. For further information about the demodulation methods of LDV signals, the reader may refer to [59, 147, 151, 152].

3.2. Resolution of Laser Doppler Vibrometry

The resolution within a bandwidth B or the smallest detectable displacement or velocity is a relevant parameter for a measuring instrument. By analyzing the noise sources it is possible to know the resolution limit.

The main noise sources in LDVs are the light induced noise (shot noise), the thermal noise (Johnson noise), and the signal processing and decoding noise. Thermal noise in the detector and in the amplifier can be neglected. The ultimate limit is set by the light induced noise [59, 147, 151–153]. The root mean square (RMS) shot noise of the detector expressed in volts - U_{sn} - is defined by the equation

$$U_{\mathrm{sn}}^2 = 2 \cdot R_{\mathrm{TIA}}^2 \cdot K_{\mathrm{PD}}^2 \cdot h \cdot \frac{c}{\lambda} \cdot B \cdot (W_{\mathrm{r}} + \Psi \cdot W_{\mathrm{m}}), \tag{3.5}$$

where $h = 6.626 \cdot 10^{-34}$ Js is the Plank constant and $c = 299792458$ m/s is the speed of light.
The signal-to-noise ratio, SNR, of the shot noise limited detector signal for a bandwidth B is

$$\mathrm{SNR}(B) = \frac{U_{\mathrm{TIA,RMS}}^2}{U_{\mathrm{sn}}^2} = \frac{\frac{U_{\mathrm{TIA}}^2}{2}}{U_{\mathrm{sn}}^2}, \tag{3.6}$$

where $U_{\mathrm{TIA,RMS}}$ is the root mean square value of the signal of the amplifier U_{TIA}. Since the demodulation term of equation 3.3 can be expressed as a sum of Bessel functions of the first kind, if modulation indexes are small [59, 151, 153], U_{TIA} for the balanced detector can be written as

$$U_{\mathrm{TIA}} = 2 \cdot R_{\mathrm{TIA}} \cdot K_{\mathrm{PD}} \cdot \epsilon \cdot \sqrt{\Psi}\sqrt{W_{\mathrm{r}} W_{\mathrm{m}}} \cdot \frac{2\pi s_0}{\lambda}, \tag{3.7}$$

where s_0 is the displacement amplitude of a sinusoidal vibration.
The description of the derivation of these equations is reported in Rembe, Siegmund, et al. [59], Chiariotti, Rembe, et al. [147], and Rembe and Mignanelli [153]. By substituting equations 3.5 and 3.7 in 3.6, the displacement vibration resolution limit $s_{\mathrm{RL}} = s_0$ in m is obtained for

$$\mathrm{SNR}(B) \cdot \sqrt{2} = 1. \tag{3.8}$$

The factor $\sqrt{2}$ is introduced to consider that two side-bands with uncorrelated noise contribute to the signal. Thus, $s_{\mathrm{RL}}(B)$ results in

$$s_{\mathrm{RL}}(B) = \frac{\lambda}{2\pi}\sqrt{\frac{h \cdot \frac{c}{\lambda} \cdot B \cdot (W_{\mathrm{r}} + \Psi W_{\mathrm{m}})}{2 \cdot \Psi \cdot \epsilon^2 \cdot W_{\mathrm{r}} \cdot W_{\mathrm{m}}}} = \frac{\lambda}{2\pi}\frac{1}{\sqrt{2 \cdot \mathrm{SNR}(B)}}. \tag{3.9}$$

For an IR interferometer with 10 mW laser beam power at 1 Hz bandwidth, the resolution limit $s_{\mathrm{RL,IR}}(1\mathrm{Hz})$ is about 1 fm for optimal ϵ, K_{PD} and Ψ.

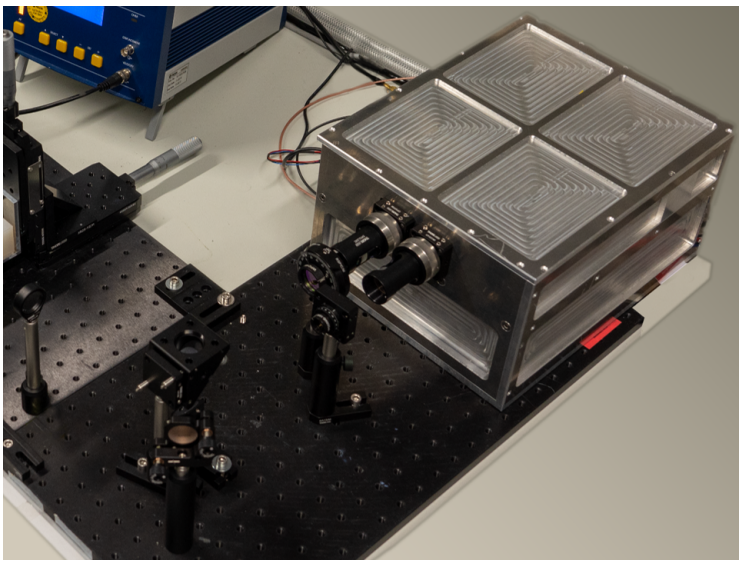

Figure 3.2.: Photo of the self-made differential DLDV (Photo by Marvin Schewe, M.Sc.).

By increasing the measuring bandwidth the $s_{\mathrm{RL}}(B)$ will increase, i.e. the resolution downgrades.

The new version of self-made vibrometer has a differential configuration: both reference and measurement beam are external (see Figure 3.2).
The DLDV presents at $B = 1$ Hz a shot noise of -111 dBm and a SNR(1Hz) of 147 dBm (measured optically with the reference and measurement beam impinging on a mirror i.e. $\Psi \approx 1$). Therefore, according to equation 3.9, the resolution limit at $B = 1$ Hz is $s_{\mathrm{RL,DLDV}}(1\mathrm{Hz}) = 7.8$ fm ($s'_{\mathrm{RL,DLDV}} = 7.8$ fm$/\sqrt{\mathrm{Hz}}$).

The measurements in this work are performed on human tissue and on tissue mimicking phantoms. For these targets, the reflecting factor Ψ is lower than 1. Therefore, for these measurements the SNR(B) decreases and the resolution limit $s_{\mathrm{RL}}(B)$ increases.

The SNR(1Hz) on the skin for the DLDV was measured and resulted between -20 dBm and -15 dBm leading to a $s_{\mathrm{RL,skin}}(1\mathrm{Hz})$ between $2.8 - 4.9$ pm i.e. $s'_{\mathrm{RL,skin}} = 2.8 - 4.9$ pm$/\sqrt{\mathrm{Hz}}$. For the silicone rubber phantom the SNR(1Hz) resulted in 112.4 dBm leading to a $s_{\mathrm{RL,sil}}(1\mathrm{Hz}) = 0.42$ pm ($s'_{\mathrm{RL,sil}} = 0.42$ pm$/\sqrt{\mathrm{Hz}}$).

As already stated, the ultimate limit is defined by the photon-shot noise. This is possible only if the signal processing and decoding noises are lower than the shot noise. The resolution of the system is then limited by its electronics, decoder range, A/D and D/A conversion [147].

3.3. Full-Field Vibrometry

The single-point LDV technique allows to measure in one point at the specimen surface. Only the velocity component in the direction of the laser beam is acquired.

In practice, it is often required to perform vibration measurements of several points on a surface; an example is the investigation of the operation deflection shapes of the surface. Such measurements could be very time consuming with a single-point LDV. More complex systems like scanning LDV (SLDV) have been developed to overcome this limitation.

SLDV allows for the measurement of different points successively [154]. The points are previously defined on a grid and the laser is directed to the predefined points automatically. The SLDV allows for the analysis of the spatial distribution of the vibrations by saving a lot of time.

However, if the target vibrates in a direction not parallel to the laser beam or the vibration changes its direction during the acquisition, only a projection of the vibration is detected. 3D-LDV systems (3D-LDV) have been developed [155] to correctly detect the tridimensional vibrations.

A 3D-scanning measurement is performed with three scanning heads which are focused in the same spot and acquire the vibrations from three different directions for all the points in the predefined grid. In this way, it is possible to perform full field 3D-vibration measurements. Scanning systems can be used for the investigation of reproducible vibrations, since the measurements at different points are not performed simultaneously.

The measurement of non-reproducible events can be performed with a multipoint vibrometer (MPV) [61–65]. The MPV is applicable for the case of non-periodic and not reproducible phenomenons like friction [156, 157] and vital signals. The measuring time is extremely reduced with the MPV.

The MPV consists on several measuring laser beams that acquire the vibrations of different points simultaneously. Alternatively, 3D measurements can be performed by pointing three different beams to the same point from three independent directions.

The multipoint measurements performed in this thesis are carried out with the MPV-800 (Polytec GmbH) [61].
The MPV-800 fully equipped (see Figure 3.3(a)) consists on six optical units. Each unit contains one heterodyne interferometer. For each optical unit, eight fiber heads are derived as showed in Figure 3.3(b). The measurement laser beam of each measurement head is decoupled from the fiber inside the fiber head and it is focused on the measurement point with the front lens.
The light scattered back by the target is then fed back to the optical unit through a second fiber-optic cable. The signals are detected in the interferometer in the optical units.
Successively, they are acquired in the acquisition box and demodulated in the PC.

The calculation of the velocity and displacement signals is also carried out in the PC.

For the extrapolation of the vibration amplitude and of the vibration direction of the target, the orientation of the laser beam in respect to the measuring point is required.

The sensor 3D Disto from Leica Geosystem® [158] calculates the positions of the points and of the optical heads in a global coordinate system.
The MPV-Software elaborates these pieces of information to calculate the measuring direction of each sensor head in respect to the measuring spot and to compute the direction of the vibration for all points.

The MPV-800 can detect vibrations up to 100 kHz with a resolution up to 0.11 $\mu m/s/\sqrt{Hz}$ [159]. Moreover, it is possible to collect up to eight additional signals simultaneously, which can be used as a reference. The MPV-800 allows for 48 simultaneous 1D vibration measurements. Since three measuring heads are required for a 3D-measurement and 48 measuring heads are available, a maximal of sixteen 3D simultaneous measurements are achievable. Both 3D and 1D measurements can be combined, too.

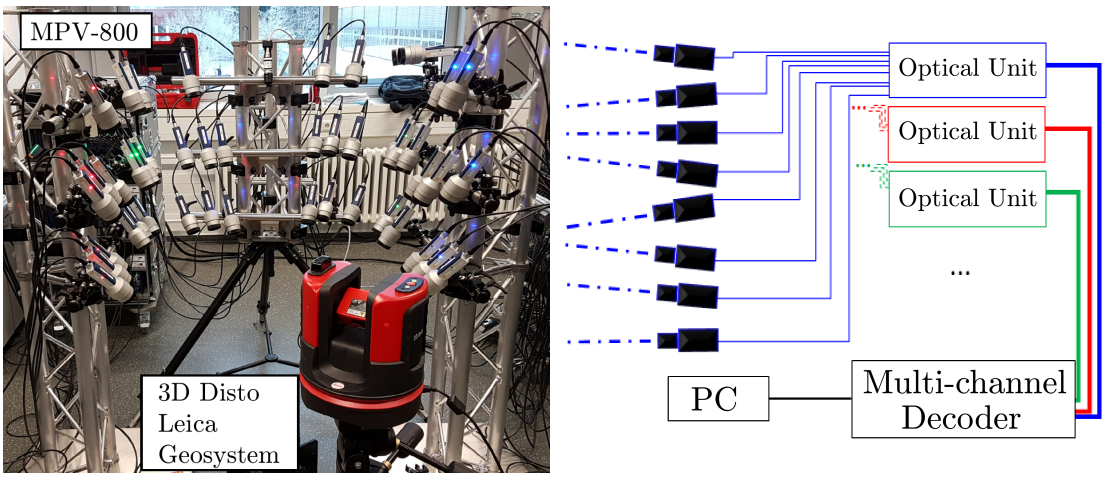

(a) (b)

Figure 3.3.: MPV-800 and 3D Disto Leica Geosystem (Photo by Dipl.-Ing. Xiaodong Cao) (a). Scheme of the MPV-800(b).

4. Optical Vibrocardiography

The goal of this chapter is to analyze the uncertainty of the PR-time detected with LDVy in non-clinical applications.

At first, the anatomy and the physiology of the human body are briefly introduced (Section 4.1) and some cardiovascular parameters are described.
Successively, the VCG signals on the thorax are described, the algorithm for the detection of the $P_{\mathrm{V}}R_{\mathrm{V}}$-time is presented and the factors that influence the pattern of the VCG signal on the thorax are introduced (Section 4.2). Some of these factors are related to the setup of the VCG measurements.
Section 4.3 analyzes the influence that the setup - measuring point position and laser beam orientation - have on the detection of the $P_{\mathrm{V}}R_{\mathrm{V}}$-time.
Finally, a model of the uncertainty for the PR-time in VCG accounting for the uncertainties delivered by the different influencing factors is presented (Section 4.4). The expanded uncertainty of the PR-time in VCG is estimated and compared with the uncertainty requirement for a reliable detection.

In this chapter, vibration velocity signals over the time t are generally referred to as $v(t)$. The subscript of v, if any, identifies a particular measurement set-up or condition.

4.1. Introduction to Cardiovascular System

This section introduces the anatomical and physiological notions needed for the understanding of this chapter. For more detailed information, the reader may refer to references [160–164].

4.1.1. Heart and Cardiovascular System

The heart is a cone-shaped muscular organ that works as a pump that pushes the blood through the vessels. It is located in the middle of the thoracic region of the human body. About two-thirds of the heart is located on the left side of the body and one third on the right side.
Figure 4.1(a) shows a schematic of the heart. The top of the heart is called the heart-base and it connects the heart to the aorta, to the vena cava, to the pulmonary trunk, and to the pulmonary veins. The apex is the lower tip of the heart and it points to the left side.

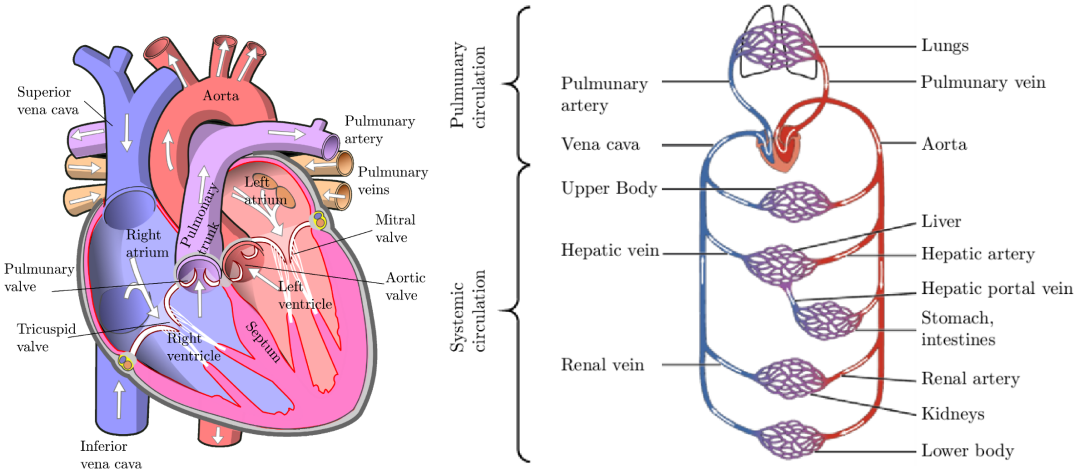

(a) (b)

Figure 4.1.: Heart anatomy (Figure by Wapcaplet - own work, distributed under a CC BY-SA 3.0 license) [165](a) and scheme of the cardiovascular system. The color red symbolizes the oxygenated blood, the color blue the deoxygenated blood and the color purple the material exchange (Figure by OpenStax College-Anatomy & Physiology, Connexions website, distributed under a CC BY 3.0 license [166])(b).

The heart is divided in two upper cavities, known as left and right atria, and two lower cavities, known as left and right ventricles. The right atrium and the right ventricle are separated by the tricuspid valve, while the left atrium and the left ventricle are separated by the mitral valve. The left and the right part of the heart do not communicate and are separated by the septum.
At the exit of the ventricles there are also valves that regulate the blood flow into the vessels: the pulmonary and the aortic valves. The pulmonary valve is located between the right ventricle and the pulmonary artery, which carries the blood to the lungs, whereas the aortic valve is located between the left ventricle and the aorta. The aorta splits in smaller arteries and transports the blood to the rest of the body [161, 162].

The heart, the blood and the blood vessels compose the cardiovascular system. The cardiovascular system has three main tasks.
The first task is the transportation of materials. The blood coming from the lungs is pumped by the heart into the arteries and circulates throughout the body to deliver nutrients and oxygen to the tissues. The blood coming from the tissue carrying waste and carbon dioxide is transported by the veins to the heart. The heart pumps the blood into the veins and the veins transport the blood to the lungs.

The second task is the protection from pathogens. The blood carries white and red blood cells, platelets and antibodies. While the white blood cells fight pathogens that have entered the body, the red blood cells and the platelets seal wounds and prevent pathogens from getting inside the body. If the body has been exposed to or has been vaccinated against a specific pathogen, the existing antibodies for this pathogen provide immunity to them.
The third task is the regulation of the internal physical and chemical properties such as body temperature [163, 167].

The circulatory system consists of two components: the pulmonary circulation loop and the systemic circulation loop.
The former is the part of cardiovascular system that carries deoxygenated blood from the right ventricle of the heart to the lungs. There, the blood gets oxygen and flows back to the heart into the left atrium.
The systemic circulation transports the highly oxygenated blood from the left ventricle to all the tissues of the body. The blood delivers oxygen to the tissues, takes the wastes and flows back as deoxygenated blood to the right atrium [163, 167]. Figure 4.1(b) shows a scheme of the two circulation loops.

4.1.2. Electrical Activity of Heart and Electrocardiogram

The contraction of the heart originates from a group of pacemaker cells placed in the sinoatrial node in the right atrium and allows the pumping function of the heart.
These cells generate a current that propagates through the atria to the atrioventricular node and forward through the bundle of His[a] and the Purkinje fibers[b] to the ventricles (Figure 4.2). The propagation of the current firstly causes the contraction of the atria and, successively, the contraction of the ventricles. This mechanism allows to pump the blood throughout the body [162].
Figure 4.2 shows the electrical conduction system of the heart.

The electrocardiograph is a measuring device that detects the electrical activity with ten electrodes placed in defined positions.
The potential between two electrodes or between an electrode and a virtual electrode is called lead. One of the two electrodes is the positive pole; the other one is the negative pole. The conventional electrocardiogram (ECG) has a total of twelve leads. There are three limb leads, three augmented limb leads and six precordial leads.

The limb leads are the leads obtained from the electrodes positioned on the left arm, on the left leg and on the right arm as shown in Figure 4.3(a). The I-lead is delivered by the measurement of the voltage between the electrodes on the left

[a] Heart muscle cells named after the cardiologist and anatomist Wilhelm His Jr., who discovered them in 1893.
[b] Conducting fibers named after Jan Evangelista Purkinje, who discovered them in 1839.

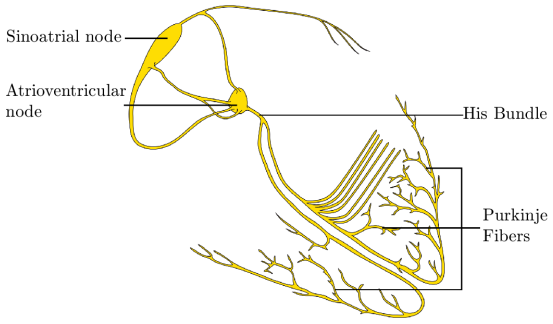

Figure 4.2.: Electrical conduction system of the heart (Figure by Madhero88; Angelito7 distributed under a CC BY-SA 3.0 license)[168].

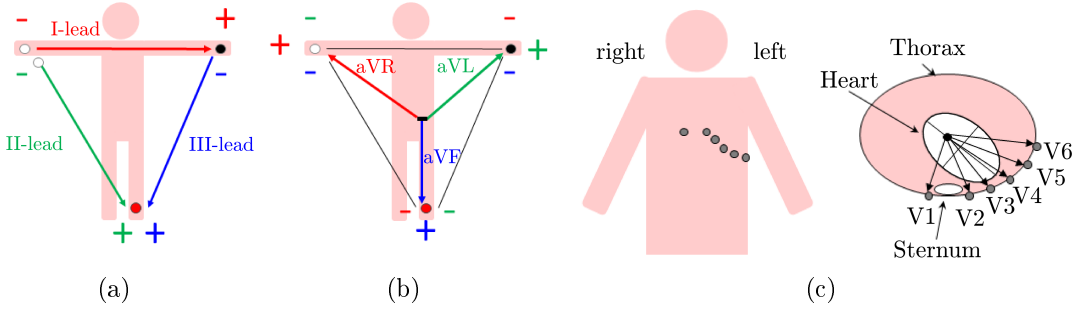

Figure 4.3.: Front view of the twelve leads of ECG: precordial leads (a), augmented limb leads (b) and precordial leads (c). The different colors in (a) and (b) represent the different leads. The plus and minus symbols identify the positive and negative poles, respectively. The left side of (c) shows the position of the electrodes and the right side shows the view from the transverse plane.

and right arm. The voltage between the electrodes on the left leg and on the right arm is the II-lead. Finally, the III-lead is directed from the left leg to the left arm.

The three augmented limb leads - aVR, aVL and aVF - are obtained from the voltage registered between each of the three electrodes of the limb leads - positive pole - and the combination of the input of the other two - negative pole - as showed in Figure 4.3(b).

The six precordial electrods V1, V2, V3, V4, V5 and V6 are presented in Figure 4.3(c). The six precordial leads are obtained by the voltage between each of them as positive pole and the common virtual electrode [164]. The common virtual electrode is obtained as the average of the acquisition from the three electrodes of the limb leads.

The II-lead is the one with the best view of the ECG because most of the electrical impulses travel along its direction and it presents the maximum amplitude

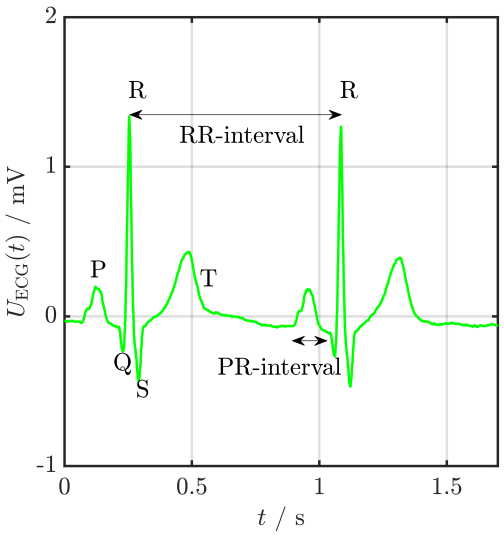

Figure 4.4.: II-Lead of ECG acquired with the amplifier Dual Bio Amp (ADinstrument) and the data acquisition board Powerlab 26/4 (ADinstrument).

of the signal during the QRS complex.
An example of acquisition of the II-lead of the ECG is the voltage signal U_{ECG} shown in Figure 4.4. The II-lead of the ECG presents at first a positive deflection which is called P-wave. The P-wave is the electrical signal of the depolarization and contraction of the atria. The P-wave is followed by an isoelectric segment and successively by the QRS-complex (see Figure 4.4). The QRS-complex represents the depolarization of the ventricles, which triggers their contraction. The ventricles repolarize during the T-wave.
The repolarization of the papillary muscles or Purkinje fibers is sometimes seen in the ECG as a small positive deflection. This wave is called U-wave [164].
Several cardiovascular parameters, which are very important for cardiologist to detect diseases, can be derived from the ECG. Here, only the heart rate, heart rate variability and PR-time are briefly explained.

4.1.2.1. Heart Rate

The interpretation of ECG usually starts with the heart rate (HR). The HR is expressed in beats per minute (bpm) and indicates the speed of the heart beat. There are several methods to measure it.

One of them starts from the detection of the RR-interval in seconds (RR)(see Figure 4.4). The computation of the heart rate in bpm is then derived as

$$\mathrm{HR} = \frac{60}{\mathrm{RR}}. \tag{4.1}$$

Normal values of heart rate are usually between 60 and 100 bpm at rest.
These values can vary depending on age and other factors. Abnormalities may indicate heart diseases such as tachycardia if the heart beats faster than 100 bpm or bradycardia if the rate beats slower than 60 bpm at rest [169]. However, during sleep and for well trained athletes, 40-50 bpm is considered a normal range.

4.1.2.2. Heart Rate Variability

The heart rate variability (HRV) is the variation of the beat-to-beat interval, i.e. RR-interval. The HRV is an indicator of the autonomic nervous system (ANS) activity [170].

The ANS controls several functions such as blood pressure, thermoregulation, etc. Its activity causes variability in the HR and for an individual in a normal physiological state it should be high. Low variability comes from aging or with progression of diseases [171]. Moreover, low heart rate variability is associated with increased mortality after acute myocardial infarction [172].
However, the HRV can be influenced by different factors such as mental and physical stress [173, 174].

The measurement of HRV has a variable duration: about 10 minutes for short term measurements and over 24 hours for long-term measurements. The evaluation of the variation in the heart rate can be done with different methods, such as time domain (statistical and geometrical), frequency domain, and non-linear methods.

One of the simplest methods is the time domain method. The RR-interval, for the calculation of parameters related to the HRV, is called NN. Some simple time domain variables can be derived. An example is the standard deviation of all NN intervals (SDNN) or the root mean square of all differences between successive NN intervals (RMSSD). The NN intervals are usually plotted over the time or beat number originating the so called tachogramm, which is one of the most used tool to observe the HRV.
Examples of frequency domain parameters are the power in very low frequency range (≤ 0.04 Hz), the power in low frequency range ($0.04 - 0.15$ Hz) and the power in high frequency range ($0.15 - 0.4$ Hz) [170].

4.1.2.3. PR-Time

The PR-interval in the ECG, also known as PR-time or PQ-interval, is one of the most important parameters for the diagnosis of CV diseases. It is defined as

the time period delimited by the start of the P-wave and by the beginning of the QRS-complex. The PR-time represents the time between the onset of the atrial depolarization and the onset of ventricular depolarization. From its duration, it is possible to discern between healthy patients and patients affected by different types of illnesses.

Normal values of the PR-interval in ECG are between 120 ms and 200 ms. Narrower intervals may indicate the presence of such illnesses as the Wolff-Parkinson-White syndrome, Lown-Ganong-Levine syndrome, or junctional rhythms [175–178]. A prolongation over 200 ms can be a symptom of a first-degree atrioventricular (AV) block (AV-Block). However, well conditioned athletes may present an asymptomatic PR-interval prolongation [164].

Since the first-degree AV-Block is associated with an increased risk of atrial fibrillation, pacemaker implantation and all-cause mortality [179, 180], differences of the PR-time of at least 20 ms need to be detected according to cardiologist expert opinion [91].

A time varying PR-interval, together with beat drops, may be associate to the other types of AV-blocks [160]. A dropped beat happens when the contraction of the atria is not followed by the contraction of the ventricles, i.e. the electrical impulse does not succeed in traveling in the normal conduction pathway, causing a delay in the ventricular depolarization or the absence of the ventricular depolarization.

4.2. VCG-Velocity Signals on Thorax

In this section, the VCG velocity signals acquired on the thorax with LDV $v(t)$ are presented. The algorithm to detect the $P_{\mathrm{V}}R_{\mathrm{V}}$-time is explained and the influencing factors to the detection of the signal are introduced.

4.2.1. Typical Pattern of VCG-Velocity Signals on Thorax

VCG measurements are carried out by pointing the LDV at the part of the body to investigate. Usually a reference measurement with a proven technology for the investigated parameter is performed as shown in Figure 4.5(a). Figure 4.5(a) shows the typical setup of VCG measurements on the thorax with a single point LDV; a simulatanuos ECG acquisition is performed.

As stated in Chapter 2, VCG measurements allow not only for the detection of the HR and of the HRV but also for the recognition of the heart sounds, of the filling time and of the heart murmurs [21, 22, 78, 129, 130]. Luik, Mignanelli, et al. [91] presented VCG measurements on the thorax. The authors recorded ECG and VCG traces from healthy patients and from patients with pacemaker affected by AV-Blocks. The measurements on sick subjects were performed during a routine follow-up. The pacemakers were inhibited for several seconds and the signals were acquired. The inhibition time was dependent on the symptoms of the

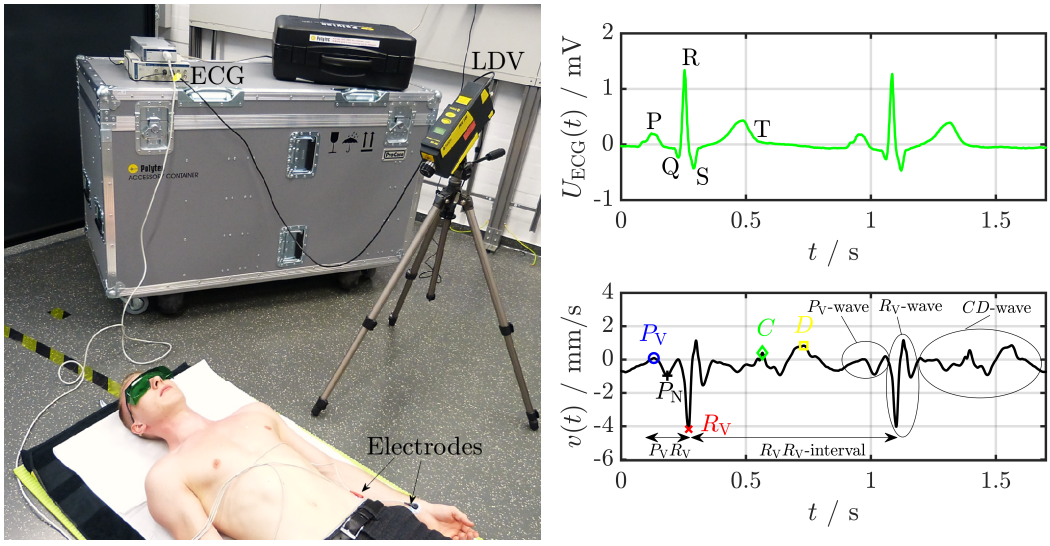

(a) (b)

Figure 4.5.: Photo of a typical setup for VCG measurements (a). Simultaneous ECG $U_{\mathrm{ECG}}(t)$ (top) and VCG-velocity signal on the thorax $v(t)$ (bottom) with their characteristic points (b).

patient. The laser beam was pointed at the skin above the third intercostal space, in correspondence to the left atrium. The point was chosen with the help of a echocardiograph.

The VCG-velocity signals of the heartbeat acquired on the thorax of healthy subjects have shown to be reproducible. As showed in [91], three main waves can be identified in the typical VCG heartbeat (Figure 4.5(b))

- the P_{V}-wave,
- the R_{V}-wave,
- the CD-wave.

The P_{V}-wave represents the vibrations generated by the electrical activation of the atria. The P_{V}-wave consists of a sequence of positive / negative / positive deflections delineated by the points P_{V} and P_{N} in the VCG pattern. However, some subjects present an additional deflection i.e. positive / negative / positive / negative / positive deflection.

The R_{V}-wave is caused by the electrical activation of the ventricles. Its pattern starts at the end of the P_{V}-wave and contains a negative peak, the R_{V}-peak. The R_{V}-peak can be used as a fiduciary point for the detection of the HR and HRV in the time domain.

The HR and the HRV can be obtained by calculating the time difference of two consecutive R_{V}-peaks, the $R_{\mathrm{V}}R_{\mathrm{V}}$-interval. The $R_{\mathrm{V}}R_{\mathrm{V}}$-interval corresponds to the RR-interval in the ECG signal (see Figure 4.4).
By localizing the P_{V}-wave and the R_{V}-peak in healthy subjects it is possible to detect in VCG signals the time interval corresponding to the PR-interval in the ECG.

In this work, the wave that follows the R_{V}-wave is called the CD-wave. It consists of two prominent waves which come up at the end of the ventricle relaxation and determine the end of a beat. The maximum of the first prominence is identified with the letter C and the maximum of the second prominence with the letter D.
While the P_{V}-wave and the R_{V}-wave are directly related to the ECG, the CD-wave may be correlated to the venous back-flow of the blood. Further studies need to be carried out to verify this assumption [91].
Vibrations acquired from measurements on patients with an AV-block of third degree led to the detection of the vibrations generated by a dropped beat. Consequently, the pattern delivered by isolated P-waves were detected.
The positive/negative/positive deflections of the P_{V}-wave were also traceable in these measurements during sinus rhythm and fusion beats[c]. Hence, the authors conclude that a reliable beat to beat detection of the $P_{\mathrm{V}}R_{\mathrm{V}}$-interval is feasible.

[c] A fusion beat happens when electrical impulses from different sources act upon the same region of the heart simultaneously [181].

4.2.2. Detection of $P_V R_V$-Interval

There are two possibilities to detect in VCG signal a time interval corresponding to the PR-time in ECG. Mignanelli, Luik, et al. [182] and Mignanelli and Rembe [183] presented first attempts to automatically detect the PR-interval in VCG.
A first possibility for the computation of the $P_V R_V$-interval in VCG-signals is a peak detection algorithm for the point R_V-peak and a maximum search algorithm for the P_V-point. The subtraction of the time instant of P_V from the time instant of R_V - t_{P_V} and t_{R_V}, respectively - delivers the $P_V R_V$-interval

$$P_V R_V = t_{R_V} - t_{P_V}. \tag{4.2}$$

The PR-time in the ECG is the time difference between the onset of the P-wave and the onset of the QRS-complex and not between the maximum and the minimum of the corresponding waves as in VCG. Thus, for the estimation of the PR-time in VCG, a calibration that takes this aspect into account is required.
In Luik, Mignanelli, et al. [91] this calibration factor was calculated for the case that the measuring direction is perpendicular to the thorax surface of the patient.

A second possibility for the detection of the PR-time in VCG is the detection of the starting point of the P_V-wave. The R_V-peak is detected as mentioned before and the time interval between the starting point of the P_V-wave and the R_V-peak can be calculated. The time calibration factor must be adapted to this case. Reference [183] presents a method for the automatic detection of the starting point of the P_V-wave. The authors adopted a pattern recognition approach which utilizes the least square method. However, it was noticed that the starting point of the P_V-wave is not always clearly recognizable since interference from other vibrations sources sometimes occurs. The origin of these other vibrations have not yet been investigated. Therefore, all the analyses carried out in this work employ the first algorithm.

As already mentioned, the first algorithm applies a peak search for the R_V-peak. Successively, a maximum search for the P_V-point in the time segment[d] preceding each R_V-peak is employed.
The time instant of the P_V-point is then subtracted to the corresponding time instant of the R_V-peak and the $P_V R_V$-time is obtained (See equation 4.2).
While the R_V-peak is mostly clearly identifiable, it might be difficult to identify the maximum of the P_V-wave in presence of high frequency noise.
Moreover, the P_V-wave presents sometimes two maxima in its first or second positive deflection. An example is presented in Figure 4.6; the red circle highlights the two maxima on the first positive deflection of a P_V-wave. Considering the first or the second maximum would deliver a different value of the $P_V R_V$-time.

[d] The duration of this time segment needs to be adapted depending on the time characteristics of the signal.

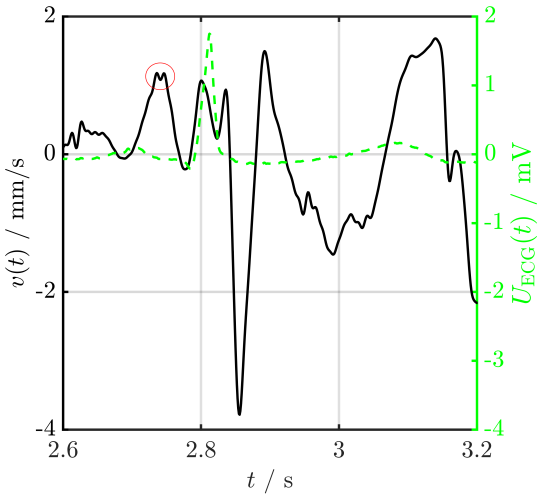

Figure 4.6.: Particular case of a VCG heart-beat $v(t)$ with a P_V-wave with two maxima (red circle). The black dash-dotted line is the simultaneous ECG signal $U_{ECG}(t)$.

However, since the origin of this phenomenon is not known yet [91], the $P_V R_V$-time is calculated with the greater of both maxima.

The algorithm used for the detection of the characteristic points P_V and R_V is usually applied after the filtering of the signal. In this work, a zero-padding bandpass filter ($0.6 - 100$ Hz) in frequency domain is employed as in Mignanelli, Bauer, et al. [184] (see Appendix A).

4.2.3. Influencing Factors of VCG-Signal on Thorax

Several factors have an influence on the pattern of the VCG-signal acquired on the thorax. These factors are related to the origin and the generation of the vibration of the heart or to other vibrations generated by the body or to the setup of the measurement. These factors influence the extraction of the $P_V R_V$-time, leading to errors.

VCG signals are strongly affected by the peculiarity of each subject. They are influenced not only by the complexity of the exciting electrical signal (ECG), but also by the complexity of the mechanical nature of the propagating wave through the tissue stratification. The electrical signal which causes the contraction of the heart is different from person to person.
As the heart contracts, vibrations are originated and they propagate through different tissue layers. The tissue layers are different from person to person.
Finally, these vibrations are detected on the skin with a LDV.

The factors that influence the vibration signals are the time and amplitude characteristics of the electrical signal, the mechanical response of the heart, the damping due to the tissue stratification, and the interference with other biological vibrations like breathing and blood pressure wave through the vessels.
All of these factors depend on the specific characteristics of each subject at the moment of the measurement, such as the heart and respiratory rate and the CV and respiratory diseases.
Other factors are the conformation of the body, which is measurable with the body mass index (BMI), and the physical activity performed by the subject [183].

The shape, the amplitude, and the time duration of the typical waves vary depending on the status of the subject at the moment of the measurement.
To investigate the contribution to the extraction of CV parameters resulting from the above mentioned factors, a large cohort of subject is needed. For this reason they could not be investigated in this thesis.

External interfering factors like noise or vibrations that contain unneeded information have an influence on the shape of the VCG signals. For the correct estimation of CV parameters, these disturbances have to be removed with filters. If the aim of the measurement is to extract heart or blood flow signals, as for the case of the PR-time, the vibrations generated by the respiration are considered disturbances, too.

These disturbances are analyzed in the Master's thesis of Hao Wang [185], which I supervised. The first type of disturbances are occasional disturbances, which occur only sometimes.
These disturbances are involuntary movements of the subject during the measurements. Even if they happen occasionally, they are mostly so severe that the characteristic features in these time segments are not recognizable anymore. Involuntary movements have a broadband nature in the frequency domain. If possible, it is convenient to ignore for the analysis the time segments corresponding to such movements [185].
The second type of disturbances for the extraction of the heart pulse is the vibrations generated by breathing. Breathing is a quasi-sinus component typically below 0.6 Hz, which can be high-pass filtered. The third type of disturbance is the high-frequency noise due to the laser-speckle. This disturbance can be reduced by a low-pass filter. The VCG signal has relevant components up to 100 Hz [118, 119]. Therefore, the cut-off frequency for the low pass-filter is usually set to 100 Hz.

If the subject is speaking during the measurement, the VCG signal presents a modulation due to the vibrations generated by the voice. The human voice has frequency components higher than 100 Hz; therefore, it can be considered as high frequency noise. However, it is preferable that the subject remains still during the measurements.

For the detection of the $P_{\mathrm{V}}R_{\mathrm{V}}$-time, both respiration and high-frequency noise must be removed. Both components may lead to delays and affect the value of

the $P_V R_V$-time. The filtering of the disturbances reduces these delays as shown in Mignanelli, Bauer, et al. [184] and in the Appendix A.
To evaluate the contribution of the post-processing (algorithm and filter) to the extraction of CV parameters reliably, the post-processing method should be tested on a large sample of signals. The contribution of the uncertainty resulting from the post-processing could not be investigated in this thesis. However, a preliminary investigation on a small sample is reported in the Appendix A.

Other external factors as the metrological properties of the LDV, the measurement point and the laser beam orientation can also alter the measurements and lead to uncertainties in the detection of parameters. These contributions can be relevant especially for tracking applications. In tracking applications, the subject usually moves and, therefore, the measuring point and the laser beam orientation are difficult to set to adjust precisely. The algorithms chosen for the post-processing also yield their contribution to the uncertainties.

Usually, only the uncertainties of the post processing to the desired parameter are calculated [23]. The contribution to the uncertainties resulting from the setup features and resulting from the measuring conditions are considered mostly ideal. For great deviations from the ideal conditions, as in daily measurements or in tracking applications, this assumption leads to an erroneous determination of the extracted cardiovascular parameter, as for example the PR-time.

According to cardiologist expert opinion, a 20 ms increment of the PR-interval in the ECG is associated with an adjusted hazard ratio of 1.22 for pacemaker implantation, of 1.11 for atrial fibrillation, and of 1.08 for all-cause mortality. Clinical data suggest that an uncertainty lower than 20 ms is required for a reliable detection of the PR-interval in ECG [91, 179]. As stated in Paragraph 4.1.2.3, values of the PR-interval lower than 120 ms and greater than 200 ms are related to CV diseases. Therefore, the uncertainty of the $P_V R_V$-interval in VCG must be lower than 20 ms and a statistical significance analysis is necessary to asses for which values of the $P_V R_V$-interval CV diseases are reliably detectable and discernible from the healthy condition with at least 95% certainty.

In this work, the external interferences of the set up are analyzed. Section 4.3 analyzes the influence of the setup - measurement point position and laser beam orientation - to the extraction of the $P_V R_V$-time by performing measurements with the multipoint vibrometer.

In Section 4.4 a model for the calculation of the uncertainty of the PR-time in VCG by accounting for the contributions of the influence factors described in Section 4.3 is introduced. The uncertainty calculation is performed according to the Guide to the expression of uncertainty in measurement (GUM) [134]. Finally, the value of the uncertainty of the PR-time in VCG signal is estimated and compared to the requirements for a reliable detection.

4.3. Influence of Setup for Detection of $P_V R_V$-Interval

As explained in Chapter 2, the resolution of the LDV is more than sufficient for the detection of physiological signals in the human body.
However, there are some issues related to the setup that must be considered for a reliable detection of cardiovascular parameters.
The laser beam orientation of the LDV and the position of the measuring point have an influence on the detection of the VCG-signal on the thorax and, therefore, on the extraction of the $P_V R_V$-time.
The influence of these factors can be analyzed with measurements performed with the multipoint vibrometer.

This section presents at first, the motivation to investigate the contribution of the laser beam orientation and measuring point position on the detection of the $P_V R_V$-time with the multipoint vibrometer (Subsection 4.3.1). Successively, the measurement with the multipoint vibrometer are shown and discussed (Subsection 4.3.2)

4.3.1. Motivation

The following paragraphs (4.3.1.1 and 4.3.1.2) present an analysis performed to investigate the contribution of the laser beam orientation and the position of the measuring point on the detection of the $P_V R_V$-time.
The reasons to analyze the influence of the laser beam orientation and the measuring point position on the detection of the $P_V R_V$-time with multipoint vibrometer measurements are explained in Paragraph 4.3.1.3.

4.3.1.1. Laser Beam Orientation

A single-point LDV measures the vibrations parallel to the laser beam which are also called out-of-plane vibrations. If a target vibrates in another direction relative to the direction of the laser beam, the detected amplitude is the projection of the vibration in the direction of the laser beam.
In particular, the velocity amplitude $v_i(t)$ measured with the LDV from the direction identified by the unit vector $\boldsymbol{e}_i$ is

$$v_i(t) = \boldsymbol{e}_i \cdot \boldsymbol{v}(t) = \parallel \boldsymbol{v}(t) \parallel \cos\gamma, \tag{4.3}$$

where $\boldsymbol{v}(t)$ is the velocity vibration vector of the target in the three-dimensional space and γ is the angle between $\boldsymbol{v}(t)$ and the laser beam direction $\boldsymbol{e}_i$.
Therefore, if the laser beam is not aligned to the direction of the vibration of the target, the LDV would detect a lower amplitude of a factor $\cos\gamma$ in respect to the

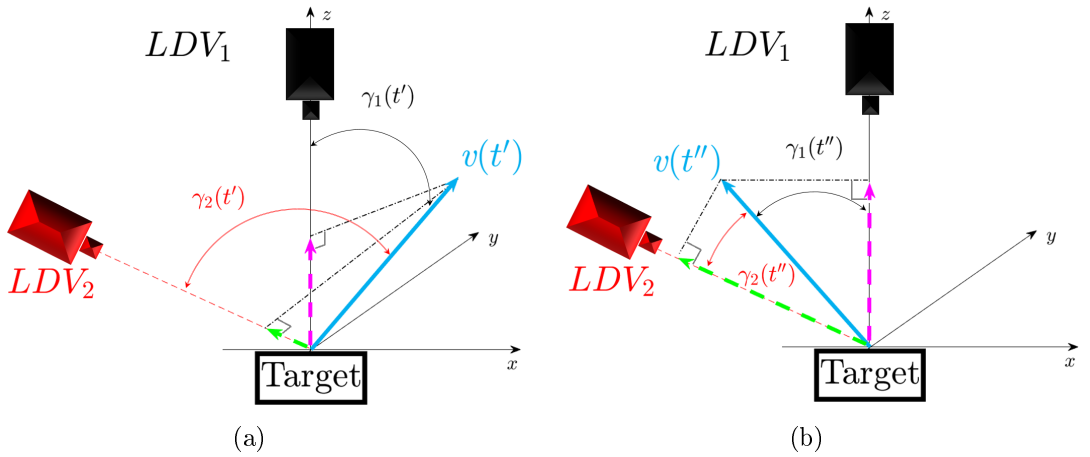

Figure 4.7.: Vectors of the vibration of the target $\boldsymbol{v}_(t)$ at the time instant t' and t'', (a) and (b), respectively. The vectors with dashed magenta lines are the projection of $\boldsymbol{v}(t)$ acquired with the LDV directed as LDV_1. The vectors with the dashed green lines are the projection of $\boldsymbol{v}(t)$ along the direction of LDV_2.

actual one. The detected amplitude can be easily corrected if the angle γ is known. However, in most of cases the angle γ is not known a priori, especially if the velocity vector changes its direction over the time t as shown in Figure 4.7.
Figure 4.7(a) shows the velocity vector of target $\boldsymbol{v}(t)$ at the time instant t'. The dashed magenta vector and the dashed green vector are the projections of $\boldsymbol{v}(t')$ in the direction of LDV_1 (black LDV) and of LDV_2 (red LDV), respectively.
The angle between the vector $\boldsymbol{v}(t')$ and the laser beam of the LDV_1 and the LDV_2 are called $\gamma_1(t')$ and $\gamma_2(t'')$, respectively. In this example, the amplitude of $\boldsymbol{v}(t')$ is acquired more reliably from the direction of LDV_1, since $\gamma_1(t')$ is lower than $\gamma_2(t')$.
Figure 4.7(b) presents the vector $\boldsymbol{v}(t)$ at the time t'' similarly as in Figure 4.7(a). In this example, the amplitude of $\boldsymbol{v}(t'')$ is acquired more reliably from the direction of LDV_2, since $\gamma_2(t'')$ is lower than $\gamma_1(t'')$.
Therefore, there is not always an optimal laser beam orientation.
The acquisition of 3D vibrations with a single point LDV may deliver different signal amplitudes over time if performed from different directions.
Consequently, the parameters extracted from these signals could differ depending on the laser beam orientation.
A preliminary analysis is carried out to analyze the direction of the vibration of the thorax. The aim is to determine if the orientation of the laser beam has a remarkable influence on the extraction of the $P_V R_V$-interval, similarly as shown in Mignanelli, Bauer, et al. [184].

First Experiments Demonstrating the Problem The aim of the preliminary experiments is to determine if the orientation of the laser beam has an influence on the detection of the $P_{\mathrm{V}}R_{\mathrm{V}}$-interval similarly as shown in Mignanelli, Bauer, et al. [184].
At first, the 3D-velocity vector of the vibration on the thorax is presented. Successively, the influence of the laser beam orientation on the detection of the $P_{\mathrm{V}}R_{\mathrm{V}}$-time is shown.

For the reconstruction of the 3D-velocity vector $\boldsymbol{v}(t)$, three simultaneous measurements from three independent directions are needed[e].

Therefore, two couples of measurements were performed with the setup described in Figure 4.8(a).
Two LDVs were employed: the OFV-303 (LDV_1) and the PDV-100 (LDV_2), both from the company Polytec GmbH. The LDV_1 was oriented perpendicularly to the ground along the z-axis ($\vartheta_1 = 90°$). The LDV_2 was directed to the same spot on the thorax from a different direction. The direction is defined by the angles φ and ϑ. The acquisition point lies on the third intercostal space on the left parasternal region similarly as in reference [91]. The second lead of the ECG was used as a reference; it was acquired simultaneously to the signals of LDV_1 and LDV_2 with the data acquisition board PowerLab 4/26 (ADInstrument) using a sample rate of 1 kHz.

The first couple of measurements were performed with the LDV_2 oriented with $\vartheta_2 = 60°$ and $\varphi_2 = 0°$, according to Figure 4.8(b).
The signal obtained from the LDV_1 acquired in this configuration is called $v_1(t)$.
The signal obtained from the LDV_2 acquired in this configuration is called $v_2(t)$.
In the second couple of acquisition, the LDV_2 is oriented with $\vartheta_3 = 60°$ and $\varphi_3 = 90°$. The signal obtained from LDV_2 acquired in this configuration is called $v_3(t)$.
The ECG signals were used for the synchronization of the two pairs of measurements to obtain three synchronous independent vectors for the reconstruction of the 3D-vector.

After the synchronization, the signals $v_1(t)$, $v_2(t)$ and $v_3(t)$ can be seen as the scalar product of the 3D-vector $\boldsymbol{v}(t)$ with the unit vectors $\boldsymbol{e}_1$, $\boldsymbol{e}_2$ and $\boldsymbol{e}_3$ in the direction of the measurement according to equation 4.3.
The direction vectors expressed in Cartesian coordinates are (Figure 4.8)(b)

$$\begin{aligned} \boldsymbol{e}_1 &= \boldsymbol{e}_z \\ \boldsymbol{e}_2 &= \cos\vartheta_2 \cos\varphi_2 \boldsymbol{e}_x + \cos\vartheta_2 \sin\varphi_2 \boldsymbol{e}_y + \sin\vartheta_2 \boldsymbol{e}_z \\ \boldsymbol{e}_3 &= \cos\vartheta_3 \cos\varphi_3 \boldsymbol{e}_x + \cos\vartheta_3 \sin\varphi_3 \boldsymbol{e}_y + \sin\vartheta_3 \boldsymbol{e}_z, \end{aligned} \tag{4.4}$$

[e] These measurements were acquired for the analysis presented in the master's thesis of Mareike Klarmann [186], which I supervised.

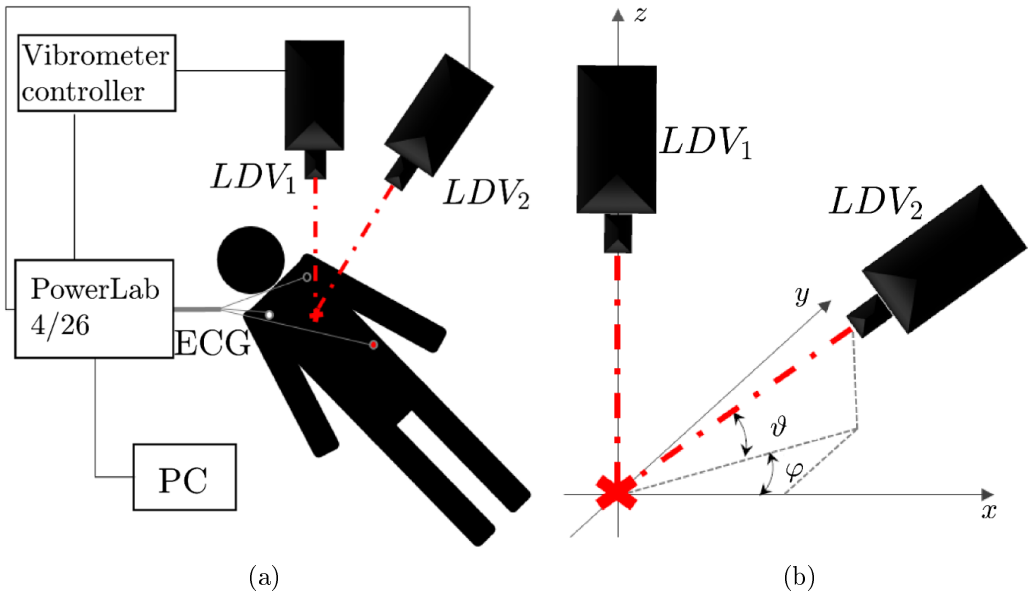

(a) (b)

Figure 4.8.: Measurement setup used for the preliminary investigation of the influence of the laser beam orientation in VCG signals on the thorax in (a). Details of the configuration of the LDVs: LDV_1 is oriented perpendicularly to the ground and LDV_2 is directed from a different direction defined by the angles φ and ϑ in (b).

where $\boldsymbol{e}_x$, $\boldsymbol{e}_y$ and $\boldsymbol{e}_z$ are the unit vectors that define the $x-, y-$ and $z-$directions of the Cartesian coordinate system.
Therefore, for every time instant t, the 3D-vector $\boldsymbol{v}(t)$ can be expressed as

$$\begin{Bmatrix} v_1(t) \\ v_2(t) \\ v_3(t) \end{Bmatrix} = \boldsymbol{E}\boldsymbol{v}(t) \rightleftharpoons \boldsymbol{v}(t) = \begin{Bmatrix} v_x(t) \\ v_y(t) \\ v_z(t) \end{Bmatrix} = \boldsymbol{E}^{-1} \begin{Bmatrix} v_1(t) \\ v_2(t) \\ v_3(t) \end{Bmatrix}, \tag{4.5}$$

where

$$\boldsymbol{E} = \begin{bmatrix} 0 & 0 & 1 \\ \cos\vartheta_2 \cos\varphi_2 & \cos\vartheta_2 \sin\varphi_2 & \sin\vartheta_2 \\ \cos\vartheta_3 \cos\varphi_3 & \cos\vartheta_3 \sin\varphi_3 & \sin\vartheta_3 \end{bmatrix}. \tag{4.6}$$

Figure 4.9(a) shows the reconstruction of the 3D-velocity vector $\boldsymbol{v}(t)$ in Cartesian coordinates for the heart-beat segment presented in Figure 4.9(b).
The axes of Figure 4.9(a) show the velocity amplitude in x-, y- and z-direction; the orientation of the axes with respect to the body can be evicted from the description in the figure.
The 3D-vector $\boldsymbol{v}(t)$ in Figure 4.9(a) changes amplitude and direction during the

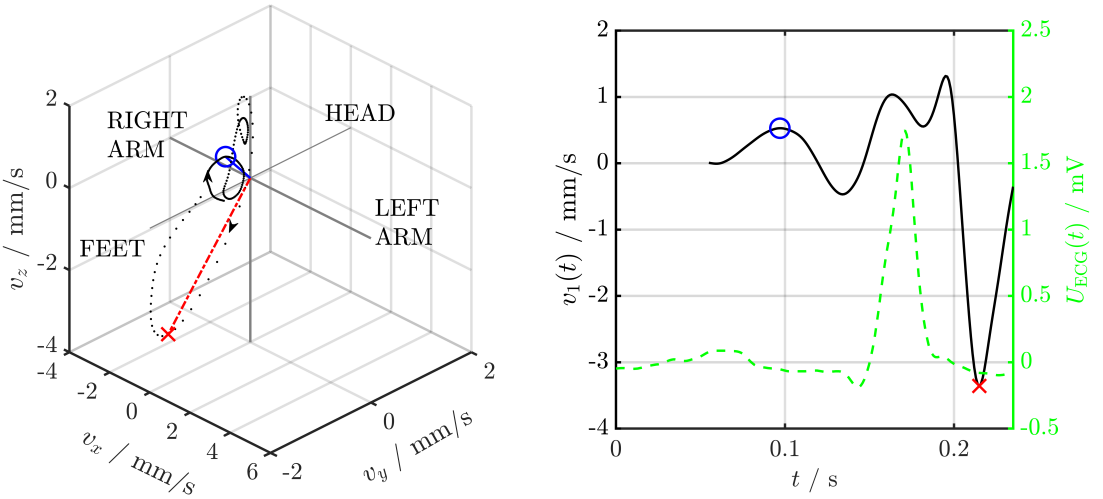

(a) (b)

Figure 4.9.: 3D-velocity vector $\boldsymbol{v}(t)$ in Cartesian coordinates (black dots). The trajectories of the P_{V}-point and R_{V}-peak are the continuous blue and the dash-dot red line, respectively (a). Segment of the velocity vector v_2 (black line) used for the reconstruction of the 3D-vector and simultaneous ECG (green dashed line) used for the synchronization of the signals (b). In both figures, the blue circle is the P_{V}-point and the red cross is the R_{V}-peak.

heart-beat. The trajectories of the characteristic points P_{V} and R_{V} are oriented in two different directions.
This implies that there is not an optimal laser beam orientation for a proper detection of the VCG signal. Therefore, for the measurement of the $P_{\mathrm{V}}R_{\mathrm{V}}$-interval, the direction perpendicular to the floor (z-axis) is chosen as reference ($\vartheta = 90°$).
As a consequence, it is necessary to investigate how the variation of the measurement orientation with respect to the reference position affect the detection of the characteristic parameters of the VCG on the thorax.

The analysis of the influence of the laser-beam orientation for the detection of the $P_{\mathrm{V}}R_{\mathrm{V}}$-time was performed to understand if there is a range of angles where the detection of the $P_{\mathrm{V}}R_{\mathrm{V}}$-interval is more reliable.
A couple of simultaneous measurements with the two LDVs with different angles of incline (see Figure 4.8(b)) in the xz-plane ($\varphi = 0°$) was carried out.
The reconstruction of the 3D-vector indicates no preferred direction; therefore, the LDV_1 was always pointed along the direction defined by $\vartheta_1 = 90°$ and considered as the reference measurement, $v_{90°}$. Acquisitions with the LDV_2 pointed at different

values of ϑ were performed.
The signals obtained from LDV_2 are called v_ϑ where the angle ϑ was changed between the following values: $40°, 60°, 120°$ and $140°$.
The vibrations generated by the respiration usually bring their contribution to the signal amplitude. They are angle-dependent and, commonly, the frequency contents are in the range up to 0.6 Hz.
The high frequency noise components are characterized by frequency greater than 100 Hz [118]. Therefore, a zero-padding band-pass filter in frequency domain (0.6 Hz − 100 Hz), was applied to the signals to remove the breathing and noise components (see the filter technique F_3 in the Appendix A).

The P_VR_V-interval has been related to the PR-time in the ECG [91] and, therefore, it contains relevant medical information. As already mentioned before, an uncertainty lower than 20 ms is required for a reliable detection of the PR-interval [91]. Hence, the P_VR_V-interval has to be affected as little as possible by disturbances.
For each couple of simultaneous measurements, the P_VR_V-interval was calculated as the difference between the time instants of the R_V-peak and the maximum of the P_V-wave as showed in equation 4.2.
The P_VR_V-interval obtained from the vibration acquired with the reference configuration $v_{90°}$ is called $P_VR_{V90°}$.
The P_VR_V-interval obtained from LDV_2 at the different angles ϑ - v_ϑ - is called $P_VR_{V\vartheta}$.
To quantify the influences on the detection of P_VR_V-interval of the laser beam orientation, two figures of merit were introduced.
By defining $\Delta P_VR_{V\vartheta}$ as

$$\Delta P_VR_{V\vartheta} = P_VR_{V90°} - P_VR_{V\vartheta}, \tag{4.7}$$

its mean value $\overline{\Delta P_VR_{V\vartheta}}$ over $N = 30$ heartbeats

$$\overline{\Delta P_VR_{V\vartheta}} = \frac{1}{N}\sum_{i=1}^{N}\left(\Delta P_VR_{V\vartheta,i}\right) \tag{4.8}$$

and its variation sd_ϑ

$$sd_\vartheta = \sqrt{\frac{1}{N-1}\sum_{i=1}^{N}(\Delta P_VR_{V\vartheta,i} - \overline{\Delta P_VR_{V\vartheta}})^2} \tag{4.9}$$

were selected as figures of merit.
The more $\overline{\Delta P_VR_{V\vartheta}}$ deviates from zero, the greater is the influence of the laser beam orientation in the detection of the P_VR_V-interval.

Figure 4.10 shows the measurements at different angles. The projections of the 3D-vector measured from different angles show distortions of the signal with respect

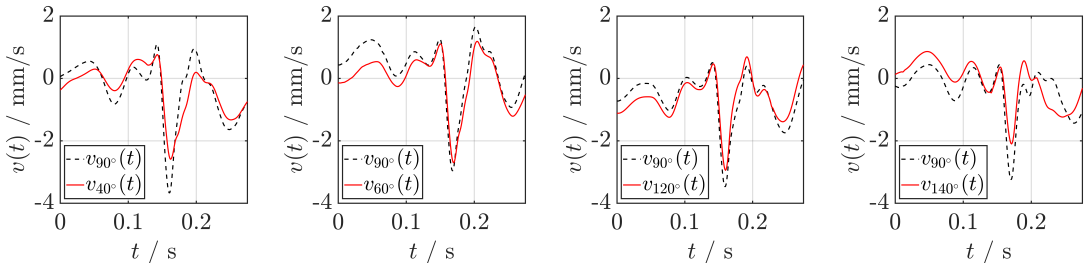

Figure 4.10.: VCG signals at different orientation of LDV_2 (red line): $v_{40°}$ (a), $v_{60°}$(b), $v_{120°}$ (c) and $v_{140°}$ (d). The black dashed line is the corresponding simultaneous reference signal acquired with LDV_1, $v_{90°}$.

Table 4.1.: Results of the figures of merit calculated for VCG signals at different angles ϑ.

ϑ / °	$\overline{\Delta P_V R_{V\vartheta}}$ / ms	sd_ϑ / ms
40°	-13.02	0.43
60°	3.50	0.51
120°	-4.66	0.48
140°	-16.5	0.51

to the perpendicular configuration.
The results obtained are presented in Table 4.1. Table 4.1 shows remarkable differences between the investigated beam directions. Great deviations of $\overline{\Delta P_V R_{V\vartheta}}$ are found for the signals $v_{40°}$ and $v_{140°}$, while the signals $v_{60°}$ and $v_{120°}$ have similar results. The values of sd_ϑ are similar for the different cases and are considerably smaller than the systematic error.
It can be evinced that the configurations at $\vartheta = 40°$ and $\vartheta = 140°$ present a stronger amplitude difference in respect to the ones at $\vartheta = 60°$ and $\vartheta = 120°$.
The results of this analysis show that $\overline{\Delta P_V R_{V\vartheta}}$ remains less than 5 ms for a maximum angle deviation of 30° from the perpendicular direction at $\vartheta = 90°$ in the defined xz-plane.
These first experiments demonstrate that the laser beam orientation has an influence on the $P_V R_V$-time.

4.3.1.2. Measurement Point Position

In non-laboratory conditions, without an ultrasonography device, the point directly above the left atrium used for the measurements in reference [91] cannot be detected precisely; this is the case of home-health monitoring or for tracking applications, where the subject is moving.
Therefore, a wide area needs to be considered to perform VCG measurements on the thorax. The measuring point position is an important factor to consider for the uncertainty computation.

Generally, the characteristic vibration pattern differs from point to point. Luik, Mignanelli, et al. [91] presented a measurement with a diode-pumped solid state multipoint laser vibrometer on the thorax of one healthy subject. The multipoint vibrometer used has twelve laser beams [62]. Therefore, twelve points on the left side of the thorax could be measured simultaneously. The signals were acquired with the sampling frequency of 20 kHz and the acquisition time of 400 ms.
Five out of twelve points presented the typical VCG pattern. The P_V- and R_V-wave were clearly recognized in the patterns of these points. The points were located in the left parasternal region between the third and sixth intercostal spaces. An area of about 4 cm×15 cm was identified for a reliable acquisition of the signal pattern. The remaining points were not suitable for automated analyses since their vibrations presented a reduced amplitude and a biphasic dominant peak. This might be caused by adverse positions of the points as, for example, a close distance to a rib.

It was noticed that the $P_V R_V$-time differs from point to point, depending on the measuring location. In fact, the P_V- and R_V-waves are originated by different sources (atria and ventricles) that reside in different locations.
Therefore, each wave reaches each measuring point with different delays depending on the distance from the sources. This delay leads to different values of the $P_V R_V$-time. For the VCG measurement of reference [91], the maximum deviation of the $P_V R_V$-time between the points with a clear VCG signature is lower than 4 ms.

However, the laser beam orientation during these measurement was not perpendicular to the ground for all the points.
The measurement conditions are, therefore, not suitable for a reliable uncertainty analysis. In fact, as shown in Paragraph 4.3.1.1, the laser beam orientation has an influence in the detection of the $P_V R_V$-time.

4.3.1.3. Discussion

In this Paragraph, the need of measurements with the multipoint vibrometer for the investigation of the influence of the setup on the detection of the $P_V R_V$-interval is explained.

Paragraph 4.3.1.1 shows that the laser beam orientation has an influence on the value of the $P_V R_V$-time and Paragraph 4.3.1.2 shows that the location of the measuring point on the thorax has also an influence on the value of the $P_V R_V$-time. However, the analysis presented on those paragraphs should be improved to perform a reliable uncertainty determination for the $P_V R_V$-time.

In fact, the experiments of Paragraph 4.3.1.1 consider only the deviation of the $P_V R_V$-interval in the xz-plane, i.e. two dimensional case.
As shown in Figure 4.9(a), the vibrations on the thorax change direction continuously during the heartbeat.
Therefore, the two dimensional analysis of paragraph 4.3.1.1 is not complete. In order to extend the analysis to the three-dimensional case, the influence of the orientation of the laser beam also in the direction of the angle φ must be considered (see Figure 4.8(b)); this is possible by performing measurements with the multipoint vibrometer (MPV).
With the multipoint measurements, the influence of the orientation of the laser beam defined by both angles φ and ϑ can be investigated. A three-dimensional analysis is particularly important for tracking applications, where the subject moves and, therefore, the direction of the laser beam changes with respect to the reference measuring condition.

An additional advantage to perform measurements with the multipoint vibrometer is that there is no need for an artificial synchronization of the signal as for the measurements described in this paragraph. In fact, with the MPV, all the signals are simultaneously acquired. Therefore, there are no errors generated by the manual synchronization of the measurements and the resolution is the same for every measuring heads.

Finally, the multipoint measurements on the thorax can be performed to estimate the influence of the measurement point position to the detection of the $P_V R_V$-time for the configuration with perpendicular irradiation, which is a suitable measuring condition for a reliable uncertainty analysis.
The influence of the measuring point position is important for non-clinical applications and in all the applications where the measuring point above the left atrium is difficult to identify. The pattern and the extraction of the $P_V R_V$-time should be detected reliably at more than one spot for non-laboratory applications.
Subsection 4.3.2 presents the measurements performed with the MPV-800 to analyze the influence of the laser beam orientation and the influence of the measuring point position for the detection of the $P_V R_V$-time.

4.3.2. Multipoint Measurements for Detection of Uncertainties

In this subsection, the influence of the measuring point position and of the laser beam orientation on the detection of the $P_V R_V$-time are calculated for the case of the subject lying supine.
At first, the setup used for the measurement is presented (Paragraph 4.3.2.1), then the measurements are analyzed (Paragraph 4.3.2.2) and the influence of the measuring point position and the influence of the laser beam orientation on the detection of the $P_V R_V$-interval are highlighted (Paragraph 4.3.2.3).

4.3.2.1. Setup

Measurements on the thorax of one volunteer were carried out with the multipoint vibrometer MPV-800 (Polytec GmbH) [61] as shown in Figure 4.11. The volunteer has a body mass index BMI = 26.2.
The vibrations of fifteen points p located in the left parasternal area of the thorax were simultaneously acquired with a sampling frequency of 1 kHz. The vibrations of each point were measured from three independent directions.

The sensor 3D Disto from Leica Geosystem® [158] was used to calculate the positions of the points p and of the optical heads in a defined global Cartesian

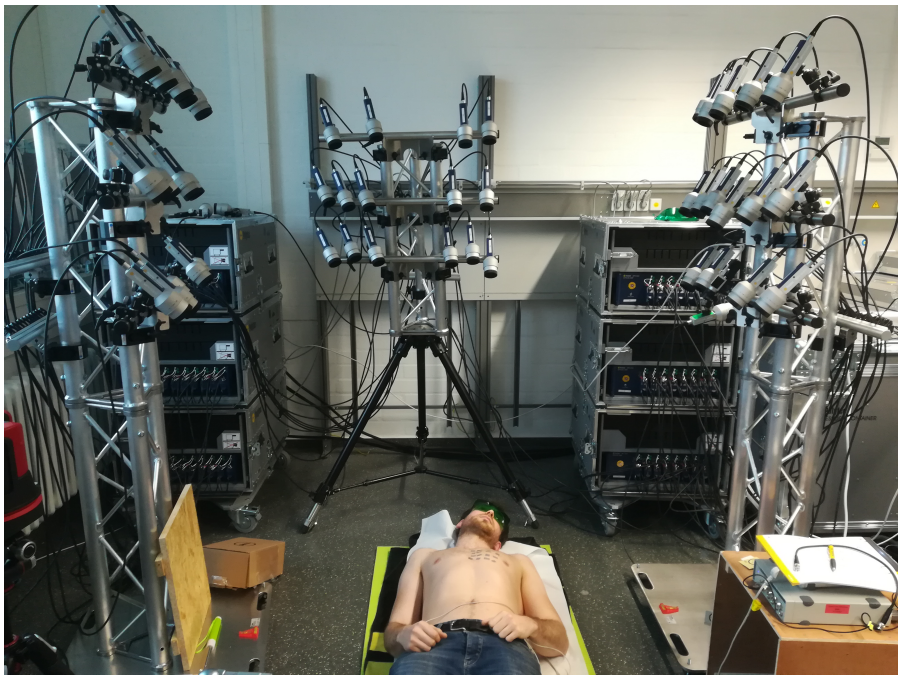

Figure 4.11.: Photo of the setup of the multipoint measurements with MPV-800 on the thorax of a volunteer.

coordinate system. The MPV-Software elaborates these pieces of information to calculate the measuring direction of each sensor head in respect to the measuring spot.
Measurements were performed and the MPV-Software delivers the 3D-velocity vector of each point in the global Cartesian coordinates similar as described in equation 4.5. Here, each point (p), was measured with three different measuring heads, from the three different directions $\boldsymbol{e}_{1\mathrm{p}}$, $\boldsymbol{e}_{2\mathrm{p}}$ and $\boldsymbol{e}_{3\mathrm{p}}$ similarly as in Paragraph 4.3.1.1. The directions were calculated by the software with the data delivered by the sensor 3D Disto.
The three corresponding measured amplitudes at the point p over the time t are called $v_{1,\mathrm{p}}(t)$, $v_{2,\mathrm{p}}(t)$ and $v_{3,\mathrm{p}}(t)$ and can be written as the scalar product between the 3D-vector at the time t of the measuring point p $\boldsymbol{v}_{\mathrm{p}}(t)$ and the direction defined by $\boldsymbol{e}_{1\mathrm{p}}$, $\boldsymbol{e}_{2\mathrm{p}}$ and $\boldsymbol{e}_{3\mathrm{p}}$, respectively (See equation 4.3).
The unit vectors of the measuring directions can be expressed in Cartesian coordinates with the xy-plane on the floor and the z-axis perpendicular to it

$$\boldsymbol{e}_{i,\mathrm{p}} = \cos\vartheta_{i,\mathrm{p}}\cos\varphi_{i,\mathrm{p}}\boldsymbol{e}_x + \cos\vartheta_{i,\mathrm{p}}\sin\varphi_{i,\mathrm{p}}\boldsymbol{e}_y + \sin\vartheta_{i,\mathrm{p}}\boldsymbol{e}_z, \tag{4.10}$$

where $i = 1, 2, 3$ identifies the direction of the measurement and the angles φ and ϑ are defined in Figure 4.8(b).
The vector of the point p $\boldsymbol{v}_{\mathrm{p}}(t)$ was reconstructed by the MPV-Software in Cartesian coordinates with the equation 4.5.
Therefore, the components of the 3D-vector along the $x-$,$y-$ and $z-$axis - $v_{x,\mathrm{p}}(t)$, $v_{y,\mathrm{p}}(t)$ and $v_{z,\mathrm{p}}(t)$ - are computed by the software.

Figure 4.12 presents the scheme of the setup used for the multipoint measurements. For a clear representation, Figure 4.12 shows only the measure on one point. The acquisition takes place in all the spots marked with a white cross, simultaneously.
Additionally, the II-lead of the ECG amplified with the amplifier Dual Bio Amp (ADInstrument) was sent to the acquisition box of the MPV-800 and it was simultaneously recorded to have a physiological reference signal. To detect the vibrations generated only by the heartbeat, the subject was asked to hold his breath during the measurements.

Low frequency disturbances and high frequency noise were removed using a zero-padding filter in the frequency domain with a passband bandwidth $0.6 - 100$ Hz[f]. Seventeen heartbeats were selected and the mean 3D-vector is calculated for the analysis in the Paragraph 4.3.2.2.

[f]The filter technique used is the F_3 described in A.

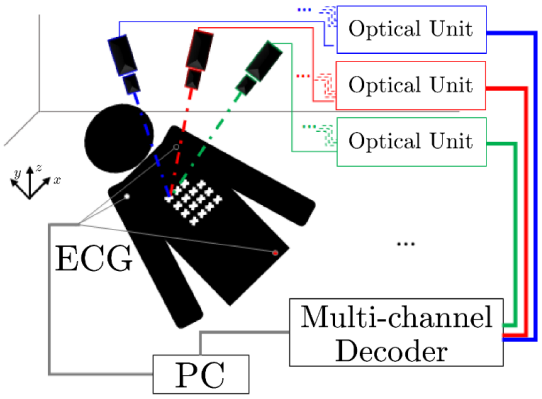

Figure 4.12.: Scheme of the measurement with the MPV-800.

4.3.2.2. Analysis

In this paragraph, the vibrations on the thorax acquired with the MPV are analyzed; the mean 3D-vector is calculated for all the investigated points and for different laser beam orientations.
The aim of the analysis is to identify at which locations on the thorax and for which laser beam orientation the typical pattern of the VCG-heartbeat is recognizable. Consequently, in the following paragraph (Paragraph 4.3.2.3), the influence of the setup on the detection of the $P_V R_V$-time is quantified for the points and the laser beam directions where the pattern is recognizable.

The mean 3D-velocity vector of the heartbeat of each point, p, $\overline{\boldsymbol{v}}_\mathrm{p}(t)$, is calculated as

$$\overline{\boldsymbol{v}}_\mathrm{p}(t) = \begin{Bmatrix} \overline{v}_{x,\mathrm{p}}(t) \\ \overline{v}_{y,\mathrm{p}}(t) \\ \overline{v}_{z,\mathrm{p}}(t) \end{Bmatrix} = \frac{1}{N} \cdot \begin{Bmatrix} \sum_{i=1}^{N} v_{x,\mathrm{p},i}(t) \\ \sum_{i=1}^{N} v_{y,\mathrm{p},i}(t) \\ \sum_{i=1}^{N} v_{z,\mathrm{p},i}(t) \end{Bmatrix}, \tag{4.11}$$

where $N = 17$ is the number of selected beats.
To perform the mean value, the VCG-heartbeats were synchronized using the ECG signal. The time segment of each VCG-heartbeat is obtained by selecting the 500 samples before and after the sample corresponding to the R-peak of the simultaneous acquired ECG.

The velocity components of the mean 3D-vector acquired perpendicularly to the floor for different points p - $v_{z,\mathrm{p}}(t)$ - is considered as a reference for the investigation ($v_{z,\mathrm{p}}(t) = v_{90°,\mathrm{p}}(t)$). All the graphics in Figure 4.13(a-c,e-p) show the mean over the seventeen beats of the z-components of the vibrations for each point p, $\overline{v}_{z,\mathrm{p}}(t)$. Figure 4.13(d) presents the projection on the xy-plane of the spatial distribution of the points p centered in point p = 1 with coordinate $(0, 0, 0)$.
Among the investigated points, only the points p $= 10, 11, 12, 13, 14, 15$ present the typical pattern of the VCG clearly. The points p $= 1, 2, 3, 4, 5, 6, 7, 8, 9$ present

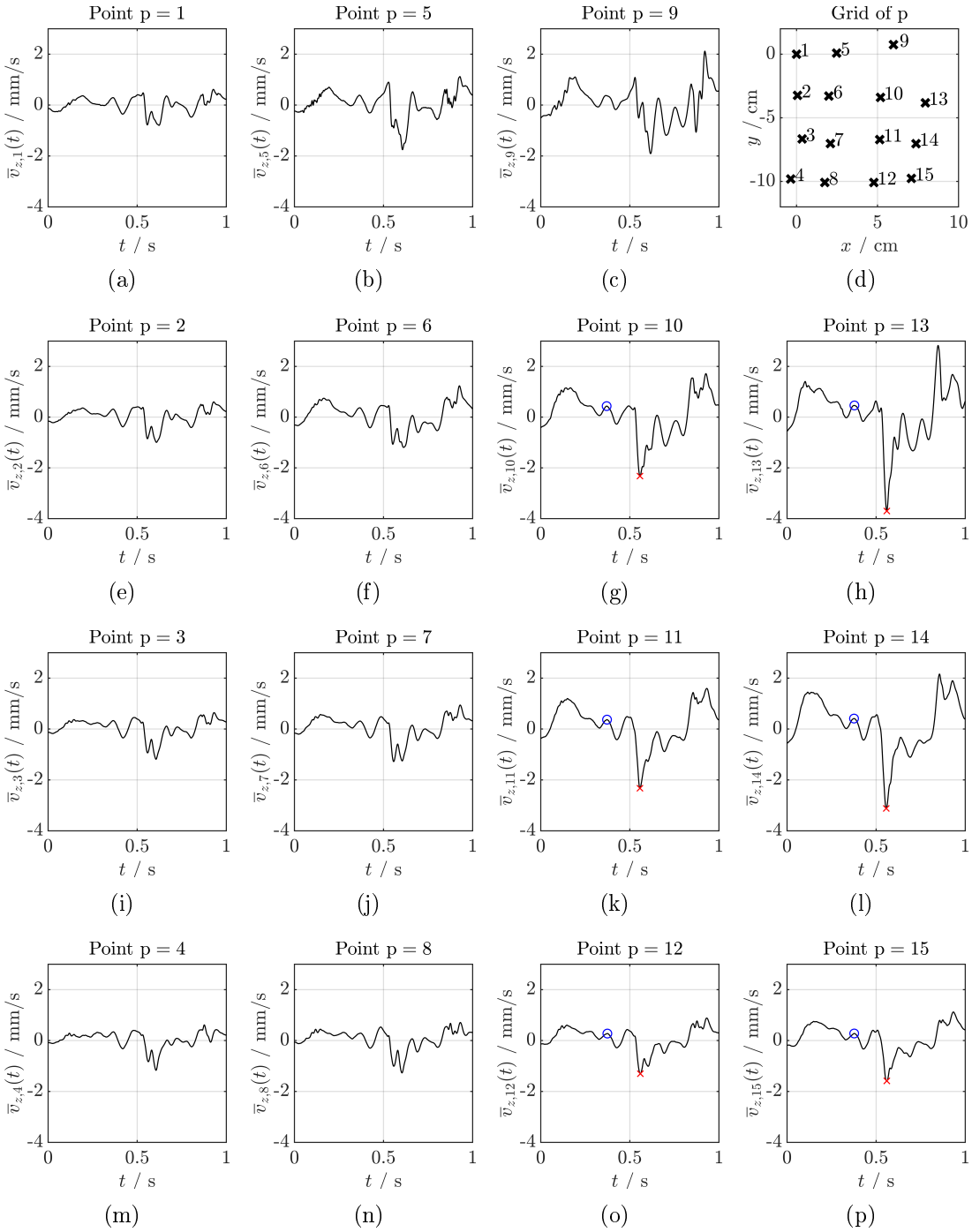

Figure 4.13.: MPV-velocity signals for the fifteen points p (a-c) and (e-p). Position of the points on the xy-plane (d). The P_{V}-point and R_{V}-peak of the signals acquired at the points p $= 10, 11, 12, 13, 14, 15$ are marked with a blue circle and a red cross, respectively.

Table 4.2.: Direction of the P_V-vector at the different points p.

p	10	11	12	13	14	15
ϑ / °	52.7	53.8	46.6	52.5	50.1	41.2
φ / °	-42.8	-33.6	-22.7	-23.8	-19.6	-20.9

Table 4.3.: Direction of the R_V-vector at the different points p.

p	10	11	12	13	14	15
ϑ / °	-74.8	-76.5	-80.4	-77.6	-79.0	-73.2
φ / °	169.9	-131.7	96.7	-105.4	-171.1	100.0

a biphasic R_V-peak which could be caused by adverse position such as the close distance to a ribs similarly as in [91].
Only the points with the best pattern (p $= 10, 11, 12, 13, 14, 15$) were considered for the analysis, whereas the other points were excluded.

Figure 4.14 shows the 3D-vectors $\overline{\boldsymbol{v}}_{\mathrm{p}}(t)$ for the points p $= 10, 11, 12, 13, 14, 15$. Table 4.2 and Table 4.3 show the direction of $\overline{\boldsymbol{v}}_{\mathrm{p}}(t)$ at the time instants corresponding to the P_V-point and R_V-peak detected in the projection $\overline{v}_{z,\mathrm{p}}(t)$, respectively. The P_V-point and R_V-peak in the time signal can be seen in Figure 4.13(g,h,k,l,o,p). The values of φ and ϑ for the P_V-vector have a maximum deviation among the points of $\approx 13°$ and $\approx 23°$, respectively (See Table 4.2). The values of ϑ for the R_V-vector are presented in Table 4.3 and show a maximum deviation among the points of $\approx 7°$, which is lower with respect to the maximum deviation of the angle ϑ among points for the P_V-vector.
However, the maximum deviation of the angle φ of the R_V-vector is greater than the one of the P_V-vector. The different direction between the points can be explained with the complex motion of the heart during its pumping function.

Since the P_V- and R_V-vectors are oriented in different directions, there is not one laser beam orientation for the optimal detection of both waves. Therefore, it is necessary to identify for which laser beam orientations the pattern of the VCG-heartbeat can be reliably detected. The laser beam directions are defined by the angles φ and ϑ defined in Figure 4.8(b).

The first step to identify for which angles φ and ϑ the VCG pattern is still recognizable, the projections of the 3D-vector in the directions defined by the angels φ and ϑ is computed. The unit vector $\boldsymbol{e}_{\varphi,\vartheta}$ identifies an arbitrary laser beam direction defined by the angles φ and ϑ.
The projections of the mean 3D-vector $\overline{\boldsymbol{v}}_{\mathrm{p}}(t)$ directed along the directions $\boldsymbol{e}_{\varphi,\vartheta}$ are called $v_{\mathrm{p},\varphi,\vartheta}$. The projections $v_{\mathrm{p},\varphi,\vartheta}(t)$ are calculated with equation 4.3.
In other terms, $v_{\mathrm{p},\varphi,\vartheta}(t)$ represents the VCG-velocity signal as if it was detected from the direction $\boldsymbol{e}_{\varphi,\vartheta}$. The projections $v_{\mathrm{p},\varphi,\vartheta}(t)$ are calculated for the directions

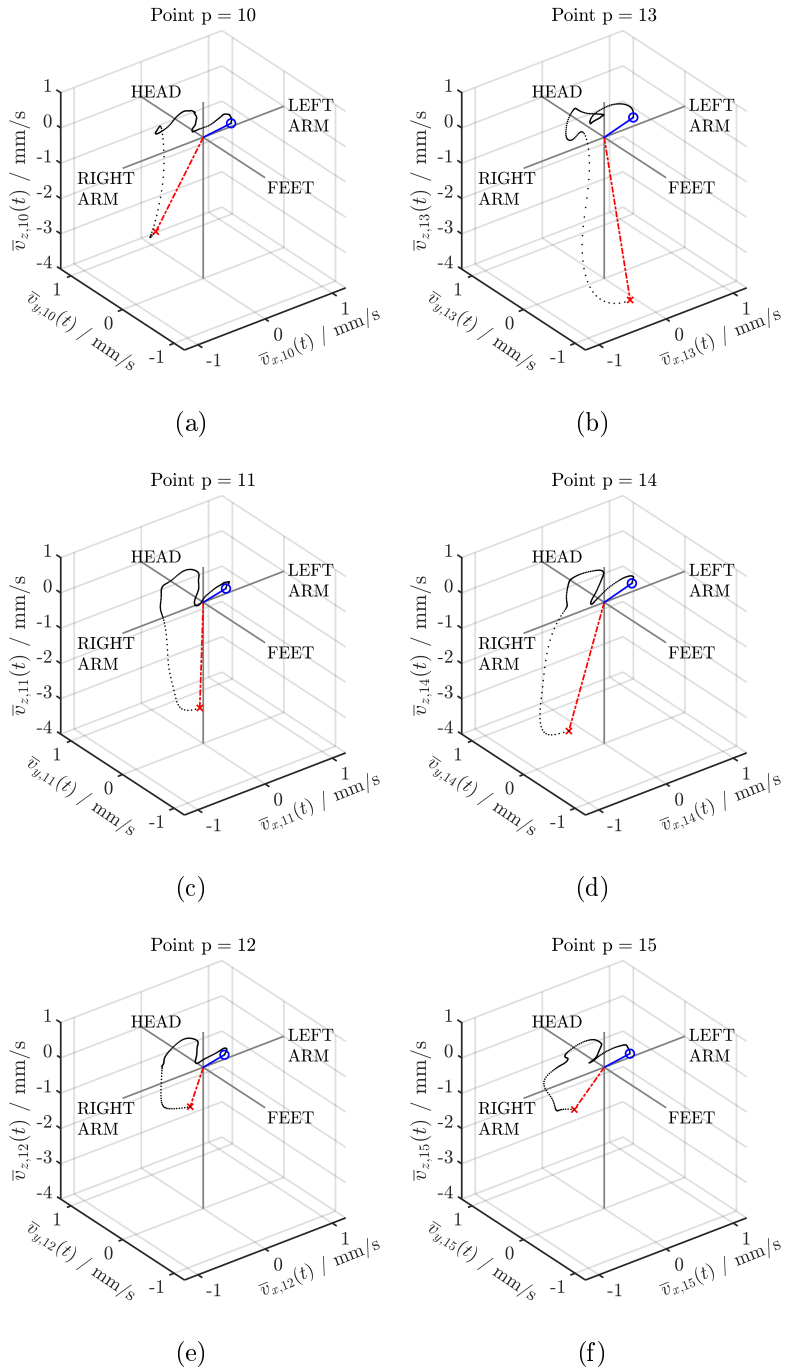

Figure 4.14.: 3D-vectors $\overline{\boldsymbol{v}}_{\mathrm{p}}(t)$ of the points $\mathrm{p} = 10, 11, 12, 13, 14, 15$ during the $P_{\mathrm{V}}R_{\mathrm{V}}$-interval. The blue circles are the P_{V}-points and the red crosses are the R_{V}-peaks. The trajectory of the P_{V}-points and of the R_{V}-peaks are the blue continuous lines and the red dashed lines, respectively.

$\boldsymbol{e}_{\varphi,\vartheta}$ where the angle φ varies from $-180°$ to $180°$ and the angle ϑ varies from $0°$ to $90°$ both with a step size of $1°$.
Only the positive values of the angle ϑ are considered because, for definition, negative values of the angle ϑ are under the floor and, therefore, not applicable.

There are combinations of the angles ϑ and φ where the projection of the 3D-vector does not present clearly recognizable P_V- and R_V-wave patterns; this happens because the direction of the projection is not aligned to the instantaneous directions of $\overline{\boldsymbol{v}}_p(t)$ for most of the time[g]. Therefore, these projections have to be excluded from the analysis.

A method based on the cross-correlation is used to decide which directions $\boldsymbol{e}_{\varphi,\vartheta}$ should be excluded.
The normalized cross-correlation between the VCG reference signal $\overline{v}_{z,p}(t)$ and its projections $v_{p,\varphi,\vartheta}(t)$ is performed using the Matlab function *xcorr.m* with the normalization option *"normalized"*. This option normalizes the sequence so that the autocorrelation of the two signals is equal to 1 at zero lag [187].
The maximum value of the normalized cross-correlation is called $c_{p,\varphi,\vartheta}$ and is calculated for every defined direction $\boldsymbol{e}_{\varphi,\vartheta}$. The maximum of the correlation $c_{p,\varphi,\vartheta}$ varies from 0 to 1. Only the directions $\boldsymbol{e}_{\varphi,\vartheta}$ where every angle φ presents a value of $c_{p,\varphi,\vartheta}$ greater than 0.8 in all the considered points are selected for the analysis. The others are excluded.

Figure 4.15 shows the colormap of the maximum of the correlation $c_{p,\varphi,\vartheta}$ over the angles φ and ϑ. For values of ϑ greater than $39°$ (black dashed line), all the points present a value of $c_{p,\varphi,\vartheta}$ greater than 0.8 for all the angles φ.
Therefore, the computation of the $P_V R_V$-time is performed for the projections in all the directions with the angle ϑ greater than $39°$ (φ varies from $-180°$ to $180°$).

4.3.2.3. Results

In this paragraph, the influence of the setup on the detection of the $P_V R_V$-time is quantified for the detection at measuring points and for laser beam orientations where the pattern of the VCG signal on the thorax is reliable.
These ranges of points and laser beam orientations are identified in the previous paragraph ($p = 10, 11, 12, 13, 14, 15$ and $\vartheta > 39°$).

The $P_V R_V$-interval of the VCG reference signal, $\overline{v}_{z,p}(t)$, is called $P_V R_{Vp,90°}$ and it is detected as described in equation 4.2.
The $P_V R_{Vp,90°}$ was computed for the seventeen heartbeats chosen for the points $p = 10, 11, 12, 13, 14, 15$ according to equation 4.2.
The mean value of the $P_V R_V$-time for the point p, $\overline{P_V R_{Vp,90°}}$ is

$$\overline{P_V R_{Vp,90°}} = \frac{1}{N} \sum_{i=1}^{N} P_V R_{Vp,i}, \tag{4.12}$$

[g] i.e. the angle γ in equation 4.3 is great for the whole heartbeat.

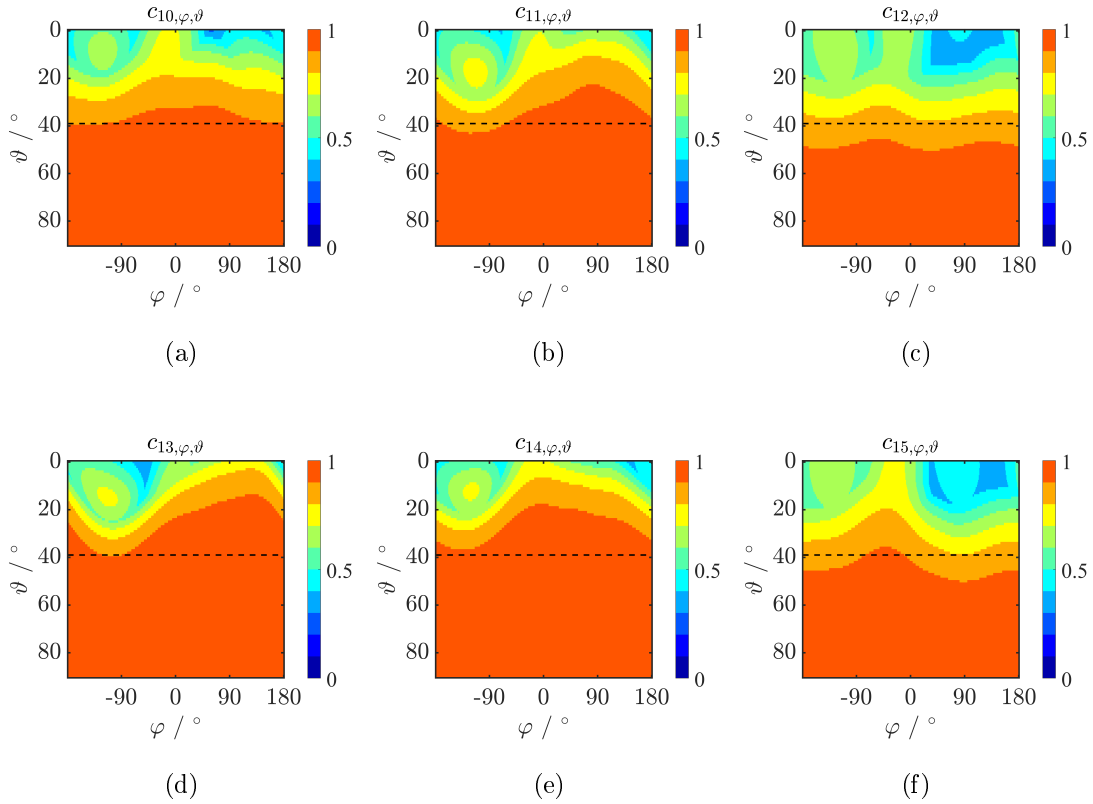

Figure 4.15.: Colormap of the values of $c_{\mathrm{p},\varphi,\vartheta}$ over the angles φ and ϑ. The black dashed line is at $\vartheta = 39°$.

Table 4.4.: $\overline{P_\mathrm{V}R_{\mathrm{V}\mathrm{p},90°}}$ for the points $\mathrm{p} = 10, 11, 12, 13, 14, 15$.

p	10	11	12	13	14	15
$\overline{P_\mathrm{V}R_{\mathrm{V}\mathrm{p}}}$ / ms	185.82	186.53	191.65	185.53	186.82	187.00

where $\mathrm{p} = 10, 11, 12, 13, 14, 15$ identifies the point.

The maximum deviation among the mean $P_\mathrm{V}R_\mathrm{V}$-time of the different points $\overline{P_\mathrm{V}R_{\mathrm{V}\mathrm{p},90°}}$ is

$$\Delta P_\mathrm{V}R_{\mathrm{V}\mathrm{p},90°} = \max(\overline{P_\mathrm{V}R_{\mathrm{V}\mathrm{p},90°}}) - \min(\overline{P_\mathrm{V}R_{\mathrm{V}\mathrm{p},90°}}). \tag{4.13}$$

The maximum value of $\Delta P_\mathrm{V}R_{\mathrm{V}\mathrm{p},90°}$ is obtained from point $\mathrm{p} = 12$ and the minimal from point $\mathrm{p} = 13$ leading to a $\Delta P_\mathrm{V}R_{\mathrm{V}\mathrm{p},90°}$ of ≈ 6 ms.
Therefore, for the points investigated, the deviation of the $P_\mathrm{V}R_\mathrm{V}$-time is up to 6 ms for the reference configuration with the laser beam oriented perpendicular to the floor.

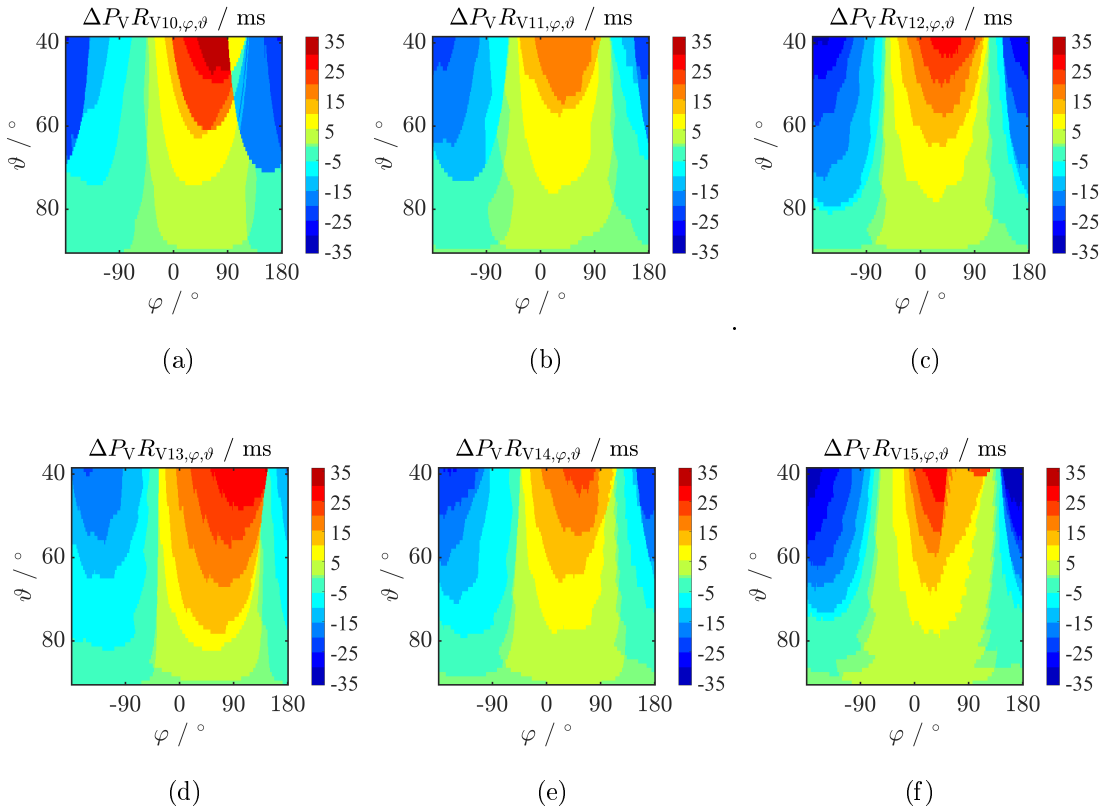

Figure 4.16.: Colormap of the values of $\Delta P_{\mathrm{V}}R_{\mathrm{Vp},\varphi,\vartheta}$ for the points 10 to 15. The color-bar represents the values of the difference $\Delta P_{\mathrm{V}}R_{\mathrm{Vp},\varphi,\vartheta}$ in ms.

The $P_{\mathrm{V}}R_{\mathrm{V}}$-interval of an arbitrary projection $v_{\mathrm{p},\varphi,\vartheta}(t)$ is called $P_{\mathrm{V}}R_{\mathrm{Vp},\varphi,\vartheta}$. The deviation between the time interval $P_{\mathrm{V}}R_{\mathrm{Vp},\varphi,\vartheta}$ and $P_{\mathrm{V}}R_{\mathrm{Vp},90^\circ}$ for the measuring point p is computed as

$$\Delta P_{\mathrm{V}}R_{\mathrm{Vp},\varphi,\vartheta} = P_{\mathrm{V}}R_{\mathrm{Vp},90^\circ} - P_{\mathrm{V}}R_{\mathrm{Vp},\varphi,\vartheta}. \tag{4.14}$$

Figure 4.16 shows the deviation of the $P_{\mathrm{V}}R_{\mathrm{V}}$-interval, $\Delta P_{\mathrm{V}}R_{\mathrm{Vp},\varphi,\vartheta}$, resulting from the laser beam orientation, for each investigated point. The color bar represents the value of $\Delta P_{\mathrm{V}}R_{\mathrm{Vp},\varphi,\vartheta}$ expressed in ms.
It can be noticed that, for each point, there are regions with lower and higher deviation of $\Delta P_{\mathrm{V}}R_{\mathrm{Vp},\varphi,\vartheta}$.
In all the graphics, the greater deviations of $\Delta P_{\mathrm{V}}R_{\mathrm{Vp},\varphi,\vartheta}$ occur for lower values of the angle ϑ. For small deviations of ϑ from the reference value $\vartheta = 90°$, the deviation $\Delta P_{\mathrm{V}}R_{\mathrm{Vp},\varphi,\vartheta}$ seems to be very close to zero.

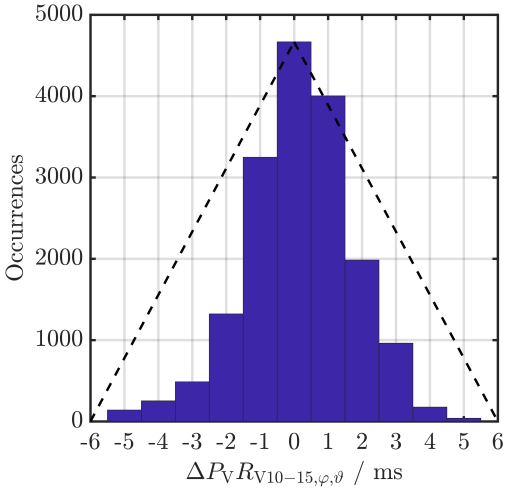

Figure 4.17.: Histogram of the occurrences of the deviation $\Delta P_V R_{V_p,\varphi,\vartheta}$ for the points 10 to 15 for the range of angles $82° \leq \vartheta < 90°$. The black dashed lines define the triangular distribution of the occurrences.

By adjusting the setup in practice, a maximal deviation 8° from the reference laser beam orientation $\vartheta = 90°$ can be assumed.
For 8° from the reference laser beam orientation $\vartheta = 90°$, i.e. $82° \leq \vartheta < 90°$, the deviation between the $P_V R_V$-interval acquired with the reference configuration and with a different configuration $\Delta P_V R_{V_p,\varphi,\vartheta}$ is included within the interval $-5 \text{ ms} \leq \Delta P_V R_{V_p,\varphi,\vartheta} \leq 5 \text{ ms}$ for all the angles φ and for all the investigated points.
A deviation $\Delta P_V R_{V_p,\varphi,\vartheta}$ equal to 5 ms could be considered an acceptable value. For angles greater than $\vartheta = 82°$, the $\Delta P_V R_{V_p,\varphi,\vartheta}$ assumes smaller values as |5 ms|. In Figure 4.17 the distribution of the difference $\Delta P_V R_{V_p,\varphi,\vartheta}$ for the directions defined by the angels $82° \leq \vartheta < 90°$ is presented. The distribution has a triangular form with the maximum at $\Delta P_V R_{V_p,\varphi,\vartheta} = 0$ ms.

4.4. Reliability of Detection of $P_V R_V$-Interval

This chapter aims to prove the reliability of the detection of the PR-time in VCG signal for daily measurements.
According to cardiologist expert opinion [91], clinical data suggest that an uncertainty lower than 20 ms is required for a reliable detection of the PR-interval.
In this work, a model for the calculation of the uncertainty according to the Guide to the Expression of Uncertainty in Measurement (GUM) [134] is presented.
For a reliable detection of cardiovascular diseases (such as AV-Blocks of I Type) and of healthy condition, the results should be statistically significant. The ranges of values that allow to state with 95% certainty that a diagnosis is correct need to be detected, i.e. the significance level α should be $\alpha < 0.05$ [188, 189]. Therefore, a statistical significance analysis is performed to asses for which values of the $P_V R_V$-interval the healthy condition and CV diseases are detectable with a significance level $\alpha < 0.05$. The method for the computation of the uncertainty according to GUM consists on the following steps:

- Definition of a model of the measurements,
- Evaluation of the type-A and type-B standard uncertainties,
- Determination of the combined uncertainty,
- Determination of the expanded uncertainty,
- Expression of the uncertainty.

The type-A uncertainties are statistically determined and the type-B uncertainties are not statistically determined [134].

In a previous work, a first model for the calculation of the uncertainty is presented [91]. This model is described in Subsection 4.4.1 and it is valid for measurements performed in clinical environments where the measuring point above the left atrium could be detected with the echocardiograph. The LDV was oriented perpendicularly to the defined measuring spot, and therefore, the laser beam orientation was different for each subject.

In this work (Subsection 4.4.2), the uncertainty of the $P_V R_V$-time is computed for a reference configuration. The reference configuration requires that the laser beam of the LDV is directed perpendicularly to the floor; this leads to an easier alignment of the laser beam, and therefore, to a more reproducible and more suitable setup for daily measurements with respect to the laser beam configuration of [91].
A more detailed analysis with respect to reference [91] is performed. In particular, the new model proposed in Subsection 4.4.2 considers the contribution to the uncertainty resulting from the measuring point position; this contribution is relevant for non-clinical applications where the spot direct above the left atrium is

not identifiable with the help of an echocardiograph.
Moreover, the contribution to the uncertainty resulting from a deviation of the laser beam orientation from the reference setup condition is considered.

In the Subsection 4.4.1 the state of the art of the uncertainty estimation is introduced and in the Subsection 4.4.2 the improved uncertainty estimation is described. Finally, the statistic significance of the result is discussed in Subsection 4.4.3.

4.4.1. State of the Art of Uncertainty Estimation

In Luik, Mignanelli et al. [91] a method for the computation of the uncertainty according to GUM is performed.
Vibration measurements of healthy subjects were acquired on the thorax. The LDV was pointed at the third intercostal space in correspondence to the left atrium with the help of an ultrasound scanner or echocardiograph.
The laser beam was oriented perpendicular to the thorax and, therefore, the laser beam orientation is different for every subject.
Twenty heart beats for each measurement were selected to perform a statistical analysis for the $P_{\mathrm{V}}R_{\mathrm{V}}$-time in comparison to the PR-interval in the simultaneous acquired ECG signal[h] and a method for the determination of the reliability of the PR-interval of the VCG on the thorax is described. In this study, a limited number of subjects were investigated.
For clinical applications, statements about the accuracy must be based on studies with a larger cohort. Nevertheless, the proposed method could be used for the determination of the uncertainties of the PR-time in VCG when a significant sample of subjects is available in the future.
The determination of the uncertainties is performed according to the Guide to the Expression of Uncertainties in Measurements (GUM) [134].

At first, a calibration factor $\Delta_{\mathrm{ECG,VCG}}$ is calculated; it compensates the systematic error resulting from the different definition of the PR-time in the ECG and in the VCG[i]. The calibration factor $\Delta_{\mathrm{ECG,VCG}}$ is determined as the average deviation between the PR-interval of the ECG and the $P_{\mathrm{V}}R_{\mathrm{V}}$-interval obtained from the VCG. The compensated $P_{\mathrm{V}}R_{\mathrm{V}}$-time is called $P_{\mathrm{V}}R_{\mathrm{V\,comp}}$ and it is obtained by adding $\Delta_{\mathrm{ECG,VCG}}$ to the measured $P_{\mathrm{V}}R_{\mathrm{V}}$-time

$$P_{\mathrm{V}}R_{\mathrm{V\,comp}} = P_{\mathrm{V}}R_{\mathrm{V}} + \Delta_{\mathrm{ECG,VCG}}. \tag{4.15}$$

[h] The values reported in [91] present a calculation error. Here the corrected values are reported.
[i] The PR-time in ECG is defined as the time difference between the start of the P-wave and the start of the QRS-complex while the PR-time in VCG is defined as the time difference between the maximum of the vibration generated by the P-wave and the minimum of the vibration generated by the QRS-complex.

For seven measurements on seven subjects of reference [91], the factor $\Delta_{\mathrm{ECG,VCG}}$ results in ≈ 11 ms. The compensated measurement value $P_{\mathrm{V}}R_{\mathrm{V\,comp}}$ of the PR-time in VCG can be transcribed as the PR-time duration in ECG (PR) plus the sum of the type-A, A_Δ, and type-B, B_Δ, measurement deviations

$$P_{\mathrm{V}}R_{\mathrm{V\,comp}} = \mathrm{PR} + \mathrm{A}_\Delta + \mathrm{B}_\Delta. \tag{4.16}$$

The type-A uncertainty takes into account the variation of the PR-time in VCG and it was calculated as follows. Firstly, for each j-th subject, the standard deviation of the 20 beats, sd_j, was calculated as

$$sd_j = \sqrt{\frac{1}{N-1}\sum_{i=1}^{N}(P_{\mathrm{V}}R_{\mathrm{V},i} - \overline{P_{\mathrm{V}}R_{\mathrm{V}}})^2}, \tag{4.17}$$

where $N = 20$ is the number of the beats selected for the analysis.
The type-A uncertainty for each j-th subject is

$$u_{\mathrm{A},j} = t_{(68\%)}(N)sd_j, \tag{4.18}$$

where $t_{(68\%)}(N)$ is the Student-t factor for a confidence interval of 68.27% for the twenty beats $t_{(68\%)}(20) = 1.027$.
The type-A uncertainty u_{A} is obtained by averaging the values of the standard deviation $sd_j(P_{\mathrm{V}}R_{\mathrm{V}})$

$$u_{\mathrm{A}} = \frac{1}{J}\sum_{j=1}^{J} sd_j(P_{\mathrm{V}}R_{\mathrm{V}}), \tag{4.19}$$

where $J = 7$ measurements. For the selected seven measurements of reference [91], u_{A} resulted in $u_{\mathrm{A}} \approx 7$ ms.

The type-B uncertainty estimates the influence of the anatomical and physiological characteristics on the PR-time in VCG. Due to the limited cohort of subjects, statistical evaluations could not be carried out. The database was inadequate to identify the specific hemodynamic, anatomic and mechanic features that determine the differences of VCG signals of different subjects.
The type-B uncertainty includes also the influence of the laser beam orientation[j].

The maximum positive/negative deviation between the $P_{\mathrm{V}}R_{\mathrm{V}}$-interval and PR-time on ECG was calculated from the measurements and it resulted in ≈ 13 ms/-22 ms. Since the deviation does not have a clear statistical distribution, a rectangular distribution with the maximum span $b = 22$ ms was assumed. The unknown systematic uncertainties have to be estimated conservatively, so that higher uncertainties than in a detailed analysis are delivered.

[j]The LDV was oriented from different directions for the different measurements.

The standard uncertainty of a rectangular distribution is $b/\sqrt{(3)}$ [134].
Therefore, the type-B uncertainty u_{B} is

$$u_{\mathrm{B}} = \frac{b}{\sqrt{3}} \tag{4.20}$$

and it results in $u_{\mathrm{B}} \approx 13$ ms.
For a general result of a measurement m expressed in function of other quantities $(w_1, w_2, ...w_j..., w_J)$ through a function g

$$m = g(w_1, w_2, ..., w_J), \tag{4.21}$$

the combined uncertainty u_{c} is defined, according to GUM [134], as

$$u_{\mathrm{c}}^2 = \sum_i^N \left(\frac{\partial g}{\partial w_j} \right)^2 u(w_j)^2, \tag{4.22}$$

where $u(w_j)$ is the uncertainty related to the quantity w_j and J is the number of input quantities.
The model of equation 4.16 is simple and all the sensitivity coefficients $\frac{\partial g}{\partial w_j}$ are 1.
The combined uncertainty for the model of equation 4.16, u_{c}, is easily calculated as

$$u_{\mathrm{c}} = \sqrt{u_{\mathrm{A}}^2 + u_{\mathrm{B}}^2}. \tag{4.23}$$

The combined uncertainty u_{c}results in $u_{\mathrm{c}} \approx \pm 15$ ms The expanded uncertainty, u_{e}

$$u_e = K \cdot u_{\mathrm{c}} \tag{4.24}$$

should be lower than 20 ms for a reliable detection of the PR-interval Park, On, et al. [179]. The expanded uncertainty is $u_e < 20$ ms for a coverage factor $K = 1.33$ which corresponds to a confidence interval of about 82% [91].

As mentioned before, this model of uncertainty is valid if the measuring point is above the left atrium. This ideal condition of the setup is not realistic for daily measurements at home or for tracking applications.
Moreover, the laser beam orientation for the measurement in reference [91] changes depending on the anatomical characteristic of the subject.
A fixed setup would lead to more reproducible measurements.

The new model of the measurements presented in the Subsection 4.4.2 is valid not only for the measuring point above the left atrium but for also for a wide area in the left parasternal region of the thorax for measurements performed on a lying subject with the LDV oriented perpendicularly to the floor.
These measuring conditions are chosen because of their more realistic applicability in daily monitoring.
In the new model presented, the contribution to the uncertainties resulting from the measuring point position and from the laser beam orientation are analyzed in details separately.

4.4.2. Uncertainty Estimation According to GUM

In this subsection, a new model with respect to the one reported in Luik, Mignanelli, et al. [91] of the PR-time measurements from VCG signal on the thorax is proposed. The uncertainty of the $P_V R_V$-time is calculated and compared to the requirement of 20 ms.

The model of equation 4.16 can be analyzed in detail to consider other uncertainty contributions as

$$P_V R_{V\,\mathrm{comp}} = \mathrm{PR} + \mathrm{A}_\Delta + \sum_{i=1}^{N} \mathrm{B}_{\Delta,i}, \tag{4.25}$$

where N is the amount of type-B uncertainty contributions considered.
This work contemplates only one type-A uncertainty. In a general formulation, the model of equation 4.25 can include more than one type-A uncertainty contribution. Therefore, the term A_Δ should be substituted with the term $\sum_{j=1}^{J} \mathrm{A}_{\Delta,j}$, where J is the amount of type-A uncertainty contributions considered.

The configuration with the laser beam orientation perpendicular to the skin used in [91] is difficult to employ. To perform reproducible measurements on each subject, a more suitable setup condition is chosen.
The VCG measurements taken as references in this work are all directed perpendicularly to the ground and not to the skin. This implies that a new calibration factor $\Delta_{\mathrm{ECG,VCG}}$ with respect to the one of [91] should be calculated for the case of perpendicular laser irradiation.
For the configuration with perpendicular irradiation, the calibration factor is called $\Delta_{\mathrm{ECG,VCG,s,90°}}$. A new type-A and a new type-B uncertainty values should also be computed.
The anatomical and physiological variation among subjects is considered in a different way as in [91] by including them in the calibration factor $\Delta_{\mathrm{ECG,VCG,s,90°}}$, where the subscript $_\mathrm{s}$ highlights the dependence on the subject characteristics. The calibration factor $\Delta_{\mathrm{ECG,VCG,s,90°}}$ is explained in Paragraph 4.4.2.1. The estimation of the calibration factor $\Delta_{\mathrm{ECG,VCG,s,90°}}$ and all the uncertainties related to these aspects are addressed to future works.
The model presented is valid not only for the measuring point above the left atrium but for also for a wide area in the left parasternal region of the thorax.

4.4.2.1. Model of Measurements

The model of the $P_V R_V$-measurement of equation 4.25 is employed to determine the expanded uncertainty of the PR-time acquired from VCG signals. The model of equation 4.25 is analyzed in detail with the uncertainty contributions delivered by the influence factors examined in the Section 4.3.
The analysis of the Sections 4.3 shows that the measuring point position and the

laser beam orientation have an influence in the detection of the $P_{\mathrm{V}}R_{\mathrm{V}}$-time and, therefore, they must be considered in the computation of the uncertainties.
The model of the measurement is

$$P_{\mathrm{V}}R_{\mathrm{V\,comp}} = \mathrm{PR} + \mathrm{A}_{\Delta,90^\circ} + \mathrm{B}_{\Delta,\mathrm{p}} + \mathrm{B}_{\Delta,\varphi,\vartheta}, \tag{4.26}$$

where PR is the PR-time in ECG and $P_{\mathrm{V}}R_{\mathrm{V\,comp}}$ is the compensated time obtained similarly as defined in the equation 4.15 but with a new calibration factor $\Delta_{\mathrm{ECG,VCG,s},90^\circ}$. The calibration factor of this approach is the systematic error between the PR time in ECG and $P_{\mathrm{V}}R_{\mathrm{V}}$ acquired along the z-axis for a particular class of subject s. A class of subjects includes subjects with similar tissue stratification. Subjects with similar tissue stratification have similar vibration response to the electrical signal generated by the heart. Therefore, they have similar duration of both PR-time and $P_{\mathrm{V}}R_{\mathrm{V}}$-interval. Subjects with different tissue stratification may have similar duration of the PR-time but a different duration of the $P_{\mathrm{V}}R_{\mathrm{V}}$-time. The classification can be based on indexes related to the physical characteristics (body mass index and body shape index), on the health condition (diseases) and on the lifestyle (regular physical activity, smoke) of the subjects. The value of $\Delta_{\mathrm{ECG,VCG,s},90^\circ}$ for the different classes can be determined statistically with a wider cohort.

The error $\mathrm{A}_{\Delta,90^\circ}$ is the random error accounting for the variation of the PR-time in VCG and it can be evaluated as a type-A uncertainty. The subscript 90° is to remind that the analysis considers the configuration with the LDV perpendicular to the floor.
The unknown systematic errors that can be estimated with the type-B uncertainty are: $\mathrm{B}_{\Delta,\mathrm{p}}$ and $\mathrm{B}_{\Delta,\varphi,\vartheta}$.
The error $\mathrm{B}_{\Delta,\mathrm{p}}$ is the error due to the measuring point position and the error $\mathrm{B}_{\Delta,\varphi,\vartheta}$ is the one due to laser beam orientation.
In the next paragraphs, the type-A and type-B uncertainties are computed, combined and expanded.
Finally, the results are discussed.

4.4.2.2. Type-A Uncertainty

The type-A uncertainty takes into account the variation of the PR-time in VCG; it integrates the contribution of various factors that can be statistically estimated. One of these factors is the measuring error resulting from the post-processing (algorithm, filtering technique).
In Appendix A, I performed a preliminary analysis on a small statistic sample to estimate roughly the influence of the disturbances and their filtering for the detection of the $P_{\mathrm{V}}R_{\mathrm{V}}$-time.
According to the results, the sole contribution of the disturbance enhanced by the filtering is lower than 2 ms.

The estimation of the separate type-A uncertainty contributions requires a relevant statistical sample; which was not available. Therefore, I estimated the total value of the type-A uncertainty that includes different contribution as the one resulting from the disturbances enhanced by the filtering.

The type-A uncertainty is calculated for the VCG signal directed along the z-axis ($\vartheta = 90°$).

Firstly, for each measurement point p, the standard deviation of the 17 selected beats, $sd_{\mathrm{p},90°}$, was calculated for the single measurement as

$$sd_{\mathrm{p},90°} = \sqrt{\frac{1}{N-1}\sum_{i=1}^{N}(P_{\mathrm{V}}R_{\mathrm{V}\,\mathrm{p},90°,i} - \overline{P_{\mathrm{V}}R_{\mathrm{V}}}_{\mathrm{p},90°})^2}, \tag{4.27}$$

where $N = 17$ is the number of the beats selected for the analysis. The values of $sd_{\mathrm{p},90°}$ are reported in Table 4.5.

The type-A uncertainty for the single measurement at the point p is calculated as

$$u_{\mathrm{A,p},90°} = t_{(68\%)}(N) \cdot sd_{\mathrm{p},90°}, \tag{4.28}$$

where $t_{(68\%)}(N)$ is the Student-t factor for a confidence interval of 68.27% for the 17 beats, $t_{(68\%)}(17) = 1.032$.

The averaged type-A uncertainty over the six points $p = 10$ to $p = 15$ is:

$$u_{\mathrm{A},90°} = \frac{1}{6}\sum_{\mathrm{p}} u_{\mathrm{A,p},90°}. \tag{4.29}$$

Therefore, the type-A uncertainty $u_{\mathrm{A},90°}$ for one measurement of the P_VR_V-time results in $u_{\mathrm{A},90°} = 15.75\ \mathrm{ms} \approx 16\ \mathrm{ms}$.

Table 4.5.: Standard deviation $sd_{\mathrm{p}}(P_{\mathrm{V}}R_{\mathrm{V}\,\mathrm{p},90°})$ for the points p = 10 to p = 15.

p	10	11	12	13	14	15
$sd_{\mathrm{p}}(P_{\mathrm{V}}R_{\mathrm{V}\,\mathrm{p},90°})$ / ms	13.71	13.89	15.87	15.42	15.27	17.45

For cases such as healthy subjects at rest, where the PR-time is almost stable, the uncertainty of the PR-time in VCG could be estimated for the mean value as

$$u_{\mathrm{A,p},90°,\mathrm{mean}} = \frac{t_{(68\%)}(N)}{\sqrt{N}} \cdot sd_{\mathrm{p},90°}. \tag{4.30}$$

The type-A uncertainty would reduce of a factor $\sqrt{N}$.

Since the measurement of this work is performed on an healthy subject at rest, the averaged type-A uncertainty

$$u_{\mathrm{A},90°,\mathrm{mean}} = \frac{1}{6}\sum_{\mathrm{p}} u_{\mathrm{A,p},90°,\mathrm{mean}}. \tag{4.31}$$

In this example, the type-A uncertainty calculated results in $u_{\mathrm{A},90^\circ,\mathrm{mean}} = 3.82$ ms, i.e. $u_{\mathrm{A},90^\circ,\mathrm{mean}} \approx 4$ ms, with $N = 17$. However, for the monitoring under physical load or for subjects affected by cardiovascular diseases (such as AV-Blocks), the uncertainty of the PR-time in VCG must be estimated for the single measurement (heartbeat).

4.4.2.3. Type-B Uncertainty: Measuring Point Position

The uncertainty contribution resulting from the measuring point position is computed starting from the maximum deviation among the $P_\mathrm{V}R_\mathrm{V}$-time of the different points for the signal acquired perpendicular to the ground $\Delta P_\mathrm{V}R_{\mathrm{Vp},90^\circ}$ (see equation 4.13).
A rectangular distribution with a span of $b = \Delta P_\mathrm{V}R_{\mathrm{Vp},90^\circ}$ is assumed.
The standard uncertainty for a rectangular distribution is $b/\sqrt{3}$ [134]. Hence, the uncertainty resulting from the measuring position is computed as

$$u_{\mathrm{B,p}} = \frac{b}{\sqrt{3}} = \frac{\Delta P_\mathrm{V}R_{\mathrm{Vp},90^\circ}}{\sqrt{3}}. \tag{4.32}$$

The value of $\Delta P_\mathrm{V}R_{\mathrm{Vp},90^\circ}$ obtained from 4.3.2.3 is $\approx$ 6 ms; this leads to an uncertainty contribution $u_{\mathrm{B,p}} = 3.53$ ms ≈ 4 ms.

4.4.2.4. Type-B Uncertainty: Laser Beam Orientation

The contribution resulting from the uncertainty of the laser beam orientation can be expressed as a type-B uncertainty, which is called $u_{\mathrm{B},\varphi,\vartheta}$.
I assume that by the adjustment of the LDV, a maximal deviation of 8° between the laser beam orientation of the LDV and the perpendicular position occurs. According to Figure 4.16, for an angle variation within 8° from the direction perpendicular to the floor[k] and for all measured points, the maximal $P_\mathrm{V}R_\mathrm{V}$-time deviation $\Delta P_\mathrm{V}R_{\mathrm{Vp},\varphi,\vartheta}$ is 5 ms, independently from the value of the angle φ.
The type-B uncertainty resulting from the laser beam orientation $u_{\mathrm{B},\varphi,\vartheta}$ is valid for the laser beam directions defined by $82^\circ \leq \vartheta < 90^\circ$, independently from the value of the angle φ.

The fact that the uncertainty $u_{\mathrm{B},\varphi,\vartheta}$ is valid for all the angles φ is very important for the reproducibility of the setup. In fact, while the position perpendicular to the floor is easy to set, the x- and y-components vary with the orientation of the subject's body on the floor. Therefore, the position in the xy-plane is not clearly reproducible.

According to Figure 4.17, the distribution of $\Delta P_\mathrm{V}R_{\mathrm{Vp},\varphi,\vartheta}$ seems to have a triangular form: the lower deviations among all the measurement points seem to

[k] According to Figure 4.8(b): $82^\circ \leq \vartheta < 90^\circ$

be more probable. Therefore, a triangular probability distribution can be assumed for the computation of the standard uncertainty resulting from the laser beam orientation. The upper and lower bounds of the triangular distribution $\pm b$ are set where the number of occurrences is zero; therefore, $b = 6$ ms is chosen.
The standard uncertainty of a triangular distribution is $b/\sqrt{6}$ [134]. The contribution to the uncertainty resulting from the laser beam orientation $u_{\mathrm{B},\varphi,\vartheta}$ can be calculated as

$$u_{\mathrm{B},\varphi,\vartheta} = \frac{b}{\sqrt{6}} = \frac{6 \text{ ms}}{\sqrt{6}} = 2.45 \text{ ms} \approx 3 \text{ ms}. \tag{4.33}$$

4.4.2.5. Combination of Uncertainty

In this paragraph the combined uncertainty is estimated for the single and for the mean value of the $P_V R_V$-time. For the case of patients with diseases or for measurements under physical efforts, the uncertainty for the single value should be determined. The combined uncertainty for the mean value, can be used in such cases where the PR-time is almost stable, such as for health subject at rest.

The combined uncertainty is obtained as described in Subsection 4.4.1 with the equation 4.22.
The model of equation 4.26 is simple and linear and all the sensitivity coefficients are 1.
The combined uncertainty, for the case of a single measurements performed in the left parasternal region of the thorax with the laser beam perpendicular to the floor with a maximal deviation of 8° from this position, is calculated as

$$u_{\mathrm{c}} = \sqrt{u^2_{\mathrm{A},90^\circ} + u^2_{\mathrm{B,p}} + u^2_{\mathrm{B},\varphi,\vartheta}}. \tag{4.34}$$

The type-A uncertainty is $u_{\mathrm{A},90^\circ} \approx 16$ ms for the single measurement. The uncertainty resulting from the measuring point position is $u_{\mathrm{B,p}} \approx 4$ ms and the uncertainty resulting from the laser beam orientation is $u_{\mathrm{B},\varphi,\vartheta} \approx 3$ ms.
The combined uncertainty of equation 4.34 results in $u_{\mathrm{c}} \approx 17$ ms. The uncertainty of type A for the investigated subjects is the dominant contribution to the uncertainties. Generally, the value of the combined uncertainty u_{c} can diminish if a more detailed analysis of the uncertainty contribution is performed. In this work, I decided to estimate all the uncertainty contribution conservatively.

The combined uncertainty for the mean measurements is calculated as

$$u_{\mathrm{c,mean}} = \sqrt{u^2_{\mathrm{A},90^\circ,\mathrm{mean}} + u^2_{\mathrm{B,p}} + u^2_{\mathrm{B},\varphi,\vartheta}}. \tag{4.35}$$

The type-A uncertainty for the mean value over $N = 17$ measurements is $u_{\mathrm{A},90^\circ,\mathrm{mean}} \approx 4$ ms (see Paragraph 4.4.2.2), leading to the combined uncertainty value $u_{\mathrm{c,mean}} \approx 6$ ms.

The values of the combined uncertainty u_c and $u_{c,mean}$ can be reduced with a more precise alignment. In particular by reducing the investigation area (excluding point 12 and 13) from the analysis of the influence of the measuring point, the type-B uncertainty $u_{B,p}$ decrease to $u_{B,p} = 0.68$ ms ≈ 1 ms. By considering a more precise adjustment with a laser beam orientation with a maximal deviation of 2°from the reference direction, the type-B uncertainty $u_{B,\varphi\vartheta}$ decrease to $u_{B,\varphi\vartheta} = 1.22$ ms $\approx$ 1 ms.
By considering a more precise alignment, the values of the combined uncertainty reduces to u_c reduces to $u_c \approx 16$ ms and $u_{c,mean} \approx 4$ ms. A lower type-A uncertainty could be achieved by optimizing the algorithm for the detection of the $P_V R_V$-time and the filtering technique for the post-processing; this is only possible if a significant statistical sample is available.

4.4.2.6. Expansion of Uncertainty

The expanded uncertainty can be computed with equation 4.24. For the case of the single measurement, the requirement that the u_e has to be lower than 20 ms is met only for a maximal coverage factor of $K = 1.17$ (with $u_c \approx 17$ ms). This corresponds to a confidence interval of $\approx 76\%$ which is not sufficient.

For the case of healthy subject at rest, the expanded uncertainty is called $u_{e,mean}$ and it results $u_{e,mean} \approx \pm 18$ ms with a coverage factor of $K = 3$ and, therefore, it satisfy the requirement to be lower than 20 ms for a confidence interval of 99.73%. However, this requirement alone is not sufficient to determine if the healthy condition or CV diseases can be detected reliably. Therefore, the statistic significance of the results need to be discussed.

4.4.3. Statistic Significance of the Result

As mentioned in Paragraph 4.1.2.3, normal values of PR-time are between 120 ms and 200 ms; PR-time values lower than 120 ms and greater than 200 ms are related to CV diseases. In this paragraph I identified for which range of values of $P_V R_{V\,comp}$, it is possible to say with 95% certainty that a diagnosis is correct. According to the statistic significance theory [188, 189], the acceptable rejection region comprises 5% of the probability distribution. This can be expressed with the signaficance level α. Therefore, the result is statistic significant if the significance level is $\alpha < 0.05$. Here, I identify

- the range of $P_V R_{V\,comp}$ values that allow the detection of the healthy condition with at least 95% probability
- the ranges of $P_V R_{V\,comp}$ values that allow the detection of CV diseases with at least 95% probability

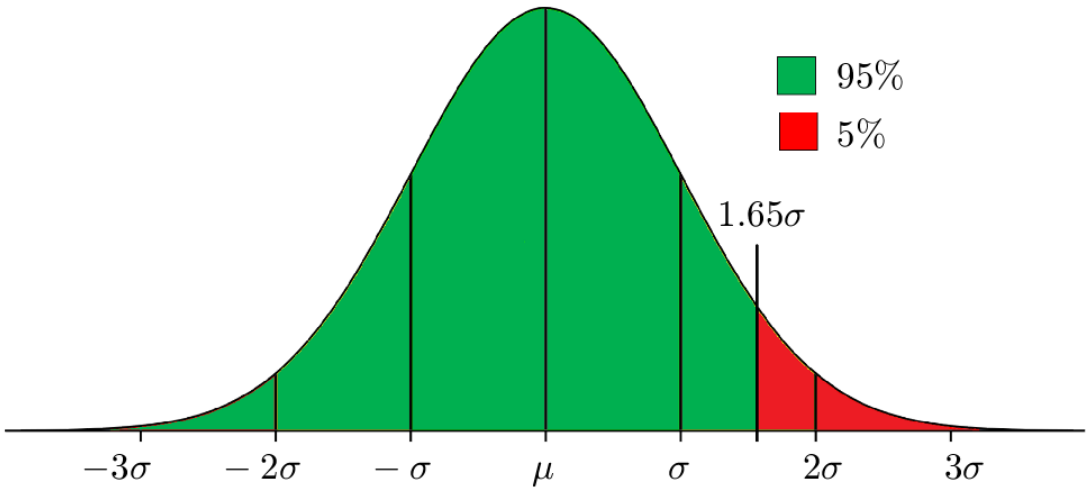

Figure 4.18.: Rejection region for a significance level $\alpha = 0.05$ for a one side configuration by assuming a normal distribution, where μ and σ are the expected value and the standard deviation, respectively.

for the case of the single measurement and for the case of the mean measurement. To identify the above mentioned ranges, the 5% rejection region can be allocated to one side of the sampling distribution, as in a one-tailed test as shown in Figure 4.18.

At first, I analyzed the range of $P_{\mathrm{V}}R_{\mathrm{V_{comp}}}$ values that allow for the detection of the healthy condition and of the presence of CV diseases with at least 95% probability for the case of a single measurement. Figure 4.19(a) shows the range of $P_{\mathrm{V}}R_{\mathrm{V_{comp}}}$ where the healthy condition can be reliably detected (green area) and where the rejection region is greater than 5% (gray area). It is not possible to say with 95% probability that the patient is healthy if the value of $P_{\mathrm{V}}R_{\mathrm{V_{comp}}}$ is included in the gray area. The combined uncertainty for the case of the single measurement with a precise alignment, is $u_{\mathrm{c}} \approx 16$ ms. For the single measurement we can consider the standard deviation $\sigma = u_{\mathrm{c}} \approx 16$ ms. According to Figure 4.18 and by considering the symmetry of the normal distribution, the values of $P_{\mathrm{V}}R_{\mathrm{V_{comp}}}$ for a reliable detection of the healthy condition are included in the interval

$$120 \text{ ms} + 1.65 \cdot \sigma < P_{\mathrm{V}}R_{\mathrm{V_{comp}}} < 200 \text{ ms} - 1.65 \cdot \sigma \tag{4.36}$$

with $\sigma = u_{\mathrm{c}} \approx 16$ ms.
Therefore, the reliable range for the detection of the healthy condition for the case of a single measurements results in 146.4 ms $< P_{\mathrm{V}}R_{\mathrm{V_{comp}}} <$ 173.6 ms. Figure 4.19(b) shows the range of $P_{\mathrm{V}}R_{\mathrm{V_{comp}}}$ where CV diseases can be reliably detected (green area) and where the rejection region is greater than 5% (gray area). For values of $P_{\mathrm{V}}R_{\mathrm{V_{comp}}}$ in the gray area, it is not possible to say with 95% probability

that the patient is ill.
Similarly as computed for the healthy condition, the ranges where CV diseases can be reliably detected are:

$$P_{\mathrm{V}}R_{\mathrm{V\,comp}} < 120\ \mathrm{ms} - 1.65 \cdot \sigma = 93.6\ \mathrm{ms} \tag{4.37}$$

and

$$P_{\mathrm{V}}R_{\mathrm{V\,comp}} > 200\ \mathrm{ms} + 1.65 \cdot \sigma = 226.4\ \mathrm{ms}. \tag{4.38}$$

To summarize, for the case of a single measurement with a precise alignment, the healthy condition can be reliably detect for values of $P_{\mathrm{V}}R_{\mathrm{V\,comp}}$ within the range $146.4\ \mathrm{ms} < P_{\mathrm{V}}R_{\mathrm{V\,comp}} < 173.6\ \mathrm{ms}$ and CV diseases can be reliably diagnosed for $P_{\mathrm{V}}R_{\mathrm{V\,comp}} < 93.6\ \mathrm{ms}$ and $P_{\mathrm{V}}R_{\mathrm{V\,comp}} > 226.4\ \mathrm{ms}$.

The same analysis is performed for the case of the mean value measurement with $N = 17$. Figure 4.20(a) shows the range of $P_{\mathrm{V}}R_{\mathrm{V\,comp}}$ where the healthy condition can be reliably detected (green area) and where the rejection region is greater than 5% (gray area), for the case of the mean value measurement with precise alignment. The combined uncertainty for the case of the mean value measurement with a precise alignment, is $u_{\mathrm{c,mean}} \approx 4$ ms, Therefore, the standard deviation σ is $\sigma = u_{\mathrm{c,mean}} \approx 4$ ms. Similarly to the case of the single measurements, it is possible to compute the range for a reliable detection of the healthy condition with equation 4.36. In this case, the reliable range of the values $P_{\mathrm{V}}R_{\mathrm{V\,comp}}$ for the detection of the healthy condition is $126.6\ \mathrm{ms} < P_{\mathrm{V}}R_{\mathrm{V\,comp}} < 193.4\ \mathrm{ms}$. The range of the values $P_{\mathrm{V}}R_{\mathrm{V\,comp}}$ for the detection of CV diseases is shown in Figure 4.20(b). The ranges are computed with the equations 4.37 and 4.38 with $\sigma \approx 4$ ms instead of $\sigma \approx 16$ ms. The reliable ranges of $P_{\mathrm{V}}R_{\mathrm{V\,comp}}$ for the detection of CV are $P_{\mathrm{V}}R_{\mathrm{V\,comp}} < 113.4\ \mathrm{ms}$ and $P_{\mathrm{V}}R_{\mathrm{V\,comp}} > 206.6\ \mathrm{ms}$.

If a precise alignment as the one described in this section is not achievable, the method and the model for the detection of the uncertainty proposed in this chapter can be adapted to this case, too. In particular, by calculating the contribution to the uncertainty of the laser beam orientation and of the measuring point position, a new value of the combined uncertainty is obtained. By computing equations 4.36, 4.37 and 4.38 with the new value of the combined uncertainty, the reliable range of value for the case can be detected.

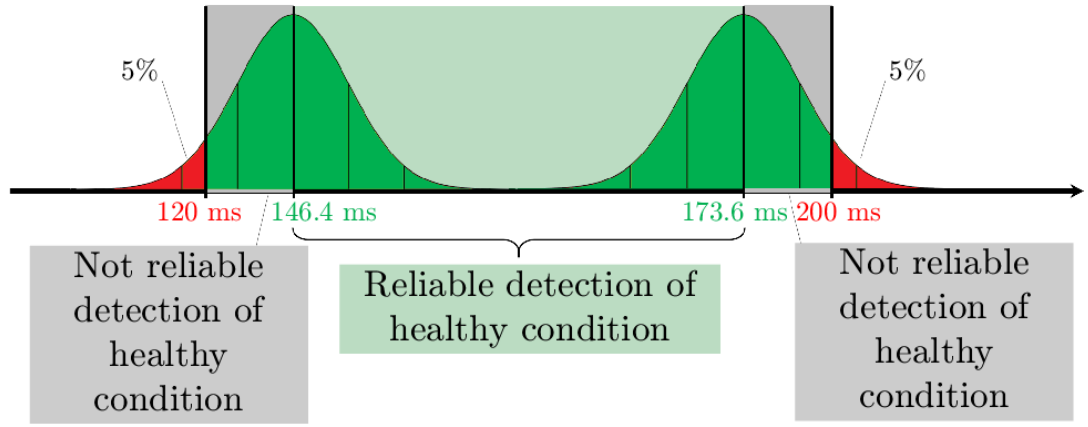

(a)

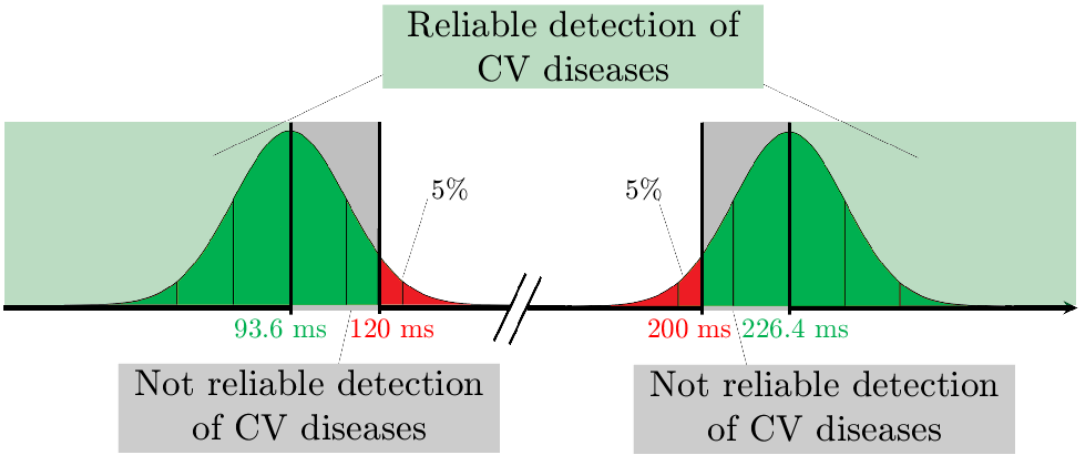

(b)

Figure 4.19.: Range of $P_V R_{V\,comp}$ where the healthy condition (a) and the CV diseases (b) can be reliably detected (green area) and where the rejection region is greater than 5% (gray area), for the case of the single measurement with precise alignment.

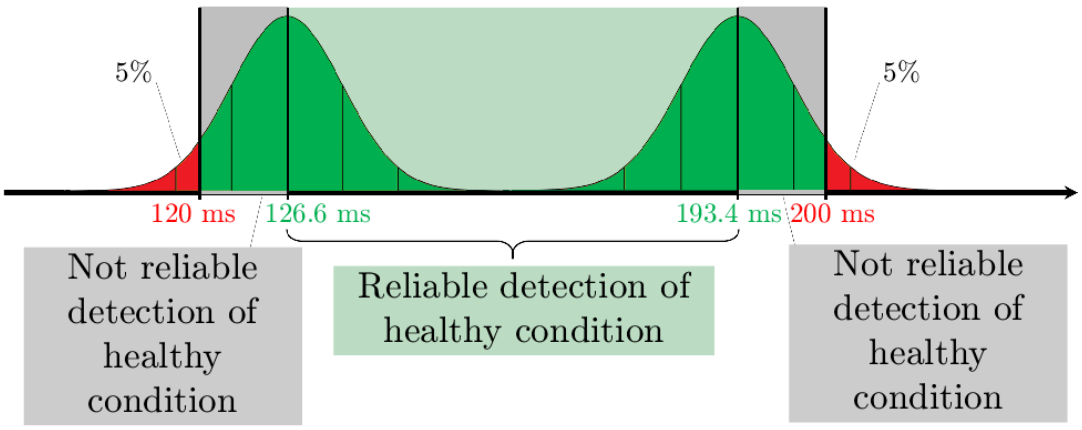

(a)

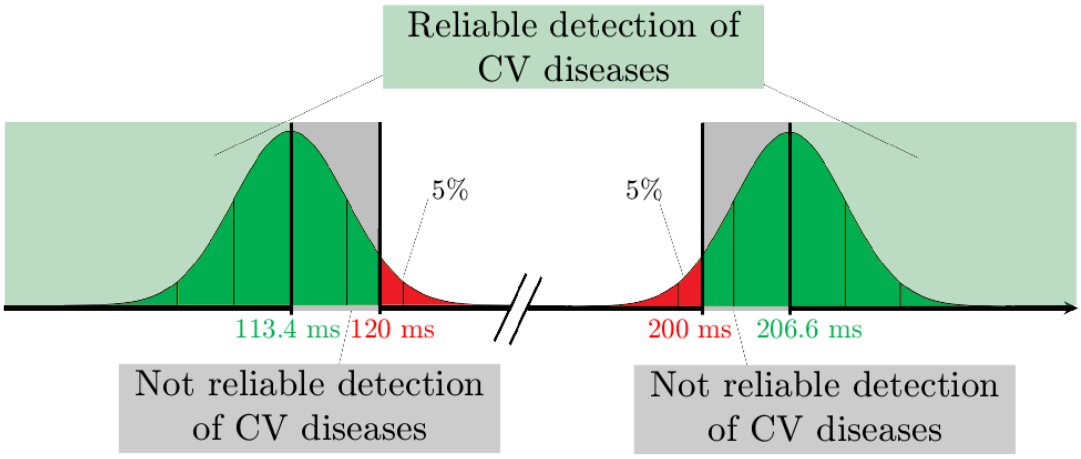

(b)

Figure 4.20.: Range of $P_{\mathrm{V}}R_{\mathrm{V\,comp}}$ where the healthy condition (a) and the CV diseases (b) can be reliably detected (green area) and where the rejection region is greater than 5% (gray area), for the case of the mean value measurement ($N = 17$) with precise alignment.

5. Photoacoustic Imaging with LDV

This chapter analyses the possibility to employ laser Doppler Vibrometery for photoacoustic imaging (PAI).

Section 5.1 introduces the theory of PAI. In particular, since tumors can be approximated by spheres with higher optical absorption with respect to the surrounding tissue, the case of an absorbing spherical source is analyzed.
The detection conditions of PAI signals are discussed in Section 5.2. Therefore, a model for the generation and propagation of PA signals and its detection with a LDV is derived.

Successively, measurements on silicone rubber phantoms are presented and discussed in Section 5.3. Section 5.4 proves that experiments on silicone tissue-mimicking phantoms validate the model. Finally, the validated model with breast-tissue parameters reveals the limits of tumor detection with LDVy-based PAI. The feasibility for performing PAI measurements with LDV is breast tissue is analyzed (Section 5.5).

5.1. Introduction to Photoacoustic Imaging

Photoacoustic imaging (PAI) is a technique used for the detection of brain lesions, hemodynamic monitoring and breast cancer diagnosis.
PAI is based on the photoacoustic effect (PA). This technique is widely described in references [94–96].
When a short laser pulse irradiates the tissue, the light is locally absorbed, and converted into heat. The temperature of the irradiated object rises and, consequently, induces a pressure rise p through thermoelastic expansion.
The heated region presents a fractional volume expansion

$$\frac{\mathrm{d}V}{V} = -\kappa p + \beta T, \tag{5.1}$$

where κ is the isothermal compressibility, β is the coefficient of volume expansion, and T is the change in temperature. Assuming that the laser pulse is shorter than the thermal and stress relaxation times, the term $\mathrm{d}V/V$ is negligible [94] and the initial pressure p_0 can be calculated as

$$p_0 = \frac{\beta T}{\kappa} = \frac{\beta A_\mathrm{e}}{\kappa \rho C_\mathrm{V}} = \Gamma A_\mathrm{e}. \tag{5.2}$$

The temperature increase T is the specific optical energy deposition A_e divided by the density of the material ρ and the heat capacity at constant volume C_V.
The Grüneisen parameter $\Gamma = \beta/(\kappa\rho C_\mathrm{V})$ can be expressed also as $\Gamma = \beta v_\mathrm{s}^2/C_\mathrm{P}$ where v_s is the sound velocity in the medium and C_P is the heat capacity at constant pressure.

Assuming that all the absorbed energy is converted into heat [94, 96], p_0 can be expressed as

$$p_0 = \Gamma \mu_\mathrm{a} F, \tag{5.3}$$

where F denotes the optical fluence of the laser beam and μ_a denotes the optical absorption coefficient. If the assumption of total heat conversion is not applicable, a multiplying factor η_{th} must be considered. The factor η_{th} indicates the percentage of heat conversion.

The originated pressure propagates in the tissue according to the general photoacoustic equation, which is derived from the generalized Hooke's law, and the equation of motion [94]:

$$\left(\bigtriangledown^2 - \frac{1}{v_\mathrm{s}}\frac{\partial^2}{\partial t^2}\right) p(\boldsymbol{r}, t) = -\frac{\beta}{\kappa v_\mathrm{s}^2} \cdot \frac{\partial^2 T(\boldsymbol{r}, t)}{\partial t^2}. \tag{5.4}$$

Equation 5.4 considers the tissue as a homogeneous and non-dissipative medium; the pressure at the location $\boldsymbol{r}$ and time instant t is indicated as $p(\boldsymbol{r}, t)$, the sound velocity in the material is v_s and it is constant for an homogeneous and non-dissipative medium. The solution to equation 5.4 can be found with the Green's function approach, as the response to a temporal and spatial impulse.
The solution can be used to estimate the photoacoustic pressure generated by an arbitrary heterogeneous optically absorbing object heated by a laser pulse in stress and thermal confinement conditions.
A detailed description of the derivation of equation 5.4 and its solution can be found in Wang and Wu [94], Wang [96], and Diebold [190]. In particular, Diebold [190] reports the solution of the equation for one, two and three dimensional cases, especially for a slab, a cylinder and a sphere.

A homogeneously heated sphere could represent an early stage heated tumor in breast tissue [191]. Tumors are characterized by a higher blood content with respect to the surrounding tissue, and therefore, at certain wavelengths, they have a higher light absorption. The PA signal generated by a small heated sphere is analyzed in Subsection 5.1.1.

5.1.1. Photoacoustic Signal of a Homogeneously Heated Sphere

A small homogeneously heated sphere generates a pressure perturbance $p(r, t)$ where t is the time and r is the distance from the center of the sphere (Figure

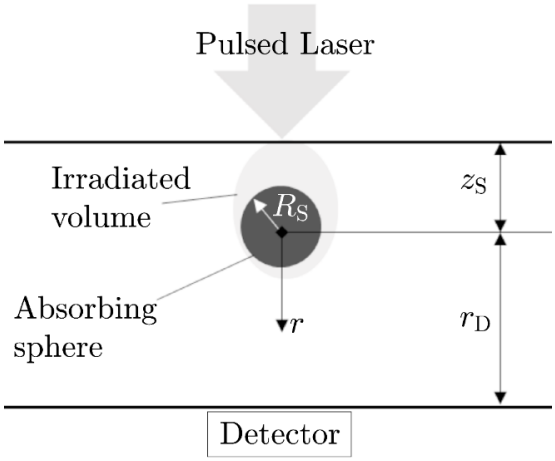

Figure 5.1.: Schematic of the setup for photoacoustic measurements. The sphere is located at the depth z_S from the irradiated surface. For measurements in transmission configuration, the signal is acquired at the distance $r = r_D$ from the center of the sphere.

5.1). For a non-dispersive, infinite medium, the resulting pressure $p(r,t)$ is the sum of the following three contributions:

$$p(r,t) = p_{in}(r,t) + p_{out}(r,t) + p_{inr}(r,t). \tag{5.5}$$

The initial pressure rise resulting from the laser pulse originates two equal pressure waves $p_{in}(r,t)$ and $p_{out}(r,t)$ traveling in opposite directions, according to the wave equation. The pressure wave $p_{in}(r,t)$ is a converging spherical compression wave that travels inward and the pressure wave $p_{out}(r,t)$ is a diverging spherical compression wave that travels outwards [94, 96].
The third wave $p_{inr}(r,t)$ is a divergent spherical rarefaction wave that originates when the wave $p_{in}(r,t)$ travels through the center of the sphere. The pressure wave $p_{in}(r,t)$ is reflected at the center of the sphere and becomes a diverging spherical wave with opposite sign (rarefaction wave). The opposite sign is due to the Gouy-phase shift of π that occurs to waves when they travel through their focus [192].
The three waves of equations 5.5 can be written as

$$\begin{aligned}
p_{in}(r,t) &= \frac{p_0}{2}\left(1 + \frac{v_s t}{r}\right) H(r + v_s t) H(R_S - r - v_s t) \\
p_{out}(r,t) &= \frac{p_0}{2}\left(1 - \frac{v_s t}{r}\right) H(r - v_s t) H(R_S - r + v_s t) \\
p_{inr}(r,t) &= \frac{p_0}{2}\left(1 - \frac{v_s t}{r}\right) H(-r + v_s t) H(R_S + r - v_s t),
\end{aligned} \tag{5.6}$$

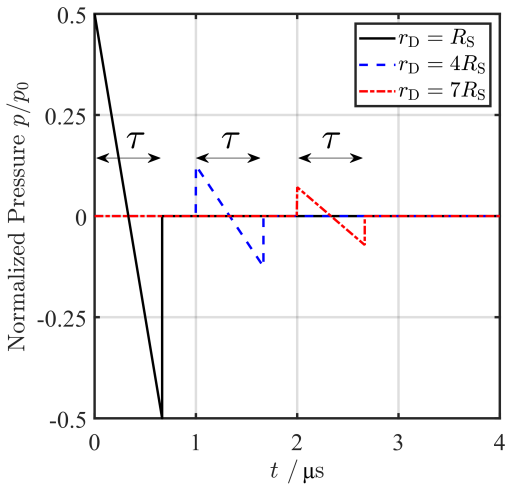

Figure 5.2.: Signals generated by a heated sphere with $R_S = 0.5$ mm at different detection distances r_D. The signals are computed according to equation 5.5 [94].

where $H(\cdot)$ is the Heaviside function and R_S is the radius of the sphere.
The signal resulting from the irradiation of a sphere has a bipolar shape or N-shape. The amplitude is inversely proportional to the distance r from the absorbing sphere and directly proportional to the initial pressure p_0.

Figure 5.2 shows the bipolar signal obtained from a small sphere with radius $R_S = 0.5$ mm acquired at different detection distances r_D. The signal of Figure 5.2 is obtained by computing the equation 5.5 according to Figure 5.1, where the transducer is positioned at the distance r_D from the sphere [94, 96]. A unitary pressure together with the typical sound velocity in soft tissue $v_s = 1540$ m/s [193] was chosen for the computation. Equation 5.5 is applicable also for measurements with other configurations as, for example, in reflection mode or from the side. In the reflection configuration the sensor is at the same side of the excitation and, therefore, the detection distance r_D is equal to the depth of the sphere z_S. The depth z_S is the distance between the surface irradiated by the pulse laser and the center of the sphere (see Figure 5.1). In the configuration from the side, the pulse laser and the detector are oriented with 90° angle between them.

The bipolar signal generated by the sphere has a duration τ that depends on the radius of the sphere R_S and on the sound velocity v_s

$$\tau = \frac{2R_S}{v_s}. \tag{5.7}$$

Therefore, the dimension of the absorbing object is decisive for both amplitude and time duration of the photoacoustic signals. As a consequence, the frequency

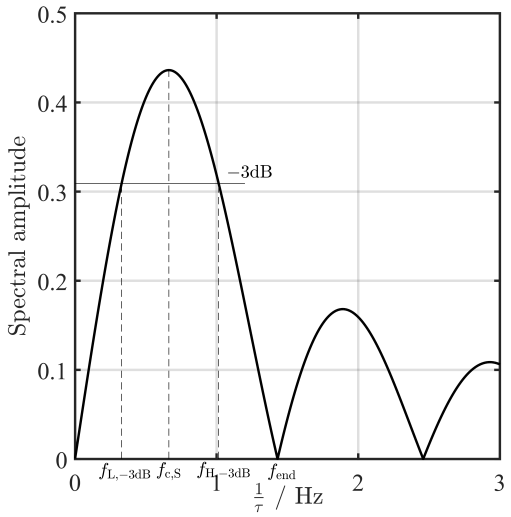

Figure 5.3.: Spectral amplitude for a unitary pressure pressure generated by a laser pulse inside an absorbing sphere versus the frequency parameter $1/\tau$ computed according to [194].

spectrum is determined by the size of the object.
Objects with small radius generate a photoacoustic signal with higher frequency components with respect to objects with greater radius. The latter present a spectrum shifted to the lower frequencies.
As showed in reference [194], for a unitary pressure, the frequency spectrum appears as a sequence of oscillations that rapidly decrease (Figure 5.3).
The maximum of the spectrum amplitude is the central frequency of the first oscillation

$$f_{\mathrm{c,S}} = \frac{0.66}{\tau}. \tag{5.8}$$

Most of the energy content of the signal resides in the half-power bandwidth which, in this case, corresponds to the interval between the frequencies $f_{\mathrm{L},-3\mathrm{dB}}$ and $f_{\mathrm{H},-3\mathrm{dB}}$ [195], where

$$\begin{aligned} f_{\mathrm{L},-3\mathrm{dB}} &= \frac{0.33}{\tau}, \\ f_{\mathrm{H},-3\mathrm{dB}} &= \frac{1.02}{\tau}. \end{aligned} \tag{5.9}$$

The end of the first oscillation of Figure 5.3 is at

$$f_{\mathrm{end}} = \frac{1.43}{\tau}. \tag{5.10}$$

Ideally, without taking into account the acoustic attenuation, the amplitude of the positive peak of the bipolar signal when the photoacoustic wave reaches the detection point at r_{D} [191, 195, 196] is

$$p_{\hat{\mathrm{M}}} = \frac{1}{2r_{\mathrm{D}}} p_0 R_{\mathrm{S}} = \frac{1}{2r_{\mathrm{D}}} \Gamma \mu_{\mathrm{a}} F R_{\mathrm{S}}, \tag{5.11}$$

where F is the laser fluence at the depth of the object z_{S}.

In this work, the value of the fluence F is estimated with the following equation

$$F = F_0 e^{-\mu_{\mathrm{eff}} z_{\mathrm{S}}}, \tag{5.12}$$

where F_0 is the fluence at the surface after specular reflection losses and μ_{eff} is the effective optical attenuation in the tissue.
Equation 5.12 is the solution of the diffusion approximation in one dimension [197, 198]. This simple model was chosen to ease the calculation in the next sections. For a detailed analysis, F should include a factor accounting for the increase of fluence under the surface.
The recorded signals at the surface are then evaluated for the reconstruction of maps of the absorption of the laser source.

In this work, the image reconstruction is not contemplated. For algorithms about image reconstruction in PAI, the reader may refer to the references [95, 96].
The equation 5.4 takes into account the case of a non dispersive medium. However, when acoustic signals propagate through dispersive media, energy losses due to the thermal consumption caused by the viscosity occur. Therefore, the deeper the signal travels in the medium, the more its amplitude decreases. Soft tissue and breast tissue have typical acoustic attenuation coefficients [196, 199]. The acoustic attenuation of the pressure wave traveling through a medium plays an important role for the correct reconstruction of the photoacoustic image.

5.1.2. Frequency Dependent Attenuation

The assumption of an ideal non attenuating acoustic medium in PAI may produce distortions of the photoacoustic signal and, consequently, artifacts in the reconstructed image.

PA signals need a broadband detection, and since ultrasonic attenuation is frequency dependent, this aspect should be considered.
In La Rivière, Zhang, et al. [199], the authors propose an image reconstruction method taking account for the frequency-dependent attenuation. The acoustic attenuation of the wave traveling through a medium plays an important role in ultrasound imaging. Soft tissue has a typical frequency dependent acoustic attenuation $\mu_{\mathrm{att}}(f)$ which was experimentally demonstrated to linearly increase with the frequency f [199]

$$\mu_{\mathrm{att}}(f) = \alpha_0 \mid f \mid^q, \tag{5.13}$$

where f is the frequency expressed in MHz, α_0 and q are positive constants.
In particular, α_0 is the acoustic attenuation coefficient. The constant q depends on the tissue water content and can vary between 1 and 2. For soft tissue in a frequency range of $0.5 - 10$ MHz, q is almost 1 [200]. The average value of α_0 for soft tissue is $\alpha_0 \sim 0.54$ dB cm^{-1}MHz^{-1} and for breast tissue is $\alpha_0 \sim 0.75$ dB cm^{-1}MHz^{-1} [201].
A loss term $L(t)$ convolving the pressure $p(\boldsymbol{r}, t)$ is added to the photoacoustic equation (5.4) resulting in

$$\left(\bigtriangledown^2 - \frac{1}{v_\mathrm{s}}\frac{\partial^2}{\partial t^2}\right) p(\boldsymbol{r}, t) + L(t) * p(\boldsymbol{r}, t) = -\frac{\beta}{\kappa v_\mathrm{s}^2} \cdot \frac{\partial^2 T(\boldsymbol{r}, t)}{\partial t^2}. \tag{5.14}$$

The solutions of this equation are generally computationally intensive.

In La Rivière, Zhang, et al. [199] the authors pursued a different approach. The authors showed that the Fourier transform of the attenuated pulse is related to the unattenuated pulse. This approach is very useful for image reconstruction. In particular, the algorithm of La Rivière, Zhang, et al. [199] allows for the investigation of the effects of frequency-dependent attenuation on the image resolution and distortion. However, effects originated by the finite bandwidth of the sensor, which can reduce the significance of frequency-dependent attenuation influence, are not considered in this method.

The aim of Chapter 5 is to understand under which conditions the LDV can detect PA signals. For the analysis of the conditions, it is sufficient to estimate the attenuation of the main peak of the N-shaped signal.

I express the amplitude of the attenuated peak p_M as the product between the unattenuated peak $p_{\hat{\mathrm{M}}}$ in equation 5.11 and a factor that takes into account the attenuation due to the energy loss of the signal propagating through medium as in Mignanelli and Rembe [202]

$$p_\mathrm{M} = p_{\hat{\mathrm{M}}} \cdot e^{-\overline{\mu}_\mathrm{att} \cdot r_\mathrm{D}}, \tag{5.15}$$

where $\overline{\mu}_\mathrm{att}$ is the mean value of the attenuation coefficient $\mu_\mathrm{att}(f)$, between the frequencies $f = f_{\mathrm{L},-3\mathrm{dB}}$ and $f = f_{\mathrm{H},-3\mathrm{dB}}$, where the most content of the energy of the signal resides

$$\overline{\mu}_\mathrm{att} = \frac{\int_{f_{\mathrm{L},-3\mathrm{dB}}}^{f_{\mathrm{H},-3\mathrm{dB}}} \mu_\mathrm{att}(f)\, df}{f_{\mathrm{H},-3\mathrm{dB}} - f_{\mathrm{L},-3\mathrm{dB}}} = \frac{\int_{f_{\mathrm{L},-3\mathrm{dB}}}^{f_{\mathrm{H},-3\mathrm{dB}}} \alpha_0 \mid f \mid^q \, df}{f_{\mathrm{H},-3\mathrm{dB}} - f_{\mathrm{L},-3\mathrm{dB}}} = \frac{0.67}{\tau} \cdot \alpha_0. \tag{5.16}$$

The constant q is set to 1. The coefficient α_0 is often expressed in literature in dB cm^{-1}MHz^{-1} and it has to be converted in Np cm^{-1}MHz^{-1} (1 Np = 8.686 dB) for performing the calculations of equation 5.15.
By calculating the pressure p_M with the attenuation $\overline{\mu}_\mathrm{att}$, a constant attenuation over the frequency is assumed. I introduced the parameters $\Delta p_{\mathrm{M,L}}$ and $\Delta p_{\mathrm{M,H}}$ to

quantify the deviation by considering the attenuation $\overline{\mu}_{\mathrm{att}}$ constant in the frequency range $f_{\mathrm{L},-3\mathrm{dB}} - f_{\mathrm{H},-3\mathrm{dB}}$ and the acoustic attenuation for the frequencies $f_{\mathrm{L},-3\mathrm{dB}}$ and $f_{\mathrm{H},-3\mathrm{dB}}$

$$\Delta p_{\mathrm{M,L}} = \frac{p_{\hat{\mathrm{M}}} \cdot e^{-\overline{\mu}_{\mathrm{att}} \cdot r_{\mathrm{D}}} - p_{\hat{\mathrm{M}}} \cdot e^{-\mu_{\mathrm{att}}(f_{\mathrm{L},-3\mathrm{dB}}) \cdot r_{\mathrm{D}}}}{p_{\hat{\mathrm{M}}} \cdot e^{-\overline{\mu}_{\mathrm{att}} \cdot r_{\mathrm{D}}}} \cdot \ 100\% \tag{5.17}$$

$$\Delta p_{\mathrm{M,H}} = \frac{p_{\hat{\mathrm{M}}} \cdot e^{-\overline{\mu}_{\mathrm{att}} \cdot r_{\mathrm{D}}} - p_{\hat{\mathrm{M}}} \cdot e^{-\mu_{\mathrm{att}}(f_{\mathrm{H},-3\mathrm{dB}}) \cdot r_{\mathrm{D}}}}{p_{\hat{\mathrm{M}}} \cdot e^{-\overline{\mu}_{\mathrm{att}} \cdot r_{\mathrm{D}}}} \cdot \ 100\%, \tag{5.18}$$

where $\mu_{\mathrm{att}}(f_{\mathrm{L},-3\mathrm{dB}})$ and $\mu_{\mathrm{att}}(f_{\mathrm{H},-3\mathrm{dB}})$ are the values of the attenuation for the frequencies $f_{\mathrm{L},-3\mathrm{dB}}$ and $f_{\mathrm{H},-3\mathrm{dB}}$, respectively. In the case of the photoacoustic signal generated by an absorbing sphere in soft tissue with a radius ($R_{\mathrm{S}} = 1$ mm) and a relatively small distance between the detector and the defect ($r_{\mathrm{D}} = 1$ cm) (Figure 5.1), $\Delta p_{\mathrm{M,L}}$ and $\Delta p_{\mathrm{M,H}}$ are lower than ∓ 1.7 %, respectively.
In cases like this one, the acoustic attenuation $\overline{\mu}_{\mathrm{att}}$ could be used for the whole spectrum of the pulse since $\Delta p_{\mathrm{M,L}}$ and $\Delta p_{\mathrm{M,H}}$ are small.
This approximation simplifies the problem and the amplitude of the attenuated peak can be estimated with equation 5.15.
This simplification can be applied mostly for relatively small distances r_{D} and relative great values of the radius R_{S}.
It is advisable to check the values of $\Delta p_{\mathrm{M,L}}$ and $\Delta p_{\mathrm{M,H}}$ before using this approximation. In particular, the parameter Δp_{M}

$$\Delta p_{\mathrm{M}} = \max(|\Delta p_{\mathrm{M,L}}| \ , |\Delta p_{\mathrm{M,H}}|) \tag{5.19}$$

is introduced to estimate if the proposed approximation leads to great percent errors.

5.1.3. Velocity/Displacement Signal at the Boundary

At the boundary between skin and air, assuming that at the distance r_{D} the photoacoustic wave can be approximated as a plane wave, the relation between the pressure p and the velocity v [203] is

$$v(t) = \frac{2 \cdot p(t)}{Z}. \tag{5.20}$$

The acoustic impedance Z is the product between the sound velocity v_{s} and the density of the medium ρ. The unit of Z is Rayl, i.e. Ns/m^3.
The factor 2 results from the impedance mismatch between the tissue and the air; the impedance of the tissue is more than a factor 10^3 greater with respect to the impedance of the air. The velocity signal (Figure 5.4(top)) is directly proportional to the pressure. Thus, except for an amplitude factor, it has the same characteristics in time and in frequency domain of the pressure signal.

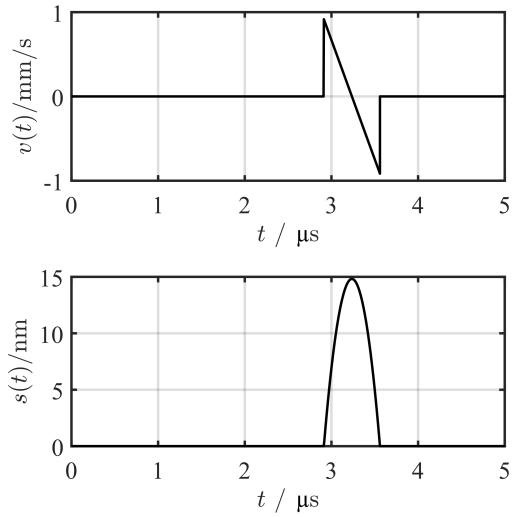

Figure 5.4.: Velocity (top) and displacement (bottom) signals at the boundary generated by an absorbing sphere with $R_\mathrm{S} = 0.5$ mm at distances $r_\mathrm{D} = 10 \cdot R_\mathrm{S}$, $z_\mathrm{S} = 1$ cm, $\mu_\mathrm{a} = 0.6$ cm^{-1} and $F_0 = 1000$ J/m^2. The acoustic attenuation is not considered.

The peak of the velocity can be expressed as:

$$v_{\hat{\mathrm{M}}} = \frac{2 \cdot p_{\hat{\mathrm{M}}}}{Z} = \frac{1}{Z r_\mathrm{D}} \Gamma \mu_\mathrm{a} F R_\mathrm{S}. \tag{5.21}$$

Equation 5.20 can be expressed also in terms of displacement s

$$s(t) = \int \frac{2 \cdot p(t)}{Z} \mathrm{d}t. \tag{5.22}$$

The displacement signal in a non-dispersive medium is presented in Figure 5.4(bottom).
Its maximum amplitude is $s_{\hat{\mathrm{M}}}$

$$s_{\hat{\mathrm{M}}} = \frac{1}{2}\left(\frac{2 \cdot p_{\hat{\mathrm{M}}}}{Z} \cdot \frac{\tau}{2}\right) = \frac{p_{\hat{\mathrm{M}}}}{Z} \cdot \frac{\tau}{2}, \tag{5.23}$$

where τ is the duration of the N-shaped signal.
The value of $s_{\hat{\mathrm{M}}}$ can be expressed in dependence of all relevant parameters of the setup and the excitation (R_S, r_D, z_S and μ_a) by combining equations 5.7, 5.11 and 5.23:

$$s_{\hat{\mathrm{M}}} = \frac{R_\mathrm{S}^2}{Z \cdot v_\mathrm{s}} \frac{1}{2 r_\mathrm{D}} \Gamma \mu_\mathrm{a} F. \tag{5.24}$$

By considering the attenuated peak of the pressure signal of equation 5.15, the velocity attenuated peak is

$$v_{\mathrm{M}} = \frac{1}{Z r_{\mathrm{D}}} \Gamma \mu_{\mathrm{a}} F R_{\mathrm{S}} e^{-\overline{\mu}_{\mathrm{att}} r_{\mathrm{D}}} \tag{5.25}$$

and the displacement attenuated peak s_{M} is

$$s_{\mathrm{M}} = \frac{R_{\mathrm{S}}^2}{Z \cdot v_{\mathrm{s}}} \frac{1}{2 r_{\mathrm{D}}} \Gamma \mu_{\mathrm{a}} F e^{-\overline{\mu}_{\mathrm{att}} r_{\mathrm{D}}}. \tag{5.26}$$

Equations 5.25 and 5.26 are employed in the analyses performed in the Section 5.4 and Section 5.5.

5.2. Detection conditions of Photoacoustic Imaging Signals

In this section, the detection conditions for PAI measurements performed with the LDV are discussed.
At first, the detection conditions for PA signals are described. In Subsection 5.2.1, these detection conditions are applied to the case of commercial LDVs.

Conversely to the classic ultrasound signals, the ultrasonic signals generated by the photoacoustic effect are broadband [204].
In the previous Section (Section 5.1), the broadband spectrum of the typical photoacoustic signals generated by a spherical absorbing object is presented.
The characteristic frequencies are strictly related to the dimensions of the absorbing object.
In particular, the smaller the object is, the wider the signal frequency contents are. Therefore, broadband ultrasound sensors are required for PAI detection.

To be able to detect the PA signals without degradation, at least two main conditions need to be fulfilled:

1. The maximal detectable frequency of the sensor has to be greater than the characteristic frequencies of the photoacoustic signals. A relative bandwidth $B_{\mathrm{rel}} = 1.5$ with respect to the central frequency f_{c} is necessary for enhanced sensitivity [205][a] where

$$B_{\mathrm{rel}} = \frac{B}{f_{\mathrm{c}}} = \frac{f_{\mathrm{H}} - f_{\mathrm{L}}}{f_{\mathrm{c}}}. \tag{5.27}$$

   The frequencies f_{H} and f_{L} are the upper and the lower frequencies of the measurement bandwidth $B = f_{\mathrm{H}} - f_{\mathrm{L}}$ of the sensor, respectively.
   Since the bandwidth is symmetric with respect to the central frequency, it is possible to rewrite the frequencies f_{H} and f_{L} as $f_{\mathrm{L}} = f_{\mathrm{c}}(1 - \frac{1}{2} \cdot B_{\mathrm{rel}})$ and $f_{\mathrm{H}} = f_{\mathrm{c}}(1 + \frac{1}{2} \cdot B_{\mathrm{rel}})$, respectively. Moreover, the upper frequency f_{H} should be at least ten times higher as the lower frequency f_{L} in order to reliably detect objects with different sizes [195]. Since sensors with a relative bandwidth B_{rel} of 1.5 are needed for a proper reconstruction of PA signals [195], I assumed that the upper frequency of the sensor f_{H} allows for a good detection of the PA signals generated by a sphere S_i, if the spectrum of the signals has a central frequency $f_{\mathrm{c,S}_i}$ such that

$$f_{\mathrm{c,S}_i} \leq \frac{f_{\mathrm{H}}}{1 + \frac{1}{2} \cdot B_{\mathrm{rel}}} = f_{\mathrm{c,S,\hat{M}}}, \tag{5.28}$$

   where $f_{\mathrm{c,S}_i}$ is the central frequency of the signal generated by the absorbing sphere S_i.

[a] B_{rel} of 150% correspond to the specification of a percentual bandwidth of 1.5 in [195].

The frequency $f_{\mathrm{c,S,\hat{M}}}$ is the maximal central frequency that the PA signal generated by an absorbing sphere can have for a proper reconstruction and it is related to the minimal detectable object with a radius $R_{\mathrm{S,min}}$ (see Subsection 5.2.1)[b]. Figure 5.5 shows the spectra generated by three absorbing spheres with radius R_{S1}, R_{S2} and R_{S3}. In particular, the relation between the radii is:

$$R_{\mathrm{S1}} > R_{\mathrm{S2}} > R_{\mathrm{S3}}. \tag{5.29}$$

Only the spheres with radius R_{S1} and R_{S2} are reliably detectable since, according to equation 5.28, the following applies

$$f_{\mathrm{H}} - f_{\mathrm{c,S_1}} > \frac{1}{2} B_{\mathrm{rel}} f_{\mathrm{c,S_1}} \tag{5.30}$$

and

$$f_{\mathrm{H}} - f_{\mathrm{c,S_2}} = \frac{1}{2} B_{\mathrm{rel}} f_{\mathrm{c,S_2}}. \tag{5.31}$$

Therefore, the frequency $f_{\mathrm{c,S_2}}$ is equal to the frequency $f_{\mathrm{c,S,\hat{M}}}$ and the radius R_{S2} is the minimal detectable radius $R_{\mathrm{S,min}}$.

2. The pressure, the velocity or the displacement at the boundary has to be greater than the resolution of the sensor. In the case of the LDV, the minimal detectable velocity or the minimal detectable displacement has to be lower than the velocity/displacement at the boundary generated by the photoacoustic effect.

5.2.1. Detection Limit of Commercial LDVs

To evaluate the limits of LDV for the detection of photoacoustic signals, the detection conditions 1. and 2. defined above need to be applied to the typical metrological characteristics of LDV.

As mentioned in Chapter 3, the displacement resolution in LDV is limited by the shot noise that has white noise characteristics. This means that the spectral density of the signal is constant over the frequencies.
The noise-equivalent root-mean-square displacement resolution in the bandwidth B, $s_{\mathrm{RL}}(B)$, can be expressed as

$$s_{\mathrm{RL}}^2(B) = \int_{f_{\mathrm{L}}}^{f_{\mathrm{H}}} S_s df = S_s \cdot (f_{\mathrm{H}} - f_{\mathrm{L}}), \tag{5.32}$$

[b] The frequency f_{L} also limits the detection of the signal, however, as described in Subsection 5.2.1, for a LDV the lower frequency f_{L} is ≈ 0; therefore the condition $f_{\mathrm{c,S}} - f_{\mathrm{L}} \geqslant \frac{1}{2} B_{\mathrm{rel}} f_{\mathrm{c,S}}$ is always verified for $B_{\mathrm{rel}} < 2$.

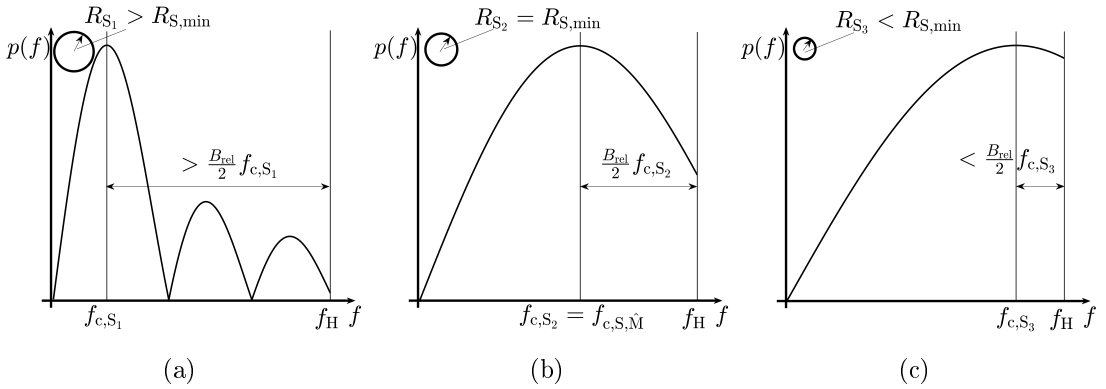

Figure 5.5.: Spectra of three absorbing spheres with radius R_{S1} in (a), R_{S2} in (b) and R_{S3} in (c). For the sphere with radius R_{S2} the frequency difference $f_H - f_{c,S_2}$ is equal to $\frac{1}{2}B_{rel}f_{c,S_2}$. The frequency f_{c,S_2} is therefore equal to the frequency $f_{c,S,\hat{M}}$ and the radius R_{S2} is the minimal detectable radius $R_{S,min}$. The sphere with radius R_{S1} is reliably detectable since the frequency difference $f_H - f_{c,S_1}$ is greater than $\frac{1}{2}B_{rel}f_{c,S_1}$. The sphere with radius R_{S3} is not reliably detectable since the frequency difference $f_H - f_{c,S_3}$ is lower than $\frac{1}{2}B_{rel}f_{c,S_3}$.

where $S_s = s'^2_{RL}$ is the power spectral density of the noise displacement signal[c] in m^2/Hz, f_H and f_L are the upper and the lower limits of the bandwidth B, respectively. In the same way, the noise-equivalent root-mean square velocity resolution $v_{RL}(B)$ can be written as

$$v^2_{RL}(B) = \int_{f_L}^{f_H} S_v df, \tag{5.33}$$

where S_v is the power spectral density of the velocity signal[c] in $(m^2/s^2)/Hz$

$$S_v = (4\pi^2 f^2) S_s. \tag{5.34}$$

Therefore, the velocity resolution limit v_{RL} of equation 5.33 results in

$$v_{RL}(B) = \sqrt{4\pi^2 S_s \frac{f_H^3 - f_L^3}{3}} = 2\pi s_{RL}(B) \sqrt{\frac{(f_L^2 + f_L f_H + f_H^2)}{3}}. \tag{5.35}$$

For the case of a LDV, the value of the typical displacement resolution s'_{RL} is $s'_{RL} \approx 30\ fm/\sqrt{Hz}$ [59] and the typical bandwidth is about few MHz.
The commercial available vibrometer controller OFV-2500-2 (Polytec GmbH)[206]

[c] It is referred to as power spectral density, since the unit is proportional to the power.

has a velocity resolution limit[d] v'_{RL} of 0.5 µm/s/$\sqrt{\mathrm{Hz}}$ for the central frequency ($f_{\mathrm{c}} = 1.5$ MHz) of its bandwidth (0.5 Hz − 3 MHz). The relation between v'_{RL} for the central frequency and the displacement resolution s'_{RL} is

$$s'_{\mathrm{RL}} = \frac{v'_{\mathrm{RL}}}{2\pi f_{\mathrm{c}}}. \tag{5.36}$$

For the OFV-2500-2, the displacement resolution s'_{RL} results in 53 fm/$\sqrt{\mathrm{Hz}}$.

Another commercial LDV is the OFV-5000 Xtra Laser Vibrometer with the velocity decoder VX-09 (Polytec GmbH) [207]. It performs measurements with a velocity resolution for the central frequency of $v'_{\mathrm{RL}} = 0.04$ µm/s/$\sqrt{\mathrm{Hz}}$ and the bandwidth between $f_{\mathrm{L}} = 0.5$ Hz and $f_{\mathrm{H}} = 2.5$ MHz. According to equation 5.36 the OFV-5000 Xtra Laser Vibrometer VX-09 has a displacement resolution limit $s'_{\mathrm{RL}} = 5.09$ fm/$\sqrt{\mathrm{Hz}}$.

For commercial vibrometers, the following is valid: $f_{\mathrm{L}} << f_{\mathrm{H}}$. Therefore, I assume the bandwidth B is equal to upper frequency f_{H}, $B = f_{\mathrm{H}}$ and equation 5.32 results in

$$s^2_{\mathrm{RL}}(B) = S_s \cdot B. \tag{5.37}$$

For a proper reconstruction of a PA signal with LDV, the central frequency of the signal, $f_{\mathrm{c,S}_i}$, has to be lower than the maximal central frequency, $f_{\mathrm{c,S,\hat{M}}}$, detectable with the bandwidth of the sensor by considering detection condition of equation 5.27 (See Figure 5.5).

For the OFV-5000 Xtra Laser Vibrometer VX-09, the maximal central frequency achievable, $f_{\mathrm{c,S,\hat{M}}}$, with f_{H} fixed at 2.5 MHz and according to equation 5.28, is $f_{\mathrm{c,S,\hat{M}}} = 1.43$ MHz.
Equation 5.7 and 5.8 relate the central frequency $f_{\mathrm{c,S}}$ to the corresponding radius of the object R_{S} (see Figure 5.5). Therefore by substituting the maximal central frequency $f_{\mathrm{c,S,\hat{M}}}$ to $f_{\mathrm{c,S}}$, it delivers

$$R_{\mathrm{S,min}} = 0.33\frac{v_{\mathrm{s}}}{f_{\mathrm{c,S,\hat{M}}}}. \tag{5.38}$$

The minimal detectable absorbing object with LDV in soft tissue ($v_{\mathrm{s}} = 1540$ m/s [193]) has a radius $R_{\mathrm{S,min}} = 357$ µm. For breast tissue ($v_{\mathrm{s}} = 1510$ m/s [193]) the radius $R_{\mathrm{S,min}}$ is 350 µm.
A bandwidth B_{rel} of 0.75 provides a good compromise between resolution and noise level [195]. With a $B_{\mathrm{rel}} = 0.75$ the $f_{\mathrm{c,S,\hat{M}}}$ increases to 1.81 MHz; with this condition the minimal detectable radius $R_{\mathrm{S,min}}$ decreases to 281 µm for soft tissue and 275 µm for breast tissue.

For the case of the OFV-2500-2, the upper frequency of the bandwidth f_{H} is $f_{\mathrm{H}} = 3$ MHz, the minimal detectable object in soft/breast tissue has a radius

[d] Measuring characteristics for the range 100 mm/s/V which has been used for the measurements reported in Section 5.3.

$R_{\mathrm{S,min}} \approx 300$ µm for a relative bandwidth $B_{\mathrm{rel}} = 1.5$. For a relative bandwidth $B_{\mathrm{rel}} = 0.75$ the minimal radius is $R_{\mathrm{S,min}} \approx 230$ µm.

Objects with a radius $R_{\mathrm{S,min}}$ are detectable only if the condition 2. is met. Accordingly to this, the assumption that the displacement resolution of LDV at a given bandwidth B, $s_{\mathrm{RL}}(B)$ has to be sufficient to detect at least the maximal displacement amplitude at the boundary s_{M}

$$s_{\mathrm{RL}}(B) < s_{\mathrm{M}}. \tag{5.39}$$

In Section 5.3 and 5.4 measurements with the vibrometer controller OFV-2500-2 are performed.
The theoretical limits of LDV for photoacoustic measurements in breast tissue are investigated for the case of the commercial LDV OFV-5000 Xtra Laser Doppler vibrometer with the velocity decoder VX-09. The reason resides on its higher resolution with respect to other commercial products. As mentioned before, its resolution $s'_{\mathrm{RL}} = 5.09$ fm/$\sqrt{\mathrm{Hz}}$ approaches the theoretical resolution limit of LDV with IR-technology $s'_{\mathrm{RL,IR}} = 1$ fm/$\sqrt{\mathrm{Hz}}$ [153].
According to equations 5.36 and 5.37, for the OFV-5000 Xtra Laser Doppler vibrometer VX-09 the following is valid [207]

$$s_{\mathrm{RL}}(B) = s_{\mathrm{RL}}(2.5\ \mathrm{MHz}) = s'_{\mathrm{RL}} \cdot \sqrt{B} = \frac{v'_{\mathrm{RL}}}{2\pi f_{\mathrm{c}}}\sqrt{B} = 8\ \mathrm{pm} \tag{5.40}$$

where $v'_{\mathrm{RL}} = 0.04$ µm/s/$\sqrt{\mathrm{Hz}}$, the bandwidth $B \approx 2.5$ MHz and the central frequency of the bandwidth $f_{\mathrm{c}} = 1.25$ MHz.

5.3. Photoacoustic Measurements with LDV

In this section, examples of photoacoustic measurements with the self-made differential IR-LDV (DLDV) are presented.
At first the set-up (Subsection 5.3.1) and the preparation of the phantom simulating the breast tissue with tumors inside (Subsection 5.3.2) are described.
Successively, the acquired signals are presented and their time characteristics are analyzed (Subsection 5.3.3) and discussed (Subsection 5.3.4).
The aim of these measurements is to show if the typical photoacoustic signals presented in the theory are detectable with LDV on silicone rubber phantoms that mimic breast or soft tissue with tumors.

In this section, vibration velocity signals over time and voltage signals over time are generally referred to as $v(t)$ as $U(t)$, respectively.

5.3.1. Measurement Setup

The setup used for PAI measurements with LDV on tissue mimicking phantoms is shown in Figure 5.6.
A transmission mode configuration is adopted: the detection occurs on the opposite side of the excitation. For the photoacoustic excitation, the pulsed laser Eazy-Brilliant (Quantel) is employed.
The Eazy-Brilliant is a Q-switch Nd-Yag Laser with a 1064 nm wavelength, a beam diameter of 6 mm, a maximal energy of 330 mJ and a pulse duration of 5 ns.

To adjust the energy of the laser beam, the variable attenuator 2-EWP-T-1064 of the company Altechna is placed at the exit of the laser beam. The attenuator consists of a rotating $\lambda/2$ waveplate and a Brewster type polarizer. By turning the $\lambda/2$ waveplate of an angle ξ, the energy of the laser beam can be continuously varied without alteration of other beam parameters.

The pulsed laser is pointed at the sample. In order to have a spatially wider laser spot, a beam expander with a magnitude factor of 3 has been designed and placed between the attenuator and the sample. Therefore, the laser beam has a beam diameter of ≈ 18 mm when it impinges on the sample.

The phantom is placed on a manual stage. The manual stage allows for the measurement of different points without changing the alignment between the excitation laser and the self-made differential IR-LDV (DLDV). The self-made differential IR-LDV measures the vibration of the phantom from the opposite side with respect to the excitation.

The DLDV was chosen for the measurements because of its high resolution. The measurements described in this chapter do not need a differential configuration; therefore, the external reference beam of the DLDV is pointed to a mirror leading to a single point LDV configuration.

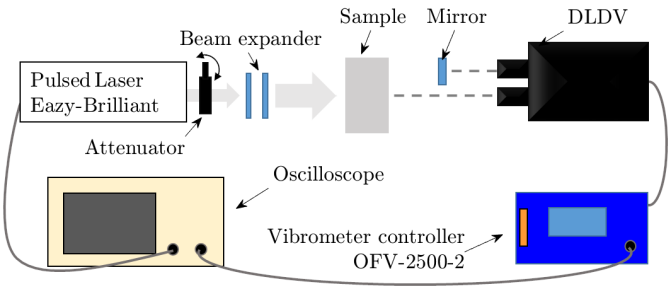

(a)

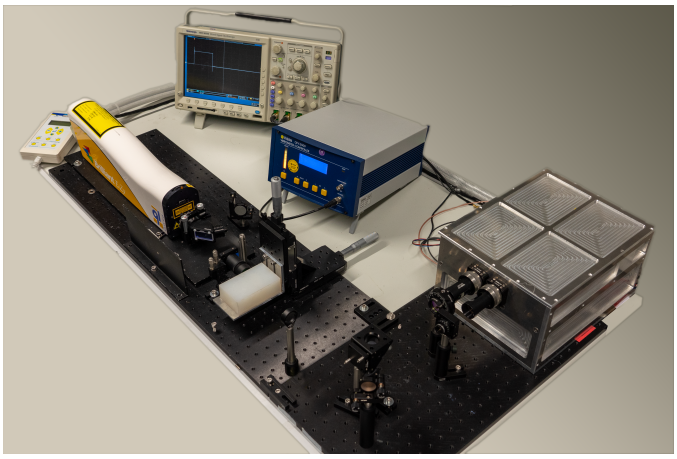

(b)

Figure 5.6.: Schematic (a) and photo (b) of the PAI measurement setup with the self-made differential IR-LDV (DLDV) (Photo by Marvin Schewe, M.Sc.).

The signal of the DLDV is sent to the vibrometer controller (OFV-2500-2 Polytec) for the demodulation. The velocity decoder of the vibrometer controller has a bandwidth $B = 0.5$ Hz $- 3$ MHz and a resolution limit of 0.5 µm $s^{-1}/\sqrt{\text{Hz}}$ for the selected range of 100 mm s^{-1}/V.
The demodulated velocity signal together with the Q-switch output of the excitation laser are acquired with an oscilloscope and the data is transferred to a PC.
The Q-switch signal is acquired to have a trigger for the synchronization of the time averaging process and for the identification of the time instant of the laser shot.

5.3.2. Phantom

Gelatine phantoms and silicone rubber phantoms were prepared to mimic soft and breast tissue. However, the properties of the gelatin phantoms are unstable during the measurements. Therefore, the tissue-mimicking phantoms prepared for the measurements of this thesis are made of silicone rubber.
Silicone rubber phantoms are often used in biomedical applications to mimic human tissue [208]. The mechanical properties of silicone rubber are very similar to the ones of soft tissue. However, the optical properties should be adjusted.
The following preparation procedure is common to all phantoms produced for the measurements in this thesis.

The phantoms were realized with the two-components - A and B - room temperature vulcanize (RTV) silicone Dragon Skin 10$^{\text{TM}}$ from the company Smooth On.
The preparation procedure for the simulation of the breast tissue consists on mixing the two components - A and B - in ratio 1:1. During the stirring, small air bubbles are generated. The entrapped air is removed with a vacuum pump. The mixture is then poured in the mold and let to harden for seven hours.

Spherical phantom were produced to simulate tumors.
The mixture used for the generation of tumors is the same as for breast tissue but India ink is added to one of the components, in order to achieve a higher value of optical absorption μ_{a}. The optical absorption of the silicone rubber spheres is called $\mu_{\text{a,sil}}$. Figure 5.7(a) shows the molds used to generate the spherical inclusions.

A phantom with inclusions is produced to simulate breast tissue with tumors. Its preparation consists of three main phases.
The first phase is the generation of the spherical inclusions which mimic the tumors. For example, the spheres inside the phantom of Figure 5.7(d) are obtained by adding 0.07 g ink to 64.92 g component A and then mixed together to 64.98 g component B.
In the second phase, the spheres are suspended with the aid of a metallic grid in the mold of the phantom as depicted in Figure 5.7(b).
The mixture for the simulation of the soft tissue is poured until it reaches the spheres as shown in Figure 5.7(c). When this first layer is hardened, the metal grid is removed. In this way, the spheres are fixed at the desired position. The third phase consists of pouring a second layer of the mixture of the soft tissue and waiting for the phantom to harden.

Figure 5.7(d) shows the phantom used to simulate the soft tissue with tumors. Its dimensions are 99.42 mm x 59.67 mm x 33.53 mm, where $d = 59.67$ mm is the width and $d_{\text{heigth}} = 33.53$ mm is the height.
The phantom has five spherical inclusions S_i where the index $i = 1, 2, 3, 4, 5$ identifies the sphere. The five spheres have a radius $R_{\text{S}} = 2.5$ mm and are located at different depth z_{S_i} according to Figure 5.1: $z_{\text{S}_1} = 2.53$ mm, $z_{\text{S}_2} = 3.86$ mm,

$z_{S_3} = 4.39$ mm, $z_{S_4} = 5.97$ mm, $z_{S_5} = 6.67$ mm. The values of the distance of the sphere S_i from the detection point r_{D_i} are obtained by the subtraction between the distance d and the depth z_{S_i} of each sphere.

$$r_{D_i} = d - z_{S_i}. \tag{5.41}$$

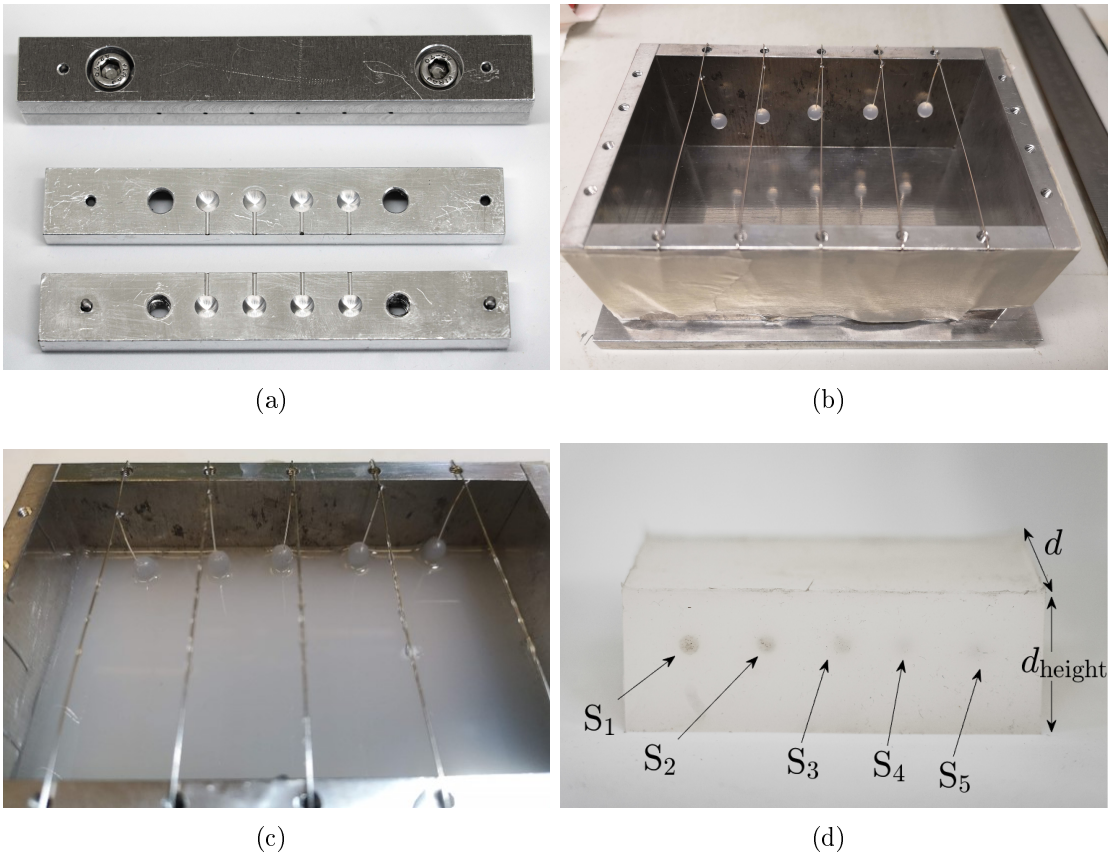

(a) (b)

(c) (d)

Figure 5.7.: Molds for the generation of the silicone rubber spheres (Photo by Marvin Schewe, M.Sc.)(a). Phase two of the preparation of the phantom with spherical inclusions (b,c). The spheres are suspended with the aid of a metallic grid in the mold of the phantom (b). The mixture for the simulation of the soft tissue is poured untill it reaches the spheres(c). Silicone rubber phantom with spherical inclusions used for the simulation of breast tissue with tumors (d) (Photo by Marvin Schewe, M.Sc.).

5.3.3. Time Characteristics of PA Signals Acquired with LDV

This section presents the signals acquired with the self-made DLDV according to the setup in Figure 5.6.
At first, the velocity signals originated by silicone rubber spheres are presented. Successively, measurements on a silicone phantom with and without spherical inclusions are shown.
In this section, only the time characteristics of the signals are analyzed.

5.3.3.1. LDV Measurements of Silicone Rubber Spheres

Silicone rubber spheres with a radius $R_S = 2.5$ mm and $R_S = 5$ mm were generated with the molds of Figure 5.7(a).
In this paragraph, the PA signals generated by the irradiation of those spheres are acquired with the LDV and analyzed.
The setup used for the measurements is the same as the setup in Figure 5.6; a detailed scheme is shown in Figure 5.8.
However, for these measurements the LDV used is the OFV-300 (Polytec GmbH)[e].

One hundred and twenty-eight signals were acquired and time-averaged for both spheres. The DC-component of the averaged signal was removed and the high-frequency noise was filtered with a wavelet-denoising filter exploiting the Daubechies wavelet db4 [209, 210].
The frequency content of the signal generated by an absorbing sphere depends on the dimension of the sphere (see equations 5.8-5.10). Hence, frequencies up to 1.2 MHz are selected for the signal of the sphere with a radius $R_S = 2.5$ mm and frequencies up to 610 kHz for the one with a radius of $R_S = 5$ mm.
The signals obtained from LDV measurements performed on the silicon rubber spheres are shown in Figure 5.9.

According to Subsection 5.1.1, the signal generated by a heated sphere has a bipolar signature whose duration is related to the dimension of the sphere and the sound velocity.
The signal generated by the sphere with $R_S = 2.5$ mm (Figure 5.9(a)) results in a succession of bipolar waves.
The first bipolar wave is generated by the photoacoustic effect. The second can be explained as the reflection of the first wave when it reaches the opposite boundary. The wave travels through the sphere and will be transmitted at the measurement

[e]The OFV-300 (Polytec GmbH) was used for these measurements instead of the DLDV. The photodiodes of the DLDV have a high responsivity at 1064 nm. If the pattern of interest occurs immediately after the laser shot, like in this case, it is not recognizable. Therefore, to perform these measurements with the self-made vibrometer, a Notch filter at the wavelength of the excitation laser is required.

point with a delay.
The delay between the successive bipolar waves of Figure 5.9(a) corresponds to the time that the acoustic wave needs to travel a distance equal to the diameter with a sound velocity $v_{\mathrm{s,sil}}$ of the material, in this case of the silicone rubber (subscript $_{\mathrm{sil}}$).
For a free boundary condition, such as in this case, the velocity amplitude of the reflected wave has the same amplitude as the amplitude of the impinging wave.
The reduced amplitude of the second peak and the successive peaks can be explained with the attenuation due to the propagation of the sound wave in the material.
The shape of the successive waves changes with respect to the first one. This happens probably because of the interference with other reflections.
The first N-shaped wave is the one generated by the photoacoustic effect and it has a time duration between the positive and negative peak $\tau = 4.41$ µs.
In Figure 5.9, the time duration τ is delimited by the red dots.
According to equation 5.7, for a sphere with a radius 2.5 mm, the sound velocity results in

$$v_{\mathrm{s,sil}} = \frac{2R_{\mathrm{S}}}{\tau} = 1129 \text{ m/s}. \tag{5.42}$$

Similar conclusions can be taken for Figure 5.9(b) which represents the signal of a sphere with radius $R_{\mathrm{S}} = 5$ mm acquired with LDV.
Also in this case, the signal appears like a sequence of bipolar-waves . The time duration between the positive and negative peak is, as expected, greater with respect to the previous one.
The time duration of the N-shaped signal is $\tau = 8.74$ µs. The calculated sound velocity $v_{\mathrm{s,sil}}$ according to equation 5.42 for a radius with radius $R_{\mathrm{S}} = 5$ mm is $v_{\mathrm{s,sil}} = 1144$ m/s, which deviates of few m/s from the value obtained from the previous measurement.

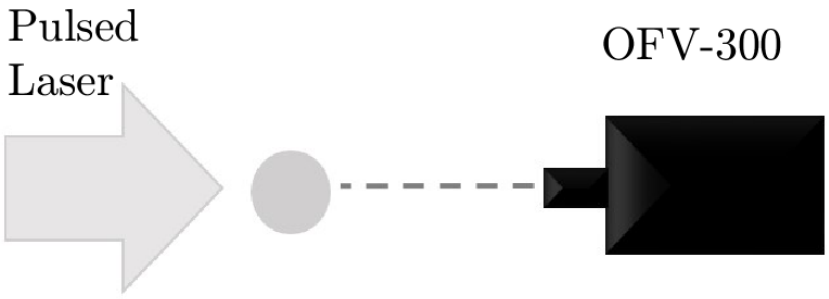

Figure 5.8.: Scheme of the setup for the measurements on silicon rubber spheres.

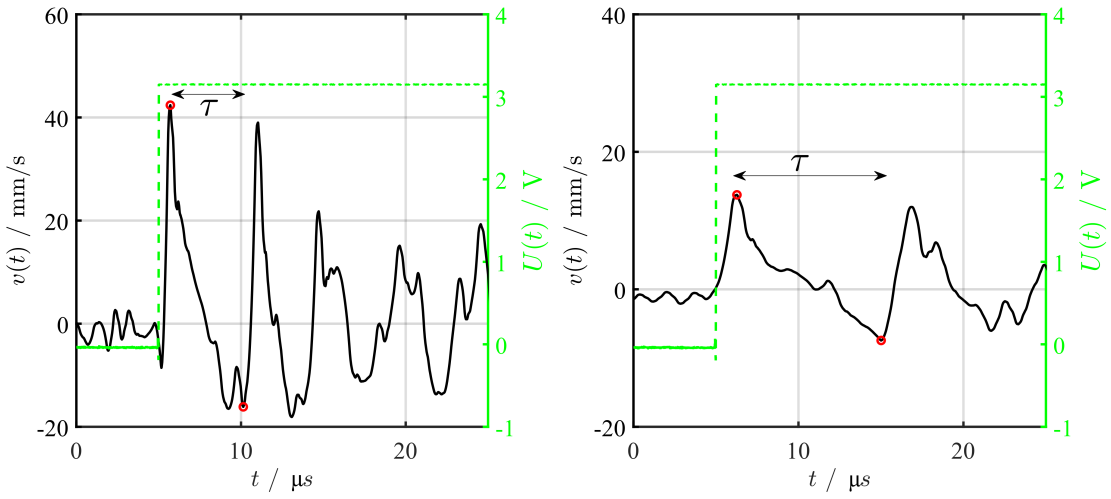

Figure 5.9.: LDV-Velocity signal generated by the PA effect on spheres with the radius $R_S = 2.5$ mm in (a) and $R_S = 5$ mm (black continuous lines) in (b), respectively. The red dots delimit the duration of the PA signal generated by the absorbing sphere, τ. The green dashed line represent the trigger signal of the excitation laser $U(t)$.

5.3.3.2. LDV Measurements on a Phantom in Absence of Spherical Inclusions

In this paragraph, the time characteristics of the PA signals acquired with the DLDV on the tissue phantom of Figure 5.7(d) in absence of inclusions are analyzed. Figure 5.10(a) illustrates this configuration; the excitation laser impinges on the surface of the phantom where there are no inclusions underneath. Figure 5.10(b) reveals a typical signal detected with the self-made IR vibrometer from the silicone phantom described in Subsection 5.3.2 in the absence of absorbing spheres along the distance $d = 59.67$ mm.

The signals were acquired with the setup described in Section 5.3.1. A sample frequency of 50 MHz and an acquisition time of 200 µs were employed. The measurement consisted of 128 averaged signals. High-frequency noise and low frequency disturbances were removed with a wavelet-denoising filter exploiting the Daubechies wavelet db4 [209, 210]. The filtered signals are obtained from the difference between the approximation at level 5 and at level 11. The frequency range selected is, therefore, between 12.21 kHz and 781.13 kHz. The high vibration amplitudes at time $t = 0$ s of Figure 5.10(b) marked with a dashed blue rectangle (I) are generated from two contributions. The first contribution is related to the

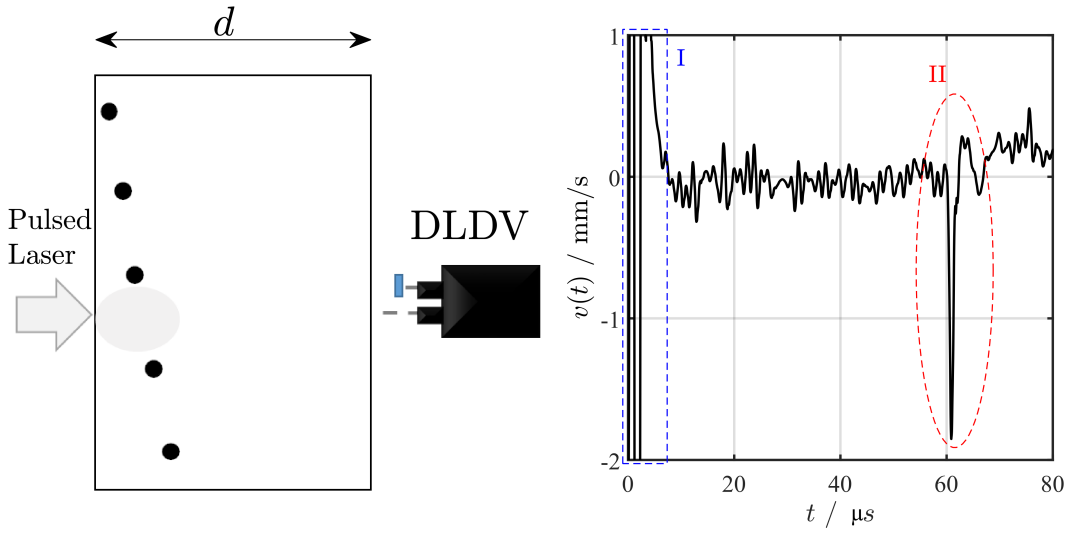

Figure 5.10.: Measurement on the phantom in absence of inclusions: Scheme of the setup (a), LDV-Velocity signal generated by the PA effect on the phantom surface (b).

light of the pulse laser and the second is related to the thermoelastic expansion. The photodiodes of the self-made vibrometer DLVD are InGaAs photodiodes which have a high responsivity at 1064 nm. They detect the light of the laser shot passing through the sample. These vibrations are superimposed to the vibration generated by the thermoelastic expansion of the surface where the measuring spot is located. These vibrations (Pattern I) are not interesting for the aim of the thesis.

The PA signal generated from the irradiated surface is instead relevant for this work. The vibration generated by the irradiated surface (II) are marked with a dashed red ellipse.
The shape and the time duration of the signal generated from the surface depends on the combination of several factors such as the optical, thermic and acoustic properties of the irradiated material, the characteristics of the laser irradiation and the boundary conditions. These aspects are not considered here. For detailed information about the stress induced by a pulsed laser, the reader may refer to the references [211, 212].
For the silicone rubber phantom used for these measurements, the PA signal generated by the irradiated surface presents a stress (i.e. velocity) transient with a negative peak. The transient occurs at a time equal to the distance that the wave travels divided by the sound velocity.
For the signal in Figure 5.10 the traveled distance is $d = 59.67$ mm. The descending

peak starts about 60 µs after the laser shot occurring at $t = 0$ s. The negative peak appears at about 61 µs. This leads to a sound velocity of $v_{s,sil} \approx 1000$ m/s, which is a plausible value for the Dragon Skin silicone rubber used to build the phantom. A similar value of sound velocity is reported in Cafarelli, Miloro, et al. [213]. However, since the starting point of the signal is difficult to detect and there is a delay between the trigger signal and the laser shot, the value of the sound velocity of the silicone rubber in the tissue mimicking phantom is estimated with the method described in Paragraph 5.4.1.3.

5.3.3.3. LDV Measurements on a Phantom in Presence of Spherical Inclusions

The signals acquired on the silicone phantom of Figure 5.7(d) in the presence of absorbing spheres show both patterns generated by the sphere and by the surface. Figure 5.11(a) represents a scheme of the setup of the measurement performed on the phantom in presence of absorbing spheres.
The signals were filtered with the same wavelet-denoising filter employed for the measurements of Paragraph 5.3.3.2. The spheres S_1, S_2, S_3, S_4 and S_5 have a radius $R_S = 2.5$ mm and they are placed at different depths z_{S_i} (see Subsection 5.3.2) and, since the distance between the two phantom surfaces d is the same for all the spheres, they have different detection distances r_{D_i} (see Figure 5.11(a)).
Figure 5.11(b) shows the pattern obtained from the measurements on correspondence of the five spheres. As for the signals of Paragraph 5.3.3.2, the high amplitude at time $t = 0$ s (Pattern I in Figure 5.10) is not relevant.
All the signals present the pattern II of Figure 5.10(b). In particular, the negative peak is at about 61 µs. As explained before, this represents the signal of the irradiated surface. The N-shaped pattern generated by the spheres is present in all the signals. The sphere S_1 of Figure 5.11(a) generates the velocity signal acquired with the DLDV of Figure 5.11(b) denoted with S_1; the same applies to the other spheres S_i. The sphere S_1 is positioned at the lowest depth $z_S = z_{S_1}$ and, therefore, at the greatest distance $r_D = r_{D1}$. The signal in the graphic denoted with S_5 is the one of the sphere S_5 positioned at the greatest depth $z_S = z_{S_5}$ and the smallest distance $r_D = r_{D5}$.
As expected, as we look at the graphs from the top to the bottom, the positive peaks (marked with red circles) are shifted to the left with respect to the previous graphic.

The first plot from the top shows the signal of the sphere S_1 located at the depth $z_{S_1} = 2.53$ mm. In this case, the negative peak of the N-shaped signal and of the surface are not well discernible because of the close distance between the sphere and the surface. The other spheres are located at greater depth z_S; therefore, in the other plots the negative peak generated by the irradiation of the surface and the negative peak of the N-shaped signal are clearly separated. The greater the

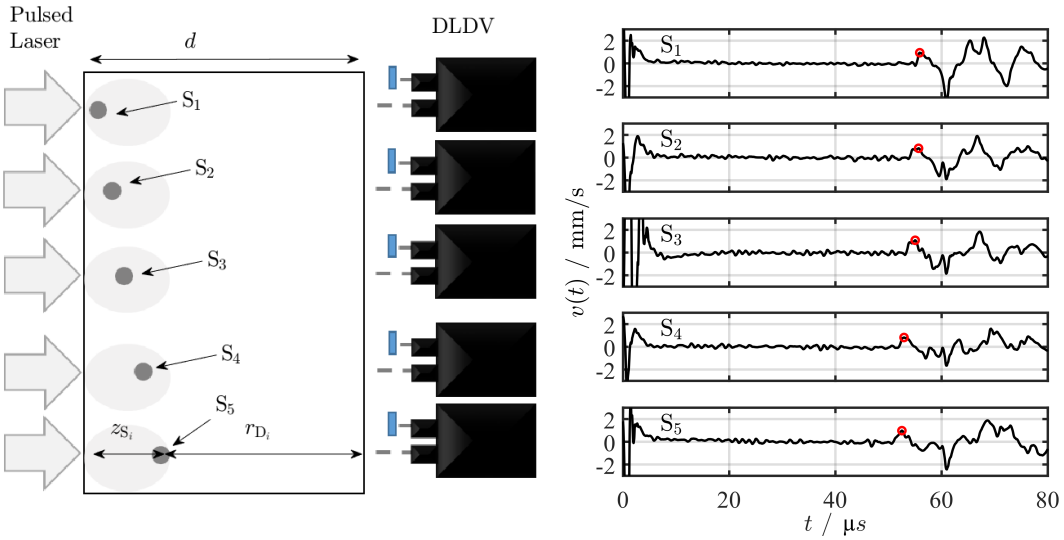

(a) (b)

Figure 5.11.: Measurement on the phantom in presence of inclusion: Scheme of the setup to acquire the PA signals generated by the five spheres (a) and their corresponding velocity signals acquired on the opposite surface with respect to the excitation (b). The red circle identifies the maximum of the N-shaped signal generated by the sphere.

depth z_S, the greater is the time difference between the two negative peaks. The time duration of the N-shaped signal is in the expected range, $\tau \approx 4-5$ ms for all the five signals.

5.3.4. Discussion

This section shows the photoacoustic signals generated on silicon rubber phantoms detected with LDVy.
The signals obtained from the experiments present the expected characteristics in time domain.
In particular, the measurements on the silicone rubber spheres with different radius showed the typical N-shaped or bipolar signal described in the theory. The duration of the signals is also compatible with the expected value relative to the sphere dimension.
The measurements on the phantom in the absence of spherical inclusions deliver two characteristic patterns related to the two surfaces of the phantom: the surface of the phantom where the measuring spot is located and the surface where the pulsed laser impinges.
The measurements on the phantom in the presence of spherical inclusions present

both patterns: the negative peak of the irradiated surface and the N-shaped pattern related to the spheres. In particular, the duration of the N-shaped signal is compatible with the the dimension of the sphere and the sound velocity in the silicone rubber. A superimposition of the patterns delivered by the irradiated surface of the phantom and the N-shaped signal is sometimes present in the signals. However, the first positive peak is always clearly identifiable.
Since the spheres of the phantom are positioned at different distances from the detectors, the N-shaped patterns of the spheres appear at different time instants, as expected: the greater the distance between the sphere and the detector is, the greater is time difference between the laser shot and the of time when the N-shaped signal appears.

These first measurements show the feasibility of LDV measurements for PAI to detect spherical inclusions on tissue phantoms reliably, because they are conform with the theory. In the next section the model for the generation and propagation of PA signals and its detection with a LDV proposed in Section 5.1 is validated by experiments on silicone tissue-mimicking phantoms.

5.4. Reliability of Measurements

The aim of this Section is to verify the reliability of the LDV measurements performed in this thesis.

The measurements of Subsection 5.3.3 were carried out on the tissue mimicking phantom, since measurements on breast tissue with tumors could not be performed. As reported in Subsection 5.3.4, the experiments on the tissue mimicking phantom showed that the the signals acquired with the LDV present the characteristic patterns in the time domain of the photoacoustic signals.

In this section, the model for the generation and propagation of PA signals and its detection with a LDV proposed in Sections 5.1 and 5.2 is validated. To validate the model, the properties of the tissue-mimicking phantom and of the experiment setup must be known. The optical properties of the phantom needed for the computation are not known and could not be evaluated experimentally. Therefore, to validated the model an approach based on the parameter identification of the optical properties is proposed. The optical properties to be determined are the optical absorption of the silicone spheres and the optical attenuation of the silicone rubber. In Subsection 5.4.1, the parameter identification method is presented and the validation is discussed.

According to the model of the theory, the detection range for a sphere with a radius R_S can be estimated by verifying the condition of equation 5.39. The maximum of the displacement signal $s_\mathrm{M,meas}$ calculated with equation 5.26 should be greater than the displacement resolution of the IR-LDV in the experiments $s_\mathrm{RL,meas}$.

Once all the parameters for the computation of $s_\mathrm{M,meas}$ and $s_\mathrm{RL,meas}$ are estimated, the detection range of the spheres in silicon phantoms is discussed in Subsection 5.4.2 according to equation 5.39.

5.4.1. Method for Identification of Optical Absorption

A parameter identification is performed to detect the optical properties of the silicone rubber.
PAI measurements with LDV according to the setup of Figure 5.6 must be performed to estimate them.

The model chosen for the representation of the physical response is the positive peak of the velocity signal acquired with the DLDV with the setup of Figure 5.6. The attenuated velocity peak, v_M is calculated with equation 5.25 and it is proportional to the attenuated peak of the displacement signal s_M. By explicating all the terms of equation 5.25, v_M results in

$$v_\mathrm{M} = \frac{1}{r_\mathrm{D} Z} \frac{\beta v_\mathrm{s}^2}{C_\mathrm{P}} \mu_\mathrm{a} F_0 e^{-\mu_\mathrm{eff} z_\mathrm{S}} R_\mathrm{S} e^{-\overline{\mu}_\mathrm{att} \cdot r_\mathrm{D}}. \tag{5.43}$$

To perform the identification of the optical parameters, experimental and simulated data of the attenuated velocity peak v_{M} are needed.
The experimental data of the attenuated velocity peak v_{M} are called $v_{\mathrm{M,meas}}$, while the simulated data of the attenuated velocity peak v_{M} are called $v_{\mathrm{M,sim}}$.
Since the measurements are performed on silicone rubber phantoms, the thermal and acoustic properties of the silicon rubber assume in their variable name the subscript $_{\mathrm{sil}}$ to distinguish them from the typical properties of breast or soft tissue introduced in Section 5.1.
Therefore, the optical absorption coefficient of the tumor μ_{a} is replaced with the optical absorption coefficient of the absorbing silicon rubber sphere $\mu_{\mathrm{a,sil}}$.
The effective optical attenuation for breast tissue μ_{eff} is replaced with the total attenuation of the silicone rubber resulting from optical scattering and optical absorption $\mu_{\mathrm{tot,sil}}$.
Therefore, the simulated attenuated velocity peak amplitude v_{M} can be written as

$$v_{\mathrm{M,sim}} = \frac{1}{r_{\mathrm{D}} Z_{\mathrm{sil}}} \frac{\beta_{\mathrm{sil}} v_{\mathrm{s,sil}}^2}{C_{\mathrm{P,sil}}} \mu_{\mathrm{a,sil}} F_0 e^{-\mu_{\mathrm{tot,sil}} z_{\mathrm{S}}} R_{\mathrm{S}} e^{-\overline{\mu}_{\mathrm{att,sil}} \cdot r_{\mathrm{D}}}. \tag{5.44}$$

Both optical parameters $\mu_{\mathrm{tot,sil}}$ and $\mu_{\mathrm{a,sil}}$ are unknown and must be determined. The thermal (β_{sil} and $C_{\mathrm{P,sil}}$) and acoustic (Z_{sil}, $v_{\mathrm{s,sil}}$ and $\overline{\mu}_{\mathrm{att,sil}}$) parameters of the silicone rubber together with the laser fluence (F_0) were estimated experimentally. The method used for the fitting of the experimental data exploits the least-square algorithm presented in Hartmann and Gilbert [214].

The values of the optical absorption $\mu_{\mathrm{a,sil}}$ and of the effective optical attenuation in tissue $\mu_{\mathrm{tot,sil}}$ that minimize the function g,

$$g(\mu_{\mathrm{a,sil}}, \mu_{\mathrm{tot,sil}}) = \frac{1}{2} \sum_{i=1}^{N} (v_{\mathrm{M,sim}_i}(\mu_{\mathrm{a,sil}}, \mu_{\mathrm{tot,sil}}) - v_{\mathrm{M,meas}_i})^2, \tag{5.45}$$

are calculated with the MATLAB® subroutine lsqnonlin.m.
The function $g(\mu_{\mathrm{a,sil}}, \mu_{\mathrm{tot,sil}})$ is the square of the norm of the residuum between the simulated and the experimental data. The variable N represents the number of experiments, $v_{\mathrm{M,meas}_i}$ is the i-th component of the vector of the attenuated peak amplitude obtained from the experiments $\boldsymbol{v}_{\mathrm{M,meas}}$.
The simulated data $v_{\mathrm{M,sim}_i}$ is the component of the vector of the simulated data $\boldsymbol{v}_{\mathrm{M,sim}}$ corresponding to the experiment $v_{\mathrm{M,meas}_i}$. The simulated data is calculated with the equation 5.44.
Since the problem has bounds ($\mu_{\mathrm{a,sil}}, \mu_{\mathrm{tot,sil}} > 0$) the MATLAB function uses a trust-region-reflective algorithm which requires to provide a gradient. Here, the gradient is numerically calculated.
For the optimization process of $g(\mu_{\mathrm{a,sil}}, \mu_{\mathrm{tot,sil}})$, the residuum has been normalized

by the different amplitudes of the experimental data.
To estimate the quality of the identification, the coefficient of determination R^2

$$R^2 = 1 - \frac{\sum_{i=1}^{N_D}(v_{\mathrm{M,meas}_i} - v_{\mathrm{M,sim}_i})^2}{\sum_{i=1}^{N}(v_{\mathrm{M,meas}_i} - \overline{v}_{\mathrm{M,meas}})^2}, \tag{5.46}$$

is determined, where $\overline{v}_{\mathrm{M,meas}}$ is the mean value of all the experimental data $v_{\mathrm{M,meas}_i}$. The value of R^2 varies in the interval $0 \leq R^2 \leq 1$. If $R^2 \approx 0$ the fit is bad. For a very good fit, R^2 has to be ≈ 1.

However, according to reference [214] other parameters to estimate the quality of the fit are needed. The matrix of the second partial derivative is called Hessian matrix $\boldsymbol{H}$

$$\boldsymbol{H} = \begin{bmatrix} \dfrac{\partial^2 g}{\partial \mu_{\mathrm{a,sil}} \partial \mu_{\mathrm{a,sil}}} & \dfrac{\partial^2 g}{\partial \mu_{\mathrm{a,sil}} \partial \mu_{\mathrm{tot,sil}}} \\ \dfrac{\partial^2 g}{\partial \mu_{\mathrm{tot,sil}} \partial \mu_{\mathrm{a,sil}}} & \dfrac{\partial^2 g}{\partial \mu_{\mathrm{tot,sil}} \partial \mu_{\mathrm{tot,sil}}} \end{bmatrix} \tag{5.47}$$

and its determinant $\det \boldsymbol{H}$ delivers information about the uniqueness of the solution. The determinant of the Hessian $\det \boldsymbol{H}$ has to be greater than zero to have an unique local minimum.
The fit is performed for measurements on the silicone rubber phantom of Figure 5.7(d).

The next paragraphs (5.4.1.1, 5.4.1.2, 5.4.1.3 and 5.4.1.4) present the experimentally estimation of the:

- geometrical characteristics of the phantom (R_{S}, z_{S}, r_{D} and d),
- thermal characteristics of the phantom (β_{sil} and $C_{\mathrm{P,sil}}$),
- acoustic characteristics of the phantom (Z_{sil}, $v_{\mathrm{s,sil}}$ and $\overline{\mu}_{\mathrm{att,sil}}$),
- laser fluence at the surface F_0.

Successively, the measurements performed with the setup of Figure 5.6 to detect the attenuated velocity peak $v_{\mathrm{M,meas}}$ are presented.
Since two parameters - $\mu_{\mathrm{tot,sil}}$ and $\mu_{\mathrm{a,sil}}$ - need to be determined, two independent variables of the model of equation 5.43 must be varied during the experiments.
Therefore, two different type of experiments need to be carried out.
Experiments at different depths of the sphere z_{S} and at different energy levels of the pulsed laser, to which different values of fluence F_0 correspond, were performed (Paragraph 5.4.1.5).

Finally, the optical parameters estimated with the method described in this paragraph are presented and the quality of the fit is discussed (Paragraph 5.4.1.6).

5.4.1.1. Geometrical Characteristics

The phantom used for the measurements is shown in Figure 5.7(d) and its geometrical characteristics are already described in Subsection 5.3.2:

- the radius of all the spheres S_i is $R_S = 2.5$ mm where $i = 1, 2, 3, 4, 5$
- the depth of the spheres are $z_{S_1} = 2.53$ mm, $z_{S_2} = 3.86$ mm, $z_{S_3} = 4.39$ mm, $z_{S_4} = 5.97$ mm, $z_{S_5} = 6.67$ mm
- the dimension d of the phantom is 59.67 mm
- the distance between each sphere and the detector r_{D_i} is calculated according to equation 5.41

The values of the depth z_{S_i} and the dimension d of the phantom were measured with a caliper gauge at the end of phase two and at the end of phase three of the preparation of the phantom, respectively. Their values are obtained by performing the mean value over 10 measurements.

5.4.1.2. Thermal Characteristics

The thermal characteristics of the phantom are the coefficient of volume expansion β_{sil} and the heat capacity at constant pressure $C_{\text{P,sil}}$.
The coefficient of volume expansion β_{sil} is determined with measurements performed using the optical dilatometer DIL 806 from the company TA instruments [215].
The heat capacity at constant pressure $C_{\text{P,sil}}$ is determined using the differential scanning calorimeter (DSC) DSC 404 F3 Pegasus® of the company Netzsch [216]. The DIL 806 and the DSC 404 F3 Pegasus® are available at the Institute of Non-Metallic Materials, TU Clausthal. For both measurements, silicone rubber samples were prepared. Figure 5.12(a) shows the 10 silicon rubber specimens used for the measurements with the DIL 806 and Figure 5.12(b) shows the 10 silicon rubber specimens used for the measurements with the DSC. These specimens are prepared with the procedure for the simulation of breast tissue described in Subsection 5.3.2.

The value of the coefficient of volume expansion β_{sil} is derived from the measurement of the coefficient of linear thermal expansion α_{T° performed with the optical dilatometer DIL 806. The silicon rubber can be considered isotropic [217]. Since the problem involves small temperature changes and small deformations, the simplification

$$\beta_{\text{sil}} = 3 \cdot \alpha_{T^\circ} \tag{5.48}$$

is valid.

Figure 5.13(a) presents a scheme of the measuring principle of the DIL 806. At first, the specimen is placed inside the furnace. The initial length l_0 and the

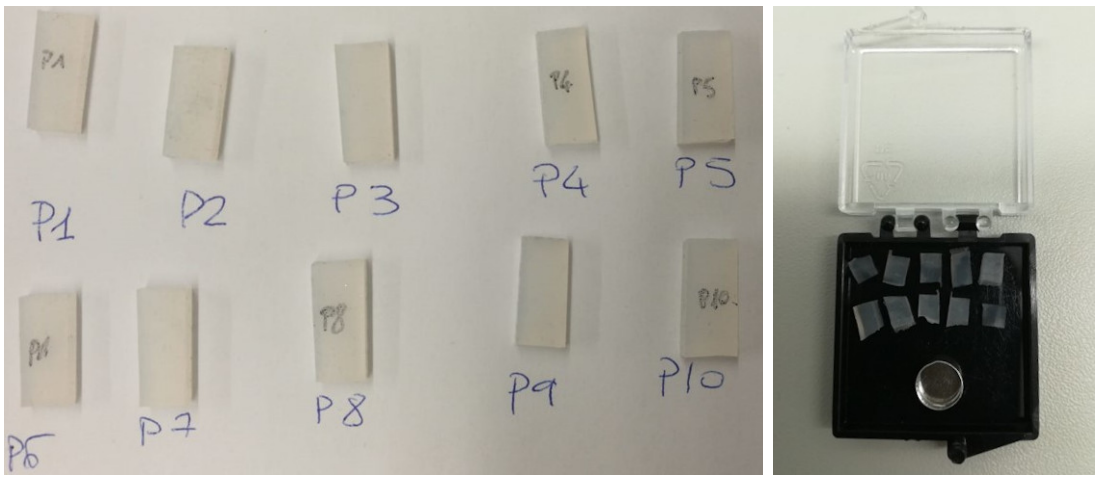

(a) (b)

Figure 5.12.: Samples for the measurement with the optical dilatometer (a). Specimen for the DSC measurements and crucible (b).

change of length Δl during the heating and cooling processes are measured without contact by exploiting the shadowed light method [215].
A broad-width planar light beam generated by a LED impinges on the sample. The CCD sensor detects the shadow. A digital edge-detection processor evaluates the signal and a precise measurement of the dimensional change is obtained.

The heating process consisted of three phases. During the first phase, the sample is maintained for 30 minutes at room temperature (about 25°C). In the second phase the sample is heated from room temperature to 80°C with a speed of 1 K/min. During the third phase, the sample is brought back to the initial temperature. The second phase is used for the calculation of α_{T°.

The value of coefficient of linear thermal expansion α_{T° was calculated for 10 silicon rubber samples between the 30°C and 70° C

$$\alpha_{T^\circ} = \frac{1}{N}\sum_{i}^{N}\frac{1}{l_{0,i}}\frac{\Delta l_i}{\Delta T} = 260.95 \cdot 10^{-6}\ \mathrm{K}^{-1}, \tag{5.49}$$

where the index $i = 1,..N$ identifies the specimen and $N = 10$, ΔT is the temperature difference $\Delta T = 70° - 30° = 40°\mathrm{C}$, $l_{0,i}$ is the initial length of the sample i, $\Delta l_i = l_i - l_{0,i}$ is the change in length of the sample measured with the DIL 806 and l_i is the final lenght of the sample i.

Figure 5.13(b) shows the percent strain $\Delta l/l_0$ over the sample temperature T_{sample} for the 10 samples. The coefficient of linear thermal expansion α_{T° was used for the calculation of the coefficient of volumetric thermal expansion β_{sil} according to equation 5.48. Therefore, β_{sil} resulted in $7.83 \cdot 10^{-4}\ \mathrm{K}^{-1}$.

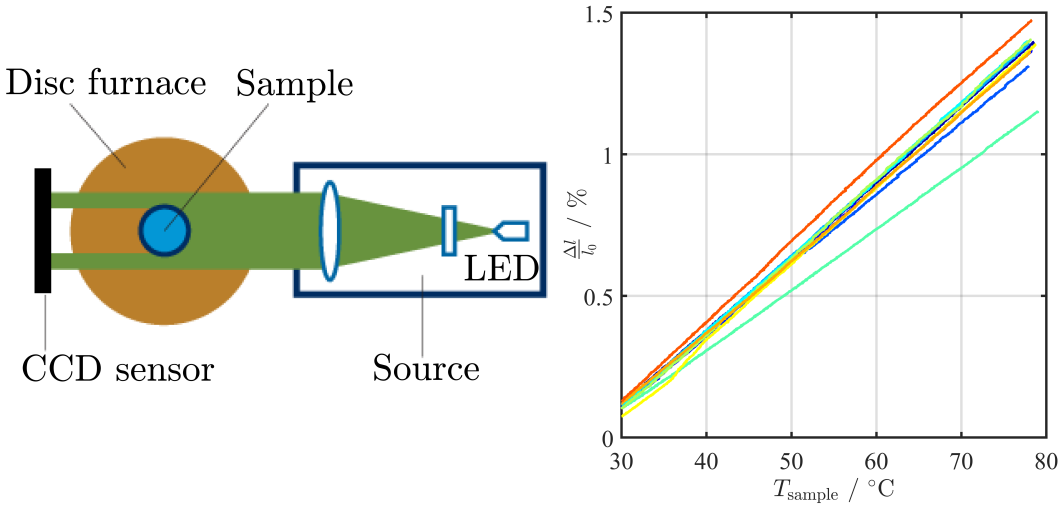

(a) (b)

Figure 5.13.: Measurement principle of the optical dilatometer DIL 806 [215] (Copyright by TA Instruments, reproduced with permission)(a). Measurement performed with the Optical Dilatometer DIL06 (second phase)(b).

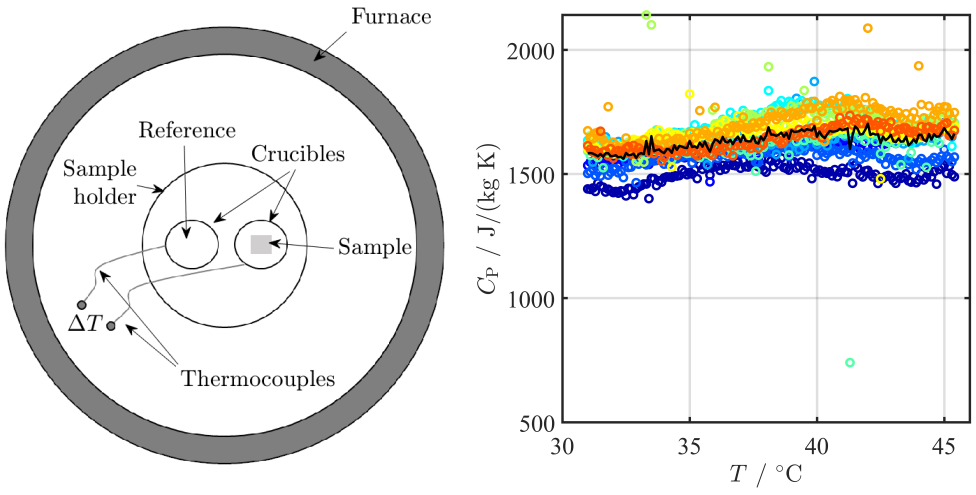

(a) (b)

Figure 5.14.: Measurement principle of the DSC [216] (a). Measurements performed with the DSC(b). The black line represents the mean curve obtained from the 10 measurements (colored circles).

Measurements with the differential scanning calorimeter (DSC) DSC 404 F3 Pegasus® of the company Netzsch [216] allowed the detection of the heat capacity at constant pressure $C_{\mathrm{P,sil}}$ of the silicon rubber. The DSC measurements of 10 samples (see Figure 5.12(b)) were performed.
Figure 5.14(a) shows the measuring principle of the DSC. The DSC has two crucibles inside the furnace. The sample was placed in one of them. The other one was left empty. The measurement was performed in nitrogen atmosphere. The DSC measures the heat flow and the temperature in the sample and in the reference with thermocouples. Their difference is proportional to the value of $C_{\mathrm{P,sil}}$ [218].
At first, the samples were maintained at the room temperature (25°C) for 10 minutes. Then, they were heated from room temperature to 50°C with a heating rate of 1 K/min. The heating rate was constant starting from about 31°C; therefore, the values of $C_{\mathrm{P,sil}}$ at lower temperatures were excluded from the measurements.
Figure 5.14(b) shows the data acquired with the DSC. Since photoacoustic measurements involve temperature changes in the range of mK, only the values of $C_{\mathrm{P,sil}}$ between 31°C and 35°C are considered.
The value of the heat capacity for the silicone rubber used in this work, $C_{\mathrm{P,sil}}$, is calculated as

$$C_{\mathrm{P,sil}} = \frac{1}{N}\frac{1}{J}\sum_{i}^{N}\sum_{j}^{J} C_{\mathrm{P,sil},i}(T_j), \tag{5.50}$$

where $j = 1..J$, $J = 40$, $T_j = 31°, 31.1°, ...35°\mathrm{C}$ is the temperature with a step of 0.1°C and $i = 1, ..N$ identifies the specimen measured and $N = 10$.
The heat capacity at constant pressure $C_{\mathrm{P,sil}}$ is 1588.9 J/(kg K).

5.4.1.3. Acoustic Characteristics

The sound velocity, the acoustic impedance and the acoustic attenuation of the phantom were determined.

The acoustic impedance is $Z_{\mathrm{sil}} = \rho_{\mathrm{sil}} v_{\mathrm{s,sil}}$. The density ρ_{sil} is given in the datasheet of the material, $\rho_{\mathrm{sil}} = 1070\ \mathrm{kg/m^3}$. Therefore, only the sound velocity $v_{\mathrm{s,sil}}$ and the acoustic attenuation $\overline{\mu}_{\mathrm{att,sil}}$ need to be determined.

The value of the sound velocity is expected to be around ≈ 1000 m/s as stated in Paragraph 5.3.3.2. However, since there is delay between the trigger signal and the laser shot, I chose to estimate the sound velocity with another method, which is independent from the trigger signal.
The phantom of Figure 5.7(d) was measured from different sides as depicted in Figure 5.15(a).
The measurements were performed in the absence of spherical inclusions along the width d and along the height d_{height}.

One hundred and twenty-eight signals were acquired with a sample frequency of 50 MHz and an acquisition time of 200 µs. The signals were averaged. The high-frequency noise and low frequency disturbances were removed from the averaged signal with the wavelet-denoising filter described in Paragraph 5.3.3.2.
Therefore, only the frequency components between 12.21 kHz and 781.13 kHz are considered.
Figure 5.15(b) shows the signal acquired at the distance d (red dashed line) and the signal acquired at the distance d_{height} (black continuous line).
As explained in Subsection 5.3.3, the signal generated from the irradiated surface has a negative peak.
In the second signal, the same pattern is present but it appears delayed and attenuated, because the wave traveled a wider distance.
The sound velocity can been calculated as

$$v_{\text{s,sil}} = \frac{d - d_{\text{height}}}{t_{\text{delay}}}, \tag{5.51}$$

where $d = 59.67$ mm and $d_{\text{height}} = 33.53$ mm.
The time delay between the arrival time of the negative peaks in the two signals is $t_{\text{delay}} = 26.24$ µs, the path difference $d - d_{\text{height}}$ is known; therefore, $v_{\text{s,sil}}$ results in 996 m/s.
This value is similar to the one found in the literature [213, 219].

The other acoustic parameter is the attenuation of the velocity peak, $\overline{\mu}_{\text{att,sil}}$. The simplification of equation 5.16 that estimates the attenuation is not needed here, since it was possible to estimate the value of the attenuation of the peak $\overline{\mu}_{\text{att,sil}}$ experimentally.

Two phantoms with different widths d_1 and d_2 and a spherical inclusion with $R_{\text{S}} = 2.5$ mm (Figure 5.16(a)) were prepared according to the procedure described in Subsection 5.3.2.
The inclusions of the two phantoms have the same value of the optical absorption $\mu_{\text{a,sil}}$ and they were placed at the same position $z_{\text{S}} = 2.5$ mm.
Since the two phantoms have different lengths ($d_1 \neq d_2$), their values of r_{D} (r_{D_1} and r_{D_2}) are different.
Measurements with the setup of Figure 5.16(b) were performed on the two phantoms with the same acquisition parameters as the measurements for the detection of the sound velocity of the phantom $v_{\text{s,sil}}$.

According to equation 5.10, the signals generated by an absorbing sphere with $R_{\text{S}} = 2.5$ mm and with the sound velocity $v_{\text{s,sil}} = 996$ m/s, have frequency components up to $f \approx 300$ kHz.
A wavelet-denoising filter exploiting the Daubechies wavelet db4 [209, 210] is applied to the signals. The difference between the approximation at level 6 and the level 11 is performed; the bandwidth of the filtered signal is between 12.21 kHz and 390.63 kHz. Thus, all the relevant components of the signal generated by the

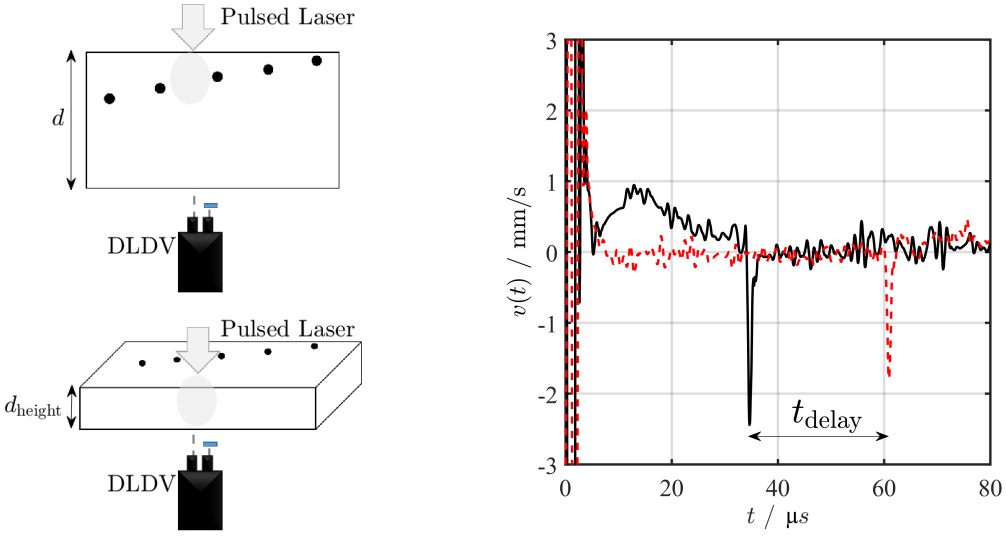

Figure 5.15.: Schematic setup for the measurement of the sound velocity (a) and LDV-velocity signals acquired with the setup described in (b). The dashed red line is the signal acquired at the distance d and the black line is the signal acquired at the distance d_{height}(b).

sphere are included.
The sound attenuation coefficient for the peak of the photoacustic signal generated by a sphere with $R_{\text{S}} = 2.5$ mm is computed from the measurement of the attenuated velocity peak of the phantom with the width d_1 and of the phantom with the width d_2, $v_{\text{M},1}$ and $v_{\text{M},2}$, respectively.
Since the radius $R_{\text{S}} = 2.5$ mm, the depth of the sphere $z_{\text{S}} = 2.5$ mm and the material characteristics are the same in the two phantoms and the laser fluence was kept constant during the measurements, $v_{\text{M},1}$ and $v_{\text{M},2}$ can be written as

$$v_{\text{M},1} = \frac{G}{r_{\text{D}_1}} e^{-\overline{\mu}_{\text{att,sil}} \cdot r_{\text{D}_1}} \tag{5.52}$$

$$v_{\text{M},2} = \frac{G}{r_{\text{D}_2}} e^{-\overline{\mu}_{\text{att,sil}} \cdot r_{\text{D}_2}}, \tag{5.53}$$

where $G = \frac{1}{Z_{\text{sil}}} \frac{\beta_{\text{sil}} v_{\text{s,sil}}^2}{C_{\text{P,sil}}} \mu_{\text{a,sil}} F_0 e^{-\mu_{\text{tot,sil}} z_{\text{S}}} R_{\text{S}}$, $r_{\text{D}_1} = d_1 - z_{\text{S}_1}$ and $r_{\text{D}_2} = d_1 - z_{\text{S}_2}$.
Figure 5.16(c) shows the acquisition for the phantom with the width $d_1 = 4.72$ cm and Figure 5.16(d) the acquisition with $d_2 = 3.35$ cm.
The red points on the pattern of both graphics delimit the start and the maximum amplitude of the peak. The difference in amplitude between these two points is

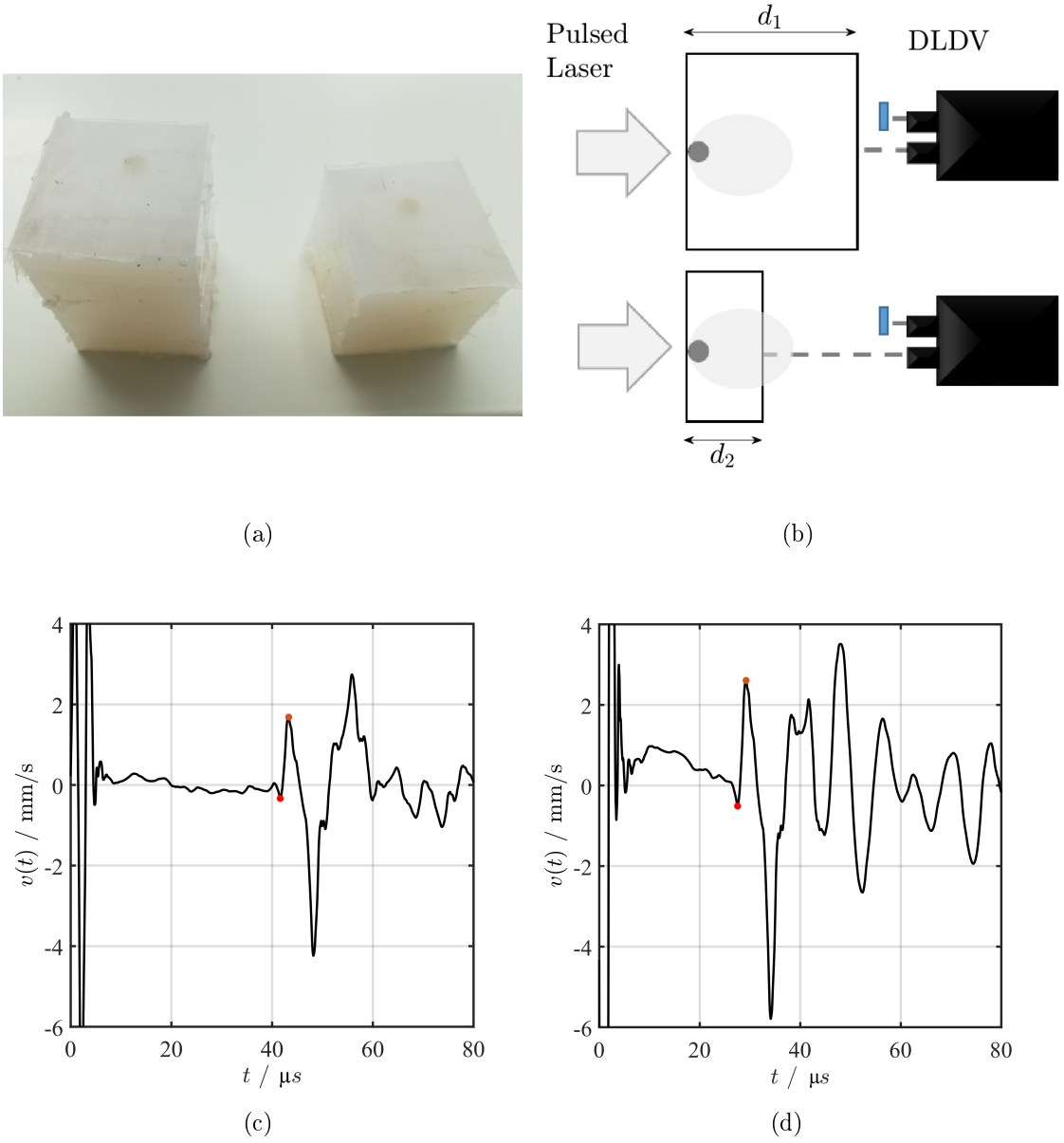

Figure 5.16.: Silicon rubber phantoms (a) and schematic setup (b) for the measurement of the acoustic attenuation. LDV-velocity signal (c) acquired at the distance d_1 with the setup described in (b). LDV-velocity acquired at the distance d_2 (d) with the setup described in (b). The red points in (c) and (d) indicate the limits of the amplitudes $v_{\mathrm{M},1}$ and $v_{\mathrm{M},2}$, respectively.

taken for the calculation of $\overline{\mu}_{\text{att,sil}}$. In particular, the value of $v_{\text{M,1}}$ is 2.017 mm/s and the value of $v_{\text{M,2}}$ is 3.119 mm/s. The attenuation in Np/cm results in

$$\overline{\mu}_{\text{att,sil}} = \frac{\ln\left(\frac{v_{\text{M,2}} \cdot r_{\text{D}_2}}{v_{\text{M,1}} \cdot r_{\text{D}_1}}\right)}{r_{\text{D}_1} - r_{\text{D}_2}} = 0.051 \text{ Np/cm}. \tag{5.54}$$

This value is in the same range as the sound attenuation values for RTV silicone rubber found in literature [219–221].

5.4.1.4. Laser Fluence

The laser fluence is defined as the optical energy per unit area. The energy E of the laser is estimated with the pyroelectric energy sensor ES220C from the company Thorlabs [222] as shown in Figure 5.17. The laser diameter at the surface of the irradiated object[f] r_{PL} is defined for an intensity drop of $1/\text{e}^2$.
In the model of equation 5.44, the fluence F is

$$F = F_0 e^{-\mu_{\text{tot,sil}} z_{\text{S}}}, \tag{5.55}$$

where $\mu_{\text{tot,sil}}$ is the total attenuation coefficient of the silicone phantom which is due to the contribution of both absorption and scattering.
The fluence of a Gaussian beam at the surface of the phantom is

$$F_0 = \frac{2E_0}{\pi r_{\text{PL}}^2}, \tag{5.56}$$

where E_0 is the energy at the surface of the phantom. The laser beam radius at $1/\text{e}^2$ is estimated to be $r_{\text{PL}} = 9$ mm. The factor 2 is due to the the energy distribution of the laser beam [223]. The energy of the pulsed laser can be adjusted by rotating of an angle ξ the $\lambda/2$ waveplate of the attenuator, as showed in Figure 5.17. The energy of the laser beam E was detected directly at the exit of the attenuator. The energy of $N = 100$ laser-shots were acquired and the mean value is used to calculate the fluence for the specific polarizer configuration.
The energy at the surface of the phantom is

$$E_0 = (1 - \Psi_{\text{air/sil}}) \frac{1}{N} \sum_{i=1}^{N} E_i = (1 - \Psi_{\text{air/sil}}) \overline{E}, \tag{5.57}$$

where $\overline{E}$ is the mean energy and $\Psi_{\text{air/sil}}$ is the reflection factor.
The reflection factor considers the loss of energy resulting from the reflection between the air and the silicone phantom and its value was estimated experimentally

[f] The beam divergence of the radius r_{PL} is considered negligible.

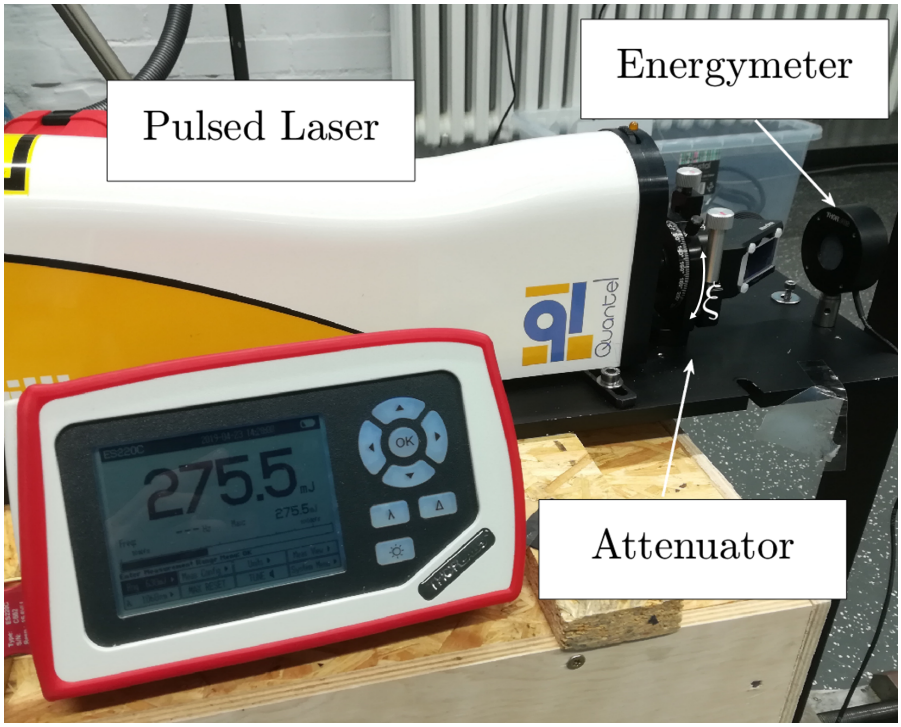

Figure 5.17.: Setup for the estimation of the energy of the pulsed laser.

$\Psi_{\text{air/sil}} \approx 1\%$.
The energy of the laser beam E was detected for four different angles of the attenuator ξ_j: $\xi_1 = 60°$, $\xi_2 = 70°$, $\xi_3 = 80°$ and $\xi_4 = 90°$.
The fluence F_0 and the mean energy $\overline{E}$ are estimated for the four angles ξ_j. In the configuration with the angle ξ_j, the value of the mean energy is $\overline{E}_j$, the value of the energy at the surface is $E_{0,j}$ and the value of the fluence at the surface is $F_{0,j}$ with $j = 1, 2, 3, 4$.
The values of $\overline{E}_j$, $E_{0,j}$ and $F_{0,j}$ are reported in Table 5.1. Only the value of the fluence $F_{0,1}$ is lower than the maximal permissible exposure on the skin of 1000 J/m^2 conform with the laser safety norm [224].

Table 5.1.: Values of the detected mean energy $\overline{E_j}$ and of the fluence and the energy at the surface, $F_{0,j}$ and $E_{0,j}$.

	$\overline{E}_j$ / mJ	$E_{0,j}$ / J/m^2	$F_{0,j}$ / J/m^2
$\xi_1 = 60°$	91.93	91.01	715.28
$\xi_2 = 70°$	175.36	173.71	1364.47
$\xi_3 = 80°$	245.73	243.27	1912.01
$\xi_4 = 90°$	277.62	274.84	2160.11

5.4.1.5. PAI Measurements with DLDV on Silicone Rubber Phantom with Inclusions to Determine its Optical Properties

To determine the optical absorption of the silicone rubber spheres, experiments at different depths of the sphere z_S and at different energy levels $\overline{E}_j$ must be performed.

The velocity signals generated by the photoacoustic effect on the five spherical inclusions of the phantom were measured with the setup of Figure 5.6 for the energy levels $\overline{E}_j$ of the laser beam calculated in the previous paragraph (Table 5.1).
For each inclusion and energy level, 128 velocity signals were acquired with a sampling frequency of 50 MHz and were averaged in time domain. The averaged signals were filtered using the same wavelet-denoising filter used for the analysis of the sound attenuation (Paragraph 5.4.1.3)with the frequency range between 12.21 kHz and 390.63 kHz.
Measurements on the five spheres S_i with four energy levels $\overline{E}_j$ delivered 20 experimental values of the attenuated velocity peak $v_{M,meas}$.

Figure 5.18 presents a schematic of the measurements performed. Figure 5.19 shows the signals generated by the sphere located at z_{S_4} for the four different energy levels. In particular Figure 5.19 presents the signals obtained with $\overline{E}_1$ in (a), $\overline{E}_2$ in (b), $\overline{E}_3$ in (c) and $\overline{E}_4$ in (d).
The value of the attenuated velocity peak v_M is computed as the amplitude difference between the two red dots in each graphic. The red dots are the marks of the on-set and the maximum of the N-shaped signal. As expected, the value of $v_{M,meas}$ increases proportionally to the energy level of the excitation.
The components of the vector $\boldsymbol{v}_{M,meas}$ of equation 5.45 can be written as

$$v_{M,meas}(\overline{E}_j, z_{S_i}), \tag{5.58}$$

where $j = 1, 2, 3, 4$ identifies the energy level and $i = 1, 2, 3, 4, 5$ the sphere that generates the signal, respectively.
The components of the simulated data of the attenuated velocity peak $v_{M,sim}$ of equation 5.44 are

$$v_{M,sim}(\overline{E}_j, z_{S_i}) = \frac{1}{r_{D_i} Z_{sil} \pi r_{PL}^2} \frac{\beta_{sil} v_{s,sil}^2}{C_{P,sil}} \mu_{a,sil} 2(1 - \Psi_{air/sil}) \overline{E}_j e^{-\mu_{tot,sil} z_{S_i}} R_S e^{-\overline{\mu}_{att,sil} \cdot r_{D_i}}, \tag{5.59}$$

where $r_{D_i} = d - z_{S_i}$.

The experimental data and the simulated data of v_M are presented in the Figures 5.20 and 5.21.

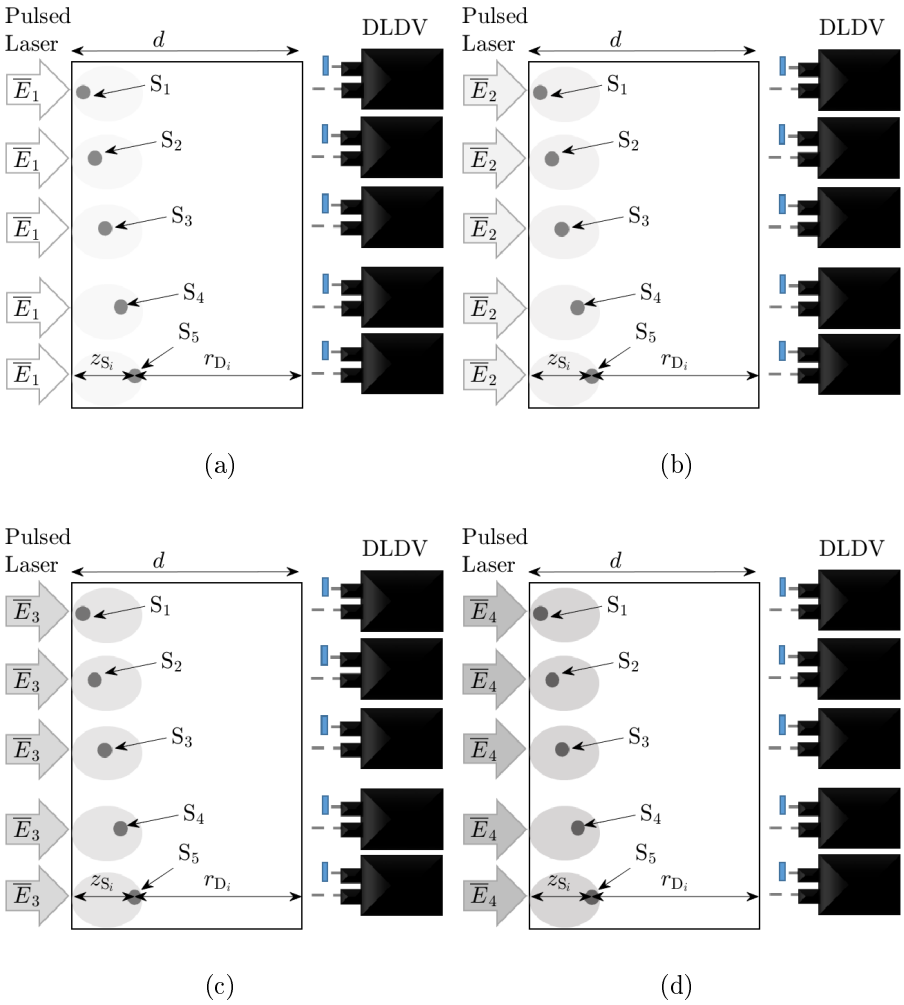

Figure 5.18.: Scheme of the measurements performed on the five spheres S_i with four different energy level: $\overline{E}_1$ in (a), $\overline{E}_2$ in (b), $\overline{E}_3$ in (c) and $\overline{E}_4$ in (d).

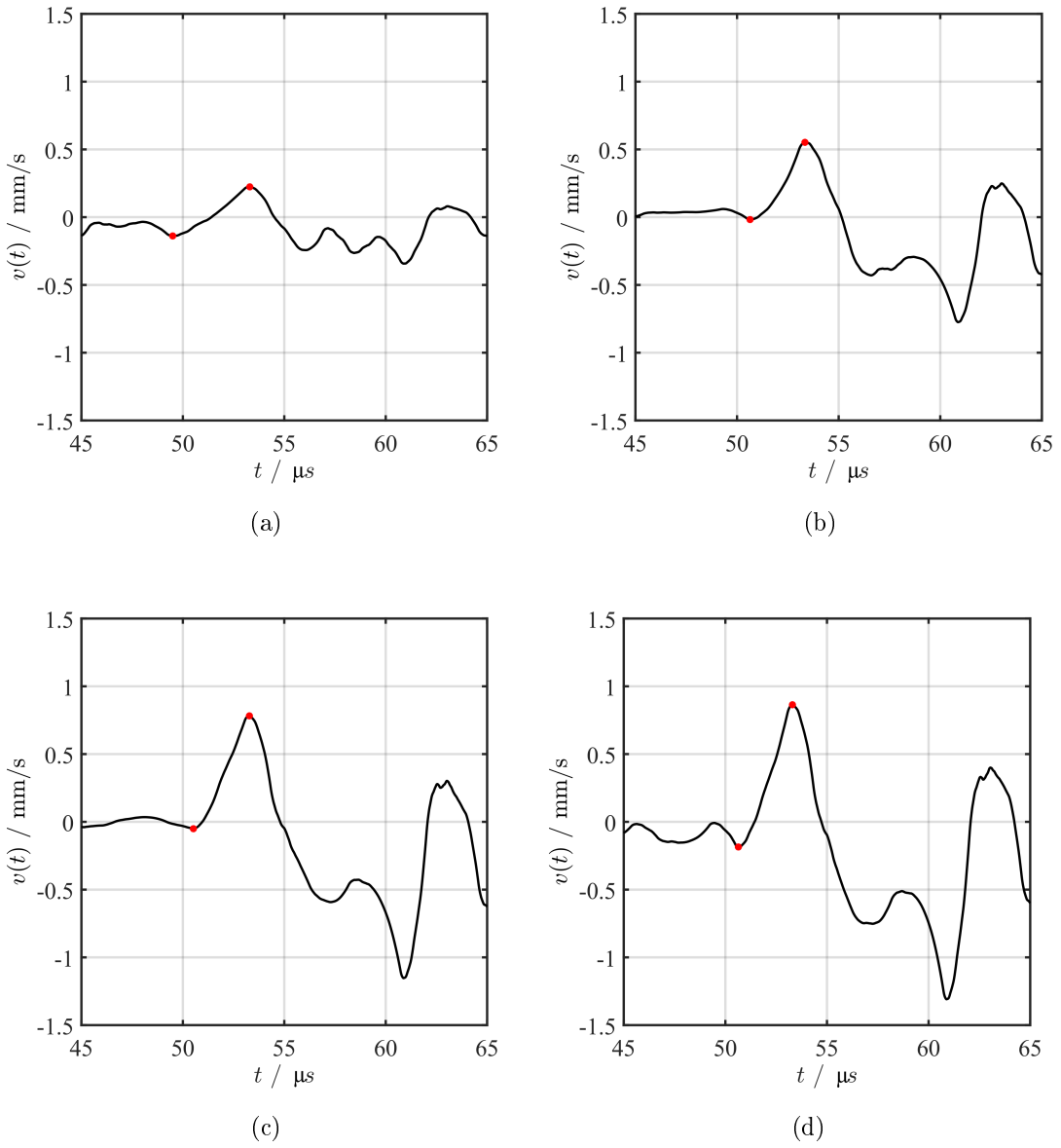

Figure 5.19.: LDV-velocity signals acquired with the setup described in Figure 5.6. The signals are generated by the sphere located at z_{S_4} with $\overline{E}_1$ (a), $\overline{E}_2$ (b), $\overline{E}_3$ (c) and $\overline{E}_4$ (d). The red dots in each graphic indicate the on-set and the maximum of the N-shaped signal, respectively. The amplitude difference between these points was used for the computation of v_M.

5.4.1.6. Determination of Optical Parameters

The minimization of the function g (equation 5.45) calculated for the experiments $v_{\mathrm{M,meas}}(\overline{E}_j, z_{\mathrm{S}_i})$, allowed to find the optimum value for the optical absorption $\mu_{\mathrm{a,sil}} = 38.65\ \mathrm{m}^{-1}$ and the total optical attenuation $\mu_{\mathrm{tot,sil}} = 45.97\ \mathrm{m}^{-1}$.
The coefficient of determination of equation 5.46 is $R^2 = 0.9539$; therefore, the quality of the fit is good and, therefore, the model of the theory is validated.
The determinant of the Hessian matrix calculated with MATLAB® resulted in $\det \boldsymbol{H} = 1.82 \cdot 10^{-7}$, and thus, the MATLAB® routine finds a unique local minimum.
According to [214] the confidence interval for a 68.27% confidence level for each identified parameter can be calculated as the root of the diagonal element of the covariance matrix. The optical absorption $\mu_{\mathrm{a,sil}}$ has a deviation $\Delta\mu_{\mathrm{a,sil}} = \pm 2.32\ \mathrm{m}^{-1}$ and the total optical attenuation $\mu_{\mathrm{tot,sil}}$ has a deviation of $\Delta\mu_{\mathrm{tot,sil}} = \pm 12.13\ \mathrm{m}^{-1}$.

Figure 5.20 and 5.21 show the fit of the experimental data acquired with the setup of Figure 5.18 to the model computed with the optimal values of $\mu_{\mathrm{a,sil}}$ and $\mu_{\mathrm{tot,sil}}$ obtained from the minimization of the function g.

In particular, Figure 5.20 shows the amplitude of the velocity peak over the energy level. The continuous black lines represent the fits obtained from the parameter identification procedure. The red circles are the experimental data.
Starting from the top, the black line interpolates the experiment data of v_{M} (red circles) performed at different energy levels on the sphere S_1 at the depth z_{S_1}. The second graph from the top shows the fit of the data obtained from the inclusion at the depth z_{S_2}. The experimental velocity amplitudes generated by the sphere at the depth z_{S_3} are presented in the third graph from the top together with its fit. The fourth graph from the top shows the fit for the signal of the sphere at the depth z_{S_4} and the last one is the fit for the signals of the inclusion at the depth z_{S_5}. Figure 5.21 shows the fit of $v_{\mathrm{M,meas}}(\overline{E}_j, z_{\mathrm{S}_i})$ over the depth z_{S}. As in Figure 5.20, the continuous black lines in Figure 5.21 represent the fit obtained from the optimization and the red circles are the experimental data. Starting from the top, the first graphic is obtained for the measurement acquired at the energy level $\overline{E}_1$, the second one from the measurement acquired at the energy level $\overline{E}_2$, the third one the measurement acquired at the energy level $\overline{E}_3$ and the last one from the the measurement acquired at the energy level $\overline{E}_4$.

Deviations between experimental data and the interpolating curve derive from different factors.
The setup, the acquisition and the post-processing of the signals have an influence in the estimation of the optical properties.
The excitation laser is not always stable during the averages of the signal and during the whole measurements time.
It was observed that for the same configuration of polarization angle, the energy measured at the beginning and at the end of the acquisition was slightly different.

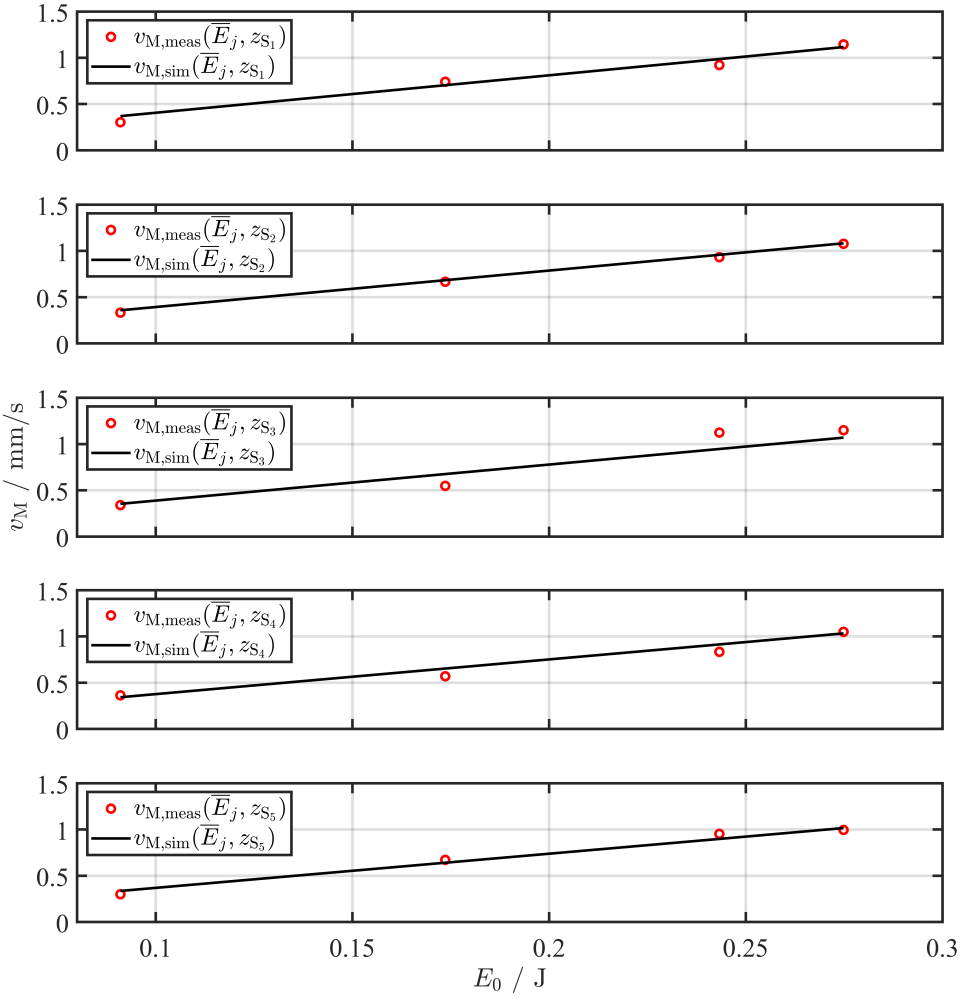

Figure 5.20.: Fit of the velocity data $v_{\mathrm{M,meas}}(\overline{E}_j, z_{\mathrm{S}_i})$ over the energy of the laser at the surface of the phantom $\overline{E}_j$. The experimental data are the red circles and their fit the black line.

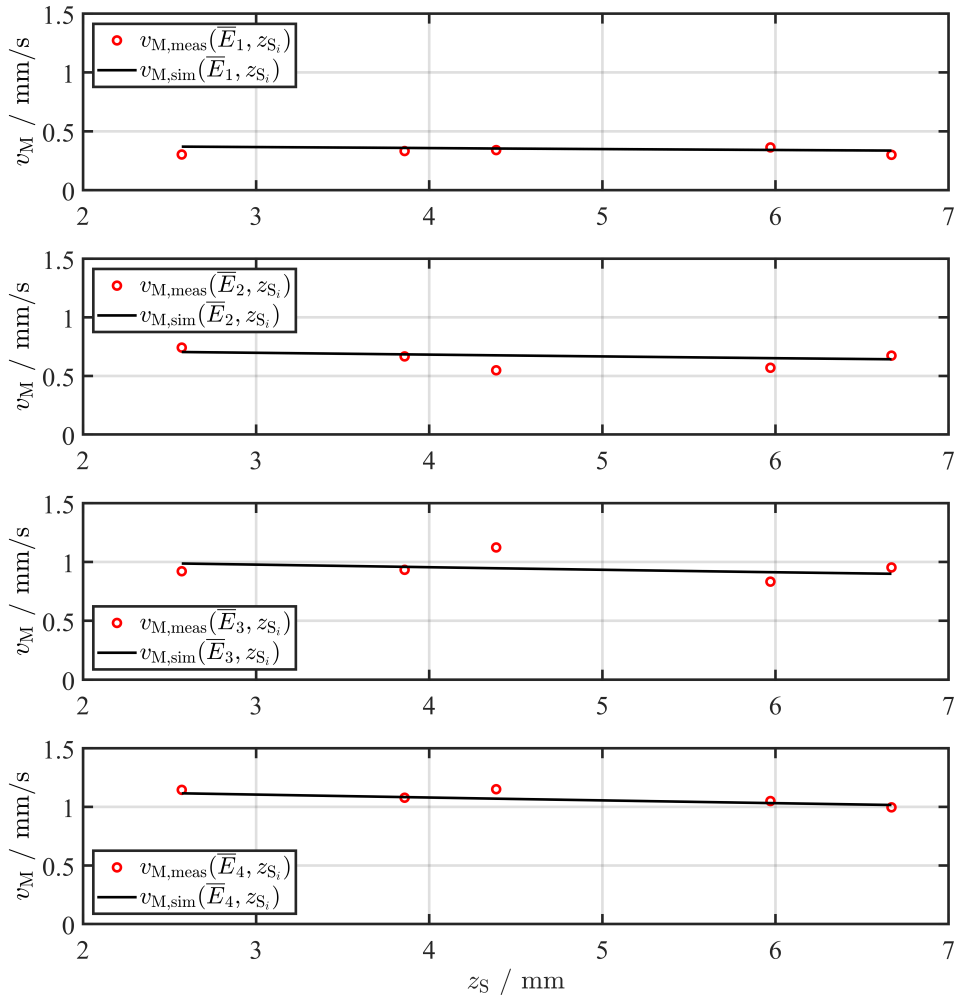

Figure 5.21.: Fit of the velocity data $v_{\mathrm{M,meas}}(\overline{E}_j, z_{\mathrm{S}_i})$ over the depth of the sphere z_{S_i}. The experimental data are the red circles and their fit the black line.

Deviations up to 10 mJ were found for the same energy configuration between the start and the end of the measurement-set.
The signals at different energy levels generated by the first sphere were firstly acquired. The same procedure was applied to the successive spheres. Therefore, the energy level $\overline{E}_j$ could change of 10 mJ between the acquisition of the signals generated by different spheres.

The excitation laser beam has a Gaussian profile. The profile of the laser is not perfect. For the measurements and for the model, it was assumed that the center of the sphere was aligned to the center of the exciting laser beam.
This condition is in practice difficult to achieve. It could happen that the spheres were not equally illuminated. This led to errors in the estimation of the energy absorbed by the sphere.
Using a flat-top laser beam instead of a Gaussian one would improve this aspect.

Errors in the estimation of the laser fluence can derive also from the beam expanding optics and the model used for the estimation of v_{M}.
If the beam expander is not perfectly adjusted, the value of the radius of the pulsed laser r_{PL} changes, leading also to errors in the computation of the laser fluence.
The model used does not consider the increase of fluence under the surface; this can also lead to inaccuracy of the results.

Another setup feature that may have an influence on the results of the fit is related to the alignment of the DLDV-laser beam.
If the DLDV is not perfectly oriented in the direction of the vibration, only a component of the amplitude of the signal is acquired.
Within 8° angle between the directions of the vibrations and of the laser beam of the DLDV, the error of the amplitude is $< 1\%$.

Moreover, the simulation assumes that the velocity peak is measured with the DLDV exactly aligned to the position on the surface corresponding to the middle of the sphere. Deviation from this position could also influence the acquired amplitude.

Regarding the signal acquisition, the synchronization of the DLDV signal and the pulse signals is achieved by using the Q-switch signal of the pulsed laser as a trigger. The delay between the Q-switch and laser-shot varies in the range of $40-80$ ns. The DLDV signals used for the averaging are not perfectly synchronized; this could lead to an attenuation of the velocity peak.

Additional uncertainties could derive from the algorithm used to denoise the signals.

Other contributions to the deviation between experimental data and fit come from the estimation of the geometrical, thermal and acoustic parameters.
The estimation of the geometrical parameter is performed with a caliper gauge.
The silicone phantom is soft and the measurement with the caliper gauge is affected by the pressure applied by the operator. The estimation of the thermal properties is also affected by uncertainties typical of the technologies used to compute them.

The method to determine the acoustic properties is based on the same setup for the PA measurement with LDV. As such, the parameters obtained are also affected by the instability of the excitation laser, of its alignment problematic and of the alignment of LDV.

Furthermore, the properties of the silicone rubber vary over time [221]. The estimated parameters could have changed between the day of the estimation and the day of the actual measurement of the phantom with the DLDV.

Since the model used for the fit is not linear, every little deviation from the nominal value of a parameter generates great deviations.

5.4.2. Discussion

The PAI measurements on the silicone rubber phantom with inclusions performed with the DLVD show the feasibility of LDVy to detect spherical inclusions at different depths: the detected patterns correspond to the expected signals according to the theory.

According to the model of the theory, the detection range for a sphere with a radius R_S can be estimated by verifying the condition of equation 5.39. The maximum of the displacement signal $s_\mathrm{M,meas}$ calculated with equation5.26 should be greater than the displacement resolution of the IR-LDV in the experiments $s_\mathrm{RL,meas}$ as defined in equation 5.39

$$s_\mathrm{RL,meas} < s_\mathrm{M,meas} = \frac{R_\mathrm{S}^2}{Z_\mathrm{sil} \cdot v_\mathrm{s,sil}} \frac{1}{2r_\mathrm{D}} \Gamma_\mathrm{sil} \mu_\mathrm{a,sil} F_0 e^{-\mu_\mathrm{eff,sil} z_\mathrm{S}} e^{-\overline{\mu}_\mathrm{att} r_\mathrm{D}}, \tag{5.60}$$

where $v_\mathrm{s,sil} = 966$ m/s, $Z_\mathrm{sil} = 1.07$ MRayl, $\Gamma_\mathrm{sil} = 0.49$ and $\overline{\mu}_\mathrm{att} = 0.051$ Np/cm were experimentally determined. The optical parameters $\mu_\mathrm{a,sil}$ and $\mu_\mathrm{eff,sil}$ resulted from the parameter identification are $\mu_\mathrm{a,sil} = 0.3865$ cm^{-1} and $\mu_\mathrm{eff,sil} = 0.4597$ cm^{-1}. The resolution of the IR-LDV for the experiments $s_\mathrm{RL,meas}$ is

$$s_\mathrm{RL,meas} = s'_\mathrm{RL,sil} \sqrt{\frac{B}{N}} = 64.30 \text{ pm}. \tag{5.61}$$

where the bandwidth B is 3 MHz, the number of averages N is 128 and the displacement resolution limit of the silicone rubber $s'_\mathrm{RL,sil} = 0.42$ pm/$\sqrt{\text{Hz}}$ was determined experimentally. The value of fluence at the surface $F_0 \approx 715$ J/m^2 used in the experiments is chosen.

Figure 5.22(a) shows the detection range for the silicone spheres in the tissue mimicking phantom with radius $R_\mathrm{S} = 2.5$ mm according to equation 5.60 in function of the depth z_S and the distance from the detector r_D. The green area identifies where the sphere is detectable and the red area where a detection is not possible. The detectable area is delimited by the depth $z_\mathrm{S} \approx 11.97$ cm and $r_\mathrm{D} \approx 19.94$ cm.

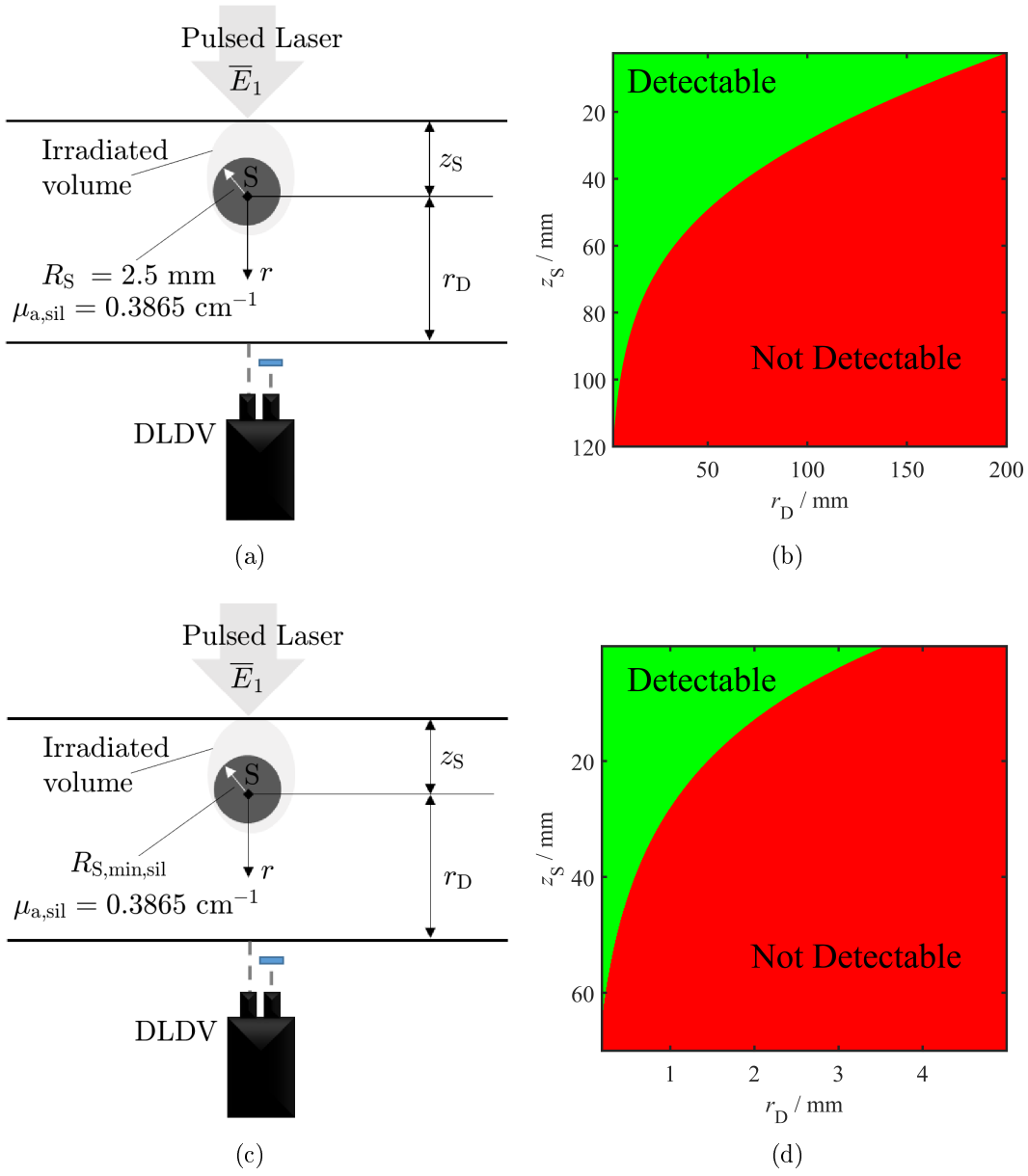

Figure 5.22.: Schematic of the setup for the detection range simulation of the silicone rubber spheres with radius $R_S = 2.5$ mm (a) and its detection range (b). Schematic of the setup for the detection range simulation of the silicone rubber spheres with radius $R_S = R_{S,min,sil} = 192$ µm (c) and its detection range (d). The displacement resolution of the experiments $s_{RL,meas} = 64.30$ pm is considered. Note that the axes have a different scale.

The spheres of the phantom of the experiment are all located in the detectable range of Fig. 5.22(a) and, therefore, the experiments agree with the model.
However, it has to be mentioned that, for the depths z_S lower than 1 mm, the estimation of the fluence according to equation 5.12 should be corrected with more accurate models [197]. Moreover, for large values of the parameter r_D, as the ones at the border of the detection range in Fig. 5.22(a), the assumption of estimating the acoustic attenuation as in equations 5.15 and 5.16 may lead to not negligible errors. In addition, reflections due to the spherical nature of the wave may influence the amplitude in near field. Here, these phenomena are not considered.
Since the model is validated, it can be extended to the case of spherical inclusions with different radius R_S. The radius of the silicone rubber spheres of the tissue mimicking phantom is $R_S = 2.5$ mm. According to equations 5.27 and 5.28 with a bandwidth $B = 3$ MHz, smaller spheres can be detected. The radius of the minimal detectable sphere in silicone rubber $R_{S,min,sil}$ for the condition of the experiments can be calculated according to equations 5.28 and 5.38 and it resulted in $R_{S,min,sil} = 192$ µm by considering a relative bandwidth $B_{rel} = 1.5$, the maximal frequency of the bandwidth $f_H = 3$ MHz and the sound velocity of the silicone rubber used $v_s = v_{s,sil} = 996$ m/s which was experimentally estimated. Fig. 5.22(b) shows the detection range for a sphere with the minimal detectable radius for silicone rubber $R_{S,min,sil} = 192$ µm. The detection range (green area) reduces in respect to the one of the sphere with $R_S = 2.5$ mm. In particular the maximal detection depth is $z_S \approx 64$ mm and the maximal distance from the detector $r_D \approx 3.6$ mm.

It must be noticed that, the displacement resolution limit on the skin measured with the DLDV $s'_{RL,skin} = 2.8\ \text{pm}/\sqrt{\text{Hz}}$ is worse than the one of the silicone rubber $s'_{RL,sil} = 0.42\ \text{pm}/\sqrt{\text{Hz}}$.
However, it is possible to obtain lower values of $s'_{RL,skin}$ with zinc-oxide cream, white eyeshadow or retro-reflective tape (see Subsection 5.5.2).

In the Section 5.5, the limits of commercial LDVs for the dection of tumors in breast tissue are analyzed and compared to commercial US detectors.

5.5. LDV for PAI Measurements in Tissue

In the previous sections the capability to detect photoacoustic signals with LDV in tissue mimicking phantoms is proved.

In particular, the LDV measurements present the characteristic patterns of the photoacoustic signals according to the theory (Section 5.3) and the model presented in Sections 5.1 and 5.2 was validated (Section 5.4).

In this paragraph, the limits of a commercial LDV for the detection of tumors in breast or soft tissue are estimated (Subsection 5.5.1) and discussed (Subsection 5.5.2) by extending the validated model to the case of breast and soft tissue.
The metrological characteristics of the OFV-5000 Xtra Laser Doppler vibrometer with the velocity decoder VX-09 (Polytec GmbH) are considered.
Subsection 5.5.3 presents a comparison between commercial LDV and classical US transducers employed in PAI.

5.5.1. Limits of LDV for PAI Measurements in Tissue

In this subsection, the limits of PAI in tissue performed with commercial LDV are theoretically determined.

The detection condition of PAI signals with LDV are already explained in the Subsection 5.2.1.
For this analysis, the metrological characteristics of the OFV-5000 Xtra Laser Doppler vibrometer VX-09 (Polytec GmbH) are chosen [207].
The OFV-5000 Xtra Laser Vibrometer with the velocity decoder VX-09 performs measurements with a bandwidth 0.5 Hz – 2.5 MHz and a displacement resolution limit $s'_{\mathrm{RL}} = 5.09\ \mathrm{fm}/\sqrt{\mathrm{Hz}}$ (see equations 5.36 and 5.40).

According to Section 5.2.1, the minimal detectable radius $R_{\mathrm{S,min}}$ for a necessary relative bandwidth $B_{\mathrm{rel}} = 1.5$ results in 350 µm for breast tissue and 357 µm for soft tissue.
With a relative bandwidth $B_{\mathrm{rel}} = 0.75$, the minimal detectable radius $R_{\mathrm{S,min}}$ decreases to 275 µm for breast tissue and to 281 µm for soft tissue.

The maximal amplitude s_{M} (equation 5.26) of the photoacoustic displacement signal generated by an irradiated sphere with the minimal detectable radius $R_{\mathrm{S,min}}$ is calculated and compared to the displacement resolution limit $s_{\mathrm{RL}}(B)$ of commercial LDVs as in equation 5.39.

The value of the maximal displacement amplitude s_{M} is evaluated in dependence of the depth of the sphere z_{S} and distance between the sphere and the measuring point r_{D} (see Figure 5.23(a)). The detection range of the sphere with radius $R_{\mathrm{S,min}}$ is defined for the values of the depth z_{S} and distance of the detection point r_{D} where the equation 5.39 is satisfied, i.e. the amplitude s_{M} is greater than the resolution limit of the LDV at its bandwidth B, $s_{\mathrm{RL}}(B) = s_{\mathrm{RL}}(2.5\mathrm{MHz}) = 8$ pm.

To compute the maximal displacement amplitude s_M of equation 5.26, the typical parameters for breast tissue are required.
The value of the effective optical attenuation depth $\mu_{eff} = 1.2$ cm^{-1} at the wavelength of the pulse laser $\lambda = 1064$ nm is taken from Oraevsky and Karabutov [195]. The sound velocity and the impedance for breast tissue are $v_s = 1510$ m/s and $Z = 1.54$ MRayl, respectively. For soft tissue the sound velocity and the impedance are $v_s = 1540$m/s and $Z = 1.63$ MRayl [193]. The Grüneisen parameter Γ for breast tissue at 37°C varies in the range $0.2 - 0.5$ [205, p. 423].

The greater the blood percentage in a tumor is, the greater is the absorption coefficient μ_a. Typical values of the absorption coefficient μ_a for normal breast vary in the range $0.03 - 0.05$ cm^{-1} at 1064 nm [225]; the optical absorption of a tumor is then greater.

To test the lower limit of LDV for PAI, the Grüneisen parameter $\Gamma = 0.2$ and the absorption coefficient $\mu_a = 0.06$ cm^{-1} are chosen.

The acoustic attenuation, $\overline{\mu}_{att}$, is calculated with the acoustic attenuation coefficient $\alpha_0 = 0.75$ dB cm^{-1}MHz^{-1}, which is typical for breast tissue. For soft tissue α_0 is 0.54 dB cm^{-1}MHz^{-1}.

Regarding the laser excitation, a pulsed laser with a wavelength $\lambda = 1064$ nm is chosen. The maximal allowed fluence according to the laser safety norm [224] at this wavelength for application in human body is $F_0 = 1000$ J/m^2.

The analysis is valid not only for the configuration in transmission, but also for the configuration with the detector positioned on the side with respect to the laser excitation. For the measurements in reflection configuration the analysis is valid by considering $r_D = z_S$.

Figure 5.23 shows for which combination of detection distance r_D and depth of the sphere z_S, a commercial LDV can detect an absorbing spherical object with a radius of $R_{S,min} = 350$ µm and optical absorption $\mu_a = 0.06$ cm^{-1}. The red range identifies where the vibration of the object is not detectable. The green range represents the combination of the detection distance r_D and depth of the sphere z_S where the displacement maximum s_M is greater than the resolution limit $s_{RL}(2.5\text{MHz})$ and thus, the small sphere is detectable. The range where s_M is greater than $s_{RL}(2.5\text{MHz})$ is delimited by the depth $z_S = 20.11$ mm if the laser spot is at the distance $r_D = R_{S,min}$. If the depth z_S is equal to $R_{S,min}$, the maximal detection distance r_D is 3.60 mm. Table 5.2 summarizes the results for breast and soft tissue for their respective minimal radius of the sphere $R_{S,min}$ obtained by considering a necessary relative bandwidth for the detection $B_{rel} = 1.5$.

For such a small detection distance r_D in combination with the acoustic attenuation $\overline{\mu}_{att}$ and the minimal detectable radius $R_{S,min}$, the effect of the acoustic attenuation delivers a deviation Δp_M lower than 2.39% (see equation 5.19), which is acceptable.
For the general case of soft tissue, the same calculation for the minimal detectable radius $R_{S,min} = 357$ µm, delivers a similar range where s_M is greater than

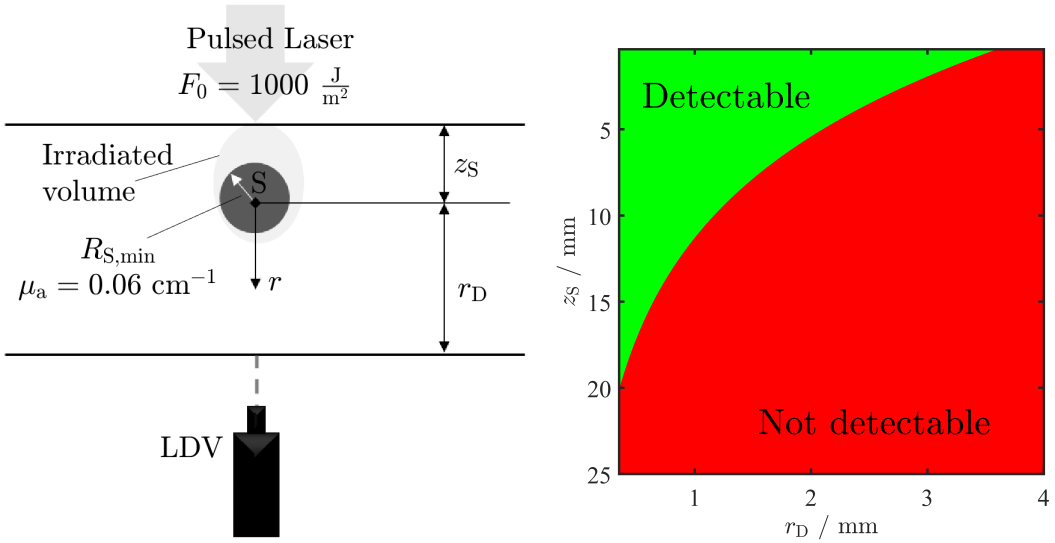

Figure 5.23.: Scheme of the setup (a). Detection range of a commercial LDV in breast tissue for a spherical object with radius $R_{S,min} = 350$ µm and absorption coefficient $\mu_a = 0.06\ \mathrm{cm}^{-1}$ (b). The green area represents the possible detection range, while the red area represents the range where the detection is not possible.

$s_{RL}(2.5\ \mathrm{MHz})$. The range is delimited in this case by the depth $z_S = 19.65$ mm and the detection distance $r_D = 3.51$ mm. The deviation Δp_M is here lower than 1.67%, which is also acceptable.
As mentioned before; a relative bandwidth B_{rel} of 0.75 provides sufficient resolution; therefore, the results obtained by considering the minimal radius $R_{S,min}$ for the relative bandwidth $B_{rel} = 0.75$ are shown in Table 5.3.
In this case the minimal radius $R_{S,min}$ is smaller for both breast and soft tissue and, therefore, the detection range gets smaller.

Table 5.2.: Detection limits of LDV with $B_{rel} = 1.5$.

Type of tissue	breast	soft
$R_{S,min}$ / µm	350	357
z_S / mm	20.11	19.65
r_D / mm	3.60	3.51
Δp_M	2.39%	1.67%

Table 5.3.: Detection limits of LDV with $B_{rel} = 0.75$.

Type of tissue	breast	soft
$R_{S,min}$ / µm	275	281
z_S / mm	18.10	17.65
r_D / mm	2.62	2.21
Δp_M	1.9%	1.33%

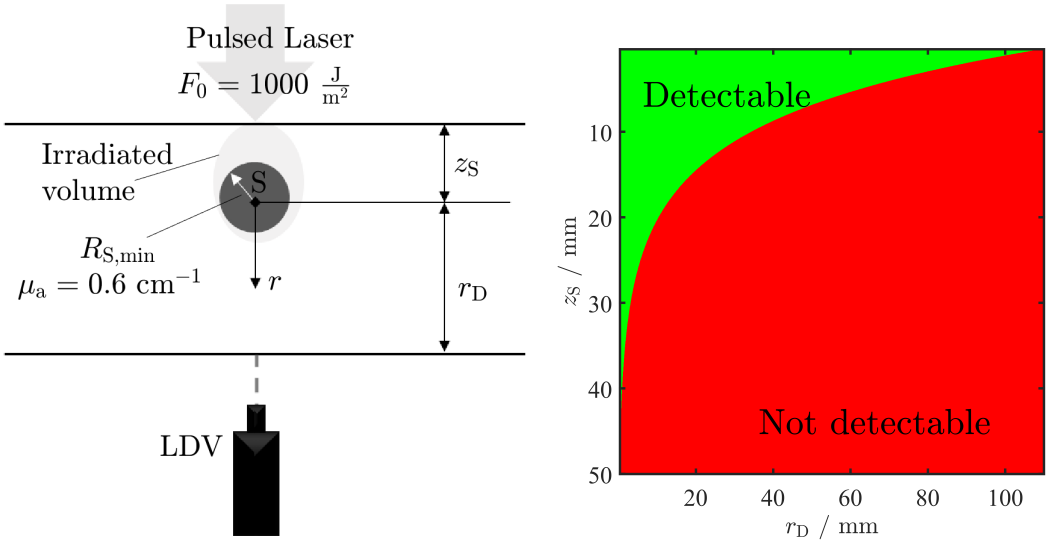

Figure 5.24.: Scheme of the setup (a). Detection range of a commercial LDV in breast tissue for a spherical object with radius $R_{\mathrm{S,min}} = 350$ µm and absorption coefficient $\mu_\mathrm{a} = 0.6\ \mathrm{cm}^{-1}$ without accounting for the sound attenuation as in [195] (b). The green area represents the possible detection range, while the red area represents the range where the detection is not possible.

It has to be noticed that, for depths z_S lower than 1 mm, the estimation of the fluence according to equation 5.12 should be corrected with more accurate models [197]. Moreover, reflections due to the spherical nature of the wave may influence the amplitude in near field. Here, these phenomena are not considered.
Oraevsky and Karabutov [195] carried out the analysis of the maximal detection depth for a tumor with different sizes performed with a PZT-5 piezoelectric-sensor. For the analysis, the authors used an absorption coefficient $\mu_\mathrm{a} = 0.6\ \mathrm{cm}^{-1}$ and the Grüneisen parameter[g] $\Gamma = 0.58$; the acoustic attenuation is not considered. To perform a comparison with the results obtained by Oraevsky and Karabutov [195] for the PZT-5, the maximum amplitude of the displacement signal s_M was calculated once again with the parameters and the conditions used in [195].
Figure 5.24 presents the detection range for the minimum detectable radius $R_{\mathrm{S,min}} = 350$ µm in breast tissue for the commercial LDV. The range is calculated with the parameters of [195] and without the term accounting for the sound

[g] In [195] the coefficient of volume expansion is $\beta = 10^{-3}\ \mathrm{K}^{-1}$ and the product of the density and the heat capacity at constant pressure is $\rho \cdot C_\mathrm{P} = 4 \cdot 10^6\ \mathrm{J/(K\ m^3)}$. From these values, the Grüneisen parameter Γ results in 0.58.

attenuation. The range of detection is delimited by a detection distance r_{D} of 10.92 cm and the depth of the sphere $z_{\mathrm{S}} = 4.82$ cm. For a radius $R_{\mathrm{S,min}} = 275$ µm; the limit of the range are $r_{\mathrm{D}} = 6.80$ cm and $z_{\mathrm{S}} = 4.62$ cm. Absorbing spheres with the same radius $R_{\mathrm{S,min}}$ can be detected at depths of $8-9$ cm with the PZT-5 sensor of Oraevsky and Karabutov [195].

In the next subsections, possible improvements of the limits of LDVy are discussed (Subsection 5.5.2) and a comparison of the resolution between US-contact sensors and LDVy is presented (Subsection 5.5.3).

5.5.2. Discussion

The detection limits of LDV for PAI measurements are presented in Table 5.2 and Table 5.3.
To summarize, tumors in the size of ≈ 350 µm can be reliably detected at depths $z_{\mathrm{S}} \leq 2$ cm for detection distances r_{D} up to $3-4$ mm.

An improvement of the performance of the LDV for PAI application can be achieved if the possibility of a detection bandwidth adapted to the dimension of the radius $B = B(R_{\mathrm{S}})$ is applicable.
According to equation 5.28 for objects with a greater radius than $R_{\mathrm{S,min}}$, the necessary detection bandwidth for a reliable detection is narrower.
With a narrower bandwidth the noise level is lower; the minimal detectable displacement that varies with the necessary bandwidth ($B_{\mathrm{rel}} = 1.5$), $s_{\mathrm{RL}}(B)$, is also lower.
In particular, equation 5.40 can be combined with equations 5.7, 5.8 and 5.28 leading to

$$s_{\mathrm{RL}}(B) = s'_{\mathrm{RL}}\sqrt{B} = s'_{\mathrm{RL}}\sqrt{0.33\frac{v_{\mathrm{s}}}{R_{\mathrm{S}}}\left(1+\frac{1}{2}B_{\mathrm{rel}}\right)}, \tag{5.62}$$

where

$$B = B(R_{\mathrm{S}}) = f_{\mathrm{H}}(R_{\mathrm{S}}) = f_{\mathrm{c,S}}\left(1+\frac{1}{2}B_{\mathrm{rel}}\right) = 0.33\frac{v_{\mathrm{s}}}{R_{\mathrm{S}}}\left(1+\frac{1}{2}B_{\mathrm{rel}}\right). \tag{5.63}$$

Figure 5.25 presents the resolution limit of the commercial vibrometer OFV-5000 Xtra Laser Vibrometer with the decoder VX-09 $s_{\mathrm{RL}}(2.5\ \mathrm{MHz})$ (red line), and its improvement by considering a detection bandwidth adapted to the radius R_{S} (equation 5.62) with the object dimension $s_{\mathrm{RL}}(B(R_{\mathrm{S}}))$ (blue dashed line) for the case the absorbing sphere in breast tissue.

Generally, a lower $s_{\mathrm{RL}}(B)$ is also reachable by considering the theoretical resolution of an IR-LDV, $s'_{\mathrm{RL,IR}}$. As mentioned in Chapter 3, the theoretical displacement resolution limit of LDV with an IR-technology is $s'_{\mathrm{RL,IR}} = 1\ \mathrm{fm}/\sqrt{\mathrm{Hz}}$, while the s'_{RL} for the commercial LDV considered is $5.09\ \mathrm{fm}/\sqrt{\mathrm{Hz}}$.
By considering the theoretical limit of the IR-technology, the detection range of

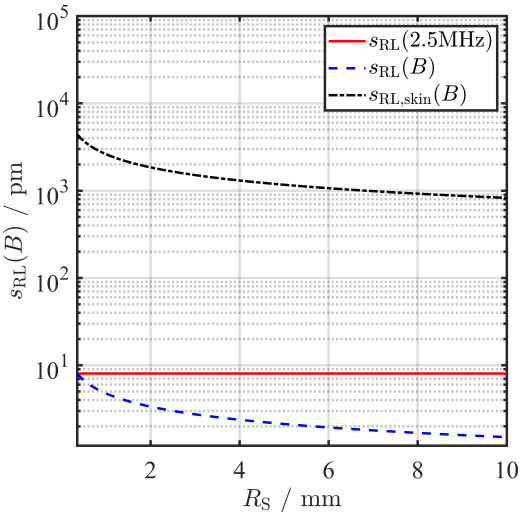

Figure 5.25.: Resolution limit for different LDV technologies as a function of the sphere dimension in soft tissue. The red continuous line is the resolution limit for a commercial LDV $s_{RL}(2.5\ MHz)$(Equation 5.40). The blue dashed line is the resolution that the commercial LDV would have with an adapted bandwidth dependent on the dimension of the object $B = B(R_S)$, $s_{RL}(B)$ (Equation 5.62). The black dashed-dot line is the resolution of the self-made differential IR-LDV on the skin with a variable bandwidth $B = B(R_S)$, $s_{RL,skin}(B)$.

the same object is greater. However, the resolution limit of $s'_{RL} = 5.09\ fm/\sqrt{Hz}$ and $s'_{RL,IR} = 1\ fm/\sqrt{Hz}$ are realistic only if the target is a mirror ($\Psi = 1$).
As explained in Section 3.2, the resolution limit of signals measured directly on the skin is worse.
Figure 5.25 reports the displacement resolution limit on the skin for the self-made differential IR-LDV at variable bandwidth $B = B(R_S)$ (black dash-dot line), $s_{RL,skin}(B)$, to show the limit of the LDV technology on the bare skin. The value of the displacement resolution limit $s_{RL,skin}(B)$ is computed according to equation 5.62 by considering the resolution $s'_{RL,skin}$ of $2.8\ pm/\sqrt{Hz}$ instead of $s'_{RL} = 5.09\ fm/\sqrt{Hz}$. The minimal detectable displacement with $s'_{RL,skin}$ rises by a factor of $\approx 5 \cdot 10^2$ with respect to the resolution limit at variable bandwidth $s_{RL}(B)$ for the commercial LDV considered. As a consequence, the detection range of PAI signals with LDV in terms of r_D, z_S and optical absorption of the tumor, μ_a decreases.
However, the value of $s'_{RL,skin} = 2.8\ pm/\sqrt{Hz}$ is only an approximate value.
The reflection index of the skin may vary depending on the skin color, on the blood perfusion, on the hydration of the skin and other factors, and it can be increased with zinc-oxide cream or with white eye-shadow.

The use of retro-reflective tape would also increase the displacement resolution limit significantly but it may obstruct the laser excitation and the contact-less aspect of the technique fades slightly away.
Another possibility to enhance the measurement on the bare skin, is to increase the laser power of the IR-laser of the LDV.
In this thesis, measurements are carried out with a self-made differential IR-LDV (DLDV) that operates with a 10 mW laser beam power. According to the laser safety norm [224], a 10 mW laser beam power at $\lambda = 1550$ nm is classified in class I (eye and skin safe). By increasing the power of the IR-laser of the DLDV, the DLDV would be classified as class 3R. With a class 3R-laser measurements on the skin are also possible without injuries, only the eye-protection is needed.
To have comparable results to the ideal case, the signal to noise ratio SNR(B) could be increased by performing averaged measurements. By averaging N measurements, the uncorrelated noise power reduces by a factor N; the SNR(B) increases by a factor N and the $s_{\mathrm{RL,skin}}(B)$ decreases with a factor $1/\sqrt{N}$ (see equation 3.9).
However, the number of measurements averages N is not arbitrary on the skin; it has to be estimated according to the maximal permissible exposure (MPE) of the skin to the pulsed laser light [224].

5.5.3. Comparison with Contact Sensors

This section aims to analyze when it is reasonable to apply LDV for the detection of PAI signals. A comparison with contact sensors, like the piezo-sensors typically used for PAI measurements, is performed.

The minimal detectable pressure for piezo-electric transducers is limited by the thermal noise [195].
Typical values of the minimal detectable pressure, p_{RMS}, for piezo-sensors are reported in Oraevsky, Andreev, et al. [196] and Oraevsky and Karabutov [195].
The authors analyzed the sensitivity of different sensors based on piezoeletric materials.
Depending on the characteristic of the material it is possible to predict the minimal detectable pressure.
The sensor presented in Oraevsky, Andreev, et al. [196] is an example. It is made of PVDF (Polyvinylidenfluorid), it has an upper frequency $f_{\mathrm{H}} = 1.4$ MHz and the minimal detectable pressure results in 0.417 Pa.

Rhyne [226] characterizes ultrasonic transducers by taking into account the noise contribution of the medium, the detector and the pre-amplifier.
Winkler, Maslov, et al. [135] evaluated the pressure resolution or noise equivalent pressure (NEP) in Pa/$\sqrt{\mathrm{Hz}}$ for commercially available US-sensors according to [226]. The authors of reference [135] report the estimated noise equivalent pressure for typical broadband US-sensors.

The estimated NEP results in the range of $0.2 - 0.6$ mPa/$\sqrt{\text{Hz}}$. A similar NEP is obtained by Basiri-Esfahani, Armin, et al. [227]. In particular, the authors achieved a NEP of $8 - 300$ µPa at a range of frequencies from 1 kHz to 1 MHz.
Reference [135] presents a list of commercially available transducers for PAI together with their characteristics and performance.
To be able to compare the minimal detectable amplitude of LDV and piezo-sensors, I estimated the minimal detectable pressure p_{RMS} of the photoacoustic sensors by considering the NEP values reported in [135] as constant for the whole bandwidth of the sensor B

$$p_{\text{RMS}}(B) = \text{NEP} \cdot \sqrt{B}. \tag{5.64}$$

The velocity or displacement resolution of LDV should be expressed in terms of pressure resolution. By combining equation 5.20 and 5.35, the pressure resolution for a IR-LDV at the interface between skin and air is

$$p_{\text{RMS,IR}}(B) = \frac{Z \cdot v_{\text{RL}}(B)}{2}. \tag{5.65}$$

with $Z = 1.63$ MRayl or $Z = 1.54$ MRayl, typical values for soft and breast tissue, respectively.
For LDV sensors, f_{L} is usually ~ 0 Hz and, therefore, the bandwidth B is equal to the value of the measurement bandwidth f_{H}.
Equation 5.65 can be expressed in function of the bandwidth B and with equation 5.35 it results in

$$p_{\text{RMS,IR}}(B) = Z\pi s_{\text{RL,IR}}(B)\frac{f}{\sqrt{3}}. \tag{5.66}$$

An initial comparison between LDVs and US-sensors is presented in Figure 5.26. Figure 5.26 reports the theoretical resolution limit for a 1550 nm heterodyne interferometer at $B = 1$ Hz, $s_{\text{RL,IR}}(1\text{ Hz}) = 1$ fm, in terms of pressure $p_{\text{RMS,IR}}(1\text{Hz})$, together with the minimal detectable pressure of a typical broadband sensors with 0.4 mPa/$\sqrt{\text{Hz}}$ resolution both with a bandwidth of 1 Hz, $p_{\text{RMS,US}}(1\text{Hz})$.
By comparing the minimal detectable pressure with 1 Hz bandwidth of the broadband sensors (dashed line) and of the theoretical limit of the IR-interferometer (continuous line) it can be deduced that LDVs have better performance for frequencies lower than $f \approx 78$ kHz for soft tissue ($f \approx 83$ kHz for breast tissue).
Therefore, IR-LDVs have better performance for the detection of tumors with a radius of about $6 - 6.5$ mm according to equation 5.8.
Broadband ultrasound sensors have generally better performance than LDV at higher frequencies.
However, the sensors mentioned in [135] are liquid-coupled piezoelectric sensors and, as such, they have the advantage of an optimal impedance matching.

For the following commercial LDVs the values of the minimal detectable pressure $p_{\text{RMS,LDV}}$ were calculated according to equation 5.66 by using $s_{\text{RL}}(B)$ instead of $s_{\text{RL,IR}}(B)$ and with $f = B$:

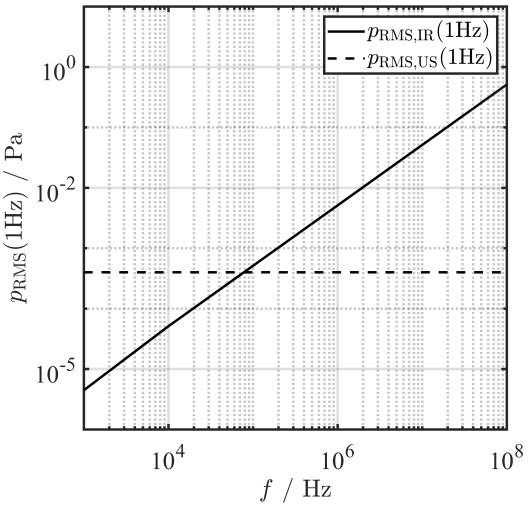

Figure 5.26.: Minimal detectable pressure for LDV and typical broadband sensor in soft tissue.

- for the OFV-2500-2 (Polytec), which has a resolution of 0.5 $\mu\mathrm{m/s}/\sqrt{\mathrm{Hz}}$ and can measure vibration from $f_{\mathrm{L}} \approx 0$ till $f_{\mathrm{H}} = \mathrm{MHz}$,

$$p_{\mathrm{RMS,LDV}} \approx 815 \text{ Pa}, \tag{5.67}$$

- for OFV-5000 Xtra Laser Vibrometer with the decoder VX-09 (Polytec), which has a typical resolution of 0.04 $\mu\mathrm{m/s}/\sqrt{\mathrm{Hz}}$ and a frequency range between $f_{\mathrm{L}} \approx 0$ and $f_{\mathrm{H}} = 2.5$ MHz,

$$p_{\mathrm{RMS,LDV}} \approx 60 \text{ Pa}. \tag{5.68}$$

Table 5.4 compares these minimal pressure values of $p_{\mathrm{RMS,LDV}}$ to minimal detectable pressure p_{RMS} of typical US-sensors based on the estimation of NEP of reference [135].

In particular, I considered a broadband sensor with NEP = 0.4 $\mathrm{mPa}/\sqrt{\mathrm{Hz}}$ and a central frequency $f_{\mathrm{c}} = 2.5$ MHz.
As stated, to acquire PA signals properly, a bandwidth of $B_{\mathrm{rel}} = 1.5$ in respect to the central frequency f_c is necessary. Commercial sensors with a bandwidth of $B_{\mathrm{rel}} = 0.75$ provide sufficient resolution.
Here, for the calculation of the minimal detectable pressure of the piezo-transducer, a $B_{\mathrm{rel}} = 0.75$ bandwidth is chosen.

Table 5.4 shows that commercially available LDVs are generally worse in terms of minimal detectable pressure as the piezo-transducer of a factor $\approx 10^2 - 10^3$. However, LDV covers also the lower range of frequency, which is important for

Table 5.4.: Resolution of different LDVs and US-sensors.

Technology $\mathbb{I}$	Sensor	$f_\mathrm{L} - f_\mathrm{H}$ / MHz	$p_{\mathrm{RMS},\mathbb{I}}$ / Pa
LDV	OFV-2500-2	$0 - 3$	815
LDV	VX-09	$0 - 2.5$	60
US	Broadband $f_\mathrm{c} = 2.5$MHz [135]	$1.6 - 3.4$	0.6
LDV	High frequency LDV [228]	$50 - 700$	$2.3 \cdot 10^4$
US	Kibero $f_\mathrm{c} = 200$ MHz [135]	$165 - 235$	17

enhanced sensitivity and contrast in the reconstructed image.
Moreover, because of the wider bandwidth, the possibility to detect objects with different sizes increases.
The ultrasonic frequency spectrum of PA signals has components from 20 kHz up to 200 MHz which can be divided in three main ranges [195].
The low range (20 kHz $-$ 2 MHz) includes the monitoring of blood vessels tumors and other tissues at a depth of up to 10 cm. The intermediate range ($1 - 20$ MHz) includes imaging at about 1 cm with a higher resolution in respect to the previous range. The high range ($1 - 200$ MHz) is for high resolution imaging of skin and and for cell microscopy.
The commercial LDV could represent a valid contact-less alternative to ultrasound detectors only for the first range. For the intermediate and high range a LDV for high frequencies could be analyzed as an alternative to the ultrasound sensors.
A LDV prototype has been developed at the Institute of Electrical Information Technology of the TU Clausthal [228]. In the frequency range $50 - 700$ MHz, it presents a displacement resolution of 0.5 pm/$\sqrt{\mathrm{Hz}}$. Its resolution in terms of $p_{\mathrm{RMS,LDV}}$ is reported in Table 5.4 together with the commercial PAI transducers for high frequencies from the company Kibero GmbH.
Usually, PAI transducers for high frequencies are focused ultrasound transducers. The PAI sensor from the company Kibero GmbH has a central frequency of 200 MHz with a relative bandwidth $B_\mathrm{rel} = 0.5$ [135]. The estimated NEP is 2 mPa/$\sqrt{\mathrm{Hz}}$.
From the comparison it emerges that also at high frequencies commercial contact sensors present a better resolution in comparison to the LDV systems. Despite this, the LDV technology takes advantages of the wider bandwidth for the detection of objects with different sizes.

In addition to the commercially available detectors, researchers have investigated several sensors exploiting different contact and non-contact techniques.
Dong, Sun, et al. [138] reported a summary of performances of different ultrasound detectors found in literature.
In particular, Hochreiner, Bauer-Marschallinger, et al. [110] designed an optical

fiber-based Mach-Zehnder interferometer. Its shot noise-limited sensitivity in terms of pressure[h] with a bandwidth B of 20 MHz is 275 Pa at the central frequency of the bandwidth for the tissue mimicking phantom developed by the authors[i].
Zhang and Beard [229] developed a miniature all-optical photoacoustic probe for endoscopic application with a Fabry-Perot ultrasound sensor for intravascular imaging application. The minimal detectable pressure at $B = 20$ MHz for a planar and a concave configuration of the sensor head is reported. For the planar configuration, it results in 1.55 kPa. The concave configuration reaches instead to a minimal detectable pressure of 8 Pa.
As mentioned in Section 3.2 the resolution limit of a IR-LDV is theoretically $s_{\mathrm{RL}}(1\ \mathrm{Hz}) = 1$ fm if all light is collected.
According to equation 5.66, the shot noise-limited sensitivity in terms of pressure[h] for the IR-LDV measured at $B = 20$ MHz is 250 Pa (125 Pa for the central frequency of the bandwidth), which is comparable with the shot noise limited sensitivity of the system realized by Hochreiner, Bauer-Marschallinger, et al. [110]. For the self-made differential IR vibrometer (DLDV) with $s_{\mathrm{RL}}(1\ \mathrm{Hz}) = 7.8$ fm, the shot noise-limited sensitivity in terms of pressure[h] at $B = 20$ MHz results in 1.95 kPa (975 Pa for the central frequency of the bandwidth).

[h] This value and the values is calculated with $Z = 1.54$ MRayls.
[i] The estimated displacement resolution of [110] at $B = 1$ Hz is ~ 1.3 fm.

6. Conclusions and Outlook

This thesis examines two relevant applications of LDV in the medical field.
In Chapter 4, laser Doppler vibrometry is employed for the acquisition of the vibrations generated by the heart itself for the detection of the cardiovascular parameter PR-time.
In Chapter 5, the feasibility of laser Doppler vibrometry for the acquisition of vibrations induced by the photoacoustic effect in the human body for the detection of tumors is investigated.

The **first scientific hypothesis** of this work is that the PR-time detected from LDV measurements on the thorax has an acceptable uncertainty for a realistic variety of measurement spot positions and angles of the incident laser beam that allow a reliable statement of the healthy condition of the patient.
Therefore, the influence of the setup features - measuring point position and laser beam orientation - on the typical pattern of the vibration signals, and consequently, on the PR-time extracted from the vibrations were investigated. The reliability of the detection of a healthy condition or CV diseases by means of the PR-time in VCG were also analyzed.
The main investigations were performed with the multipoint laser Doppler vibrometer MPV-800.

A model for the calculation of the uncertainty of the PR-time acquired from VCG-signals is presented. The uncertainty contributions related to the setup are quantified and considered in the model.
The model proposed is applicable for measurements where the measuring point might not be positioned precisely.
Moreover, the setup requires that the laser beam of the LDV is directed perpendicularly to the floor; this configuration is easy to adjust and, therefore, reproducible measurements can be performed.

The ranges of PR-time values acquired with LDV where it is possible to state with 95% certainty that a diagnosis is correct are identified.
Normal values of PR-time are included in the range 120 ms – 200 ms. For single value measurements with precise alignment the reliable range for the detection of the healthy condition is 146.4 ms – 173.6 ms. The detection of CV diseases is reliable for measured values lower than 93.6 ms and greater than 226.4 ms.
For mean value measurements with precise alignment the reliable range for the detection of the healthy condition is 126.6 ms – 193.4 ms. The detection of CV diseases is reliable for measured values lower than 113.4 ms and greater than

206.6 ms.
Therefore, for measured values included in the mentioned ranges, the detection of the PR-time and the relative diagnosis with the LDVy in non-laboratory conditions is reliable.
Therefore, the **first hypothesis is verified**: for a realistic variety of measurement spot positions and angles of the incident laser beam, the values included in the identified ranges allow for a reliable detection with LDVy of the PR-time and of the health condition of patients.

The application of LDV in clinical environments or in all the applications that require the contactless monitoring of cardiovascular parameters (see Chapter 1) could be very advantageous.
Currently, researches are focused on the realization of a miniaturized and low cost LDV [60] that will lead to a greater accessibility of the device.
Moreover, with the multipoint LDV the simultaneous recording of 48 sites on one subject or the monitoring of more subject at time with a working-distance up to 5 m is possible.
The combination of both aspects would lead to a very useful and flexible device for non-contact health measurements.

However, for daily clinical applications, this study should be reproduced with a larger statistical sample. The uncertainty model for the PR-time in VCG presented in this work could be applied to a greater cohort to obtain a statistically relevant value of the extended uncertainty.

This work not only shows the capability of the LDV measurements for the detection of the PR-time and of the health condition, but also offers a method for the investigation of the uncertainty contribution.
The method used in Section 4.3 could be employed for the investigation of the uncertainty contributions to other cardiovascular parameters detected with the LDV,.

The method proposed for the detection of the uncertainty could be extended to investigate the uncertainties in other cases such for other posture of the subject (standing or sitting) and for other paramaters.
In particular, the measurement with the multipoint vibrometer on the thorax presented in Section 4.3 could be used also for the analysis of the uncertainty resulting from the laser beam orientation and the measuring point position for the heart rate and the heart rate variability.
Similarly, the MPV-analysis could be extended to the uncertainty of other parameters obtainable from measurements on blood vessels, as already partly accomplished for the pressure on the carotid artery in Mignanelli and Rembe [230].
The estimation of the uncertainty of the measurement point and laser beam orientation for heart rate and heart rate variability could be very important not only for clinical applications or medical reasons.
The heart rate and the heart rate variability are related to physical and psycho-

logical stress factors. These parameters could be used to estimate the attention of the human in human-machine interactions [231]. Such applications require a tracking system since the subject is moving. Knowing the uncertainty depending on the measuring spot and on the laser beam orientation would allow more reliable statements related to the pieces of information extracted from the heart rate and heart rate variability.

An important remark comes out from the investigation of the tridimensional vibrations.
The measurements with the multipoint vibrometer open the possibility to detect the trajectory of the vibrations in different points.
The MPV allows to perform a complete analysis of the movement of the heart and to understand the cardiac activity by analyzing the vibrations.
In fact, the electrical activity of the heart triggers its mechanical activity. While the electrocardiogram measures the projection of the electrical activity of the heart at specific points from defined directions, the multipoint vibrometer can measure the mechanical activity of the heart at different points from different directions.
With the help of medical instrumentation such as an echocardiograph, it would be possible to select predefined anatomical positions; by pointing the lasers beams at these positions, the genesis of the vibrations can be investigated.
By combining these investigations to the current knowledge of VCG signals on the thorax (see Chapter 2) and the knowledge of cardiac mechanics obtained with accelerometers [128, 232], i.e. seismocardiography signals, it may open the possibility to perform a complete contactless ECG.
Moreover, the investigation of the 3D-vibration would open the possibility to estimate other medical parameters. Munck, Sørensen, et al. [232] suggest that by measuring the rotation motion of the ventricle and comparing it to echocardiographic measurements, other physiological parameters such as preload, afterload, and contractility could be estimated [233].

The second scientific hypothesis of this thesis is that under certain conditions the photoacoustic imaging measurements with LDV are feasible. The LDV as an optical non-contact method could overcome the limitation of the typical transducers used for PAI such as the narrow frequency bandwidth, the finite aperture size and the need of a coupling medium.
Moreover, by performing PAI contactless, there is no more interference between the excitation laser beam and the transducer when working in the reflection mode and the technique could be extended to application where usually the contact presents a problem.
In literature, several works present PAI measurements with LDV or other interferometric techniques. However, the detection range and the limits of the LDVy have not been analyzed yet.
I examined under which conditions the LDV can be deployed for the detection of small tumors.

In this thesis, the typical signals generated by the PA effect on absorbing spheres (i.e. tumors) are introduced and the feasibility to detect tumors in soft or breast tissue with LDV is analyzed theoretically and experimentally.

Experiments were carried out to prove the capability of LDV for PAI measurements. PAI measurements on a silicon phantom with spherical inclusions were performed with a self-made differential IR-LDV. The silicon phantom with spherical inclusions mimics the breast or soft tissue with tumors.

The capability of LDV to acquire PA signals reliably was proven: the acquired signals present patterns in agreement to the theoretical model. The model of the theory was validated with experiments in tissue mimicking phantoms.

A theoretical analysis with the validated model is performed to state under which conditions PAI measurements in tissue with a commercial LDV are feasible.
Additionally, a comparison with commercial US-sensors is performed.
The theoretical analysis shows that a commercial LDV with a typical bandwidth of 2.5 MHz is able to reliably detect tumors in soft or breast tissue with a radius up to ≈ 350 µm, if a necessary relative bandwidth of 150% of the central frequency is taken into consideration.
When a relative bandwidth of 75% is considered, the smallest detectable object has a radius of ≈ 280 µm.
The maximal detection depth varies depending on the fluence at the surface of the investigated object, on the acoustic, thermal and optical characteristics of the sphere and the tissue.
For the case of maximal allowed fluence at the surface and the minimal absorption value of the sphere (μ_a), the maximal detection depth, z_S, for the smallest detectable objects is ≈ 2 cm.
The maximal distance between the sphere and the detection point is $r_D \approx 3$ mm for a relative bandwidth of 150% of the central frequency. The values of z_S and r_D are slightly lower for a relative bandwidth of 75%.
For higher values of the optical absorption and Grüneisen parameter, the range of detection in terms of z_S and r_D of the minimal detectable object increases.
To summarize, **the analysis shows the theoretical feasibility of commercial LDVs for PAI detection**: a commercial LDV can detect tumors with a characteristic dimension down to ≈ 350 µm located at depth of ≈ 2 cm.

The detection capability of the LDV depends on its bandwidth and on its resolution limit. The resolution limit and the typical bandwidth of LDV were compared to the one of the commercially available contact sensors employed for PAI.
The comparison between commercially available contact sensors and commercially available LDVs shows that for frequencies lower than ≈ 83 kHz, the theoretical resolution limit of a IR-LDV is lower than the resolution limit of typical broadband sensors. As a consequence, LDV presents a better resolution for tumors with a radius greater than $6 - 6.5$ mm.

Ultrasound sensors present a better resolution for smaller tumors.
However, because of its larger detection bandwidth, the LDV can detect objects of different sizes properly. The resolution of commercial LDVs can be improved by using a bandwidth adapted to the dimension of the tumor expected. To conclude, the LDV can be employed for PAI applications reliably and it can improve and extend the application of the PAI technique where contact is unfeasible.

In this thesis, the feasibility of LDV for PAI measurements has been demonstrated; the final step of reconstruction of the photoacoustic image will be addressed to future works.
Future works aim to perform PAI measurements on tissue phantoms with the multipoint laser Doppler vibrometer.
The multipoint vibrometer allows for a simultaneous detection of the vibrations at several points, and, therefore, a photoacoustic image can be reconstructed. Photoacoustic imaging measurements with the multipoint vibrometer together with a proper reconstruction algorithm present a contactless method to measure tumors in breast or soft tissue.

A. Influence of Disturbances on Detection of $P_{\mathrm{V}}R_{\mathrm{V}}$-Interval

The vibrations of the thorax result from the interference of vibrations generated by different sources like the heart, blood vessels, lungs and so forth.
The physiology of the human body like breath and blood flow in vessels, involuntary movements and the setup of the measurement such as laser beam orientation, measuring spot position, vibration on the building and measurement instrument used influence the VCG measurements.
Therefore, the detected parameters such as the $P_{\mathrm{V}}R_{\mathrm{V}}$-interval are affected by uncertainties.

Only the vibrations generated by the heart deliver information of the PR-interval. The other vibrations are considered as disturbances and they can be reduced by filtering the signals.
For the detection of the $P_{\mathrm{V}}R_{\mathrm{V}}$-time, the vibrations generated by the respiration and high-frequency noise are considered as disturbances and must be removed. Both components may lead to delays and affect the value of the $P_{\mathrm{V}}R_{\mathrm{V}}$-time. The filtering of the disturbances may reduce these delays.

Different filtering techniques for the extraction/removal of the breathing/noise component from VCG signals are reported in literature for the acquisition on the carotid [83, 87, 133, 234] and for the acquisition on the chest [21, 24, 25, 34, 78, 86, 184, 235]. The filters used for the VCG signals on the thorax are interesting for this thesis. Most of them are aimed to the detection of the heart rate, heart rate variability and respiration period.

Morbiducci, Scalise, et al. [21] perfomed the filtering of VCG signals with an eight-order Butterworth low pass filter with a 100 Hz cut-off frequency.

In Mignanelli, Bauer, et al. [184], the authors adopted a band-pass (0.6 Hz-100 Hz) zero padding filter in the frequency domain to remove both respiration and high frequency components. The filtered signal is obtained by performing the inverse fast Fourier transform of the resulting spectrum.

In De Melis, Morbiducci, et al. [78] and Scalise, Morbiducci, et al. [235], the authors suggest the decomposition of the Daubechies 7 wavelet [209] to extract the heart rate, heart period and the respiration component. Relevant components of the signal are identified up to 7.81 Hz. The heartbeat components were identified in the sub-bands obtained from the wavelet decomposition level d9 and d10 with a sample frequency of 1 kHz. These levels correspond to the frequency ranges

$0.98 - 1.95$ Hz and $0.49 - 0.98$ Hz, respectively. The breathing component was identified in the sub-band d11, $0.25 - 0.49$ Hz.

The authors of [24, 25] proposed the wavelet Daubechies 8 [209] with details 3 for the extraction of the heart-rate and the wavelet rbio 2.2 with detail 6 for the extraction of the respiration period in preterm infants[a].

Luik and Kroschel [86] proposed another approach aimed to identify atrial fibrillation. The authors proposed a linear-phase, band-pass filter with an impulse response, a lower cut-off frequency of 0.582 Hz and an upper cut-off frequency of 48 Hz. The sampling frequency was 120 Hz.

In Kroschel and Metzler [34], the authors firstly suppressed the frequency component at 0 Hz, then extracted the respiration component of the signal with a type 2 Chebychev low-pass filter of order 6. The cut-off frequency was 0.75 Hz and the attenuation in the stopband was 60 dB. The sampling frequency was decimated to 120 Hz. However, the filter presents phase distortions and the time-related properties are changed by the filter.

The combined effect of the algorithm employed for the detection of P_VR_V-interval and the filtering technique selected for the post-processing can lead to different values of the resulting P_VR_V-interval. Therefore, an analysis of the effect of the disturbance on the detection of the P_VR_V-time is presented. The effect of the reduction of the disturbance with filters is also investigated. The filters employed are based on the one found in the literature.

This Appendix presents the analysis influence of the disturbances and their filtering on the detection of the P_VR_V-interval. The following paragraphs shows the setup and the material and methods used for the investigation, and the results obtained.

Setup, Material and Methods This paragraph presents the measurements for the investigation of the effect of the high-frequency and low frequency disturbances on the detection of the PR-time in VCG.
The aim is to compare the P_VR_V-obtained from a signal in ideal conditions to the one obtained from a signal affect by disturbances after filtering. In this way, the effect of the disturbances enhanced by the filtering on the detection of the P_VR_V-time can be quantified.

The analysis is performed starting from the acquisition of a reference signal on one subject holding his breath.
The breathing and noise components were generated and added to the reference signal with the aim to create an artificial signal affected by disturbances. The artificial signal is then filtered with different techniques.
The P_VR_V-time of the reference signal, the signal with disturbances and the filtered signals are compared to analyze the influence of the disturbance and their filtering.

[a] sample frequency 1 kHz.

The measurement setup for the acquisitions is presented in Figure A.1(a).
The vibrometer OFV-303 (Polytec) - LDV_1 - is pointed perpendicularly to the floor.
The signals were acquired with the acquisition board Powerlab 4/26 (ADInstrument). The ideal reference signal, $v_{\mathrm{ref}}(t)$, was generated by acquiring data with the LDV_1 (see Figure A.1(a)) from a subject holding his breath and by removing high frequency noise components and low frequency movements. Based on the reference signal, an artificial signal, $v_{\mathrm{art}}(t)$, was generated by adding disturbances such as breathing, $v_{\mathrm{breath}}(t)$, and high frequency noise component, $v_{\mathrm{noise}}(t)$, to the reference signal.
The artificial signal v_{art} can be written as

$$v_{\mathrm{art}}(t) = v_{\mathrm{ref}}(t) + v_{\mathrm{breath}}(t) + v_{\mathrm{noise}}(t). \tag{A.1}$$

The breathing component $v_{\mathrm{breath}}(t)$ is obtained from a simultaneous LDV_1 and respiratory-belt measurements, as shown in Figure A.1(a).
The piezo-respiratory belt is the MLT1132 Piezo Respiratory Belt Transducer from ADInstrument. The respiratory belt was positioned at the same height as the measuring point on the thorax above the atrium.
The respiratory belt delivers a voltage signal proportional to the displacement

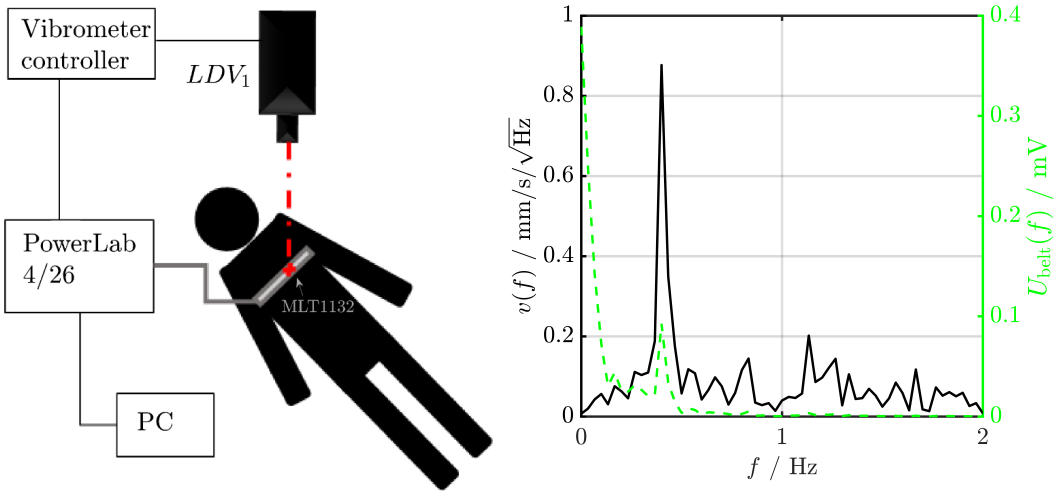

(a) (b)

Figure A.1.: Measurement setup used for the detection of the breathing component (a). Portion of the amplitude spectrum of $U_{\mathrm{belt}}(t)$, $U_{\mathrm{belt}}(f)$ (dashed green line) and of the simultaneous signal acquired with LDV_1 (continuous black line), $v(f)$ (b).

$U_{\mathrm{belt}}(t)$ but the resolution is lower compared to the high resolution of the vibrometer. Therefore, the measurement with the respiratory-belt was used only to identify the frequency components of the breath.
For this measurement, the breathing component was identified at the frequency $f = 0.4$ Hz. The LDV_1 was pointed on the respiratory belt direct above the atrium.
In this way, the cardiac signal is attenuated and only the vibration resulting from the respiration and additional noise are present.
The amplitude of the spectrum of the time signal $U_{\mathrm{belt}}(t)$ and of the simultaneous time signal acquired with LDV_1 $v(t)$ are depicted in Figure A.1(b). Successively, the velocity signal $v(t)$ was low-pass filtered with a cut-off frequency of 0.7 Hz originating the signal $v_{\mathrm{breath}}(t)$.

The high frequency noise $v_{\mathrm{noise}}(t)$ is obtained from a measurement performed with the LDV_1 impinging on retro-reflective tape on the floor. The signal was high-pass filtered with a cut-off frequency of 100 Hz.

A 10 s segment of the reference signal $v_{\mathrm{ref}}(t)$, of the disturbances - $v_{\mathrm{breath}}(t)$ and $v_{\mathrm{noise}}(t)$ - and of the artificial signal $v_{\mathrm{art}}(t)$ are presented in Figure A.2.

To summarize, the analysis of the disturbance was performed starting from the acquisition of $v_{\mathrm{ref}}(t)$ on one subject holding his breath for different intervals. The total acquisition time is 120 ms. The breathing and noise component were generated and added to $v_{\mathrm{ref}}(t)$. The signal v_{art} is generated as described in equation A.1.
The artificial signal was filtered with different techniques F_i originating the filtered signals $v_{\mathrm{F}_i}(t)$. The subscript $i = 1, 2, 3$ indicates the employed filtering techniques. Based on the filters found in the literature, the following filters F_i were tested:

- F_1: the low frequency components $(0 - 0.49$ Hz) are removed according to [235] with the wavelet Daubechies 7^{a}. The high frequency noise is filtered with a eight-order Butterworth low-pass filter with 100 Hz cut-off frequency (using the command *filter.m* in Matlab®)

- F_2: the low frequency components $(0 - 0.49$ Hz) are removed according to [235] with the wavelet Daubechies 7^{a}. The high frequency noise is removed with a zero-padding low-pass filter in frequency domain with a 100 Hz cut-off frequency

- F_3: the high frequency noise and the respiration components are removed with a zero padding band-pass filter in frequency domain 0.6 Hz-100 Hz.

Figure A.3 present the reference signals v_{ref} and the filtered signals v_{F_i}.

The goal of this section is the analysis of the effect of the disturbances and the effect of the adopted filtering technique on the extraction of the $P_{\mathrm{V}}R_{\mathrm{V}}$-time.
For this purpose, a comparison between the $P_{\mathrm{V}}R_{\mathrm{V}}$-time obtained from $v_{\mathrm{ref}}(t)$, $v_{\mathrm{art}}(t)$

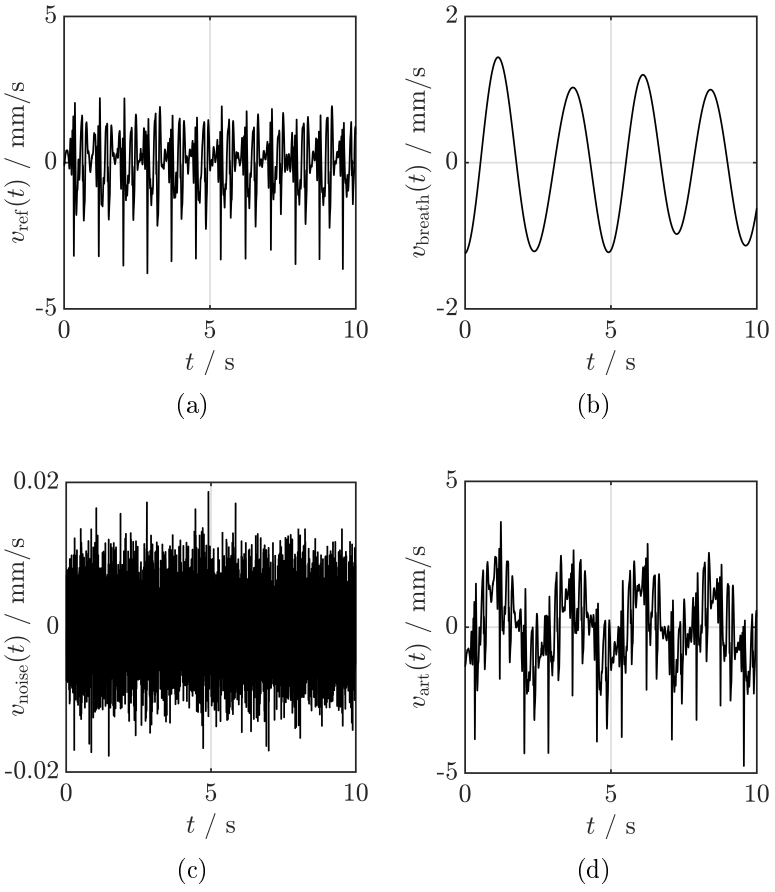

Figure A.2.: Ten seconds time segments of the signals used for the computation of the artificial signal, $v_{\mathrm{art}}(t)$: reference signal $v_{\mathrm{ref}}(t)$ (a), breathing component $v_{\mathrm{breath}}(t)$ (b), noise component $v_{\mathrm{noise}}(t)$ (c) and artificial signal, $v_{\mathrm{art}}(t)$ (d).

and $v_{\mathrm{F}_i}(t)$ is performed.
The $P_{\mathrm{V}}R_{\mathrm{V}}$-time of the reference signal, $P_{\mathrm{V}}R_{\mathrm{Vref}}$, was calculated as described in equation 4.2.
The $P_{\mathrm{V}}R_{\mathrm{V}}$-time of the signal $v_{\mathrm{art}}(t)$ is called $P_{\mathrm{V}}R_{\mathrm{Vart}}$ and the one of the signal $v_{\mathrm{F}_i}(t)$ is called $P_{\mathrm{V}}R_{\mathrm{VF}_i}$. These $P_{\mathrm{V}}R_{\mathrm{V}}$-time values are calculated according to equation 4.2, too.
The difference between $P_{\mathrm{V}}R_{\mathrm{Vref}}$ and $P_{\mathrm{V}}R_{\mathrm{Vart}}$ and the difference between $P_{\mathrm{V}}R_{\mathrm{Vref}}$ and $P_{\mathrm{V}}R_{\mathrm{VF}_i}$ are computed as

$$\Delta P_{\mathrm{V}}R_{\mathrm{Vart}} = P_{\mathrm{V}}R_{\mathrm{Vref}} - P_{\mathrm{V}}R_{\mathrm{Vart}} \tag{A.2}$$

$$\Delta P_{\mathrm{V}}R_{\mathrm{VF}_i} = P_{\mathrm{V}}R_{\mathrm{Vref}} - P_{\mathrm{V}}R_{\mathrm{VF}_i}, \tag{A.3}$$

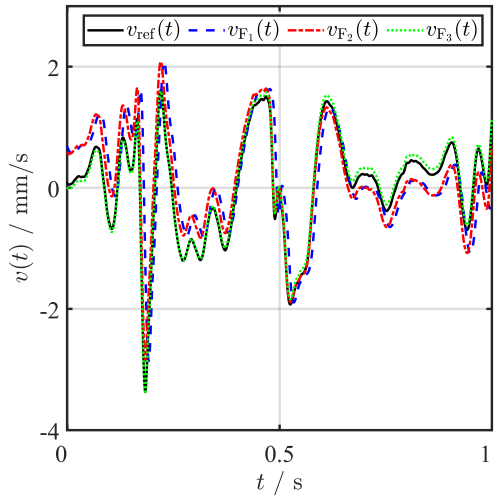

Figure A.3.: Time segment of the reference signal v_{ref} and the filtered signals v_{F_i}.

respectively. The maximum deviation $\max|\Delta P_{\mathrm{V}}R_{\mathrm{V}j}|$, the mean value $\overline{\Delta P_{\mathrm{V}}R_{\mathrm{V}j}}$ and the standard deviation sd_i of $\Delta P_{\mathrm{V}}R_{\mathrm{V\,art}}$ and $\Delta P_{\mathrm{V}}R_{\mathrm{VF}_i}$ are selected as figure of merit for the evaluation of the effect of the disturbances and their filtering, where $j = \mathrm{art}, \mathrm{F}_i$
The results are shown in the next paragraph.

Results and Discussion The algorithm for the detection of the $P_{\mathrm{V}}R_{\mathrm{V}}$-time recognized a total of 140 heartbeats in the velocity signal $v_{\mathrm{ref}}(t)$.
Sixteen heartbeats were not considered for the analysis. Most of the 16 beats were excluded because they occurred as the subject slightly moved or breathed in/out before/after holding the breath. The rest of the excluded beats presented an unclear pattern because of the interference of other waves. Therefore, 124 heartbeats were selected.

Table A.1 presents the values of $\max|\Delta P_{\mathrm{V}}R_{\mathrm{V}j}|$, $\overline{\Delta P_{\mathrm{V}}R_{\mathrm{V}j}}$, and sd_j computed for the signal $v_{\mathrm{art}}(t)$ and for the signals $v_{\mathrm{F}_i}(t)$. The first information obtained from Table A.1 is that the filtering of the disturbance has a positive effect for the computation of the $P_{\mathrm{V}}R_{\mathrm{V}}$-time, as expected.
In fact, all the filtered signals $v_{\mathrm{F}_i}(t)$ present lower values of $\max|\Delta P_{\mathrm{V}}R_{\mathrm{V}j}|$, $\overline{\Delta P_{\mathrm{V}}R_{\mathrm{V}j}}$ and sd_j with respect to ones obtained from the arbitrary signal $v_{\mathrm{art}}(t)$.
Figure A.4 shows the distribution of $\Delta P_{\mathrm{V}}R_{\mathrm{V}j}$ for the signals $v_{\mathrm{art}}(t)$ and $v_{\mathrm{F}_i}(t)$; the distribution of $\Delta P_{\mathrm{V}}R_{\mathrm{VF}_i}$ is less spread with respect to the one of $\Delta P_{\mathrm{V}}R_{\mathrm{V\,art}}$.
According to Table A.1, the filter technique F_3 seems to deliver the lowest, i.e. the best values of $\max|\Delta P_{\mathrm{V}}R_{\mathrm{V}j}|$, $\overline{\Delta P_{\mathrm{V}}R_{\mathrm{V}j}}$ and sd_j among the tested filters, followed by the technique F_1.

Table A.1.: Results of the computation of $\Delta P_{\mathrm{V}}R_{\mathrm{V}j}$ for the signals v_{art}, v_{F_1}, v_{F_2} and v_{F_3}.

	$\max\lvert\Delta P_{\mathrm{V}}R_{\mathrm{V}j}\rvert$ / ms	$\overline{\Delta P_{\mathrm{V}}R_{\mathrm{V}j}}$ / ms	sd_j / ms
$v_{\mathrm{art}}(t)$	11.00	0.30	2.46
$v_{\mathrm{F}_1}(t)$	8.00	0.05	1.29
$v_{\mathrm{F}_2}(t)$	10.00	0.11	1.78
$v_{\mathrm{F}_3}(t)$	8.00	0.02	1.10

However, by looking at Figure A.4, it is clear that the filter technique F_2 presents only a few heartbeats with the greatest value $\Delta P_{\mathrm{V}}R_{\mathrm{VF}_2} = 10$ ms. This is the case of a heartbeat with the P_{V}-wave with two similar maxima (Figure 4.6).
The effect of the disturbances and filtering technique F_2 results in the distortion of the amplitude of the two maxima; the algorithm recognizes the higher.
It can happen that in a heartbeat of the signal $v_{\mathrm{ref}}(t)$ the first maximum is higher and in the filtered signal $v_{\mathrm{F}_i}(t)$ the second one is higher, or conversely.
These values of $\Delta P_{\mathrm{V}}R_{\mathrm{V}j}$ could be considered outliers.
Outliers are also present in the distribution of F_1 and F_3. For all the three filtering techniques and for the most of the beats, $\Delta P_{\mathrm{V}}R_{\mathrm{V}j}$ is included in the interval $-2\text{ ms} \leq \Delta P_{\mathrm{V}}R_{\mathrm{V}j} \leq 2$ ms.

The technique with the most occurrences of $\Delta P_{\mathrm{V}}R_{\mathrm{V}j} = 0$ is the technique F_3. Therefore, the technique F_3 presents slightly better results than the other two techniques.
However, only the technique F_1 can be implemented for online filtering in practice.
Because of the small statistic sample, it is inappropriate to make statements about the best filtering technique, which is also strictly related to the algorithm used for the post-processing.
This analysis is not aimed to detect the best filtering technique but only to roughly estimate the influence of the disturbances enhanced by filters on the detection of the $P_{\mathrm{V}}R_{\mathrm{V}}$-time.

The contribution of the disturbances enhanced by the filtering to the uncertainty of the PR-time in VCG can be considered as a type-A uncertainty.
According to GUM [134], the type-A uncertainty related to the disturbances enhanced by the filtering technique F_i can be calculated as

$$u_{\mathrm{A,F}_i} = t_{(68\%)}(N) \cdot sd_{\mathrm{F}_i} \tag{A.4}$$

where $t_{(68\%)}(N)$ is the Student-t factor for a confidence interval of 68.27% for 124 heartbeats, $t_{(68\%)}(124) = 1.004$.
Therefore the type-A uncertainty results in $u_{\mathrm{A,F}_1} = 1.30$ ms, $u_{\mathrm{A,F}_2} = 1.8$ ms and

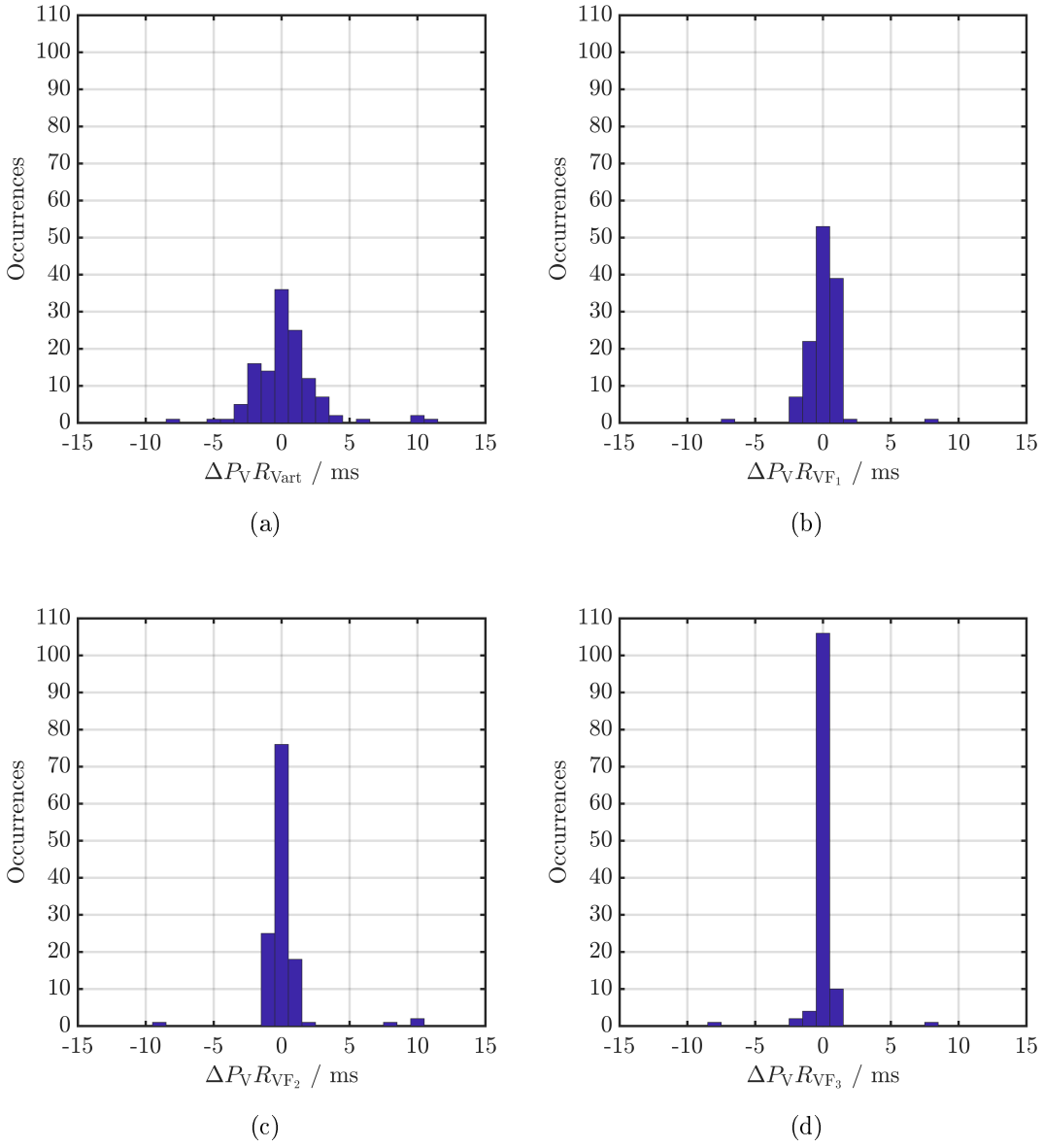

Figure A.4.: Distribution of the values $\Delta P_{\mathrm{V}}R_{\mathrm{V}j}$ of v_{art} (a), $v_{\mathrm{F_1}}$ (b), $v_{\mathrm{F_2}}$ (c) and $v_{\mathrm{F_3}}$ (d).

$u_{\mathrm{A,F_3}} = 1.14$ ms.
From this first estimation, the contribution to the uncertainty resulting from the disturbances and their filtering to the $P_{\mathrm{V}}R_{\mathrm{V}}$-time is lower than $u_{\mathrm{A,F}} \approx 2$ ms. However, to estimate this contribution reliably, a bigger statistic sample is required.

Bibliography

[1] L. Scalise. "Non Contact Heart Monitoring". In: *Advances in Electrocardiograms*. Ed. by Richard M. Millis. Rijeka: IntechOpen, 2012. Chap. 4. DOI: 10.5772/22937. URL: https://doi.org/10.5772/22937.

[2] J. Kranjec, S. Beguš, G. Geršak, and J. Drnovšek. "Non-contact heart rate and heart rate variability measurements: A review". *Biomedical Signal Processing and Control* 13 (2014), pp. 102–112. ISSN: 1746-8094. DOI: https://doi.org/10.1016/j.bspc.2014.03.004.

[3] A. Al-Naji, K. Gibson, S.-H. Lee, and J. Chahl. "Monitoring of Cardiorespiratory Signal: Principles of Remote Measurements and Review of Methods". *IEEE Access* 5 (Aug. 2017), pp. 15776–15790. DOI: 10.1109/ACCESS.2017.2735419.

[4] J. W. Rohrbaugh. "Ambulatory and Non-Contact Recording Methods". In: *Handbook of Psychophysiology, 4th Ed.* Ed. by Louis G. Tassinary John T. Cacioppo and Gary G. Berntson. Cambridge, United Kingdom: Cambridge University Press, 2019. Chap. 14.

[5] L. Mignanelli and C. Rembe. "Non-contact Health Monitoring with LDV". In: *Laser Doppler Vibrometry for Non-Contact Diagnostics*. Ed. by K. Kroschel. Cham: Springer International Publishing, 2020, pp. 1–8. ISBN: 978-3-030-46691-6. DOI: 10.1007/978-3-030-46691-6_1. URL: https://doi.org/10.1007/978-3-030-46691-6_1.

[6] L. Scalise, P. Marchionni, I. Ercoli, and E. P. Tomasini. "Simultaneous Measurement of Respiration and Cardiac Period in Preterm Infants by Laser Doppler Vibrometry". *AIP Conference Proceedings* 1457 (2012), pp. 275–281. DOI: 10.1063/1.4730567.

[7] L. Scalise, P. Marchionni, I. Ercoli, and E. P. Tomasini. "Laser measurement of respiration activity in preterm infants: Monitoring of peculiar events". In: AIP Conference Proceedings. AIP, 2012, pp. 63–68. DOI: 10.1063/1.4757824.

[8] R. L. Conder and A. A. Conder. "Heart rate variability interventions for concussion and rehabilitation". *Frontiers in psychology* 5 (2014), p. 890. ISSN: 1664-1078. DOI: 10.3389/fpsyg.2014.00890.

[9] A. Gilchrist. *Industry 4.0: The industrial internet of things*. [New York, NY]: Apress, 2016. ISBN: 978-1-4842-2046-7.

[10] H. Boyes, B. Hallaq, J. Cunningham, and T. Watson. "The industrial internet of things (IIoT): An analysis framework". *Computers in Industry* 101 (2018), pp. 1–12. ISSN: 01663615. DOI: 10.1016/j.compind.2018.04.015.

[11] A. Tsuchida, M. Bhuiyan, and K. Oguri. "Estimation of drowsiness level based on eyelid closure and heart rate variability". *1557-170X* 2009 (2009), pp. 2543–2546. ISSN: 1557-170X. DOI: 10.1109/IEMBS.2009.5334766.

[12] R. N. Khushaba, S. Kodagoda, S. Lal, and G. Dissanayake. "Driver drowsiness classification using fuzzy wavelet-packet-based feature-extraction algorithm". *IEEE transactions on biomedical engineering* 58.1 (2011), pp. 121–131. DOI: 10.1109/TBME.2010.2077291.

[13] F.-C. Lin, L.-W. Ko, C.-H. Chuang, T.-P. Su, and C.-T. Lin. "Generalized EEG-Based Drowsiness Prediction System by Using a Self-Organizing Neural Fuzzy System". *IEEE Transactions on Circuits and Systems I: Regular Papers* 59.9 (2012), pp. 2044–2055. ISSN: 1549-8328. DOI: 10.1109/TCSI.2012.2185290.

[14] A. Liu, Z. Li, L. Wang, and Y. Zhao. "A practical driver fatigue detection algorithm based on eye state". In: *2010 Asia Pacific Conference on Postgraduate Research in Microelectronics and Electronics (PrimeAsia)*. Piscataway, NJ: IEEE, 2010, pp. 235–238. ISBN: 978-1-4244-6735-8. DOI: 10.1109/PRIMEASIA.2010.5604919.

[15] A. Yuce, H. Gao, G. L. Cuendet, and J.-P. Thiran. "Action Units and Their Cross-Correlations for Prediction of Cognitive Load during Driving". *IEEE Transactions on Affective Computing* 8.2 (2017), pp. 161–175. ISSN: 1949-3045. DOI: 10.1109/TAFFC.2016.2584042.

[16] F. Coenen, B. Zhang, and C. Yan. "Driving posture recognition by convolutional neural networks". *IET Computer Vision* 10.2 (2016), pp. 103–114. ISSN: 1751-9632. DOI: 10.1049/iet-cvi.2015.0175.

[17] A. Fernández, R. Usamentiaga, J. L. Carús, and R. Casado. "Driver Distraction Using Visual-Based Sensors and Algorithms". *Sensors (Basel, Switzerland)* 16.11 (2016). DOI: 10.3390/s16111805.

[18] A. A. Lenskiy and J.-S. Lee. "Driver's eye blinking detection using novel color and texture segmentation algorithms". *International Journal of Control, Automation and Systems* 10.2 (2012), pp. 317–327. ISSN: 1598-6446. DOI: 10.1007/s12555-012-0212-0.

[19] A. Čolić, O. Marques, and B. Furht. "Driver Drowsiness Detection and Measurement Methods". In: *Driver drowsiness detection*. Ed. by Aleksandar Čolić, Oge Marques, and Borivoje Furht. Springer briefs in computer science. Cham: Springer, 2014, pp. 7–18. ISBN: 978-3-319-11534-4. DOI: 10.1007/978-3-319-11535-1{\textunderscore}2.

[20] M.-Z. Poh, D. J. McDuff, and R. W. Picard. "Non-contact, automated cardiac pulse measurements using video imaging and blind source separation". *Optics express* 18.10 (2010), pp. 10762–10774. DOI: 10.1364/OE.18.010762.

[21] U. Morbiducci, L. Scalise, M. De Melis, and M. Grigioni. "Optical Vibrocardiography: A Novel Tool for the Optical Monitoring of Cardiac Activity". *Annals of biomedical engineering* 35 (Nov. 2007), pp. 45–58. DOI: 10.1007/s10439-006-9202-9.

[22] L. Scalise and U Morbiducci. "Non-contact cardiac monitoring from carotid artery using optical vibrocardiography". *Medical Engineering & Physics* 30.4 (2008), pp. 490–497. ISSN: 1350-4533. DOI: 10.1016/j.medengphy.2007.05.008.

[23] L. Scalise, G. Cosoli, L. Casacanditella, S. Casaccia, and J. W. Rohrbaugh. "The measurement of blood pressure without contact: An LDV-based technique". In: *2017 IEEE International Symposium on Medical Measurements and Applications (MeMeA)*. IEEE, 2017, pp. 245–250. ISBN: 978-1-5090-2984-6. DOI: 10.1109/MeMeA.2017.7985883.

[24] L. Scalise, P. Marchionni, I. Ercoli, and E. P. Tomasini. "Simultaneous Measurement of Respiration and Cardiac Period in Preterm Infants by Laser Doppler Vibrometry". *AIP Conference Proceedings* 1457 (June 2012), pp. 275–281. DOI: 10.1063/1.4730567.

[25] P. Marchionni, L. Scalise, I. Ercoli, and E. P. Tomasini. "An optical measurement method for the simultaneous assessment of respiration and heart rates in preterm infants". *The Review of scientific instruments* 84 (Dec. 2013), p. 121705. DOI: 10.1063/1.4845635.

[26] J. C. Lin, J. Kiernicki, M. Kiernicki, and P. B. Wollschlaeger. "Microwave Apexcardiography". *IEEE Transactions on Microwave Theory and Techniques* 27.6 (1979), pp. 618–620. ISSN: 0018-9480. DOI: 10.1109/TMTT.1979.1129682.

[27] D. Nagae and A. Mase. "Measurement of heart rate variability and stress evaluation by using microwave reflectometric vital signal sensing". *The Review of scientific instruments* 81.9 (2010), p. 094301. DOI: 10.1063/1.3478017.

[28] A. Droitcour, V. Lubecke, Jenshan Lin, and O. Boric-Lubecke. "A microwave radio for Doppler radar sensing of vital signs". In: *Microwave Symposium Digest, 2001 IEEE MTT-S International*. IEEE, 2001, pp. 175–178. ISBN: 0-7803-6538-0. DOI: 10.1109/MWSYM.2001.966866.

[29] M.Y.W. Chia, S. W. Leong, C. K. Sim, and K. M. Chan. "Through-wall UWB radar operating within FCC's mask for sensing heart beat and breathing rate". In: *2005 European Microwave Conference*. London: Horizon House Publ, 2005, 4 pp. ISBN: 2-9600551-2-8. DOI: 10.1109/EUMC.2005.1610358.

[30] G. Lu, F. Yang, Y. Tian, X. Jing, and J. Wang. "Contact-free Measurement of Heart Rate Variability via a Microwave Sensor". *Sensors (Basel, Switzerland)* 9.12 (2009), pp. 9572–9581. DOI: 10.3390/s91209572.

[31] E. M. Staderini. "UWB radars in medicine". *IEEE Aerospace and Electronic Systems Magazine* 17.1 (2002), pp. 13–18. ISSN: 08858985. DOI: 10.1109/62.978359.

[32] I. Immoreev and T.-H. Tao. "UWB radar for patient monitoring". *IEEE Aerospace and Electronic Systems Magazine* 23.11 (2008), pp. 11–18. ISSN: 08858985. DOI: 10.1109/MAES.2008.4693985.

[33] E. Frontoni, R. Pollini, P. Russo, P. Zingaretti, and G. Cerri. "HDOMO: Smart Sensor Integration for an Active and Independent Longevity of the Elderly". *Sensors (Basel, Switzerland)* 17.11 (2017). DOI: 10.3390/s17112610.

[34] K. Kroschel and J. Metzler. "Contactless Measurement of the Respiration Frequency by Vibrometry". In: *Studientexte zur Sprachkommunikation: Elektronische Sprachsignalverarbeitung 2018*. Ed. by AndrÃ© Berton, Udo Haiber, and Wolfgang Minker. TUDpress, Dresden, 2018, pp. 310–317. ISBN: 978-3-959081-28-3.

[35] T. Schuurman, D. J. Rixen, C. A. Swenne, and J-W Hinnen. "Feasibility of Laser Doppler Vibrometry as potential diagnostic tool for patients with abdominal aortic aneurysms". *Journal of biomechanics* 46.6 (2013), pp. 1113–1120. DOI: 10.1016/j.jbiomech.2013.01.013.

[36] G. Agarwal et al. "Vibrometry: a novel noninvasive application of ultrasonographic physics to estimate wall stress in native aneurysms". *Annals of the New York Academy of Sciences* 1085 (2006), pp. 197–207. ISSN: 0077-8923. DOI: 10.1196/annals.1383.001.

[37] G. Mozes et al. "Noninvasive measurement of aortic aneurysm sac tension with vibrometry". *Journal of vascular surgery* 42.5 (2005), pp. 963–971. ISSN: 0741-5214. DOI: 10.1016/j.jvs.2005.07.012.

[38] M. C. Dahl, P. A. Kramer, P. G. Reinhall, S. K. Benirschke, S. T. Hansen, and R. P. Ching. "The efficacy of using vibrometry to detect osteointegration of the Agility total ankle". *Journal of biomechanics* 43.9 (2010), pp. 1840–1843. DOI: 10.1016/j.jbiomech.2010.02.019.

[39] M. Grigioni et al. "Laser Doppler technique for nondestructive evaluation of mechanical heart valves kinematics". In: *Sixth International Conference on Vibration Measurements by Laser Techniques: Advances and Applications*. SPIE Proceedings. SPIE, 2004, p. 99. DOI: 10.1117/12.579538.

[40] C. C. Rondini, G. L. Rossi, and L. Scalise. "Laser vibrometry and stress measurement by thermoelasticity on mechanical heart valve". In: *Sixth International Conference on Vibration Measurements by Laser Techniques: Advances and Applications*. SPIE Proceedings. SPIE, 2004, p. 124. DOI: 10.1117/12.579756.

[41] H. Hong and M. D. Fox. "Noninvasive detection of cardiovascular pulsations by optical Doppler techniques". *Journal of biomedical optics* 2.4 (1997), pp. 382–390. DOI: 10.1117/12.281529.

[42] M. Chen et al. "Laser Doppler Vibrometry Measures of Physiological Function: Evaluation of Biometric Capabilities". *IEEE Transactions on Information Forensics and Security* 5.3 (2010), pp. 449–460. ISSN: 1556-6013. DOI: 10.1109/TIFS.2010.2051542.

[43] M. Pinotti, N. Paone, F. A. Santos, and E. P. Tomasini. "Carotid artery pulse wave measured by a laser vibrometer". In: *Third International Conference on Vibration Measurements by Laser Techniques: Advances and Applications*. Ed. by Enrico P. Tomasini. SPIE Proceedings. SPIE, 1998, pp. 611–616. DOI: 10.1117/12.307747.

[44] L. Scalise, M. Grigioni, Morbiducci U., and Tomasini E. P. *A non contact measurement technique for the monitoring of a physiological condition*. Aug. 2005. URL: https://patents.google.com/patent/EP1623667A1/en.

[45] A. Campo, A. Waz, G. Dudzik, J. Dirckx, and K. Abramski. "Application of a four-channel vibrometer system for detection of arterial stiffness". *AIP Conference Proceedings* 1740.1 (2016), p. 050004. DOI: 10.1063/1.4952668. URL: https://aip.scitation.org/doi/pdf/10.1063/1.4952668.

[46] M.-Z. Poh, D. J. McDuff, and R. W. Picard. "Advancements in noncontact, multiparameter physiological measurements using a webcam". *IEEE transactions on bio-medical engineering* 58.1 (2011), pp. 7–11. DOI: 10.1109/TBME.2010.2086456.

[47] G. Da Costa. "Optical remote sensing of heartbeats". *Optics Communications* 117.5-6 (1995), pp. 395–398. ISSN: 00304018. DOI: 10.1016/0030-4018(95)00181-7.

[48] J. E. Parra and G. Da Costa. "Optical remote sensing of heartbeats". In: *Visualization of Temporal and Spatial Data for Civilian and Defense Applications*. Ed. by Glenn O. Allgood and Nickolas L. Faust. SPIE Proceedings. SPIE, 2001, pp. 113–121. DOI: 10.1117/12.438115.

[49] G. O. Allgood and N. L. Faust, eds. *Visualization of Temporal and Spatial Data for Civilian and Defense Applications*. SPIE Proceedings. SPIE, 2001.

[50] C. Takano and Y. Ohta. "Heart rate measurement based on a time-lapse image". *Medical Engineering & Physics* 29.8 (2007), pp. 853–857. ISSN: 1350-4533. DOI: 10.1016/j.medengphy.2006.09.006.

[51] V. van Rooijen, L. de Voogd-Claessen, K. Lauche, V. Jeanne, and R. van der Vliet. "Development of a new product for unrestrained heart rate measurement in swimming: a user centered design approach". *Procedia Engineering* 2.2 (2010), pp. 2693–2699. ISSN: 18777058. DOI: 10.1016/j.proeng.2010.04.053.

[52] F. P. Wieringa, F. Mastik, and A. F. W. van der Steen. "Contactless multiple wavelength photoplethysmographic imaging: a first step toward "SpO2 camera" technology". *Annals of biomedical engineering* 33.8 (2005), pp. 1034–1041. DOI: 10.1007/s10439-005-5763-2.

[53] A. Mesleh, D. Skopin, S. Baglikov, and A. Quteishat. "Heart Rate Extraction from Vowel Speech Signals". *Journal of Computer Science and Technology* 27.6 (2012), pp. 1243–1251. ISSN: 1000-9000. DOI: 10.1007/s11390-012-1300-6.

[54] M. Steffen, A. Aleksandrowicz, and S. Leonhardt. "Mobile noncontact monitoring of heart and lung activity". *IEEE transactions on biomedical circuits and systems* 1.4 (2007), pp. 250–257. ISSN: 1932-4545. DOI: 10.1109/TBCAS.2008.915633.

[55] K. Kurita. "Note: Human heartbeat measurement on the basis of current generated by electrostatic induction". *Review of Scientific Instruments* 82.2 (2011), p. 026105. ISSN: 0034-6748. DOI: 10.1063/1.3541554.

[56] W. Chen, X. Zhu, T. Nemoto, Y. Kanemitsu, K. Kitamura, and K. Yamakoshi. "Unconstrained detection of respiration rhythm and pulse rate with one under-pillow sensor during sleep". *Medical & biological engineering & computing* 43.2 (2005), pp. 306–312. ISSN: 0140-0118. DOI: 10.1007/BF02345970.

[57] X. Zhu et al. "Real-Time Monitoring of Respiration Rhythm and Pulse Rate During Sleep". *IEEE Transactions on Biomedical Engineering* 53.12 (2006), pp. 2553–2563. ISSN: 0018-9294. DOI: 10.1109/TBME.2006.884641.

[58] Y. Yeh and H. Z. Cummins. "Localized fluid flow measurements with an he–ne laser spectrometer". *Applied Physics Letters* 4.10 (1964), pp. 176–178. ISSN: 1054-660X. DOI: 10.1063/1.1753925.

[59] C. Rembe, G. Siegmund, H. Steger, and M. Wörtge. "Measuring MEMS in Motion by Laser Doppler Vibrometry". In: 2019, pp. 297–347. ISBN: 9780429186738. DOI: 10.1201/9780429186738-11.

[60] Y. Li, P. Segers, J. Dirckx, and R. Baets. "On-chip laser Doppler vibrometer for arterial pulse wave velocity measurement". *Biomed. Opt. Express* 4.7 (July 2013), pp. 1229–1235. DOI: 10.1364/BOE.4.001229. URL: http://www.osapublishing.org/boe/abstract.cfm?URI=boe-4-7-1229.

[61] C. Rembe, M. Wörtge, A. Dräebenstedt, and T. Braun. "Optisches Interferometer und Vibrometer mit solch einem optischen Interferometer". EP2808644B1. 2017.

[62] T. Haist et al. "Multipoint vibrometry with dynamic and static holograms". *The Review of scientific instruments* 84.12 (2013), p. 121701. DOI: 10.1063/1.4845596.

[63] Y. Fu, M. Guo, and P. B. Phua. "Multipoint laser Doppler vibrometry with single detector: principles, implementations, and signal analyses". *Applied optics* 50.10 (2011), pp. 1280–1288. DOI: 10.1364/AO.50.001280.

[64] E. Cupido, S. Morel, and D. Smith. "Multipoint laser doppler vibrometer for transient analysis". In: *Proceedings of IMAC XXI*. 2003.

[65] R. Changkakoti, R. V. Kruzelecky, A. K. Ghosh, and W. Zheng. "Multichannel fiber optic laser vibrometer". In: *Opto-Contact: Workshop on Technology Transfers, Start-Up Opportunities,and Strategic Alliances*. Ed. by Robert J. L. Corriveau, M. J. Soileau, and Michel Auger. SPIE Proceedings. SPIE, 1998, pp. 97–106. DOI: 10.1117/12.323515.

[66] H. Tabatabai, D. E. Oliver, J. W. Rohrbaugh, and C. Papadopoulos. "Novel Applications of Laser Doppler Vibration Measurements to Medical Imaging". *Sensing and Imaging: An International Journal* 14.1 (June 2013), pp. 13–28. ISSN: 1557-2072. DOI: 10.1007/s11220-013-0077-1.

[67] J. Sokołowski, K. Niemczyk, R. Bartoszewicz, K. Morawski, A. Bruzgielewicz, and B. Rygalska. "Round window's movability measurements with helping of LDV in evaluation of ossicular chain functioning." *Otolaryngologia Polska* 64.7 (2010), pp. 77–80. ISSN: 00306657. DOI: 10.1016/S0030-6657(10)70015-9.

[68] G. R. Ball, A. Huber, and R. L. Goode. "Scanning Laser Doppler Vibrometry of the Middle Ear Ossicles". *Ear, Nose & Throat Journal* 76.4 (1997), pp. 213–222. ISSN: 0145-5613. DOI: 10.1177/014556139707600409.

[69] I. Arechvo, N. Lasurashvili, M. Bornitz, Z. Kevanishvili, and T. Zahnert. "Laser Doppler vibrometry of the middle ear in humans: derivation dependence, variability, and bilateral differences". *Medicina* 45.11 (2009), p. 878. DOI: 10.3390/medicina45110113.

[70] D. Turcanu, D. Mârţu, E. Dalhoff, and A. W. Gummer. "Laser Doppler vibrometry: a new tool for diagnosing hearing loss with an intact eardrum". *Revista medico-chirurgicala a Societatii de Medici si Naturalisti din Iasi* 110.2 (2006), pp. 357–366. ISSN: 0048-7848.

[71] N. Donnelly et al. "Effect of cochlear implant electrode insertion on middle-ear function as measured by intra-operative laser Doppler vibrometry". *The Journal of laryngology and otology* 123.7 (2009), pp. 723–729. DOI: 10.1017/S0022215109004290.

[72] P. Castellini, L. Scalise, and G. M. Revel. "Vibration measurements for diagnosis of structural defects on human teeth". *Measurement* 27.1 (2000), pp. 29–42. ISSN: 02632241. DOI: 10.1016/S0263-2241(99)00049-4.

[73] S. C. Lea, A. D. Walmsley, P. J. Lumley, and G. Landini. "A new insight into the oscillation characteristics of endosonic files used in dentistry". *Physics in medicine and biology* 49.10 (2004), pp. 2095–2102. DOI: 10.1088/0031-9155/49/10/018.

[74] A. Kaplan. "Information Processing for Biological Signals: Application to Laser Doppler Vibrometry". PhD thesis. Washington University in St. Louis, 2011.

[75] A. D. Kaplan, J. A. O'Sullivan, E. J. Sirevaag, P.-H. Lai, and J. W. Rohrbaugh. "Hidden state models for noncontact measurements of the carotid pulse using a laser Doppler vibrometer". *IEEE transactions on biomedical engineering* 59.3 (2012), pp. 744–753. DOI: 10.1109/TBME.2011.2179297.

[76] P.-H. Lai, J. A. O'Sullivan, M. Chen, E. J. Sirevaag, A. D. Kaplan, and J. W. Rohrbaugh. "A robust feature selection method for noncontact biometrics based on Laser Doppler Vibrometry". In: *Biometrics Symposium, 2008.* Piscataway, NJ: IEEE, 9/23/2008 - 9/25/2008, pp. 65–70. ISBN: 978-1-4244-2566-2. DOI: 10.1109/BSYM.2008.4655524.

[77] S. Casaccia, E. J. Sirevaag, E. J. Richter, L. Casacanditella, L. Scalise, and J. W. Rohrbaugh. "LDV arterial pulse signal: Evidence for local generation in the carotid". In: vol. 1740. AIP Conference Proceedings. Author(s), 2016, p. 050008. DOI: 10.1063/1.4952672.

[78] M. De Melis, U. Morbiducci, and L. Scalise. "Identification of cardiac events by optical Vibrocardiograpy: comparison with Phonocardiography". *Conference proceedings : 2007 29th Annual International Conference of the IEEE Engineering in Medicine and Biology Society. IEEE Engineering in Medicine and Biology Society. Annual Conference* 2007 (2007), pp. 2956–2959. ISSN: 1557-170X. DOI: 10.1109/IEMBS.2007.4352949.

[79] C. L. Desjardins, L. T. Antonelli, and E. Soares. "A remote and non-contact method for obtaining the blood-pulse waveform with a laser Doppler vibrometer". In: International Society for Optics and Photonics, 2007, p. 64301C. DOI: 10.1117/12.701139.

[80] E. J. Sirevaag, S. Casaccia, E. A. Richter, J. A. O'Sullivan, L. Scalise, and J. W. Rohrbaugh. "Cardiorespiratory interactions: Noncontact assessment using laser Doppler vibrometry". *Psychophysiology* 53.6 (2016), pp. 847–867. DOI: 10.1111/psyp.12638.

[81] L. Casacanditella, G. Cosoli, S. Casaccia, E. P. Tomasini, and L. Scalise. "Indirect measurement of the carotid arterial pressure from vibrocardiographic signal: Calibration of the waveform and comparison with photoplethysmographic signal" (Aug. 2016), pp. 3568–3571. ISSN: 1558-4615. DOI: 10.1109/EMBC.2016.7591499.

[82] L. Casacanditella, G. Cosoli, S. Casaccia, L. Scalise, and E. P. Tomasini. "Derived Non-contact Continuous Recording of Blood Pressure Pulse Waveform by Means of Vibrocardiography". In: *Sensors*. Ed. by Bruno Andò, Francesco Baldini, Corrado Di Natale, Giovanna Marrazza, and Pietro Siciliano. Vol. 431. Lecture Notes in Electrical Engineering. Cham: Springer, 2018, pp. 365–372. ISBN: 978-3-319-55076-3. DOI: 10.1007/978-3-319-55077-0{\textunderscore}46.

[83] M. De Melis et al. "A noncontact approach for the evaluation of large artery stiffness: a preliminary study". *American journal of hypertension* 21.12 (2008), pp. 1280–1283. DOI: 10.1038/ajh.2008.280.

[84] A. Campo and J. Dirckx. "Dual-beam laser Doppler vibrometer for measurement of pulse wave velocity in elastic vessels". In: *22nd Congress of the International Commission for Optics: Light for the Development of the World*. Ed. by Ramón Rodríguez-Vera and Rufino Díaz-Uribe. SPIE Proceedings. SPIE, 2011, 80118Y. DOI: 10.1117/12.902813.

[85] A. Campo, P. Segers, and J. Dirckx. "Laser Doppler vibrometry for in vivo assessment of arterial stiffness". In: *2011 IEEE International Workshop on Medical Measurements and Applications proceedings*. Ed. by Mario Savino. Piscataway, NJ: IEEE, 2011, pp. 119–121. ISBN: 978-1-4244-9336-4. DOI: 10.1109/MeMeA.2011.5966691.

[86] A. Luik and K. Kroschel. "Laser-based remote measurement of vital parameters of the heart". In: *Optical Sensing and Detection V*. Ed. by Francis Berghmans and Anna Grazia Mignani. Proceedings of SPIE. Bellingham, Washington, USA: SPIE, 2018, p. 29. ISBN: 9781510618862. DOI: 10.1117/12.2303807. URL: https://www.spiedigitallibrary.org/conference-proceedings-of-spie/10680/2303807/Laser-based-remote-measurement-of-vital-parameters-of-the-heart/10.1117/12.2303807.full.

[87] J. Metzler, K. Kroschel, and D. Willersinn. "Automatic detection of measurement points for non-contact vibrometer-based diagnosis of cardiac arrhythmias". In: *Medical Imaging 2017: Image-Guided Procedures, Robotic Interventions, and Modeling*. Ed. by Robert J. Webster and Baowei Fei. SPIE Proceedings. SPIE, 2017, 101351S. DOI: 10.1117/12.2253654.

[88] S. Casaccia, L. Scalise, L. Casacanditella, E. P. Tomasini, and J. W. Rohrbaugh. "Non-contact assessment of muscle contraction: Laser Doppler Myography". In: *2015 IEEE International Symposium on Medical Measurements and Applications (MeMeA)*. Piscataway, NJ: IEEE, 2015, pp. 610–615. ISBN: 978-1-4799-6477-2. DOI: 10.1109/MeMeA.2015.7145276.

[89] S. Casaccia, E. J. Sirevaag, M. G. Frank, J. A. O'Sullivan, L. Scalise, and J. W. Rohrbaugh. "Noncontact Sensing of Facial Muscle Activity Using Laser Doppler Vibrometry: Time Domain Data Analysis". *Journal of Physics: Conference Series* 1149 (2018), p. 012027. ISSN: 1742-6588. DOI: 10.1088/1742-6596/1149/1/012027.

[90] P. Castellini, R. Huebner, and M. Pinotti. "Vibration measurement on artificial heart valve by laser Doppler vibrometry". In: *Fifth International Conference on Vibration Measurements by Laser Techniques: Advances and Applications*. Ed. by Enrico P. Tomasini. SPIE Proceedings. SPIE, 2002, pp. 159–167. DOI: 10.1117/12.468147.

[91] A. Luik, L. Mignanelli, K. Kroschel, C. Schmitt, C. Rembe, and L. Scalise. "Laser Doppler vibrometry as a noncontact method to detect various degrees of atrioventricular block: a feasibility study". *Future cardiology* 12.3 (2016), pp. 269–279. DOI: 10.2217/fca-2015-0008.

[92] T. L. Szabo. *Diagnostic Ultrasound Imaging: Inside Out*. Elsevier, 2014. ISBN: 9780123964878. DOI: 10.1016/C2011-0-07261-7.

[93] L. V. Wang and S. Hu. "Photoacoustic Tomography: In Vivo Imaging from Organelles to Organs". *Science (New York, N.Y.)* 335 (2012), pp. 1458–1462. DOI: 10.1126/science.1216210.

[94] L. V. Wang and H.-I. Wu. *Biomedical Optics*. Hoboken, NJ, USA: John Wiley & Sons, Inc, 2009. ISBN: 9780470177013. DOI: 10.1002/9780470177013.

[95] L. V. Wang. *Photoacoustic Imaging and Spectroscopy*. Vol. 144. CRC Press, 2009. ISBN: 978-1-4200-5991-5. DOI: 10.1201/9781420059922.

[96] L. V. Wang. "Tutorial on Photoacoustic Microscopy and Computed Tomography". *IEEE Journal of Selected Topics in Quantum Electronics* 14.1 (2008), pp. 171–179. ISSN: 1077-260X. DOI: 10.1109/JSTQE.2007.913398.

[97] X. Zhang, J. R. Fincke, C. M. Wynn, M. R. Johnson, R. W. Haupt, and B. W. Anthony. "Full noncontact laser ultrasound: first human data". *Light, science & applications* 8 (2019), p. 119. DOI: 10.1038/s41377-019-0229-8.

[98] C. Tian et al. "Non-contact Photoacoustic Imaging Using A Commercial Heterodyne Interferometer". *IEEE Sensors Journal* PP (Sept. 2016), pp. 1–1. DOI: 10.1109/JSEN.2016.2611569.

[99] G. Xu, C. Wang, T. Feng, D. E. Oliver, and X. Wang. "Non-contact photoacoustic tomography with a laser Doppler vibrometer". In: *Photons Plus Ultrasound: Imaging and Sensing 2014*. Ed. by Alexander A. Oraevsky and Lihong V. Wang. SPIE Proceedings. SPIE, 2014, p. 894332. DOI: 10.1117/12.2040290.

[100] E. Olsson, P. Gren, and M. Sjödahl. "Photoacoustic holographic imaging of absorbers embedded in silicone". *Applied optics* 50.17 (2011), pp. 2551–2558. DOI: 10.1364/AO.50.002551.

[101] R. W. Haupt and C. M. Wynn. "System and method for non-contact ultrasound". US20150148655A1. 2015.

[102] E. Zhang, J. Laufer, and P. Beard. "Backward-mode multiwavelength photoacoustic scanner using a planar Fabry-Perot polymer film ultrasound sensor for high-resolution three-dimensional imaging of biological tissues". *Applied optics* 47.4 (2008), pp. 561–577. DOI: 10.1364/ao.47.000561.

[103] Y. Hou, S.-W. Huang, S. Ashkenazi, R. Witte, and M. O'Donnell. "Thin polymer etalon arrays for high-resolution photoacoustic imaging". *Journal of biomedical optics* 13.6 (2008), p. 064033. DOI: 10.1117/1.3042260.

[104] C. M. Chow et al. "Broadband optical ultrasound sensor with a unique open-cavity structure". *Journal of biomedical optics* 16.1 (2011), p. 017001. DOI: 10.1117/1.3528014.

[105] R. Peterson, S. Solis, B. Zhang, H. Huang, and J. Y. Ye. "Sensitivity enhancement of an open-cavity-based optoacoustic sensor". *Optics letters* 38.15 (2013), pp. 2739–2741. DOI: 10.1364/OL.38.002739.

[106] H. Li, B. Dong, Z. Zhang, H. F. Zhang, and C. Sun. "A transparent broadband ultrasonic detector based on an optical micro-ring resonator for photoacoustic microscopy". *Scientific reports* 4 (2014), p. 4496. DOI: 10.1038/srep04496.

[107] B. Dong, S. Chen, Z. Zhang, C. Sun, and H. F. Zhang. "Photoacoustic probe using a microring resonator ultrasonic sensor for endoscopic applications". *Optics letters* 39.15 (2014), pp. 4372–4375. DOI: 10.1364/OL.39.004372.

[108] A. Rosenthal, D. Razansky, and V. Ntziachristos. "High-sensitivity compact ultrasonic detector based on a pi-phase-shifted fiber Bragg grating". *Optics letters* 36.10 (2011), pp. 1833–1835. DOI: 10.1364/OL.36.001833.

[109] S. A. Carp and V. Venugopalan. "Optoacoustic imaging based on the interferometric measurement of surface displacement". *Journal of biomedical optics* 12.6 (2007), p. 064001. ISSN: 1083-3668. DOI: 10.1117/1.2812665.

[110] A. Hochreiner, J. Bauer-Marschallinger, P. Burgholzer, B. Jakoby, and T. Berer. "Non-contact photoacoustic imaging using a fiber based interferometer with optical amplification". *Biomedical optics express* 4.11 (2013), pp. 2322–2331. DOI: 10.1364/BOE.4.002322.

[111] A. Hochreiner, T. Berer, H. Grün, M. Leitner, and P. Burgholzer. "Photoacoustic imaging using an adaptive interferometer with a photorefractive crystal". *Journal of biophotonics* 5.7 (2012), pp. 508–517. DOI: 10.1002/jbio.201100111.

[112] G. Rousseau, A. Blouin, and J.-P. Monchalin. "Non-contact photoacoustic tomography and ultrasonography for tissue imaging". *Biomedical optics express* 3.1 (2012), pp. 16–25. DOI: 10.1364/BOE.3.000016.

[113] G. Rousseau, B. Gauthier, A. Blouin, and J.-P. Monchalin. "Non-contact biomedical photoacoustic and ultrasound imaging". *Journal of biomedical optics* 17.6 (2012), p. 061217. DOI: 10.1117/1.JBO.17.6.061217.

[114] Y. Wang, C. Li, and R. K. Wang. "Noncontact photoacoustic imaging achieved by using a low-coherence interferometer as the acoustic detector". *Optics letters* 36.20 (2011), pp. 3975–3977. DOI: 10.1364/OL.36.003975.

[115] C. Blatter et al. "Intrasweep phase-sensitive optical coherence tomography for noncontact optical photoacoustic imaging". *Optics letters* 37.21 (2012), pp. 4368–4370. DOI: 10.1364/OL.37.004368.

[116] Z. Chen, S. Yang, Y. Wang, and D. Xing. "Noncontact broadband all-optical photoacoustic microscopy based on a low-coherence interferometer". *Applied Physics Letters* 106.4 (2015), p. 043701. ISSN: 1054-660X. DOI: 10.1063/1.4906748.

[117] J. Horstmann, H. Spahr, C. Buj, M. Münter, and R. Brinkmann. "Full-field speckle interferometry for non-contact photoacoustic tomography". *Physics in medicine and biology* 60.10 (2015), pp. 4045–4058. DOI: 10.1088/0031-9155/60/10/4045.

[118] A. Taebi. "Characterization, Classification, and Genesis of Seismocardiographic Signals". PhD thesis. University of Central Florida, 2018.

[119] H. A. Mansy, T. J. Royston, R. A. Balk, and R. H. Sandler. "Pneumothorax detection using computerised analysis of breath sounds". *Medical & biological engineering & computing* 40.5 (2002), pp. 526–532. ISSN: 0140-0118. DOI: 10.1007/BF02345450.

[120] W.W. Nichols, M. F. O'Rourke, and C. Vlachopoulos. *McDonald's blood flow in arteries: Theoretical, experimental, and clinical principles*. 6th ed. London: Hodder Arnold, 2011. ISBN: 9781444128789. URL: http://site.ebrary.com/lib/alltitles/docDetail.action?docID=10530592.

[121] N. Pomella, E. N. Wilhelm, C. Kolyva, J. González-Alonso, M. Rakobowchuk, and A. W. Khir. "Common Carotid Artery Diameter, Blood Flow Velocity and Wave Intensity Responses at Rest and during Exercise in Young Healthy Humans: A Reproducibility Study". *Ultrasound in Medicine & Biology* 43.5 (2017), pp. 943–957. ISSN: 0301-5629. DOI: 10.1016/j.ultrasmedbio.2016.12.018. URL: http://www.sciencedirect.com/science/article/pii/S0301562917300042.

[122] V. Jeyhani, S. Mahdiani, M. Peltokangas, and A. Vehkaoja. "Comparison of HRV parameters derived from photoplethysmography and electrocardiography signals". In: *2015 37th Annual International Conference of the IEEE Engineering in Medicine and Biology Society (EMBC)*. IEEE / Institute of Electrical and Electronics Engineers Incorporated, 2015, pp. 5952–5955. ISBN: 978-1-4244-9271-8. DOI: 10.1109/EMBC.2015.7319747.

[123] J. Reeves et al. "Non-Contact Measurement of Carotid Artery Pulse Wave Velocity: Neck Phantom and Preliminary In-vivo Results". eng. In: Tucson, Arizona, USA, 2017. ISBN: 978-0-692-89782-9.

[124] *Optischer Interferometrischer Recorder für die Vitalfunktionen (TRICORDER)*. (Online; accessed 15 august 2019). 2015. URL: https://www.photonikforschung.de/media/lebenswissenschaften/pdf/TRICORDER-Vor-Ort-Analytik-Projektsteck-korr2019-08-bf-C1.pdf.

[125] C. Yang and N. Tavassolian. "Combined Seismo- and Gyro-Cardiography: A More Comprehensive Evaluation of Heart-Induced Chest Vibrations". *IEEE journal of biomedical and health informatics* 22.5 (2018), pp. 1466–1475. DOI: 10.1109/JBHI.2017.2764798.

[126] P. K. Jain, A. K. Tiwari, and V. S. Chourasia. "Performance analysis of seismocardiography for heart sound signal recording in noisy scenarios". *Journal of medical engineering & technology* 40.3 (2016), pp. 106–118. DOI: 10.3109/03091902.2016.1139203.

[127] O. Lahdenoja et al. "Atrial Fibrillation Detection via Accelerometer and Gyroscope of a Smartphone". *IEEE journal of biomedical and health informatics* 22.1 (2018), pp. 108–118. DOI: 10.1109/JBHI.2017.2688473.

[128] A. Taebi, B. Solar, A. Bomar, R. Sandler, and H. Mansy. "Recent Advances in Seismocardiography". *Vibration* 2.1 (2019), pp. 64–86. DOI: 10.3390/vibration2010005.

[129] S. Koegelenberg, C. Scheffer, M. M. Blanckenberg, and A. F. Doubell. "Application of Laser Doppler Vibrometery for human heart auscultation". *Conference proceedings : 2014 36th Annual International Conference of the IEEE Engineering in Medicine and Biology Society. IEEE Engineering in Medicine and Biology Society. Annual Conference* 2014 (2014), pp. 4479–4482. ISSN: 1557-170X. DOI: 10.1109/EMBC.2014.6944618.

[130] S. Koegelenberg. "Application of laser Doppler vibrocardiography for human heart auscultation". MA thesis. University of Stellenbosch, 2014.

[131] L. Mignanelli and C. Rembe. "VCG Signals on the Thorax and Detection of the PR-Interval". In: *Laser Doppler Vibrometry for Non-Contact Diagnostics*. Ed. by K. Kroschel. Cham: Springer International Publishing, 2020, pp. 155–166. ISBN: 978-3-030-46691-6. DOI: 10.1007/978-3-030-46691-6_6. URL: https://doi.org/10.1007/978-3-030-46691-6_6.

[132] L. Mignanelli, C. Rembe, K. Kroschel, A. Luik, P. Castellini, and L. Scalise. "Medical diagnosis of the cardiovascular system on the carotid artery with IR laser Doppler vibrometer". In: vol. 1600. AIP Conference Proceedings. AIP Publishing LLC, 2014, pp. 313–322. DOI: 10.1063/1.4879597.

[133] G. Cosoli, L. Casacanditella, F. Pietroni, A. Calvaresi, G. M. Revel, and L. Scalise. "A novel approach for features extraction in physiological signals". In: *2015 IEEE International Symposium on Medical Measurements and Applications (MeMeA)*. Piscataway, NJ: IEEE, 2015, pp. 380–385. ISBN: 978-1-4799-6477-2. DOI: 10.1109/MeMeA.2015.7145232.

[134] JCGM. *Uncertainty of measurement-Part 3: Guide to the expression of uncertainty in measurement*. Tech. rep. American National Standards Institute (ANSI), Washington, DC, 2008.

[135] A. M. Winkler, K. Maslov, and L. V. Wang. "Noise-equivalent sensitivity of photoacoustics". *Journal of biomedical optics* 18.9 (2013), p. 097003. DOI: 10.1117/1.JBO.18.9.097003.

[136] J.P. Monchalin. "Optical Detection of Ultrasound". *IEEE Transactions on Ultrasonics, Ferroelectrics and Frequency Control* 33 (1986), pp. 485–499.

[137] R. Dewhurst and Q. Shan. "Optical remote measurement of ultrasound". *Measurement Science and Technology* 10 (Oct. 1999), R139. DOI: 10.1088/0957-0233/10/11/201.

[138] B. Dong, C. Sun, and H. F. Zhang. "Optical Detection of Ultrasound in Photoacoustic Imaging". *IEEE Transactions on Biomedical Engineering* 64.1 (Jan. 2017), pp. 4–15. ISSN: 0018-9294. DOI: 10.1109/TBME.2016.2605451.

[139] J.-P. Monchalin, A. Blouin, and G. Rousseau. "A non-contact system for biomedical photoacoustic imaging". *SPIE Newsroom* (2013). DOI: 10.1117/2.1201309.005104.

[140] G. Rousseau, A. Blouin, and J.-P. Monchalin. "Non-contact photoacoustic tomography and ultrasonography for brain imaging". In: *Photonic Therapeutics and Diagnostics VIII*. SPIE Proceedings. SPIE, 2012, p. 820750. DOI: 10.1117/12.906871.

[141] B. P. Payne, V. Venugopalan, B. B. Mikić, and N. S. Nishioka. "Optoacoustic tomography using time-resolved interferometric detection of surface displacement". *Journal of biomedical optics* 8.2 (2003), pp. 273–280. ISSN: 1083-3668. DOI: 10.1117/1.1559727.

[142] B. P. Payne, V. Venugopalan, B. B. Mikić, and N. S. Nishioka. "Optoacoustic determination of optical attenuation depth using interferometric detection". *Journal of biomedical optics* 8.2 (2003), pp. 264–272. ISSN: 1083-3668. DOI: 10.1117/1.1559731.

[143] S. A. Carp, A. Guerra, S. Q. Duque, and V. Venugopalan. "Optoacoustic imaging using interferometric measurement of surface displacement". *Applied Physics Letters* 85.23 (2004), pp. 5772–5774. ISSN: 1054-660X. DOI: 10.1063/1.1831569.

[144] R. W. Speirs and A. I. Bishop. "Photoacoustic tomography using a Michelson interferometer with quadrature phase detection". *Applied Physics Letters* 103.5 (2013), p. 053501. ISSN: 1054-660X. DOI: 10.1063/1.4816427.

[145] J. Eom, S. J. Park, Y. H. Kim, C. S. Lee, and B. H. Lee. "Noncontact photoacoustic tomography using optical fiber-based heterodyne interferometer". In: *23rd International Conference on Optical Fibre Sensors*. Ed. by José M. López-Higuera, Julian D. C. Jones, Manuel López-Amo, and José L. Santos. SPIE Proceedings. SPIE, 2014, p. 915795. DOI: 10.1117/12.2059013.

[146] J. Eom, S. J. Park, and B. H. Lee. "Noncontact photoacoustic tomography of in vivo chicken chorioallantoic membrane based on all-fiber heterodyne interferometry". *Journal of biomedical optics* 20.10 (2015), p. 106007. DOI: 10.1117/1.JBO.20.10.106007.

[147] P. Chiariotti, C. Rembe, P. Castellini, and M. Allen. "LDV Measurements in Structural Dynamics". In: *SEM Handbook of Experimental Structural Dynamics*. 2020.

[148] L. Fröhner. "Digitale Demodulation Phasenmodulierter Messsignale". MA thesis. Technische Universität Clausthal, 2016.

[149] M. Reinert. "Konstrution und Demonstration eines extern referenzirbaren Laser-Doppler-Vibrometers in Kompakter Bauweise". MA thesis. Technische Universität Clausthal, 2015.

[150] M. Schewe, D. Kohlmann, H. Wulfmeier, H. Fritze, and C. Rembe. "Methoden zur Minimierung des Rauscheinflusses durch Hitzeflimmern bei einem heterodynen Laser-Doppler-Vibrometer". *tm - Technisches Messen* 87.s1 (2020), s44–s49. ISSN: 0171-8096. DOI: 10.1515/teme-2020-0023.

[151] M. Johansmann, G. Siegmund, and Pineda M. "Targeting the limits of laser Doppler vibrometry". In: *Proceedings of the International Disk Drive Equipment and Materials Association*. 2015.

[152] M. Bauer, F. Ritter, and G. Siegmund. "High-precision laser vibrometers based on digital Doppler signal processing". In: *Fifth International Conference on Vibration Measurements by Laser Techniques: Advances and Applications*. Ed. by Enrico P. Tomasini. SPIE Proceedings. SPIE, 2002, pp. 50–61. DOI: 10.1117/12.468166.

[153] C. Rembe and L. Mignanelli. "Introduction to Laser-Doppler Vibrometry". In: *Laser Doppler Vibrometry for Non-Contact Diagnostics*. Ed. by K. Kroschel. Cham: Springer International Publishing, 2020, pp. 9–21. ISBN: 978-3-030-46691-6. DOI: 10.1007/978-3-030-46691-6_2. URL: https://doi.org/10.1007/978-3-030-46691-6_2.

[154] Polytec. *PSV-500 Scanning Vibrometer*. URL: https://www.polytec.com/eu/vibrometry/products/full-field-vibrometers/psv-500-scanning-vibrometer/.

[155] Polytec. *PSV-500-3D Scanning Vibrometer*. URL: https://www.polytec.com/eu/vibrometry/products/full-field-vibrometers/psv-500-3d-scanning-vibrometer/.

[156] X. Cao, B. Tarigan, C. Rembe, and H. Schwarze. "Vibrationsbasierende White-Etching-Cracks-Detektion an Wälzlagern". *tm - Technisches Messen* 85.6 (2018), pp. 443–453. ISSN: 0171-8096. DOI: 10.1515/teme-2017-0141.

[157] X. Cao and C. Rembe. "Non-Contact Damage Detection under Operational Conditions with Multipoint Laservibrometry". *Sensors (Basel, Switzerland)* 20.3 (2020). DOI: 10.3390/s20030732.

[158] *Leica 3D Disto | Leica Geosystems®*. URL: https://lasers.leica-geosystems.com/buy-3d-disto.

[159] Polytec GmbH. *MPV-800 Datenblatt*. (Online; accessed 15 august 2019). 2017. URL: https://www.polytec.com/de/vibrometrie/produkte/full-field-vibrometer/mpv-800-multipoint-vibrometer/.

[160] L. S. Lilly, ed. *Pathophysiology of heart disease: A collaborative project of medical students and faculty*. Edition 6. Philadelphia: Wolters Kluwer, 2016. ISBN: 9781451192759.

[161] G. Pocock and C. D. Richards. *The basis of medicine*. Oxford Core Texts. [Place of publication not identified]: Oxford University Press, 2006. ISBN: 978-0-19-856878-0.

[162] OpenStax College. *Anatomy and physiology*. Houston, Texas: Rice University, op. 2013. ISBN: 978-1-938168-13-0.

[163] A. C. Guyton and J. E. Hall. *Textbook of medical physiology*. 10th ed. Philadelphia: Saunders, 2001. ISBN: 978-0-7216-8677-6.

[164] A. L. Goldberger, Z. D. Goldberger, and A. Shvilkin. *Goldberger's clinical electrocardiography: A simplified approach*. 8th ed. Philadelphia, PA: Elsevier/Saunders, 2013. ISBN: 0323091563.

[165] *Heart - Wikipedia*. 2020-04-26T22:56:45.000Z. URL: https://en.wikipedia.org/wiki/Heart#/media/File:Diagram_of_the_human_heart_(cropped).svg.

[166] *2101 Blood Flow Through the Heart - File:2101 Blood Flow Through the Heart.jpg - Wikimedia Commons*. 2020-04-16T11:54:51.000Z.

[167] T. Barclay. *Cardiovascular System - Human Veins, Arteries, Heart*. 2020-05-01T06:44:57.000Z. URL: https://www.innerbody.com/image/cardov.html#continued.

[168] *File:ConductionsystemoftheheartwithouttheHeart-en.svg - Wikimedia Commons*. 2020-04-26T07:44:31.000Z. URL: https://commons.wikimedia.org/wiki/File:ConductionsystemoftheheartwithouttheHeart-en.svg#/media/File:ConductionsystemoftheheartwithouttheHeart-en.svg.

[169] V. Fuster, A. R. Wayne, and R. A. O'Rourke. *Hurst's the heart*. 10a ed., International edition. New York, N. Y.: McGraw-Hill, 2001. ISBN: 978-0071162968.

[170] "Heart rate variability: standards of measurement, physiological interpretation and clinical use. Task Force of the European Society of Cardiology and the North American Society of Pacing and Electrophysiology". *Circulation* 93.5 (1996), pp. 1043–1065. ISSN: 0009-7322.

[171] M. J. Reed, C. E. Robertson, and P. S. Addison. "Heart rate variability measurements and the prediction of ventricular arrhythmias". *QJM : monthly journal of the Association of Physicians* 98.2 (2005), pp. 87–95. ISSN: 1460-2725. DOI: 10.1093/qjmed/hci018.

[172] R. E. Kleiger, J. P. Miller, J. T. Bigger, and A. J. Moss. "Decreased heart rate variability and its association with increased mortality after acute myocardial infarction". *The American Journal of Cardiology* 59.4 (1987), pp. 256–262. ISSN: 00029149. DOI: 10.1016/0002-9149(87)90795-8.

[173] Z. Visnovcova et al. "Complexity and time asymmetry of heart rate variability are altered in acute mental stress". *Physiological measurement* 35.7 (2014), pp. 1319–1334. DOI: 10.1088/0967-3334/35/7/1319.

[174] M. Calvo et al. "Heart rate complexity analysis in Brugada syndrome during physical stress testing". *Physiological measurement* 38.2 (2017), pp. 387–396. DOI: 10.1088/1361-6579/aa513c.

[175] B. Lown, W. F. Ganong, and S. A. Levine. "The syndrome of short P-R interval, normal QRS complex and paroxysmal rapid heart action". *Circulation* 5.5 (1952), pp. 693–706. ISSN: 0009-7322. DOI: 10.1161/01.cir.5.5.693.

[176] M. E. Josephson. *Josephson's clinical cardiac electrophysiology: Techniques and interpretations*. 5th ed. Baltimore, MD and Philadelphia, PA: Wolters Kluwer, 2016. ISBN: 9781496326614.

[177] D. T. Huang and T. Prinzi, eds. *Clinical Cardiac Electrophysiology in Clinical Practice*. In Clinical Practice. London: Springer London, 2015. ISBN: 978-1-4471-5433-4.

[178] A. Bhatia, J. Sra, and M. Akhtar. "Preexcitation Syndromes". *Current problems in cardiology* 41.3 (2016), pp. 99–137. DOI: 10.1016/j.cpcardiol.2015.11.002.

[179] S.-J. Park et al. "Short- and long-term outcomes depending on electrical dyssynchrony markers in patients presenting with acute heart failure: clinical implication of the first-degree atrioventricular block and QRS prolongation from the Korean Heart Failure registry". *American heart journal* 165.1 (2013), 57–64.e2. DOI: 10.1016/j.ahj.2012.10.009.

[180] S. Cheng et al. "Long-term Outcomes in Individuals with a Prolonged PR Interval or First-Degree Atrioventricular Block". *JAMA : the journal of the American Medical Association* 301.24 (2009), pp. 2571–2577. ISSN: 0098-7484. DOI: 10.1001/jama.2009.888.

[181] M. B. Conover. *Understanding electrocardiography*. 8th ed. St. Louis, Mo.: Mosby, 2003. ISBN: 978-0-323-01905-7.

[182] L. Mignanelli, A. Luik, K. Kroschel, L. Scalise, and C. Rembe. "Auswertung von Vibrometersignalen zur Bestimmung kardiovaskulärer Parameter". *tm-Technisches Messen* 83.9 (2016). ISSN: 0171-8096. DOI: 10.1515/teme-2015-0113.

[183] L. Mignanelli and C. Rembe. "Algorithm for automatic detection of the cardiovascular parameter PR-interval from LDV-velocity signals". In: AIP Conference Proceedings. Author(s), 2016, p. 050002. DOI: 10.1063/1.4952666.

[184] L. Mignanelli, G. Bauer, M. Klarmann, H. Wang, and C. Rembe. "Influence of the measuring condition on vibrocardiographic signals acquired on the thorax with a laser Doppler vibrometer". In: *Clinical and Preclinical Optical Diagnostics*. Ed. by J. Quincy Brown and Ton G. van Leeuwen. SPIE Proceedings. SPIE, 2017, p. 1041105. DOI: 10.1117/12.2282894.

[185] H. Wang. "Testing and Comparison of different Filtering Methods applied on Vibrocardiographic (VBCG) Signals acquired on the Thorax". MA thesis. TU-Clausthal, 2017.

[186] M. Klarmann. "Untersuchung verschiedener Einflussfaktoren auf das Vibrokardiographiesignal bei Messung auf dem Thorax". MA thesis. TU-Clausthal, 2017.

[187] S. J. Orfanidis. *Optimum signal processing: An introduction*. 2nd ed. New York, NY: Macmillan, 1988. ISBN: 002389380X.

[188] J. L. Myers, A. D. Well, and R. F. Lorch Jr. *Research Design and Statistical Analysis: Third Edition*. 3rd ed. Hoboken: Taylor and Francis, 2013. ISBN: 9780805864311. URL: http://gbv.eblib.com/patron/FullRecord.aspx?p=1112541.

[189] N. J. Salkind, ed. *Encyclopedia of measurement and statistics. Vol. 1*. Thousand Oaks, Calif.: SAGE Publications, 2007. ISBN: 978-1-412-91611-0.

[190] G. J. Diebold. "Photoacoustic Monopole Radiation: Waves from Objects with Symmetry in One, Two, and Three Dimensions". In: *Photoacoustic Imaging and Spectroscopy*. Ed. by Lihong V. Wang. CRC Press, 2017, pp. 3–18. ISBN: 9781315219097. DOI: 10.1201/9781420059922-2.

[191] R. O. Esenaliev et al. "Laser optoacoustic imaging for breast cancer diagnostics: limit of detection and comparison with x-ray and ultrasound imaging". In: *Optical Tomography and Spectroscopy of Tissue: Theory, Instrumentation, Model, and Human Studies II*. Ed. by Britton Chance and Robert R. Alfano. SPIE Proceedings. SPIE, 1997, pp. 71–82. DOI: 10.1117/12.280213.

[192] G. Gouy. "Sur la propagation anomale des ondes". In: *Annales de chimie et de physique*. 6e série, t. XXIV. 1891, pp. 145–213.

[193] G. D. Ludwig. "The Velocity of Sound through Tissues and the Acoustic Impedance of Tissues". *The Journal of the Acoustical Society of America* 22.6 (1950), pp. 862–866. ISSN: 0001-4966. DOI: 10.1121/1.1906706.

[194] G. J. Diebold and P. J. Westervelt. "The photoacoustic effect generated by a spherical droplet in a fluid". *The Journal of the Acoustical Society of America* 84.6 (1988), pp. 2245–2251. ISSN: 0001-4966. DOI: 10.1121/1.397017.

[195] A. A. Oraevsky and A. A. Karabutov. "Ultimate sensitivity of time-resolved optoacoustic detection". In: *Biomedical Optoacoustics*. Ed. by Alexander A. Oraevsky. SPIE Proceedings. SPIE, 2000, pp. 228–239. DOI: 10.1117/12.386326.

[196] A. A. Oraevsky, V. A. Andreev, A. A. Karabutov, and R. O. Esenaliev. "Two-dimensional optoacoustic tomography: transducer array and image reconstruction algorithm". In: *Laser-Tissue Interaction X: Photochemical, Photothermal, and Photomechanical*. Ed. by Steven L. Jacques, Gerhard J. Mueller, Andre Roggan, and David H. Sliney. SPIE Proceedings. SPIE, 1999, p. 256. DOI: 10.1117/12.350007.

[197] B. Cox, J. G. Laufer, S. R. Arridge, and P. C. Beard. "Quantitative spectroscopic photoacoustic imaging: a review". *Journal of biomedical optics* 17.6 (2012), p. 061202. DOI: 10.1117/1.JBO.17.6.061202.

[198] X. Zhou, N. Akhlaghi, K. A. Wear, B. S. Garra, T. J. Pfefer, and W. C. Vogt. "Evaluation of Fluence Correction Algorithms in Multispectral Photoacoustic Imaging". *Photoacoustics* 19 (2020), p. 100181. ISSN: 2213-5979. DOI: 10.1016/j.pacs.2020.100181.

[199] P. La Rivière, J. Zhang, and M. A. Anastasio. "Image Reconstruction in Optoacoustic Tomography Accounting for Frequency-Dependent Attenuation". In: *Photoacoustic Imaging and Spectroscopy*. Ed. by Lihong V. Wang. CRC Press, 2017, pp. 145–154. ISBN: 9781315219097. DOI: 10.1201/9781420059922-2.

[200] N. V. Sushilov and R. S. C. Cobbold. "Frequency-domain wave equation and its time-domain solutions in attenuating media". *The Journal of the Acoustical Society of America* 115.4 (2004), pp. 1431–1436. ISSN: 0001-4966. DOI: 10.1121/1.1675817.

[201] M. O. Culjat, D. Goldenberg, P. Tewari, and R. S. Singh. "A review of tissue substitutes for ultrasound imaging". *Ultrasound in Medicine & Biology* 36.6 (2010), pp. 861–873. ISSN: 0301-5629. DOI: 10.1016/j.ultrasmedbio.2010.02.012.

[202] L. Mignanelli and C. Rembe. "Feasibility study of the employment of laser Doppler Vibrometry for photoacoustic imaging". *Journal of Physics: Conference Series* 1149 (2018), p. 012028. ISSN: 1742-6588. DOI: 10.1088/1742-6596/1149/1/012028.

[203] S. L. Kramer. *Geotechnical earthquake engineering*. Prentice-Hall international series in civil engineering and engineering mechanics. Upper Saddle River, NJ: Prentice-Hall, 1996. ISBN: 0133749436.

[204] S. Park, S. R. Aglyamov, and S. Emelianov. "10A-5 Beamforming for Photoacoustic Imaging Using Linear Array Transducer". In: *IEEE Ultrasonics Symposium, 2007*. Piscataway, NJ: IEEE Operations Center, 2007, pp. 856–859. ISBN: 978-1-4244-1383-6. DOI: 10.1109/ULTSYM.2007.219.

[205] A. A. Oraevsky. "Optoacoustic Tomography of the Breast". In: *Photoacoustic Imaging and Spectroscopy*. Ed. by Lihong V. Wang. CRC Press, 2017, pp. 411–429. ISBN: 9781315219097. DOI: 10.1201/9781420059922-2.

[206] *OFV-2500 Vibrometer Controllers*. URL: http://lb-acoustics.ro/wp-content/uploads/2016/03/OM_DS_OFV_2500_2010_08_E.pdf (visited on 10/17/2020).

[207] *OFV-5000 Modulares Vibrometer*. 2020-10-17T13:35:37.000Z. URL: https://www.polytec.com/de/vibrometrie/produkte/einpunkt-vibrometer/ofv-5000-modulares-vibrometer/ (visited on 10/17/2020).

[208] A. B. Pravdin, G. Filippidis, G. Zacharakis, T.G. Papazoglou, and V. V. Tuchin. "Tissue Phantoms". In: *Handbook of optical biomedical diagnostics*. Ed. by V. V. Tuchin. SPIE Press monograph. Bellingham, Washington, USA: SPIE PRESS, 2016. ISBN: 9781628419092. DOI: 10.1117/3.2219603.ch5.

[209] I. Daubechies. *Ten Lectures on Wavelets*. Society for Industrial and Applied Mathematics, 1992. ISBN: 978-0-89871-274-2. DOI: 10.1137/1.9781611970104.

[210] J. Sun, B. Zhang, Q. Feng, H. He, Y. Ding, and Q. Liu. "Photoacoustic Wavefront Shaping with High Signal to Noise Ratio for Light Focusing Through Scattering Media". *Scientific reports* 9.1 (2019), p. 4328. DOI: 10.1038/s41598-019-40919-6.

[211] J. R. Fincke, C. M. Wynn, R. Haupt, X. Zhang, D. Rivera, and B. Anthony. "Characterization of laser ultrasound source signals in biological tissues for imaging applications". *Journal of biomedical optics* 24.2 (2018), pp. 1–11. DOI: 10.1117/1.JBO.24.2.021206.

[212] V. E. Gusev and A. A. Karabutov. *Laser optoacoustics*. New York, NY: American Inst. of Physics, 1993. ISBN: 1563960362.

[213] A. Cafarelli, P. Miloro, A. Verbeni, M. Carbone, and A. Menciassi. "Speed of sound in rubber-based materials for ultrasonic phantoms". *Journal of ultrasound* 19.4 (2016), pp. 251–256. DOI: 10.1007/s40477-016-0204-7.

[214] S. Hartmann and R. R. Gilbert. "Identifiability of material parameters in solid mechanics". *Archive of Applied Mechanics* 88.1-2 (2018), pp. 3–26. ISSN: 0939-1533. DOI: 10.1007/s00419-017-1259-4.

[215] *Optisches Dilatometer DIL 806 – TA Instruments*. 24.2.2020. URL: https://www.tainstruments.com/dil-806/?lang=de.

[216] *DSC 404 F3 Pegasus® - NETZSCH Analyzing & Testing*. 24.2.2020. URL: https://www.netzsch-thermal-analysis.com/en/products-solutions/differential-scanning-calorimetry/dsc-404-f3-pegasus/.

[217] G. Machado, G. Chagnon, and D. Favier. "Analysis of the isotropic models of the Mullins effect based on filled silicone rubber experimental results". *Mechanics of Materials* 42.9 (2010), pp. 841–851. ISSN: 01676636. DOI: 10.1016/j.mechmat.2010.07.001.

[218] G. W. H. Höhne, H.-J. Flammersheim, and W. Hemminger. *Differential scanning calorimetry: With 19 tables*. 2., rev. and enl. ed. Berlin: Springer, 2003. ISBN: 978-3-642-05593-5.

[219] K. Zell, J. I. Sperl, M. W. Vogel, R. Niessner, and C. Haisch. "Acoustical properties of selected tissue phantom materials for ultrasound imaging". *Physics in medicine and biology* 52.20 (2007), N475–84. DOI: 10.1088/0031-9155/52/20/N02.

[220] A. Pacioni, M. Carbone, C. Freschi, R. Viglialoro, V. Ferrari, and M. Ferrari. "Patient-specific ultrasound liver phantom: materials and fabrication method". *International Journal of Computer Assisted Radiology and Surgery* 10.7 (2015), pp. 1065–1075. ISSN: 1861-6410. DOI: 10.1007/s11548-014-1120-y.

[221] L. E. Maggi, M. A. von Kruger, W. C. A. Pereira, and E. E. C. Monteiro. "Development of silicon-based materials for ultrasound biological phantoms". In: *2009 IEEE International Ultrasonics Symposium*. IEEE, 20.09.2009 - 23.09.2009, pp. 1962–1965. ISBN: 978-1-4244-4389-5. DOI: 10.1109/ULTSYM.2009.5441472.

[222] *Thorlabs - ES220C Pyroelectric Energy Sensor, Ceramic Coating, 0.185 - 25 µm, 3 J*. 26.2.2020.

[223] A. J. Welch and M. J.C. Gemert. *Optical-Thermal Response of Laser-Irradiated Tissue*. 2. ed. Dordrecht: Springer Science+Business Media B.V, 2011. ISBN: 9789048188307. DOI: 10.1007/978-90-481-8831-4. URL: http://gbv.eblib.com/patron/FullRecord.aspx?p=666701.

[224] *Safety of laser products - Part 1: Equipment classification and requirements (IEC 60825-1:2014)*. Standard. Geneva, CH: International Electrotechnical Commission, May 2014.

[225] J. G. Koelzer, G. Mitic, J. Otto, and W. Zinth. "Measurements of the optical properties of breast tissue using time-resolved transillumination". In: *Photon Transport in Highly Scattering Tissue*. Ed. by Sigrid Avrillier, Britton Chance, Gerhard J. Mueller, Alexander V. Priezzhev, and Valery V. Tuchin. SPIE Proceedings. SPIE, 1995, pp. 143–152. DOI: 10.1117/12.200841.

[226] T. L. Rhyne. "Characterizing ultrasonic transducers using radiation efficiency and reception noise figure". *IEEE transactions on ultrasonics, ferroelectrics, and frequency control* 45.3 (1998), pp. 559–566. ISSN: 0885-3010. DOI: 10.1109/58.677600.

[227] S. Basiri-Esfahani, A. Armin, S. Forstner, and W. P. Bowen. "Precision ultrasound sensing on a chip". *Nature communications* 10.1 (2019), p. 132. DOI: 10.1038/s41467-018-08038-4.

[228] R. Kowarsch and C. Rembe. "Laser-Doppler vibrometry with variable GHz heterodyne carrier via frequency-offset lock". In: *Interferometry XIX*. Ed. by Katherine Creath, Jan Burke, Michael B. North Morris, and Angela D. Davies. Proceedings of SPIE. 5200-. Bellingham, Washington, USA: SPIE, 2018, p. 10. ISBN: 9781510620698. DOI: 10.1117/12.2324725. URL: https://www.spiedigitallibrary.org/conference-proceedings-of-spie/10749/2324725/Laser-Doppler-vibrometry-with-variable-GHz-heterodyne-carrier-via-frequency/10.1117/12.2324725.full.

[229] E. Z. Zhang and P. C. Beard. "A miniature all-optical photoacoustic imaging probe". In: *Photons Plus Ultrasound: Imaging and Sensing 2011*. Ed. by Alexander A. Oraevsky and Lihong V. Wang. SPIE Proceedings. SPIE, 2011, 78991F. DOI: 10.1117/12.874883.

[230] L. Mignanelli and C. Rembe. "Uncertainty contribution of the laser-beam orientation for laser Doppler vibrometer measurements at the carotid artery". *Journal of Physics: Conference Series* 1149 (2018), p. 012025. ISSN: 1742-6588. DOI: 10.1088/1742-6596/1149/1/012025.

[231] B. Alhaji et al. "Engineering Human-Machine Teams for Trusted Collaboration". *Big Data and Cognitive Computing* 4.4 (2020). ISSN: 2504-2289. DOI: 10.3390/bdcc4040035. URL: https://www.mdpi.com/2504-2289/4/4/35.

[232] K. Munck, K. Sørensen, J. J. Struijk, and S. E. Schmidt. "Multichannel seismocardiography: an imaging modality for investigating heart vibrations". *Physiological measurement* (2020). DOI: 10.1088/1361-6579/abc0b7.

[233] P. P. Sengupta, A. J. Tajik, K. Chandrasekaran, and B. K. Khandheria. "Twist mechanics of the left ventricle: principles and application". *JACC. Cardiovascular imaging* 1.3 (2008), pp. 366–376. DOI: 10.1016/j.jcmg.2008.02.006.

[234] L. Casacanditella, G. Cosoli, S. Casaccia, J. W. Rohrbaugh, L. Scalise, and E. P. Tomasini. "Characterization and calibration of the central arterial pressure waveform obtained from vibrocardiographic signal". In: AIP Conference Proceedings. Author(s), 2016, p. 050006. DOI: 10.1063/1.4952670.

[235] L. Scalise, U. Morbiducci, and M. de Melis. "A laser Doppler approach to cardiac motion monitoring: effects of surface and measurement position". In: *Seventh International Conference on Vibration Measurements by Laser Techniques: Advances and Applications*. SPIE Proceedings. SPIE, 2006, p. 63450D. DOI: 10.1117/12.693151.